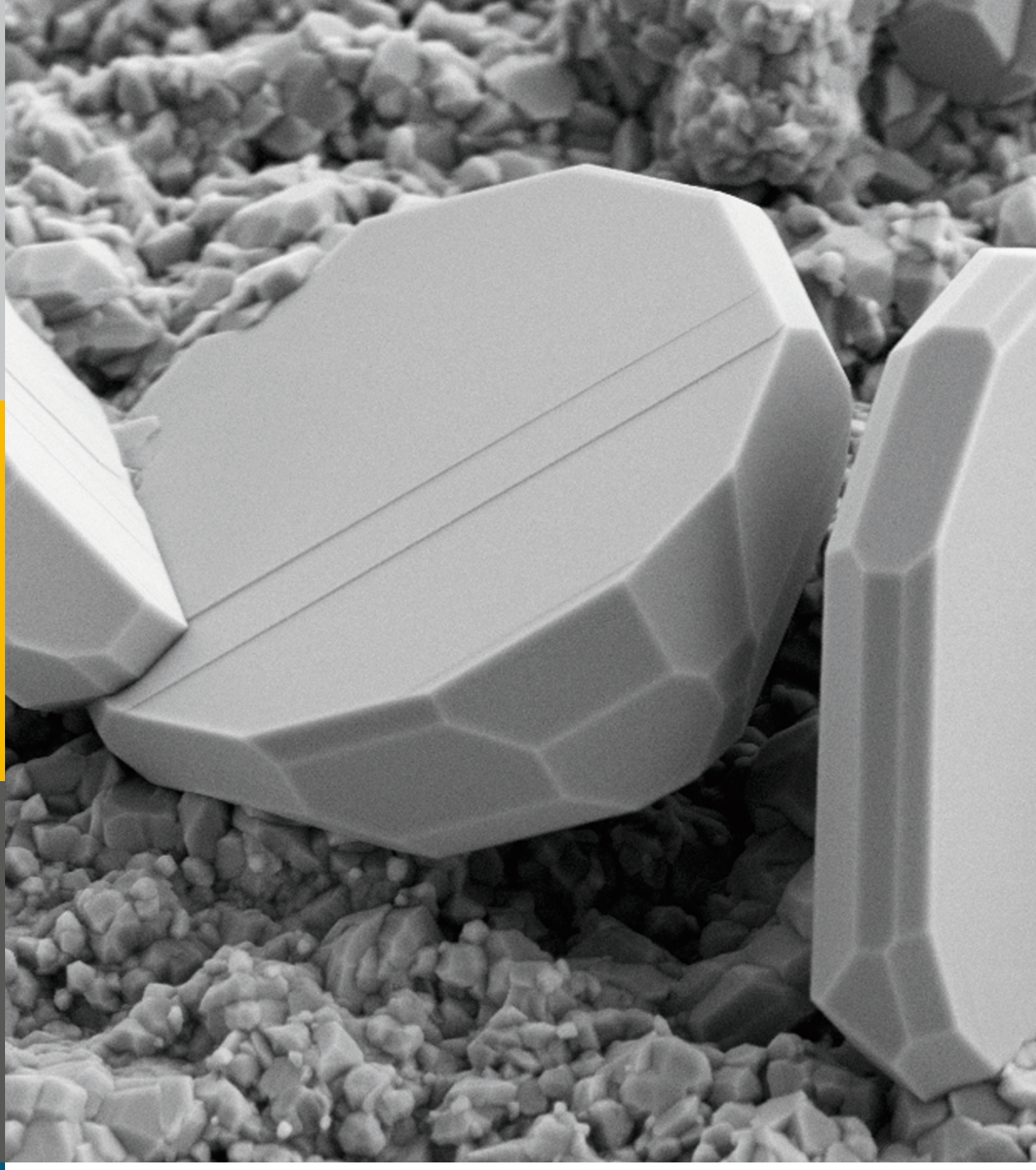

Effect of Composition, Microstructure and Component Thickness on the Oxidation Behaviour of Laves Phase Strengthened Interconnect Steel for Solid Oxide Fuel Cells (SOFC)

Cristina Asensio Jimenez

JÜLICH
FORSCHUNGSZENTRUM

Member of the Helmholtz Association

Schriften des Forschungszentrums Jülich
Reihe Energie & Umwelt / Energy & Environment Band / Volume 204

Forschungszentrum Jülich GmbH
Institute of Energy and Climate Research (IEK)
Microstructure and Properties of Materials (IEK-2)

Effect of Composition, Microstructure and Component Thickness on the Oxidation Behaviour of Laves Phase Strengthened Interconnect Steel for Solid Oxide Fuel Cells (SOFC)

Cristina Asensio Jimenez

Schriften des Forschungszentrums Jülich
Reihe Energie & Umwelt / Energy & Environment Band / Volume 204

ISSN 1866-1793 ISBN 978-3-89336-935-5

Bibliographic information published by the Deutsche Nationalbibliothek.
The Deutsche Nationalbibliothek lists this publication in the Deutsche Nationalbibliografie; detailed bibliographic data are available in the Internet at http://dnb.d-nb.de.

Publisher and Distributor: Forschungszentrum Jülich GmbH
Zentralbibliothek
52425 Jülich
Tel: +49 2461 61-5368
Fax: +49 2461 61-6103
Email: zb-publikation@fz-juelich.de
www.fz-juelich.de/zb

Cover Design: Grafische Medien, Forschungszentrum Jülich GmbH

Printer: Grafische Medien, Forschungszentrum Jülich GmbH

Schriften des Forschungszentrums Jülich
Reihe Energie & Umwelt / Energy & Environment, Band / Volume 204

D 82 (Diss., RWTH Aachen University, 2013)

ISSN 1866-1793
ISBN 978-3-89336-935-5

The complete volume is freely available on the Internet on the Jülicher Open Access Server (JUWEL) at www.fz-juelich.de/zb/juwel

List of publications

Parts of the results presented in this thesis have already been published in the following articles:

C. Asensio Jimenez, A. Chyrkin, L. Niewolak, V. Konoval, H. Hattendorf, B. Kuhn, L. Singheiser and W. J. Quadakkers, “Subsurface depletion and enrichment processes during oxidation of high chromium, Laves-phase strengthened ferritic steel”, Electrochemical and Solid-State Letters, 14 (8) P17-P20 (2011).

B. Kuhn, C. Asensio Jimenez, L. Niewolak, T. Hüttel, T. Beck, H. Hattendorf. L. Singheiser, W. J. Quadakkers, “Effect of Laves phase strengthening on the mechanical properties of high Cr ferritic steels for solid oxide fuel cell interconnect application” Material Science and Engineering *A* 528, pp.5888-5899, (2011).

C. Asensio Jimenez, L. Niewolak, H. Hattendorf, B. Kuhn, P. Huczkowski, L. Singheiser, W. J. Quadakkers, “Effect of specimen thickness on the oxidation rate of high chromium ferritic steels-the significance of intrinsic alloy creep strength”, accepted for publication in Oxidation of Metals, in press, (2012).

Kurzfassung

Der hoch-chromhaltige, Laves-Phasen verfestigte ferritische Stahl Crofer 22 H ist ein potentiell geeigneter Kandidat als Konstruktions Werkstoff für Interkonnektoren in Festelektrolyt-Brennstoffzellen (SOFCs).

Die vorliegende Arbeit hatten eine Untersuchung der SOFC-relevanten Eigenschaften, insbesondere Oxidationsverhalten und elektrische Leitfähigkeit in SOFC-Betriebsgasen als Funktion der Temperatur zum Ziel, mit Schwerpunkt auf der meist verwendeten Betriebstemperatur von 800 °C.

Die Untersuchungen an Crofer 22 H ergaben, dass der Chromverbrauch als Folge der Deckschichtbildung die Bildung einer Laves-Phasen verarmten Zone in Oberflächennähe zur Folge hat. Parallel bildet sich eine Zone an der Oxid/Stahl-Grenzfläche in der die Laves-Phase angereichert ist. Mathematische Modellierung ergab, dass die Verarmung/Anreicherung durch den Einfluss der Chromkonzentration auf die Niobaktivität in der Stahlmatrix erklärt werden kann. Zusätzlich wurde durch Versuche mit lösungsgeglühtem und gealtertem Material gezeigt, dass die oberflächennahen Umwandlungsvorgänge zumindest teilweise auf eine bevorzugte Keimbildung der Laves-Phase an der Stahl/Oxid-Grenzfläche zurück zu führen sind.

Experimentelle Untersuchungen und theoretische Betrachtungen zeigten, dass die Abhängigkeit der Oxidationsrate von der Komponenten-/Probendicke mit dem Abbau von Oxid-Wachstumsspannungen mit Kriechen des metallischen Substrats korreliert ist. Wegen der geringen intrinsischen Kriechbeständigkeit von Crofer 22 APU, zeigen dünne Proben dieses Werkstoffs bei 800 °C in Luft höhere Oxidationsraten als dicke Proben. Für den kriechbeständigeren Crofer 22 H geschieht dies nur nach einem Verlust an intrinsischer Festigkeit durch Vergröberung der Laves-Phase. In diesem Fall wird die Resistenz der dünnsten Proben gegen Kriechverformung zu gering, um signifikante Relaxation von Oxid-Wachstumsspannungen zu verhindern; dies führt zu einer erhöhten Oxidationsrate. In Anodengas trat eine deutliche Abhängigkeit der Oxidationsrate von

der Probendicke nicht auf. Dies ist wahrscheinlich auf die unterschiedliche Zusammensetzung und Mikrostruktur der Deckschichten zurück zu führen.

Wolframzusätze bis zu etwa 3 % in Nb-freiem Stahl vom Typ Crofer 22 hatten keinen signifikanten Einfluss auf das Oxidationsverhalten von Proben mit einigen Millimetern Dicke in Luft oder Anodengas. Wolframzusätze reduzieren jedoch das Oxidwachstum dünner Proben ($d < 1$ mm) während der Oxidation in Luft wegen der Erhöhung der intrinsischen Kriechbeständigkeit des Werkstoffs. Zusätze von höheren Wolframgehalten (> 4 %) resultieren bei 800 °C in der Bildung von Ausscheidungen vom Typ χ-$Cr_7Fe_{10}W_3$ und λ-$(Fe,Cr)_2W$. Wolframzusätze bis zu 7 % führen nicht zu einer Unterdrückung der Bildung von SiO_2 unterhalb der Cr-Oxidschicht bei Stählen vom Typ Crofer 22 mit typischen Si-Konzentrationen von etwa 0.25 %.

Langzeitversuche in Luft zeigten, dass ein geringer Mn-Zusatz von großer Bedentung ist für die Unterdrückung der Cr-Verdampfung.

Eine wichtige Eigenschaft von metallischen Interkonnektorwerkstoffen ist eine hohe elektrische Leitfähigkeit der oxidischen Deckschichten bei Betriebstemperatur der SOFC. Die experimentellen Ergebnisse zeigten, dass die elektrische Leitfähigkeit der Oxidschichten auf Crofer 22 H in Luft mit der von Crofer 22 APU vergleichbar ist.

Abstract

The high-Cr, Laves phase strengthened ferritic steel, Crofer 22 H, has recently been proposed as construction material for interconnects in solid oxide fuel cells (SOFC). Aim of the present investigation was to get more insight in the details of SOFC relevant properties, mostly oxidation behaviour and oxide electronic conductivity, in simulated SOFC service environments as a function of temperature, with main emphasis on the most commonly used operating temperature 800 °C.

The present studies of Crofer 22 H, showed that the consumption of chromium from the alloy as a result of chromia surface scale formation ends up in formation of a subsurface layer in which the Laves phase is depleted. In parallel, formation of a thin zone near the scale/steel interface occurs in which the Laves phase is enriched. Modeling revealed that this depletion/enrichment process can be explained by the influence of chromium concentration on the niobium activity in the alloy matrix. Moreover, experiments with solution annealed and pre-aged materials showed that the subsurface phase transformation processes are at least partially affected by preferential Laves-phase nucleation at the scale/steel interface.

Experimental results and theoretical considerations show that the specimen/component thickness dependence of the oxidation rate is related to relaxation of oxide growth stress by creep of the metallic substrate. Due to poor intrinsic creep resistance, thin Crofer 22 APU specimens exhibit enhanced oxidation rates in air at 800 °C. For the more creep resistant steel Crofer 22 H this only occurs after Laves phase coarsening which results in a substantial decrease in intrinsic creep strength of the alloy. The resistance of the thinnest samples against substantial creep deformation then becomes gradually too small to prevent substantial relaxation of oxide growth stress, leading to enhanced oxidation rates. However, in anode gas hardly any specimen/component thickness dependence of the oxidation rate was found, which is believed to be related to a different oxide scale composition and microstructure.

Tungsten additions up to approximately 3 wt. % in Nb free high Cr steel of the type Crofer 22 were found to have no substantial influence on the intrinsic oxidation properties when considering samples of a few millimeter thickness in air and in simulated anode gas. However, tungsten addition to Crofer 22 APU improves the air oxidation resistance at 800 °C of thin ($d < 1$ mm) specimens due to improved alloy creep strength. The results, in combination with previous findings revealed that adding more than 4 wt. % tungsten results at 800 °C in formation of χ-$Cr_7Fe_{10}W_3$ and/or λ-$(Fe,Cr)_2W$ precipitates. Tungsten additions up to 7 wt. % do not suppress the formation of silica sub-layers in Crofer 22 type steels with typical silicon contents of approximately 0.25 wt. %.

Presence of minor amounts of Mn were found to be crucial for suppressing Cr evaporation during air oxidation.

A major property required for a metallic interconnect material is a suitable electronic conductivity of the surface oxide scales at the SOFC service temperature. The experimental results showed that the electrical conductivity of the oxide scales formed during air exposure of Crofer 22 H were in a similar range as the values measured for Crofer 22 APU.

Table of contents

1. Introduction

Considering the global population growth and the growing demand for energy and its consequent environmental impacts, the power generation by clean, safe, efficient and environmental-friendly means is now one of the major challenges for engineers and scientists [1]. Fuel cells convert chemical energy of a fuel gas directly into electric current, and are efficient and environmentally clean, since no combustion is required. Thus, if pure hydrogen is used as fuel the only reaction product is water. Among the different fuel cell types, the solid oxide fuel cell (SOFC) appears as one of the most promising technologies. SOFCs operate at elevated temperature (typically 700-900 °C). The high temperature is needed to ensure a sufficient ionic conductivity of the solid electrolyte, and to have the advantages of high conversion efficiency and the flexibility of using hydrocarbon fuels, in addition to hydrogen [2].

The SOFC technology has progressed significantly during the last several years, however, the frequently observed deterioration of fuel cell performance can be regarded as a major technical limitation, and therefore further development is needed to make it a competitive technology. One of the possibilities to get better technological solutions is the improvement of the materials for the different cell components, i.e. anode, cathode, electrolyte and interconnect. Ferritic steels seem to be the group of materials which fulfill the necessary combination of properties required for interconnect application [3-4].

The particular requirements for the interconnect include high temperature oxidation resistance in anode and cathode environment, thermal expansion coefficient compatible with the ceramic components and a high electrical conductivity of the oxide scales under the SOFC operating conditions [5-6].

High-Cr ferritic steels are considered as the most promising construction materials for interconnects. A ferritic steel which was specifically developed for SOFC application is Crofer 22 APU [7-8]. This steel was optimized with careful control of minor alloying additions and impurities but this high purity results in a poor creep resistance at the

SOFC operating temperatures. To overcome this disadvantage which is especially relevant for very thin interconnects, a new type of ferritic steel Crofer 22 H was developed which possesses higher creep strength mainly due to Laves phase precipitates [9-10]. In the present thesis the microstructural features and oxidation properties of the Laves phase strengthened steel as function of time and temperature were investigated. Special emphasis was put on the oxide scale composition and subsurface phase transformation as function of time and temperature thereby considering possible variations in main alloy composition. Additionally, the consequence of the higher creep strength for the oxidation behavior of thin components was evaluated. Finally, the electrical conductivity of the surface oxide scales was compared with that of the high purity, near-single-phase alloys of the type Crofer 22 APU.

2. Literature review

2.1 Fuel cells

A fuel cell is a device that converts chemical energy in the fuel into electrical energy. The operating principles are similar to those of batteries. However, different to a battery, a fuel cell does not require recharging and operates as long as both fuel and oxidant are supplied externally to the electrodes [1]. In this aspect, a fuel cell is similar to a combustion engine but because it does not need a combustion step it allows much higher conversion efficiencies.

2.2 History of fuel cells

The invention of fuel cells dates back from the middle of the 19th century when William R. Grove, by connecting a hydrogen anode and an oxygen cathode, produced an electric current so he was who built the first real fuel cell. However, it was Christian Friedrich Schoenbein who first discovered the fuel cell effect [11]. Unfortunately, the development of the dynamo technology in 1866 by Werner von Siemens overshadowed the discovery of this promising energy converter.

In 1905, Wilhelm Ostwald and Nernst presented a general theory of fuel cells. But due to easily accessible and large amounts of oil and the invention of the combustion engine, fuel cells were forgotten until the middle of the 20th century. In the US Apollo space program, fuel cells exhibited their first renaissance in the 1960's [1]. The Gemini 5 was the first space shuttle using a polymer membrane fuel cell to replace the battery. Due to better performance, alkaline fuel cells were used in the Apollo missions and supplied the electric power when the USA landed on the moon in 1969 [1]. The first oil crisis in 1973 led to the second renaissance, where especially the interest for large power plants based on high-temperature fuel cells increased. Fuel cell development has been slowed down by a fear of hydrogen as a fuel. However, hydrogen is lighter than air, so it disperses quickly to a non-explosive mixture when a leak occurs. Hydrogen is non-toxic and less flammable than gasoline [12].

2.3 Principle of a fuel cell

There are three components which are necessary to the electrochemical reaction in a fuel cell: an anode, a cathode and an ion conducting electrolyte. Fuel (e.g. hydrogen) is fed to the anode and the oxidant (often oxygen from air) is fed to the cathode [13]. The fuel cell separates hydrogen and oxygen with a gas-impermeable electrolyte through which only ions can migrate and so prevent the chemical combustion [14]. Hence, two half reactions occur at the two electrodes producing ions that pass through the electrolyte and react giving off water as product at the anode side. The flow of ionic charges due to ion movement through the electrolyte is balanced by the flow of electrons through an outside circuit and produces direct current electricity [15].

2.4 Types of fuel cells

The most common classification of fuel cells is by the type of electrolyte used in the cells and includes 1) alkaline fuel cells (AFC), 2) phosphoric acid fuel cells (PAFC), 3) molten carbonate fuel cells (MCFC), 4) proton exchange membrane fuel cells (PEMFC), and 5) solid oxide fuel cells (SOFC) [16]. Broadly, the choice of electrolyte dictates the operating temperature range of the fuel cell. The operating temperature and useful life of a fuel cell dictate the physico-chemical and thermo-mechanical properties of materials used in the cell components. Table 1 shows an overview of the key characteristics of the main fuel cell types.

Table 1: Summary of major features of the various fuel cell types.[16-17].

Type	AFC	PEMFC	PAFC	MCFC	SOFC
Electrolyte	KOH	Polymer	H_3PO_4	Carbonate	Solid oxide
Fuel	H_2	H_2/CO/CH_3OH	H_2/CO	H_2/CO	H_2/CO
T (°C)	80-200	80-120	180-210	600-700	600-1000
Charge Carrier	OH^-	H^+	H^+	CO_3^{2-}	O^{2-}
Applications	Used in space vehicles, and army	Vehicles and mobile applications	Large numbers of 200kW units in use	Suitable for medium to large scale systems	Suitable for all sizes from few kW until multi MW

2.5 Solid oxide fuel cells (SOFCs)

Compared with other fuel cell systems, the main advantage of the SOFC is its ability to use not only hydrogen but also the currently available fossil fuels thus reducing the operating costs and gaining in flexibility [18]. SOFCs possess no moving parts, so the cells are free of vibration, and also eliminates noise usually associated with conventional power generation systems [13, 18-19].

In an SOFC system, the single cell is constructed with a dense, oxygen-ion-conducting electrolyte arranged between two porous electrodes [14-15] (Figure 2.1). In operation, air flows along the cathode. When an oxygen molecule contacts the cathode/electrolyte interface, it catalytically acquires electrons from the external circuit and splits into oxygen ions which migrate to the anode through the electrolyte. At the anode, oxygen ions react with the fuel (H_2 and/or CO depending on fuel used) at the anode/electrolyte interface giving off water (and/or CO_2) and liberating electrons. The electrons are transported through the anode to the external circuit and back to the cathode, providing a source of useful electrical energy in an external circuit [20].

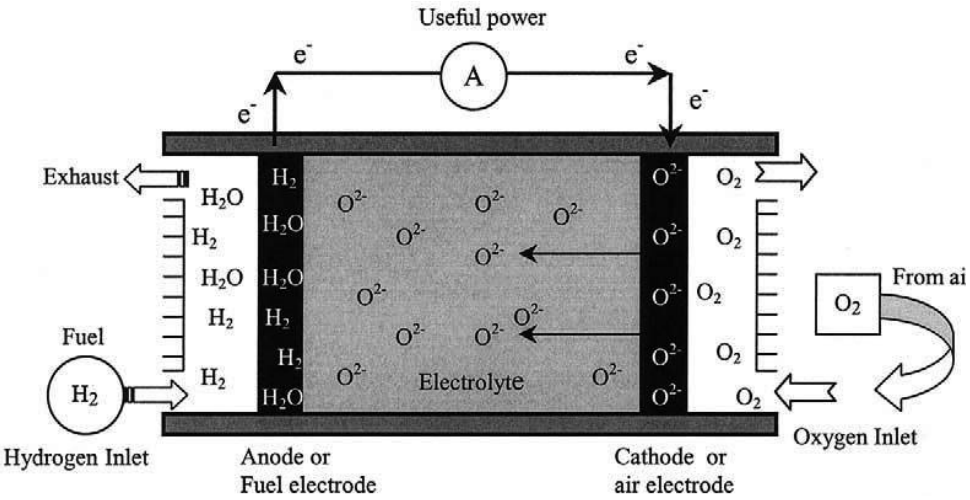

Figure 2.1: Principle of a SOFC [1].

2.6 SOFC - Technology features

2.6.1 Cell configuration

The configurations in SOFC single cells can be classified into two categories: self-supporting and external-supporting [13]. In the self-supporting configuration, one of the cell components, generally the thickest layer, acts as the cell structural support. In this way, single cells can be designed as electrolyte-supported, anode supported or cathode-supported. In the external-supporting configurations, the single cell is configured as thin layers on the interconnect or a porous substrate [13]. The Forschungszentrum Jülich uses an anode-supported cell design which has a high conductivity anode material and a very thin electrolyte allowing lower operating temperatures in the range 700–800 °C [21].

2.6.2 Stack design

In an SOFC, each single cell is connected with the next single cell by the interconnect plate and a stack is a set of connected singles cells. Taking into account the design configurations of the stack, two cases have been considered for SOFCs: the tubular and the planar design [22]. A tubular design does not need to use any sealant during operation at high temperature but shows as disadvantage that it has low power density and high cost. The planar design allows higher power densities than the tubular design [20]. However, it is very sensitive to thermal stresses and also requires high temperature gas seals at the edges of the plates to isolate the oxidant from the fuel [20]. In most planar designs, two additional components are present to improve the electrical contact between the interconnect and the anode and cathode, respectively: a Ni-wire mesh at the anode side and a ceramic contact layer with high electronic conductivity at the cathode side [18] (Figure 2.2).

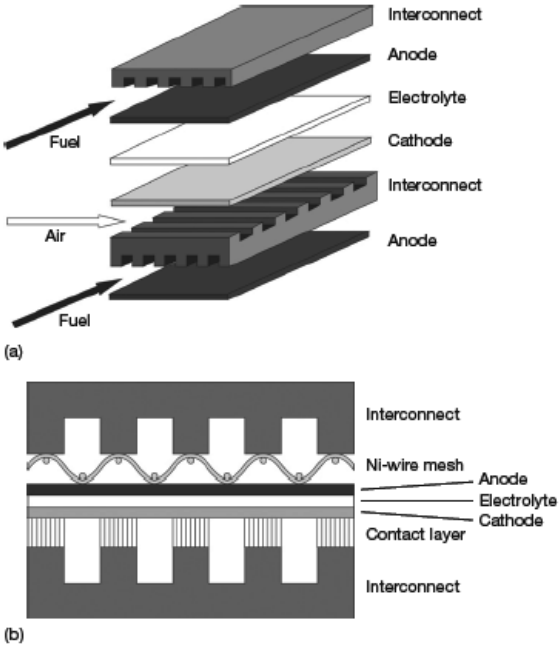

Figure 2.2: (a) Schematic configuration of a planar stack design of an SOFC and (b) schematic cross section showing the additional components for contacting the interconnect with the electrodes [18].

2.7 Materials

2.7.1 Electrolyte

After the molecular oxygen has been converted to oxygen ions it must migrate through the electrolyte to the fuel side of the cell [20]. In order for this migration to occur, the electrolyte must possess a high ionic conductivity and no electronic conductivity. It must be fully dense to prevent short circuiting of reacting gases through it and it should also be as thin as possible to minimize resistive losses in the cell [23]. There are several candidate ceramic materials for electrolytes: ytria-stabilized zirconia (YSZ), doped cerium oxide and doped bismuth oxide. YSZ has emerged as the most suitable electrolyte material. Yttria stabilizes zirconia into the cubic structure at high temperatures and also

provides oxygen vacancies at the rate of one vacancy per mole of dopant. A typical dopant level is 8-10 mol % yttria [22, 24].

2.7.2 Cathode

The cathode must be porous in order to allow oxygen molecules to reach the electrode/electrolyte interface. Today the most commonly used cathode material is lanthanum manganite ($LaMnO_3$), a p-type perovskite [25-27]. Typically, it is doped with rare earth elements (eg. Sr, Ce, Pr) to enhance its conductivity. Most often it is doped with strontium and referred to as LSM ($La_{1-x}Sr_xMnO_3$). Furthermore, no chemical reactions with the surrounding materials should occur, and the thermal expansion coefficient (TEC) should be close to that of the electrolyte to avoid mechanical stresses initiated during temperature changes [23]. A group of materials that fulfill most of the requirements for cathode materials are iron- and cobalt-containing perovskites, for example $(La,Sr)(Co,Fe)O_{3-\delta}$ (LSCF), that have already been known for their high oxygen permeability and high electrocatalytic activity. However, these materials have to be selected carefully because they have a significantly higher thermal expansion coefficient than the commonly used 8 mol % yttria-stabilised (8YSZ) electrolyte. Moreover, these types of perovskites tend to form $SrZrO_3$ with the 8YSZ electrolyte at high temperatures. To overcome these problems, an interlayer consisting of $(Ce,Gd)O_{2-\delta}$ (CGO) between cathode and electrolyte may be used [24].

2.7.3 Anode

The anode must meet most of the same requirements as the cathode for electrical conductivity, thermal expansion compatibility and porosity. Most development has focused on nickel due to its abundance and affordability [20]. However, its thermal expansion ($13.3 \times 10^{-6}\ K^{-1}$ compared with $10 \times 10^{-6}\ K^{-1}$ for YSZ) is too high to combine it in pure form with YSZ [20]; moreover, it tends to sinter and close off its porosity at operation temperatures. These problems have been solved by making the anode out of a Ni-YSZ composite. It must show high electrocatalytic activity toward oxidation of fuel gases. Porous Ni/YSZ cermet is currently the most common anode material for SOFC applications because it is used as current collector as well as oxidation catalyst. It is also

chemically stable in the anode side reducing atmospheres at high temperatures and its thermal expansion coefficient is close to that of the YSZ-electrolyte [28-29].

2.7.4 Interconnect

The interconnect or bipolar plate provides the electrical connection between various single cells, separates the fuel in the anode side from the air or oxygen in the cathode side and distributes the gases to the cells. Until recently, the main candidate for the interconnect was doped lanthanum chromite. However, the recent trend in reducing operating temperatures permits the use of metallic interconnect materials. They offer lower cost and easier fabrication than ceramics [2, 15, 30].

2.8 Requirements for interconnect materials

The main requirement which should be fulfilled for making a ceramic or metallic material suitable as construction material for SOFC interconnect are [30]:

- Coefficient of thermal expansion (CTE) similar to that of the ceramic components. For an anode supported planar cell design the CTE in the range between room temperature and 800°C should be approximately 12 x 10^{-6} K^{-1}, [30-32].
- Good workability
- Affordable materials cost
- High electronic conductivity
- Stability in the cathode and anode side service environment at the operating temperatures in the range 700 - 800°C

Considering the latter requirement it has to be borne in mind that the term “stability” does not mean that no material changes occur during exposure at the high service temperatures. Unlike noble metals common metallic construction materials are subject to oxidation when exposed to typical SOFC service environments. The requirement for “stability” can then only mean that the rates of oxidation remain within technologically

acceptable limits during the anticipated operating time of the SOFC [30, 33]. The suitability of a given material as interconnect thus largely depends on the properties of the surface oxide scales formed during high temperature service.

This also applies in relation to the requirements for high electronic conductivity. Metallic materials generally possess a sufficiently high electronic conductivity for application as interconnect in an SOFC. However, the overall applicability will mainly be governed by the far lower conductivities of the oxide layers formed on the interconnect surface during operation [34].

2.9 Fundamentals of oxidation

2.9.1 Basic thermodynamics

The oxidation reaction of a metal with an oxidizing environment leading to the formation of a metal oxide on its surface [34] can be written as:

$$xM_{(s)} + \frac{y}{2}O_{2(g)} = M_xO_{y(s)} \tag{2.1}$$

The question of whether or not a reaction can occur is answered by the second law of thermodynamics [35]. As most high temperature exposures take place at constant temperature and pressure, the second law is written in terms of the Gibbs free energy change:

$$\Delta G_{M_xO_y} = \Delta H_{M_xO_y} - T\Delta S_{M_xO_y} \tag{2.2}$$

where G is the Gibbs free energy, H is the enthalpy and S is the entropy of the system. According to this, change of the Gibbs free energy is an appropriate criterion for a prediction whether an oxidation process may occur at a given temperature [36]:

$\Delta G_{M_xO_y} < 0$, spontaneous reaction expected;

$\Delta G_{M_xO_y}$ = 0, equilibrium;

$\Delta G_{M_xO_y}$ >0, thermodynamically impossible process

For chemical reaction (2.1) the free energy change ΔG can be expressed as [36]:

$$\Delta G_{M_xO_y} = \Delta G^{\circ}_{M_xO_y} + RT \ln\left(\frac{a_{M_xOy}}{a^{x}{}_{M}\, a^{y/2}{}_{O_2}}\right) \tag{2.3}$$

where $\Delta G^{\circ}_{M_xO_y}$ is the free energy change when all species are in their standard state, R is the gas constant, T is temperature and a is the thermodynamic activity, which describes the deviation from the standard state for a given species and may be expressed for a given species i as [36]:

$$a_i = \frac{p_i}{p^{\circ}_i} \tag{2.4}$$

where p_i is the vapour pressure over the condensed species and p°_i is the partial pressure of the species in the standard state. For pure elements the chemical activity is thus equal to unity. For ideal gas is the activity equals the oxygen partial pressure.

When the metal-oxygen system is in equilibrium ($\Delta G_{M_xO_y} = 0$) the Equation (2.3) can be reduced to [36]:

$$\Delta G^{\circ}_{M_xO_y} = -RT \ln\left(\frac{a_{M_xO_y}}{a^{x}{}_{M} \cdot a^{y/2}{}_{O_2}}\right) \tag{2.5}$$

If metal and oxide prevail in pure solid form, the activities of M and M_xO_y are taken as unity and Equation (2.5) may be used to express the oxygen partial pressure p_{O_2} at which the metal and oxide coexist, i.e. the dissociation pressure of the oxide; Equation (2.5) can be written as [36]:

$$\Delta G^{\circ}_{M_xO_y} = \frac{y}{2} RT \ln\left(p_{O_2}\right) \tag{2.6}$$

or

$$p_{O_2} = \exp\left(\frac{2}{y} \cdot \frac{\Delta G^{\circ}_{M_xO_y}}{RT}\right) \tag{2.7}$$

Thermodynamically, the formation of the oxide M_xO_y is only possible if the oxygen partial pressure in the environment is higher than the dissociation pressure of the oxide.

In order to predict whether an oxidation reaction can occur under given conditions, the Ellingham-Richardson diagram is very useful (Figure 2.3). In this diagram values of standard Gibbs free energy for the formation of oxides and the respective dissociation pressures are plotted as a function of temperature. The plot allows the comparison of the thermodynamic stabilities of different oxides: the lower the dissociation pressure, the more thermodynamically stable is the oxide [37].

2.9.2 Oxidation kinetics

The oxidation process of a metal surface is not only determined by thermodynamics, also kinetic aspects have to be considered. When a metal is subjected to an oxidizing environment, oxygen molecules are dissociated on the surface and bind with the metal to metal oxide molecules [34-36]. This reaction product creates a growing barrier between the two reactants and thus further reactions are affected by solid state diffusion through this oxide scale. In many cases, the rate limiting step in scale growth is the transport of ions and electrons through the lattice via defects in the crystal structure [38] and depends therefore on the structure and mobility of lattice defects in the oxide [36].

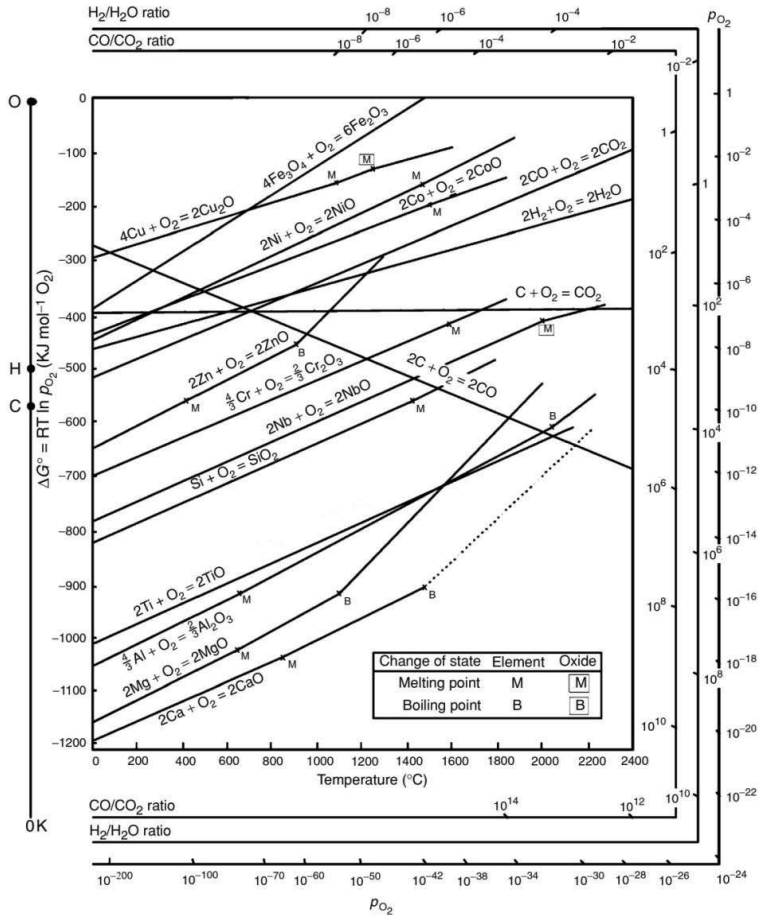

Figure 2.3: Ellingham/Richardson diagram showing standard free energies of formation for selected oxides as a function of temperature, together with corresponding equilibrium H_2/H_2O-and CO/CO_2-ratios [36].

Oxides are typically nonstoichiometric ionic compounds, meaning they are semiconductors. Electric charges are transferred by electrons for n-type and by holes for p-type semiconductors [36]. The n-type is characterized by an excess of metal interstitials or by a deficit of oxygen (or both). The resulting excess positive charge of the metal ions (or the effective positive charge of the oxygen vacancies) is compensated by additional electrons in the conduction band. In case of a p-type oxide metal vacancies and/or oxygen interstitials cause an effective negative charge that is compensated by holes (missing electrons in the valance band) [36].

The oxide scale grows in different ways, depending on the mobility of the respective electric charge carriers: either oxygen diffuses through the scale from the gas/oxide interface towards the oxide/metal interface where the oxide formation occurs, or the formation occurs at the gas/oxide interface because the metal diffuses through the scale. The first case can be described by an inward flux (towards the metal) of oxygen interstitials in addition to an outward flux of oxygen vacancies. The second case is described in the same way by an outward flux of metal interstitials and an inward flux of metal vacancies [36].

A basic model for high temperature oxidation of metals was developed by Carl Wagner [39]. It is based on several assumptions [36]:

1. The oxide layer is compact and free of pores.
2. The rate-controlling process is the migration of ions or electrons across the scale.
3. Thermodynamic equilibrium is established at both interfaces.

Hence, an oxygen activity gradient establishes across the oxide scale: the oxygen partial pressure of the gas atmosphere determines the gas/oxide interface while the other side is determined by the dissociation pressure of the oxide at the oxide/metal interface [40].

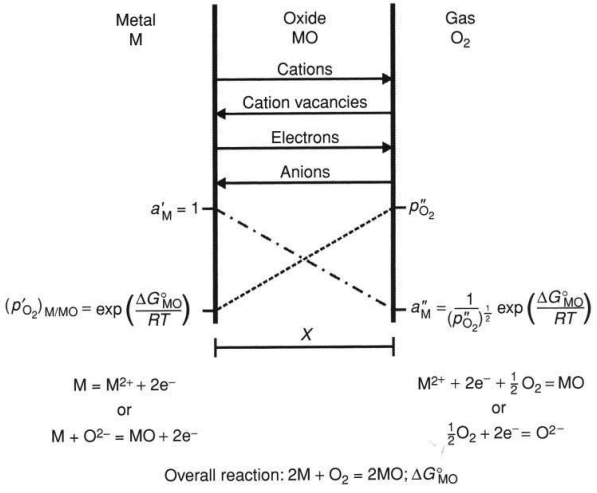

Figure 2.4: Schematic diagram of Wagner's model of oxidation [36].

Using as example a scale growth dominated by outward transport of cations, the diffusion law states that the flux j_M of metal species M is proportional to the chemical potential $\Delta\mu_M$ across an oxide scale of thickness X_{MO} [36, 41]:

$$j_M = -D_M \frac{\Delta\mu_M}{X_{MO}} \tag{2.8}$$

The scaling rate $\frac{dX_{MO}}{dt}$ is proportional to the ion flux:

$$\frac{dX_{MO}}{dt} = j_M \cdot V_{MO} \tag{2.9}$$

in which V_{MO} is the molar volume of the oxide MO. Replacing j_M in equation (2.9) with the expression (2.8) and subsequent integration yields the parabolic time dependence of the scale thickness:

$$X_{MO}^2 = 2k'_p \cdot t + C \tag{2.10}$$

with

$$k'_p = D_M V_{MO} \Delta\mu_M \tag{2.11}$$

For the case that C = 0 the thickness X_{MO} equals zero at t = 0 and thus equation (2.10) changes to $X_{MO}^2 = 2k'_p \cdot t$ (2.10.a). High temperature oxidation processes often show the parabolic oxidation rate predicted by equation 2.10. Different growth behavior (e.g. linear rate) can occur for instance during the initial stage of oxidation, when the scale is extremely thin. This is possible when the transport of oxygen from the bulk gas to the surface or the rate of the surface reaction limits the growth and the ion/electron transport is no longer rate determining. Wagner's theory also only considers lattice diffusion and does not consider e.g. short-circuit diffusion along oxide grain boundaries [34].

In the calculations of the oxidation rate constant in the following sections, the more common expression for the parabolic rate law will be used:

$$x^2 = k_p \cdot t \tag{2.12}$$

For a dense oxide scale on a metal or alloy, the oxide thickness is directly proportional to the area specific oxygen uptake per unit area (Δm e.g. in $mg \cdot cm^{-2}$). Therefore the parabolic rate equation is frequently expressed in terms of area specific weight gain Δm:

$$(\Delta m)^2 = k_w \cdot t \tag{2.13}$$

2.10 Metallic materials for interconnects

The most important properties required for an interconnect material were already summarized in section 2.8. Although La-chromite based ceramics have been considered as construction material for interconnectors, in recent years metals have gained more and more attention because they offer a number of advantages over ceramic materials: they are cheaper to fabricate than ceramics, they are less brittle and easer to machine [30]. Therefore, the downward trend in operating temperatures of 800 °C or even less allows the use of metallic interconnect materials [40, 42].

Noble metals have in a few cases been considered as interconnector materials. However, because of limited availability and high cost, this solution has been abandoned for large scale, commercial application [33]. Therefore, a number of high temperature alloys have received most attention as possible candidate metallic interconnector materials [43].

A major property of these high temperature alloys is their ability to form protective surface oxide scales which possess sufficiently slow growth rates to keep the oxidation attack beneath a technologically acceptable level. From the viewpoint of oxidation resistance, the first choice might be an alumina forming alloy because of the extremely

slow growth rates of the surface oxides. However, this slow growth rate is accompanied by an extremely low electronic conductivity of the surface scale [33].

The second type of surface oxide scale suitable to provide oxidation/corrosion protection at high temperature is silica. However, the formation and long-term stability of a protective silica scale requires quite large amounts of silicon additions in the alloy leading to alloy embrittlement. Besides, silica has a very low electronic conductivity resulting in similar problems in SOFC application as mentioned above for alumina forming alloys [30].

Chromia provides less oxidation/corrosion protection than alumina or silica [34], however, its electronic conductivity in the SOFC operation temperature range is orders of magnitude larger than that of alumina or silica. For this reason, the high temperature oxidation protection of metallic materials for interconnects is commonly achieved by chromia-based surface scales [30, 33].

Another important property for the interconnect application is a coefficient of thermal expansion (CTE) similar to the other components in the cell. Two types of commonly used high temperature alloys systems, Ni-based alloys and austenitic steels are chromia forming alloys but they possess a substantially higher CTE than the rest of the components of the cell [40]. Application of such a material would thus require a special cell design to overcome the stresses expected to be generated during thermal cycling, especially in contact and joining areas of the interconnector with other cell components. The limitations due to CTE matching restricts the choice of interconnect materials to Cr-based alloys and ferritic stainless steels [30]. Metallwerke Plansee AG developed a Cr-based alloy which possesses a CTE close to the electrolyte CTE value. This alloy, also termed oxide dispersion strengthened (ODS) alloy, has to be manufactured by a powder metallurgical approach. The main advantage of ODS materials is enhanced mechanical properties compared to conventionally melted alloys. However, a principal drawback is the relatively high cost of the material because of the complicated manufacturing process [44]. On the other hand, high-Cr ferritic stainless steels are common interconnect

construction materials due to their CTE close to the other components of the cell, especially the Ni/YSZ cermet anode, their suitable oxidation resistance and the fact that the manufacturing process is much cheaper than that for ODS alloys.

2.11 Electrical conductivity of chromia-based oxide scales

For an alloy to be used in a solid oxide fuel cell as an interconnect, the oxide scale and its interface with the underlying metal must have a minimized area specific resistance (ASR) when the electric current flows. The ASR ($\Omega \cdot cm^2$) can be calculated from the measured voltage U and the applied current I relative to the real measurement surface A on the oxide layer as follows

$$ASR = R \cdot A = \frac{U}{I} \cdot A \tag{2.14}$$

In case of a chromia forming metallic interconnect material, the ASR will be governed by the surface oxide scales rather than the bulk metal. The ASR can be minimized by reducing the scale thickness to the largest extent possible and/or increasing the scale conductivity [45].

The conductivity of the oxide is governed by its defect structure and although much research has been done, there is no unequivocal opinion of the chromia defect structure [46-47]. Most researchers claim that at temperatures above 1000°C chromia is an intrinsic electronic conductor while at lower temperatures chromia is an extrinsic conductor due to the presence of dopants or unavoidable impurities [47-51]. The electrical conductivity of bulk chromia samples at 800-1000 °C (Figure 2.5) has been reported to be in the range 1 x 10^{-2} to 5 x 10^{-2} S cm^{-1} [47, 49-52] although lower values have also been found [53-55]. A study made by Holt and Kofstad showed the influence of the dopants Mg and Ti in the conductivity of the chromia scale. Mg-doped chromia is a p-type conductor and its electronic conductivity is essentially independent of oxygen partial pressure. However, Ti-doped chromia is an n-conductor at low oxygen partial

pressure and a p-type conductor at near atmospheric oxygen partial pressure [50-51]. Nagai et al. [53, 56-57] found that the highest increase of the electronic conductivity was observed for doping chromia with NiO with independence of oxygen partial pressure. Y_2O_3 or La_2O_3-doping of chromia increased the conductivity which decreased with increasing oxygen partial pressure, however, at high temperatures, this effect was not very pronounced [30, 53, 56-57]. Other dopants such as CeO_2 or Fe_2O_3 increased the conductivity but the effect observed was far smaller than that for NiO- doped chromia [30] (Figure 2.6).

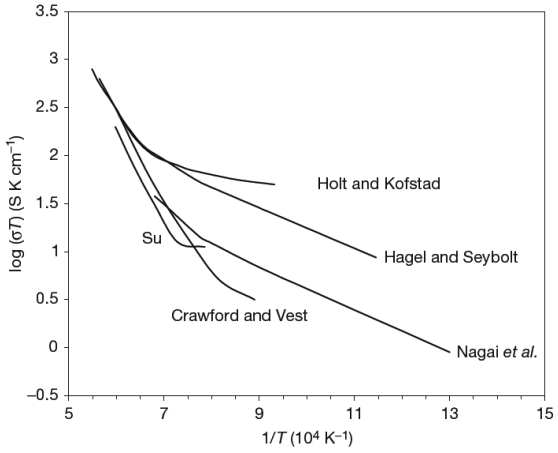

Figure 2.5: Electrical conductivity (σ) of Cr_2O_3 presented as σT as a function of reciprocal temperature in air (from reference [58] using data from [47, 49-55]).

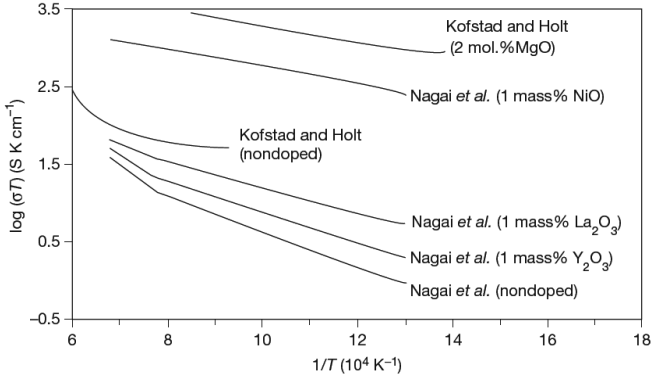

Figure 2.6: Effect of dopants on electrical conductivity (σ) of Cr_2O_3 presented as σT as a function of reciprocal temperature (from reference [58] using data from [53, 56-57]).

2.12 Ferritic steels

Ferritic steels are composed of α–Fe or ferrite (body centered cubic crystal structure (bcc)) phase. Chromium is a ferrite stabilizer at high temperature; therefore, the stability of the ferritic structure increases with chromium content [59].

In ferritic steels for high temperature application, the Cr content varies between 13 and 28 wt. %. In the case of low-Cr steels (< 5 wt. % Cr), the scales formed during high temperature exposure consist of nearly pure Fe-oxide accompanied by internal oxide precipitates of chromia and/or a mixed (spinel type) oxide $FeCr_2O_4$ [30]. With increasing Cr content, the scales become richer in spinel and chromia. Formation of a highly protective, single-phase chromia layer requires a chromium content of at least 17~20 wt. % (Figure. 2.7) depending on gas composition, temperature, exposure time, specimen surface treatment, minor alloying additions and impurities [30]. In FeCr-base alloys, minor alloying additions may substantially affect the oxidation behavior. Alloying elements frequently present in ferritic steels used for interconnects are Mn, Si, Al, Ti and the so called reactive elements (RE's) such as Hf, Y, La, Ce [30]. The first three elements are most often present in ferritic steels at levels of a few tenths of a percent. However, Ti and other oxygen active elements are commonly present in contents of less than 0.1 wt. %.

Mn possesses only a small solubility in chromia and after high temperature exposure of a ferritic steel it is frequently found in the form of Cr-Mn-spinel in the outer part of the oxide scale [18]. Al and Si are commonly used to reduce the oxygen levels in the alloy melt during steel manufacturing. After ferritic steel oxidation these elements commonly prevail as internal oxides. Sometimes silica forms a near-continuous subscale at the interface between alloy and chromia-based external layer. Often this effect is accompanied by an enhanced tendency to spallation of the external oxide scale [30]. Titanium is frequently found in the form of titania precipitates below the oxide scale. The additions of small amounts of reactive elements (e.g. Y, La) have a significant effect on

the oxidation resistance of the alloy by decreasing the scale growth rate and improving the adherence between the scale and the metallic substrate [3, 5, 59-60]

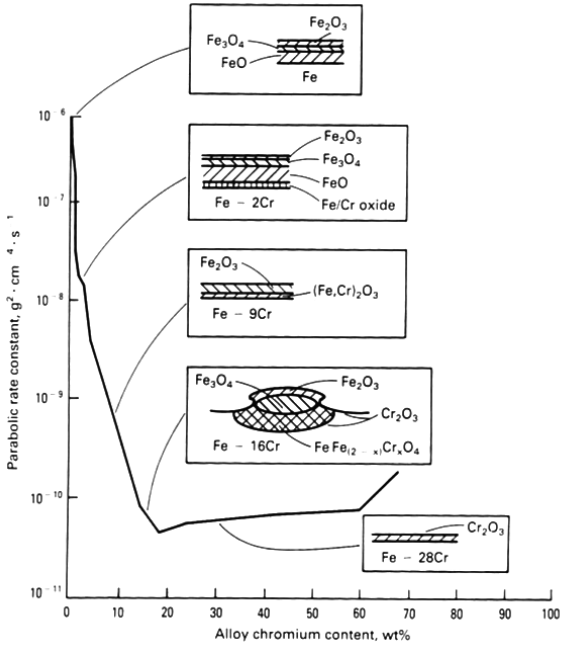

Figure 2.7: Schematic representation of the oxide scales formed on Fe-Cr alloys showing parabolic rate constant at 1000 °C in 0.13 bar oxygen as function of alloy Cr content [61].

The binary Fe-Cr phase diagram (Figure 2.8) shows which phases are to be expected at equilibrium for alloys with different chromium content as function of temperature. The phase diagram Fe-Cr possesses a closed γ-loop, therefore, additions of chromium above 13 % avoid the change from ferrite to austenite at high temperatures. The austenite or γ-Fe phase possesses a face centered cubic structure (fcc). It is not stable at temperatures below 851 °C. Metallic alloying additions such as Ni, Co and Mn tend to stabilize the austenite phase [62]. If e.g. the amount of Ni is sufficiently high, the γ-phase does not transform into α-phase when cooled from high to low temperature. The σ-FeCr phase is an intermetallic compound which may precipitate in Fe-Cr alloys with high Cr content. The phase diagram shows that this phase only exists at temperatures below approximately

820 °C. Precipitation of σ-FeCr phase severely deteriorates steel properties, and in particular, decreases ductility and impact toughness [63].

The kinetics of σ-phase formation and the precipitated amount is affected by the alloy microstructure and minor element additions. For instance, the addition of Mo is claimed to stabilize the σ-phase whereas Al, Ti and Ni in minor amounts may suppress σ-phase formation [64-66]. Sauthoff and Speller claimed that the sigma phase tends to precipitate at grain boundaries [67]. However, Hammer et al. [68] observed the preferential nucleation of σ-phase near the surface when studying the behavior of a 26 % Cr/1 % Mo ferritic steel at 700 °C in various SOFC relevant service environments. The authors found that σ-phase nucleation at 700 °C differed in anode and cathode side gases. The sigma phase formation was found to be accelerated by higher silicon contents and, remarkably, by the presence of water vapor in the exposure environment. However, Hammer et al. [68] did not find σ-phase nucleation at 700 °C in a steel containing 22 % Cr but only in the ferritic 26 % Cr and 1 % Mo steel. Niewolak et al. [66] studied steels with Cr contents ranging from 16 to 25 mass % at 600 °C and observed that higher Cr contents and/or additions of Mo had as major drawback that they enhanced the tendency to precipitation of embritteling intermetallic phases such as σ-phase.

So, to prevent the embrittlement by σ-phase formation, most of the commercially available ferritic steels do not exceed 18 wt. % of Cr. Ferritic steels with higher contents up to 28 % may be applied if the ductility is no major design problem. In SOFC applications, with a design temperature of 800°C, ferritic steels with a Cr content of 22 % are commonly used [3, 59] because under these conditions no σ-phase formation is possible according to the Fe-Cr phase diagram.

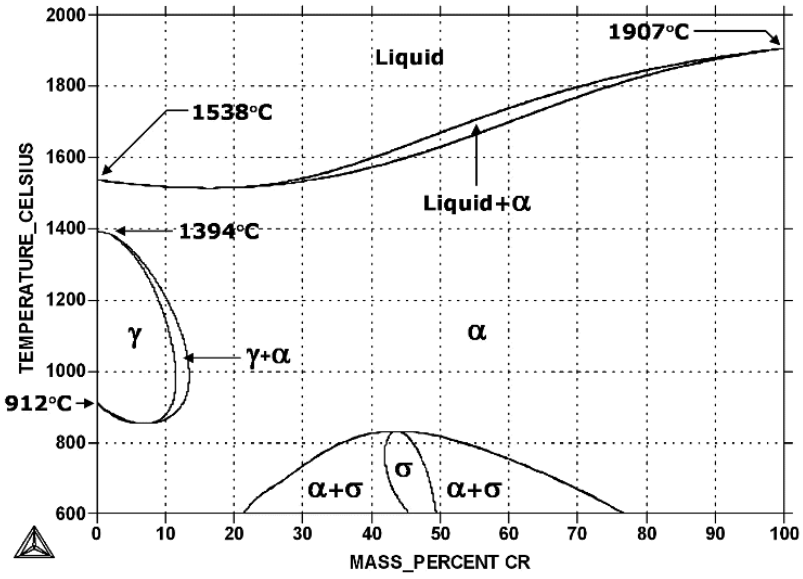

Figure 2.8: Fe-Cr phase diagram calculated using TermoCalc software [69].

A second embrittling process is in some cases important for ferritic steels. In the binary phase diagram Fe-Cr [70] the σ-phase is not stable beneath approximately 500 °C and a miscibility gap exists where the α-ferrite phase consists in equilibrium state of two bcc phases i.e. α' containing a low Cr content and α'' with high Cr content [71] leading to a loss in ductility [72]. The reaction which occurs in this temperature range is frequently termed "475 °C-embrittlement" and, as σ-phase formation, can be relieved by a heat treatment at temperatures where ferrite is stable in the given alloy.

2.13 Ferritic steels especially designed for SOFC applications

The used cell design and the service conditions are the factors which determine the optimum steel composition for an SOFC interconnector. The requirement necessary for a YSZ electrolyte-supported design is a low thermal expansion coefficient of typically 10 x 10^{-6} K^{-1} but this low value cannot be obtained with the commercially available high Cr ferritic steels [4]. The oxidation resistance might be improved by the addition of reactive elements and substantial additions of Mo or W to decrease the CTE may be used [72].

However, it is unlikely that at the high application temperature of 1000 °C in an electrolyte-supported design the oxidation rates of a ferritic steel will be sufficiently small as required for application in an SOFC.

If ferritic steels are used for interconnectors, temperatures in the range 600 to 800 °C seem to be more appropriate and thus a very thin YSZ electrolyte may be applied in an anode-supported cell design. The choice of such concepts will require an interconnector with a similar CTE as the Ni/YSZ cermet used for anodes, i.e. 11-12 x $10^{-6}K^{-1}$ [30, 32]. Ferritic steels with a Cr content of approximately 22 wt. % may fulfill this requirement [4].

Pirón et al. [59] studied Fe-Cr base model alloys with Cr contents between 16 and 25 % to evaluate the effect of various reactive elements (RE's) on scale adherence and growth rate. The optimum RE addition appeared to be La because it does not form an intermetallic compound with iron and, contrary to other RE additions (i.e. Y or Ce), it is evenly distributed in the alloy. The rate of scale growth was found to be influenced by the presence of minor alloying additions /impurities such as Mn and Ti in the alloy.

It is well known that Cr can form volatile (oxy-) hydroxide species which are reduced at the triple-phase boundaries between cathode, electrolyte and air thereby forming solid Cr_2O_3 and other Cr-rich phases which inhibit the electrochemical processes of the cell [18, 73-74]. This effect is often termed as cathode poisoning. So, a small amount of Mn was added to the model steels for obtaining formation of an external Cr/Mn spinel layer which reduces the formation of volatile Cr species [75-76]. The addition of minor amounts of Ti results in the formation of an internal oxidation zone beneath the oxide scale which results in strengthening of the region close to the surface and thus minimizes wrinkling as a result of oxidation-induced stresses. On the other hand, high Ti contents increase the chromia growth rate [59].

The result of the research by Pirón and Quadakkers was a semi-commercial alloy called JS-3 [60]. This material was commercialized by ThyssenKrupp VDM as Crofer 22 APU

[7-8]. When this material was manufactured at large scale in an electric arc furnace the concentrations of the commonly used de-oxidants aluminum and silicon were not as low as in JS-3. This had as result that the commercial steel showed during 800 °C oxidation increased internal oxidation leading to a larger growth rate of the external scale [58]. Beneath the oxide scale both alloys, JS-3 and the commercial Crofer 22 A, exhibit an internal oxidation zone. In the case of JS-3 only spherical titania precipitates are found due to the low levels of Al and Si. However, in the commercial steel needle shaped alumina precipitates can be found in the internal oxidation zone and locally a sub-layer of silica was found at the metal/oxide interface (Figure 2.9). This effect is known to be frequently accompanied by a poor adherence of the surface oxide scale [77].

To reduce the amount of Al and Si towards the low level present in JS-3, the alloy production process was changed from electric arc furnace to vacuum induction melting and this commercially available steel was designated Crofer 22 APU [7]. By defining low Al and Si contents, formation of oxide scales with very low area specific resistance was obtained [18] (Figure 2.10).

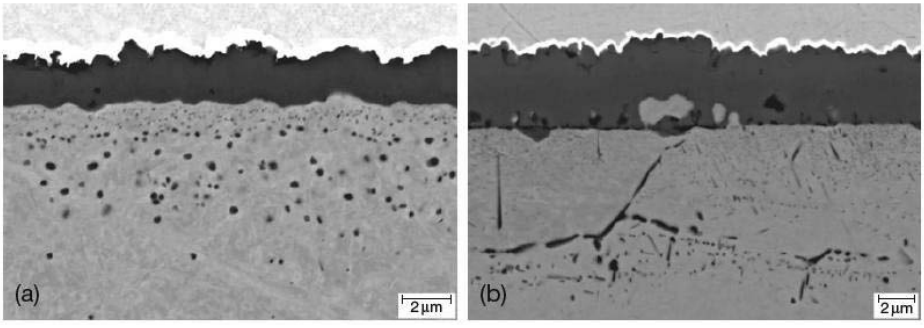

Figure 2.9: Cross sections of oxide scales on type FeCrMn(La/Ti) steels after 1000h exposure at 800°C in air showing effect of Si/Al content: (a) 0.01 % Si/Al, (b) 0.1 % Si/Al. [30].

Nonetheless, the optimized high purity ferritic steels have a number of disadvantages. First, there is an increase of the manufacturing cost and the very low concentration of minor alloying additions results in a poor creep resistance of the alloy. A new type of ferritic interconnector steel, Crofer 22 H [10, 78] was described by Frotzheim et al. [9,

79]. This steel possesses a higher creep strength than JS-3 and Crofer 22 APU. Its higher strength is related to the combination of solid solution and precipitation strengthening given by Nb and W addition. The Nb addition is mainly responsible for the formation of Laves phase of the type $Fe_2(Nb,W)$. The Laves phase was found to possess a high solubility for silicon [9]. The dissolution of silicon in the Laves phase substantially reduces the Si activity in the alloy. Given an appropriate silicon/niobium ratio the reduced activity prevents the formation of a silica sub layer beneath the chromia surface scale during high temperature oxidation. Honegger et al. [80] developed other high-Cr ferritic materials for SOFC applications that were produced by powder metallurgical techniques allowing the incorporation of oxide dispersions to achieve an oxide dispersion strengthened (ODS) steel. The mechanical alloying process allows producing materials with higher concentrations of RE's e.g. Y than in alloys produced by conventional manufacturing methods (Table 2). Therefore, the ferritic ODS steels generally exhibit lower oxidation rates than RE's containing alloys obtained by conventional alloy manufacturing methods.

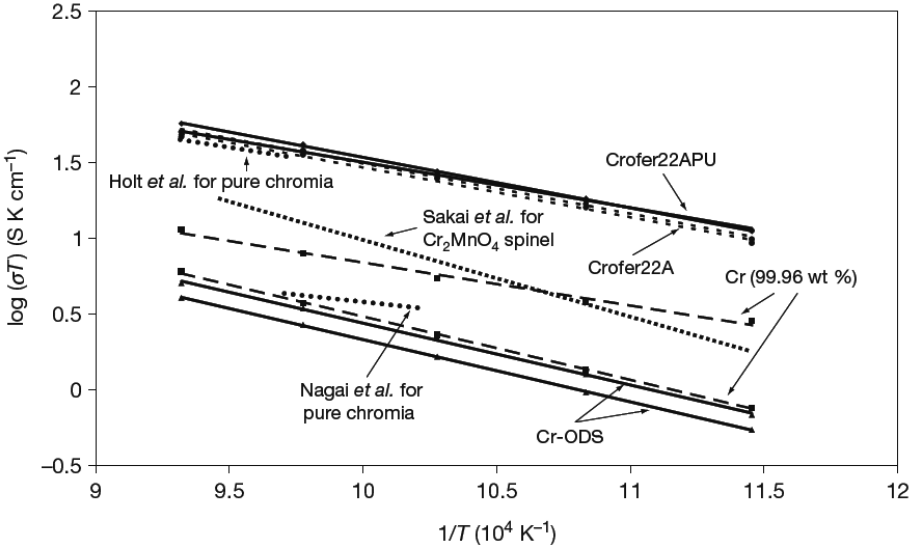

Figure 2.10: Electrical conductivity (σ) of oxide scales, plotted as σT vs. reciprocal temperature, for the two ferritic steels and the Cr-ODS-alloy compared with literature data for Cr_2O_3 [47, 49, 53] and Cr_2MnO_4 [81]. Taken from reference [82].

Table 2: Compositions of ferritic steels developed for SOFC application (wt. %).

Steel	Fe	Cr	Mn	Ti	La	Si	Al	Ni	Zr	Others additions
Crofer 22 A	Bal.	22	0.4	0.08	0.08	0.11	0.12	<0.002	-	-
Crofer 22 APU	Bal.	22	0.4	0.06	0.07	<0.01	<0.01	0.16	-	-
Crofer 22 H	Bal.	22	0.4	0.07	0.08	0.25	0.02	0.1	-	0.5 Nb, 2 W
ZMG 232	Bal.	22	0.48	0.03	<0.01	0.36	0.19	0.31	0.13	
Sanergy HT	Bal.	22	<0.5	0.03	<0.01	<0.3	0.03	0.5	0.1	0.6 Nb, 0.8 Mo
IT11	Bal.	26	0.04	0.2	<0.01	0.03	0.03	0.3	0.005	1.9 Mo, 0.24 Y*

* In form of oxide dispersion.

2.14 Effect of component thickness on oxidation behavior

Especially for mobile applications of an SOFC, a major design requirement is a reduction in weight of the fuel cell stack which may be obtained by decreasing the interconnector thickness from the common few millimeters to a few tenths of a millimeter [83-85]. It was shown for chromia forming ferritic steels that the oxidation limited lifetime of thin components is primarily governed by the chromium reservoir in the component [85-87]. If the growth of the oxide scale leads to a decrease of the alloy Cr-concentration beneath a critical level, breakaway oxidation occurs. The time at which breakaway occurs limits the usable life of the component. So, as the Cr reservoir decreases with decreasing component thickness, the lifetime will decrease with decreasing component thickness. In the temperature range 800-900 °C the observed lifetime limits may be predicted with reasonable accuracy by a similar approach to that used for FeCrAl alloys, using oxide growth rate parameters, initial alloy Cr content and critical Cr content required for protective chromia scale formation [86-87].

However, a completely new finding by Huczkowski et al. [87] was that not only the time to breakaway but also the growth of the oxide scale was affected by specimen thickness (Figure 2.11). A possible explanation given for this latter observation was that the specimen thickness dependence of the scale growth rate is affected by depletion of minor

alloying elements such as Mn in the bulk alloy and/or by internal oxidation of Si, Ti and Al [87].

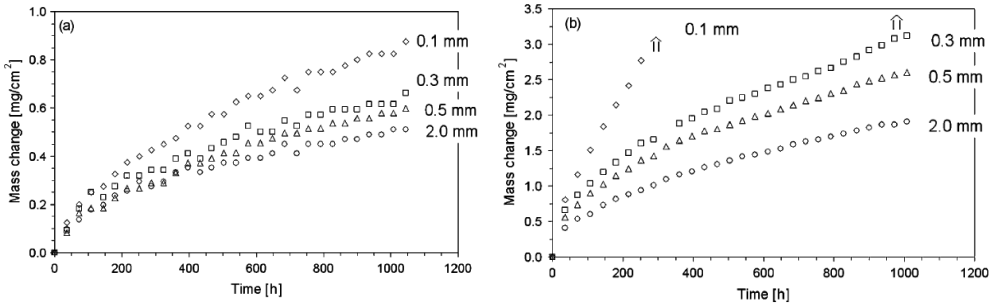

Figure 2.11: Mass change during oxidation of Crofer 22 APU in air for specimens of various thicknesses (a) 800 °C and (b) 900 °C. Arrows indicate occurrence of breakaway oxidation [86].

Comparison of the results of ferritic steels [58] with data of Ni-base alloys [88] indicate that these factors quantitatively affect the oxidation rates but they do not seem to be the main reason for the dependence of the oxidation rate on specimen thickness. It was proposed that the effect is related to compressive growth stresses in the oxide scale which can relaxed by plastic deformation of the substrate for thin specimens but are, for the same oxidation time and temperature, maintained at significant levels for thick specimens [87]. However, an unequivocal proof for this proposal could not be provided.

2.15 Ferritic steels with increased creep strength

2.15.1 Fundamentals of creep

Creep refers to the time-dependent component of plastic deformation at elevated temperatures. Although creep can take place at all temperatures above absolute zero Kelvin, creep becomes significant at temperatures, higher than approximately $0.4T_m$, where T_m is the absolute melting temperature, because diffusion can assist creep at elevated temperatures [89].

The form of a typical creep curve exhibiting strain as function of time is shown in Figure 2.12. Three stages to the creep curve may be identified:

- Primary creep, stage I: in which the strain rate decreases with time.
- Secondary (steady state) creep, stage II: in which the strain rate is constant.
- Tertiary creep, stage III: in which the creep rate increases with time.

At the end of the ternary creep stage, rupture of the material occurs.

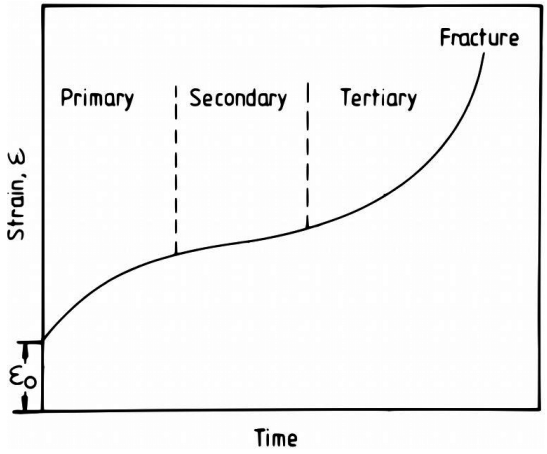

Figure 2.12: Steps in a typical creep curve of a metallic material at constant load [90].

Generally, there are three variables which may be used to analyze the creep data: time, stress, and temperature. Frequently it is found that the steady state creep rate and the applied stress (σ) are related by the so-called Norton's creep equation as follows

$$\frac{d\varepsilon}{dt} = \dot{\varepsilon} = k \cdot \sigma^n \tag{2.15}$$

where k is a constant and n is the stress exponent for creep. Depending on the material and temperature, the exponent n may vary between 3 and 10.

In the Norton equation, the k value depends on temperature

$$k = k_o \cdot \exp\left(\frac{-Q_c}{RT}\right) \tag{2.16}$$

Thus, the creep rate shows an Arrhenius type temperature dependence in which Q_c is the activation energy for creep, R is the universal gas constant and T is the absolute temperature.

2.15.2 Laves phase strengthened ferritic steel

If thin interconnects (typically of a few tenths of a millimetre) are going to be used in an SOFC stack, creep strength will be an important material property. Frotzheim et al. [79] showed that the addition of niobium to a ferritic 22 % Cr steel of the type Crofer 22 APU results in the formation of Laves phase precipitates which causes an increase of creep strength at temperatures in the range 700-800 °C. The addition of tungsten also has a beneficial effect on the creep strength due to solid solution strengthening. The combined addition of W and Nb was shown to result in the formation of finer Laves phase precipitates than in the case of single Nb addition thus improving the creep strength [9] (figures 2.13 and 2.14).

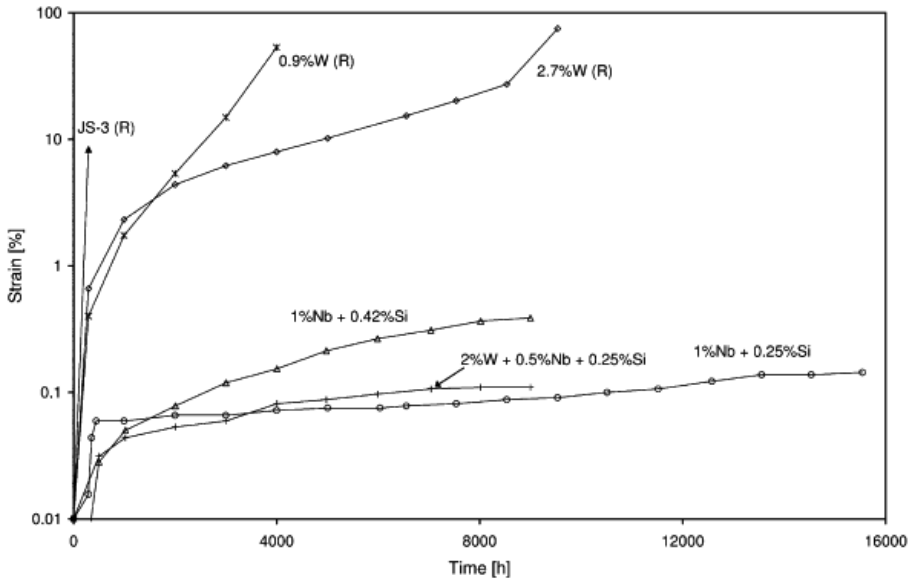

Figure 2.13: Strain vs. time for model alloys of the type Crofer 22 APU with aditions of W, Nb and/or Si during creep test at 700 °C and an applied load of 10 MPa. R indicates rupture. [9].

Frotzheim et al. [79] showed that the addition of W up to 2 wt. % does at 800 °C and 900 °C up to exposure times of 1000 hours not have a detrimental effect on the growth rate of the oxide scale while Nb produces an increase of the oxidation rate due to doping of the chromia scale and formation of subscales containing Nb-rich oxides [9, 78]

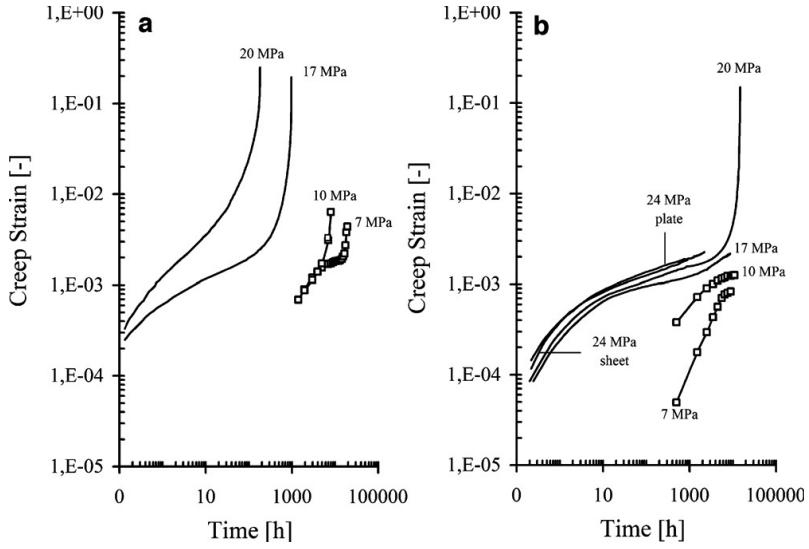

Figure 2.14: Creep curves of (a) Crofer 22 APU and (b) Crofer 22 H at 700 °C [91].

A major finding was, that this adverse effect of Nb could be suppressed by a minor Si addition, provided that the Si/Nb-weight ratio was in a specified limit. It was proposed that this was related to the substantial solubility of Si in the Laves phase, resulting in a phase stabilization and consequently a reduction in Nb activity. The solubility of Si in the Laves phase also has a consequence that the Si activity is decreased to such a level, that no silica subscale formation was found during oxidation in the temperature range 700 - 900 °C. This finding, which was applied in a new ferritic steel Crofer 22 H (Figure 2.15), has as major, technologically relevant consequence, that, different from the case of high purity steels such as Crofer 22 APU, Si additions may be used as de-oxidant during alloy manufacturing so that the Laves phase strengthened steel can be produced by conventional manufacturing methods thus substantially decreasing material cost.

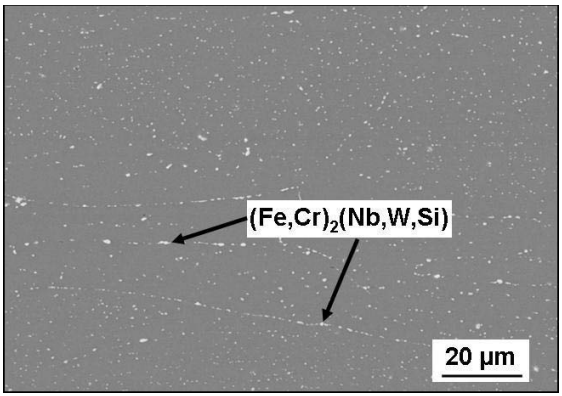

Figure 2.15: Microstructure of laboratory batch of Crofer 22 H (KUA) after 1000 h exposure in air at 800 °C showing Laves-phase precipitates [9].

3. Aims of the present study

In the present thesis, the potential suitability of Laves phase strengthened steels, containing minor additions of the de-oxidant Si in combination with the elements Nb and/or W, as construction material for SOFC interconnect is evaluated. The results of the investigations should provide the basis for a full qualification of this type of material to be used in SOFCs. Using Crofer 22 H as a basis, the short and long term oxidation behaviour in simulated cathode and anode gas as function of temperature is investigated. Thereby, main emphasis is put on the experimental determination and modeling of the oxide scale formation and phase changes occurring in the subscale layers.

By using variations in steel composition as well as heat treatment procedures, the significance of intrinsic creep strength for the oxidation behaviour, especially of thin components, is investigated.

Aiming at possible improvements of a number of steel properties, the effect of variations in content of selected alloying elements on the oxidation properties in the simulated service environments is studied. Thereby, main emphasis is put on the consequence of reducing the alloy Mn content as well as variations in W/Nb/Si contents on alloy performance. The latter subject should give insight in possibilities to replace Nb by W thus suppressing a possible adverse effect of Nb as a result of subscale oxidation during long term exposure.

In the final section the electrical conductivity of oxide scales formed on various types of Laves phase strengthened steels will be compared with that of scales formed on the near single phase, high purity steels.

4. Experimental details

4.1 Materials

In the frame of the present project model and commercial ferritic materials designed for SOFC applications were tested with the aim of the qualification of Crofer 22 H. The materials were produced by ThyssenKrupp VDM [92].

All materials used in this study were given a three letter batch designation which allows unequivocal identification of the material, the initial thickness, the manufacturer etc. Plates, sheets and foils of different thickness when made from the same melt mostly received different batch designations.

Crofer 22 APU was manufactured using vacuum induction melting in form of 16 tons ingots with subsequent hot and cold rolling to the respective final thickness (see Table 3 and 4). Samples of the plates were short time annealed by the manufacturer at 800 °C. The “as-received” microstructures of the investigated commercial Crofer 22 APU are shown in Figure 4.1. The alloy mostly consists of single-phase ferrite grains in which minor amounts of Ti-rich carbonitride precipitates were present. Sheets of 2.5 mm and 1 mm thickness showed elongated grains in rolling direction and exhibit a non-uniform grain size when comparing the inner and outer part of the samples. In the inner parts of the samples the ferrite grains tend to be larger than those close to the sample surface.

Crofer 22 H was manufactured using conventional arc melting of 30 tons ingots with subsequent hot and/or cold rolling until the final plate/sheet/foil thickness. After rolling down to the final thickness, the materials were solution annealed (at 1050 °C for several minutes depending on sheet thickness) under hydrogen atmosphere. The aim of this step was to obtain a homogeneous equiaxed microstructure and a complete dissolution of the Laves phase [93-94] to ensure improved machinability/workability. Subsequently, the material was annealed for 24 h at temperatures in the range 200-300 °C in air to remove hydrogen dissolved in the steel during the solution annealing. The final production steps

were etching/pickling and brushing to remove oxide layers formed during the heat treatment (Table 3 and 4). Generally, thicker sheets of Crofer 22 H were found to be characterized by larger grains. The average grain sizes vary between 350 µm for 2.5 mm sheet (designation MDP) to about 35 µm for the 0.3 mm foil (designation MED). The batches with 0.5 and 1 mm thickness (designation MDT and MEC respectively) show additionally a variation in grain size along its cross section. The near surface regions consist of smaller grains than the centre of the materials (Figure 4.2). An additional commercial batch of Crofer 22 H (designation NEC) was used as test material in a later part of the investigations. Different from the previously used batches, this material prevailed in form of 16 mm thick plate.

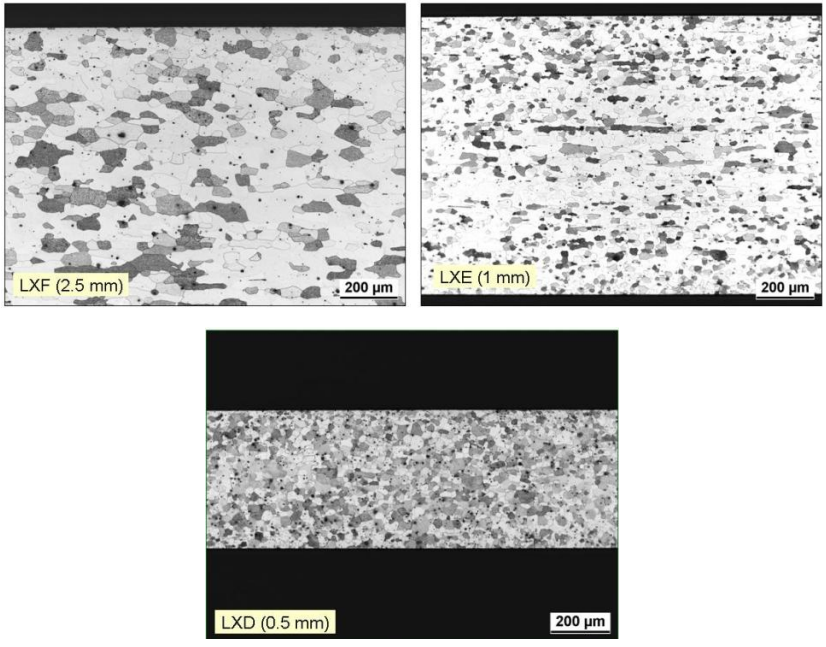

Figure 4.1: As received microstructures of investigated steel Crofer 22 APU.

Model steels were manufactured using vacuum induction melting in form of approximately 10 kg ingots. Batch KUA (Table 3 and 4) was manufactured using a chemical composition nominally corresponding to the commercially produced Crofer 22 H. The batch was hot rolled.

The “High Nb/Si” model alloy (batch LWU) was manufactured as laboratory melt from pure (4N) metals using a levitation melting method in FZJ. A 60 g ingot of the steel was four times re-melted under an argon atmosphere and finally cast in a copper mould. The ingot had the form of a rod with a diameter of approximately 10 mm and a few cm length. It had higher Nb and Si contents than the Crofer 22 H composition, however the Nb/Si ratio was similar.

A “Mn-free”model steel with the same type and amount of alloying additions as in Crofer 22 H was produced, however without addition of manganese (batch designation - specimen thickness: MKT-2 mm; MKS-1 mm; MKU-0.5 mm; MKW-0.25 mm). This material was hot and cold rolled to the respective final thickness and then solution annealed at 1050°C in a continuous furnace under pure hydrogen for several minutes depending on the thickness.

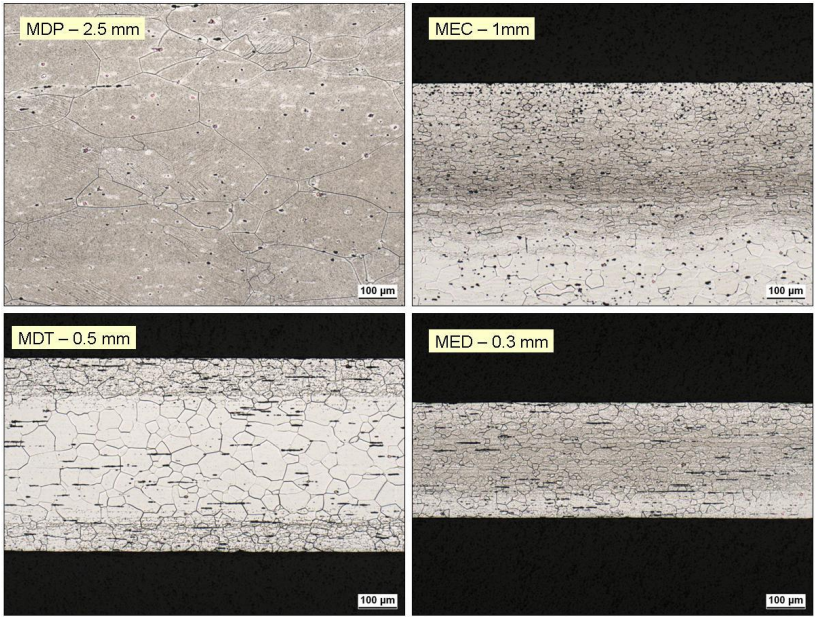

Figure 4.2: As received microstructures of investigated Crofer 22 H batches.

Three types of Nb-free, tungsten containing model alloy variants were produced, using again Crofer 22 APU as base composition:

- Tungsten alloyed steels “1W” (KCW) and “3W” (KDN) with 0.9 or 2.7 wt.% of W respectively
- Tungsten and silicon alloyed steels (“5W-0.24Si-0.03La-0.04Ti”) LFK and LJF (“5W-0.3Si”) with approximately 5 wt. % of W and 0.25 wt. % of Si and thus, one of them (batch LFK) with low amount of La and Ti
- Tungsten and silicon alloyed steel batches (“7W-0.25Si-0.03La-0.04Ti”) LFN and (“7W-0.25Si”) LJH with approximately 7 wt. % of W and 0.25 wt. % of Si and thus, one of them (batch LFN) with low amount of La and Ti

Details of other alloys used in the present thesis will be presented in the respective chapters describing experimental findings.

Table 3: Chemical composition of the commercial materials (Crofer 22 APU and Crofer 22 H) and a model alloy in wt. % measured by ICP-OES in the central division of analytical chemistry (ZCH) at FZJ.

Steel	Designation	Thickness	Cr	Mn	La	Ti	Nb	W	Al	Si
Crofer 22 APU	LXF	2.5 mm								
Crofer 22 APU	LXE	1 mm	22.9	0.45	0.066	0.062	-	-	0.006	0.019
Crofer 22 APU	LXD	0.5 mm								
Crofer 22 H	NEC	16 mm								
Crofer 22 H	MDP	2.5 mm								
Crofer 22 H	MDO	2 mm								
Crofer 22 H	MEC	1 mm	22.9	0.43	0.08	0.07	0.51	1.94	0.02	0.21
Crofer 22 H	MDT	0.5 mm								
Crofer 22 H	MED	0.3 mm								
Model alloy C. 22 H	KUA	2 mm	22.3	0.43	0.06	0.06	0.48	2.02	0.01	0.24

Table 4: Impurities in the commercial materials (Crofer 22 APU and Crofer 22 H) and a model alloy in wt. % according to hot gas extraction IR spectroscopy measured in the central division of analytical chemistry (ZCH) at FZJ.

Steel	Designation	Thickness	C	S	N	O
Crofer 22 APU	LXF	2.5 mm				
Crofer 22 APU	LXE	1 mm	0.001	0.0035	0.004	0.006
Crofer 22 APU	LXD	0.5 mm				
Crofer 22 H	NEC	16 mm				
Crofer 22 H	MDP	2.5 mm				
Crofer 22 H	MDO	2 mm				
Crofer 22 H	MEC	1 mm	0.007	<0.002	0.015	0.006
Crofer 22 H	MDT	0.5 mm				
Crofer 22 H	MED	0.3 mm				
Model alloy C. 22 H	KUA	2 mm	0.002	0.002	0.007	0.008

4.2 Specimen preparation

Samples of 20 mm x 10 mm or 10 mm x 10 mm were machined from the prevailing materials. For the oxidation studies the specimens were ground down to 1200 grit surface finish using SiC griding paper. Depending of the actual experiment, the specimen thickness varied from 0.25 to 2.5 mm. The specimens were hung on a platinum wire during exposure in the furnace to ensure homogeneous access of the oxidizing gas to the specimen surfaces. For this reason a 2 mm diameter hole was drilled close to the specimen length edge. Prior to oxidation, all samples were degreased in ethanol using an ultrasonic cleaner.

4.3 Oxidation tests

In accordance with the application of the interconnect material in the SOFC stack, the exposures of the alloys were carried out in a low- and high-pO_2 gas. To simulate the cathode environment the oxidation tests were carried out in air and to simulate the anode (fuel) atmosphere, an environment with a low equilibrium oxygen partial pressure (Ar-4%H_2-H_2O) was used. The formation of the rapidly growing Fe-base oxides in wet gases only occurs if the equilibrium oxygen partial pressure of the gas is higher than the dissociation pressure of FeO. In an Ar-H_2-H_2O gas this corresponds to a H_2/H_2O ratio near to one [95]. The Ar-4%H_2-2%H_2O gas used in some cases in the present study is thus a "borderline" case for formation of Fe-oxide scales [66] whereas a rather high concentration of water vapour of 20 % assures that the oxygen partial pressure of the gas will be well above the dissociation pressure of FeO. Therefore, the simulated anode gas Ar-4%H_2-20%H_2O was used in most of the cases in the current thesis. The oxygen partial pressure in air is approximately 0.2 bar and that of the simulated anode gas at 800 °C corresponds to a pO_2 of approximately 10^{-20} bar. Usually, the operation temperature proposed for SOFC application is approximately 800 °C [19], however higher temperatures are also considered [13]. Moreover, during exposure at 900 °C it is possible to use the higher oxidation rates at relatively short times for the prediction of the long term oxidation behaviour at 800 °C. However, this approach is not in all cases reliable due to a possible change of the oxidation mechanism at higher temperature. Therefore,

most of the present studies focused to simulate the standard conditions for SOFC operation, i.e. a temperature of 800 °C.

4.3.1 Discontinuous oxidation tests

Discontinuous oxidation experiments were conducted in specially designed horizontal furnace facilities. The reactor tube and billet container were made of sintered alumina (Alsint 99.7) to avoid contamination of specimen surfaces with volatile silicon containing species [96]. Discontinuous oxidation tests were carried out at 800 °C in laboratory air or in simulated anode gas with composition Ar-4%H_2-20%H_2O. The specimens were cooled to room temperature every 100 or 250 h for weight measurements in case of air oxidation and every 100 h in case of simulated anode gas experiments.

4.3.2 Cyclic oxidation test

Cyclic oxidation tests were carried out at 900 °C in laboratory air. Each cycle consisted of 2 h heating and 15 min cooling, whereby vertical furnaces with mobile specimen holders were used. During the cooling step the specimens were automatically removed from the furnace and pressurized air was subsequently blown on the samples. The specimens were weighted every 36 h.

4.3.3 Thermogravimetry (TG)

Short-term isothermal oxidation tests were carried out in synthetic air (mixture of nitrogen with 20 % vol. % oxygen) and Ar-4%H_2-xH_2O (maximum water content was limited by the experimental set up to 10 %) using a thermo-balance (Seratam TG 92). The isothermal exposure time was 72 h. The heating rate was 90 °C per minute, the cooling rate was approximately 10 °C per minute and the flow rate of the gas was 2 l/h.

4.4 Characterization of oxidized specimens

4.4.1 Optical metallography and electron microscopy

After the oxidation tests, the specimens were PVD (physical vapor deposition) coated with an approximately 20 nm thick gold layer to impart electrical conductivity to the

sample surface and subsequently a nickel layer with a thickness of approximately 200 μm using electroplating was applied. The Ni coating provides protection of the surface-oxide layer during subsequent mounting, grinding and polishing, and it ensures a better optical contrast between oxide and mounting material. After nickel coating, the samples were mounted in an epoxy resin, ground with SiC abrasive paper from 240 to 1200 mesh and polished down to 1 μm surface finish. The metallographic cross sections were characterized by optical metallography (OM-Leica MEF4). For SEM (scanning electron microscopy) studies the cross sections were coated with Pt. The specimens were investigated using a Leo 400/1550 SEM equipped with an Inca EDX (Energy dispersive X-ray analysis) system. For the WDX (Wavelength dispersive X-ray analysis) a Zeiss Supra 50 instrument coupled with Inca WDX was used.

4.4.2 X-ray diffraction analysis

The phase compositions of the oxide scales and the subscale zone of the oxidized specimens were analysed using an D4 ENDEAVOR XRD set-up from BRUKER AXS. The XRD patterns were obtained using a copper cathode as radiation source ($K_{\alpha,}$ wavelength 1.5419 $\mathring{A}$).

4.4.3 Plasma - SNMS analysis

Secondary neutrals mass spectroscopy (SNMS) was used for measuring the chemical composition of the oxide scales and subscale depletion zones by depth profiling. The sample is bombarded with Ar gas ions with an energy up to 0.5 keV. In the present study a Plasma SNMS type INA-3 was used [97-98]. The procedure described in Ref. [97] was used for quantification of the SNMS profiles.

4.4.4 GDOES analysis

Glow Discharge Optical Emission Spectroscopy (GDOES) was used to characterize the oxide scales with a GD Profiler HR device from Horiba Jobin Yvon. To obtain a suitable shape of the sputter crater, the analysis conditions were chosen to be 700 Pa and 60 W. The GDOES analyzer was equipped with a standard 4 mm glow discharge source and a

high resolution optical spectrometer. The measured depth profiles were quantified using a procedure similar to that applied for the SNMS analyses.

4.5 Electrical conductivity tests

The contact resistances of the oxide scales were measured using a conventional four-point method. Specimens with dimensions slightly smaller than 10 mm x 10 mm were ground to a P1200 grit surface finish and then pre-oxidized (in most cases for 100 h) at 800 °C in air. Subsequently, a layer of Pt-paste was applied to both oxidized surfaces by brush painting. The sample edges were ground to remove remnants of Pt-paste and thus avoid short circuiting of the scales. Then, a Pt-mesh was used for electrical connection. To ensure better and reproducible contact between Pt-mesh and sample a 50 g load was applied. The contact resistance was monitored in situ during 300 h of exposure at 800 °C in air and subsequently during step-wise cooling to 750, 700, 650, and 600 °C, whereby each temperature stage was run for 10 h. The exposure times were limited to 300 h because it was previously shown that during longer exposure times the oxidation kinetics and the oxide scale morphology may become substantially affected by the presence of the deposited Pt-contact layer [58]. The step-wise cooling provides a good indication for existence of a possible short circuit between Pt-electrodes and the metallic sample core caused by dissolution of the oxide scale due to presence of the Pt-contact layer [58]. A step-wise increase of the sample resistivity during cooling can be interpreted as semiconducting behaviour (typical for most oxides) and a proof for absence of a short circuit. At least two samples were tested for each material to check the reproducibility of the results. After finishing the electrical conductivity tests, specimens were cross sectioned to estimate the real thickness of the oxide scales.

5. Crofer 22 H

5.1 Time and temperature dependent changes of Laves phase strengthened steel microstructures.

5.1.1 Introductory remarks

This section presents results of experiments concentrating on the investigation of the temperature and time dependent microstructural changes of the Laves phase strengthened steels. In the experiments two different steel batches were used, i.e. KUA and LWU. Manufacturing details of the batches were described in detail in section 4.1.

The material batch KUA possesses a composition which virtually equals that of Crofer 22 H. The composition of steel LWU was Fe–22.4%Cr–1.5%W–1%Nb–0.63%Si, i.e. it had higher Nb and Si contents than the Crofer 22 H composition, however the Nb/Si ratio was similar. The reason for selecting this composition was to obtain larger amounts and coarser Laves phase precipitates which would allow an easier analysis of the precipitate composition than in the Crofer 22 H batches thus obtaining a more accurate information of the temperature dependence of the Laves and ferrite phase compositions. Additionally, the model steel LWU did not contain the minor alloying additions/impurities La, Ti, Mn. The detailed composition of batches LWU and KUA are given in Tables 5 and 6.

Table 5: Chemical composition of laboratory batch of Crofer 22 H (batch KUA) and "High Nb/Si" (batch LWU) alloy variants in wt. % measured by ICP-OES analysis in the central division of analytical chemistry (ZCH) at FZJ.

Alloy variants	Designation	Thickness	Cr	Mn	La	Ti	Nb	W	Al	Si
Crofer 22 H	KUA	2 mm	22.3	0.43	0.06	0.06	0.48	2.02	0.009	0.24
"High Nb/Si"	LWU	2 mm	22.4	<0.01	<0.01	<0.01	1.0	1.5	<0.01	0.63

Table 6: Impurities in the investigated materials in wt. % according to hot gas extraction IR spectroscopy measured in the central division of analytical chemistry (ZCH) at FZJ.

Alloy variants	Designation	Thickness	C	S	N	O
Crofer 22 H	KUA	2 mm	0.005	0.001	0.0051	0.0077
"High Nb/Si"	LWU	2 mm	0.004	0.0042	0.0004	0.0454

In a further series of investigations, similar experiments were carried out with specimens from a commercial Crofer 22 H batch (designations MDP, MEC, MDT, MED) (see Tables 3 and 4 in section 4.1). These studies should give indications, whether the time and temperature dependent microstructural changes are affected by the higher concentrations of impurities (e.g. of C, N) present in the commercial material compared to those in the lab scale variant KUA. The samples used in all these tests were cut from 10 mm diameter bars and thus prevailed as 2-3 mm thick discs. Each individual sample was enclosed in a silica glass capsule which was evacuated down to 10^{-5} mbar and subsequently heat treated at various temperatures. After annealing the encapsulated samples were quenched in water.

5.1.2 Microstructure of laboratory batch of Crofer 22 H

A first test was carried out to evaluate the time and temperature required for complete dissolution of the Laves phase. Figures 5.1 and 5.2 show microstructures of Crofer 22 H (batch KUA) heat treated for 1 h, 7 h or 24 h respectively at different temperatures. Samples annealed at 1000 or 1100 °C for at least 24 h exhibit microstructures consisting of ferrite and Laves phase. Samples heat treated at 1200 °C exhibit a recrystallized microstructure consisting of single phase ferrite.

In the second series of experiments KUA samples were initially heat treated for 1 h at 1200 °C and subsequently for 1 h, 10 h, 100 h or 500 h at 700 °C, 800 °C or 900 °C. The initial heat treatment at 1200 °C results in a homogenization of the microstructure and a complete dissolution of the Laves phase, as illustrated above. During the subsequent annealing at lower temperatures Laves phase starts to precipitate from the oversaturated ferrite matrix (Figures 5.3-5). With increasing temperature and/or annealing time, a

coarsening and redistribution of Laves phase can be observed. Precipitates located inside the ferrite grains near the grain boundaries tend to vanish. At the same time, an increasing amount of Laves phase becomes precipitated at the ferrite grain boundaries. The coarsening of precipitates occurs due to the growth of larger precipitates at the expense of smaller ones. Thus, as the larger precipitates grow, the surrounding area becomes depleted in smaller precipitates. This process is widely known as Ostwald ripening phenomenon [99-100].

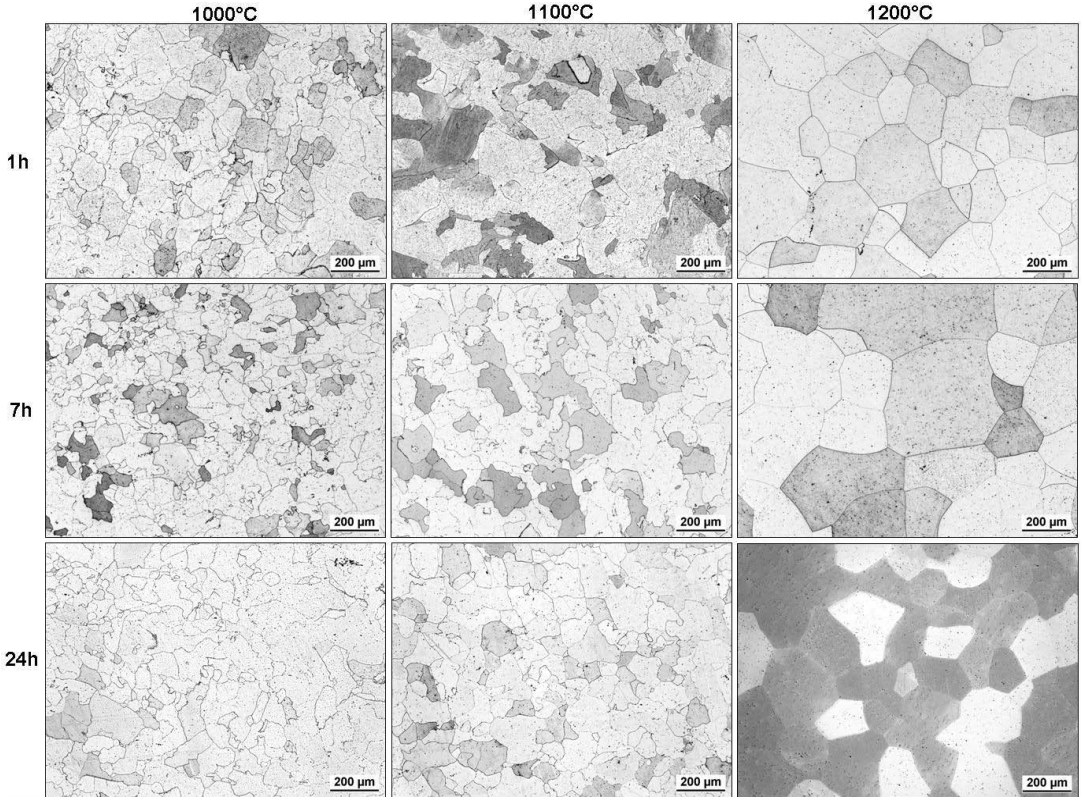

Figure 5.1*:* Optical micrographs of cross sections of the laboratory batch of Crofer 22 H (KUA) after different heat treatment times in static vacuum at different temperatures.

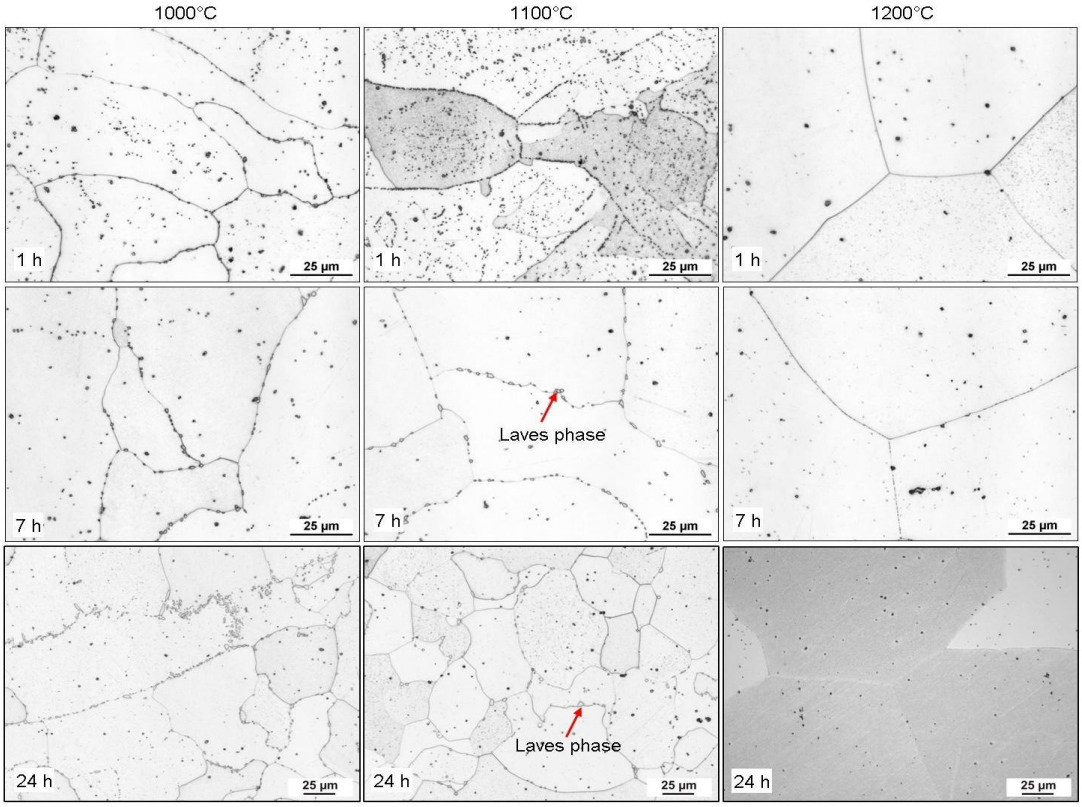

Figure 5.2*:* Optical micrographs of cross sections of the laboratory batch of Crofer 22 H (KUA) after different heat treatment times in static vacuum at different temperatures.

Figures 5.6 and 5.7 show the chemical compositions of the Laves phase and the ferrite matrix of Crofer 22 H (KUA) after annealing at different temperatures. From these results it can be concluded that increasing temperature results in:

- an increasing Si, Nb and W content in the ferrite phase
- a decreasing W and Si content in the Laves phase
- an increasing Nb content in the Laves phase.

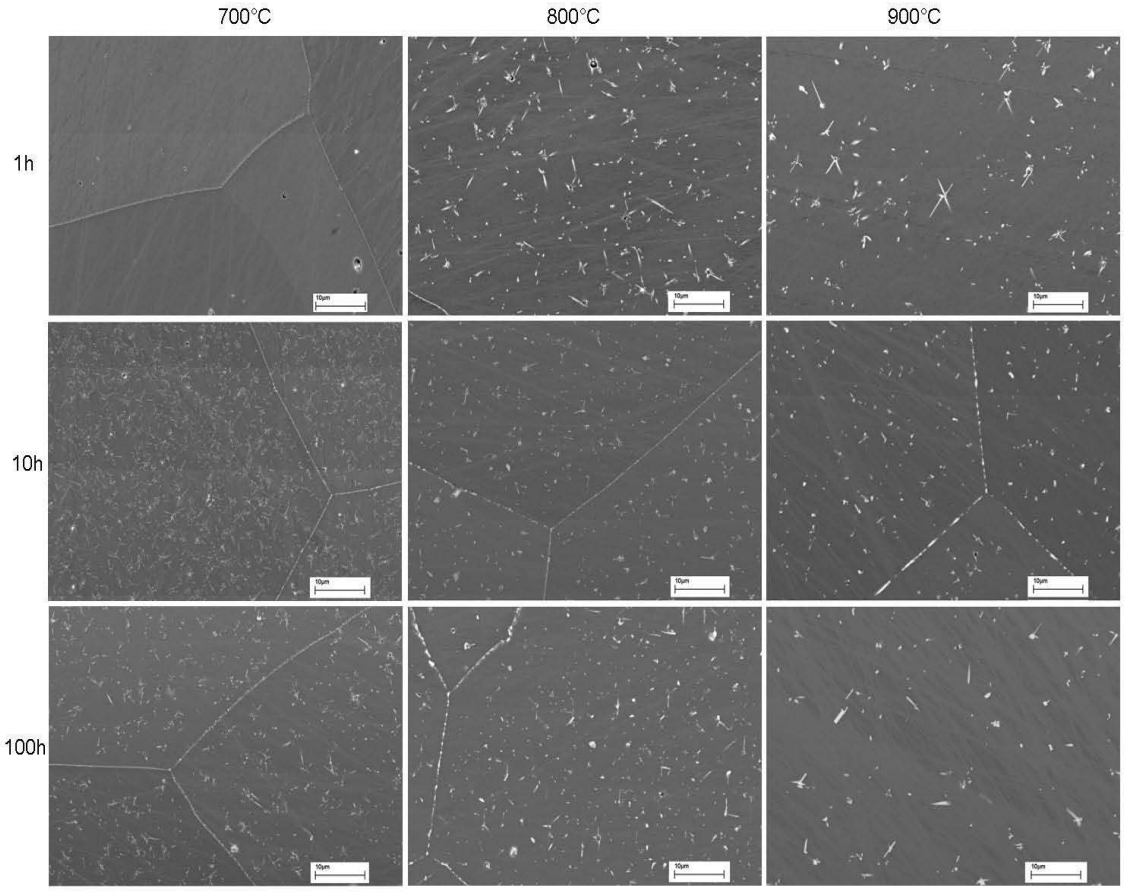

Figure 5.3: SEM/BSE images showing cross sections of the laboratory batch of Crofer 22 H (KUA) after solution annealing for 1 h at 1200 °C in static vacuum and subsequent vacuum heat treatment at 700, 800 or 900 °C for different times.

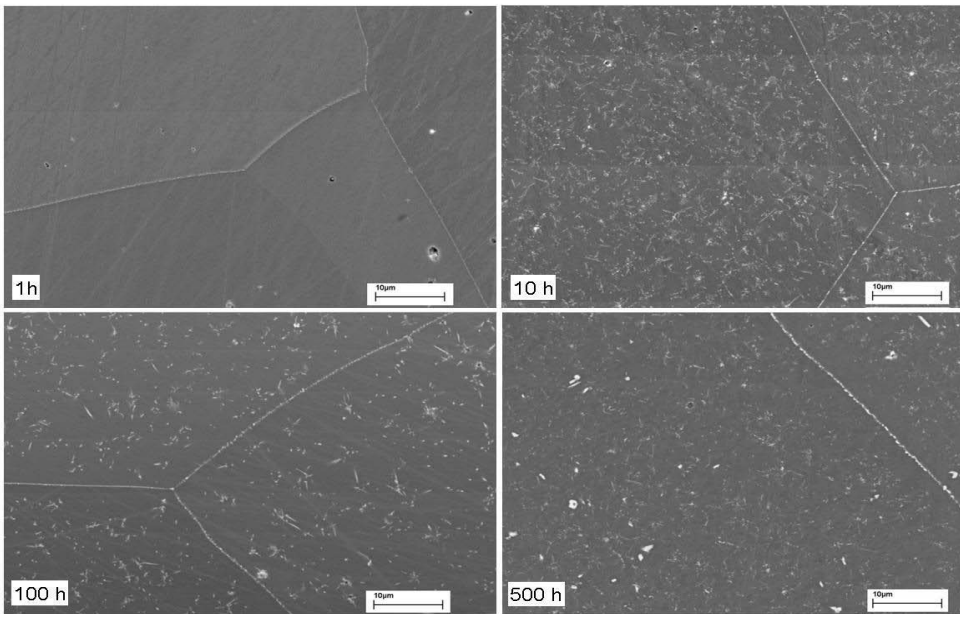

Figure 5.4: Cross sections of the laboratory alloy of the laboratory batch of Crofer 22 H (KUA) after solution annealing for 1 h at 1200 °C in static vacuum and subsequent vacuum heat treatment at 700 °C for various times.

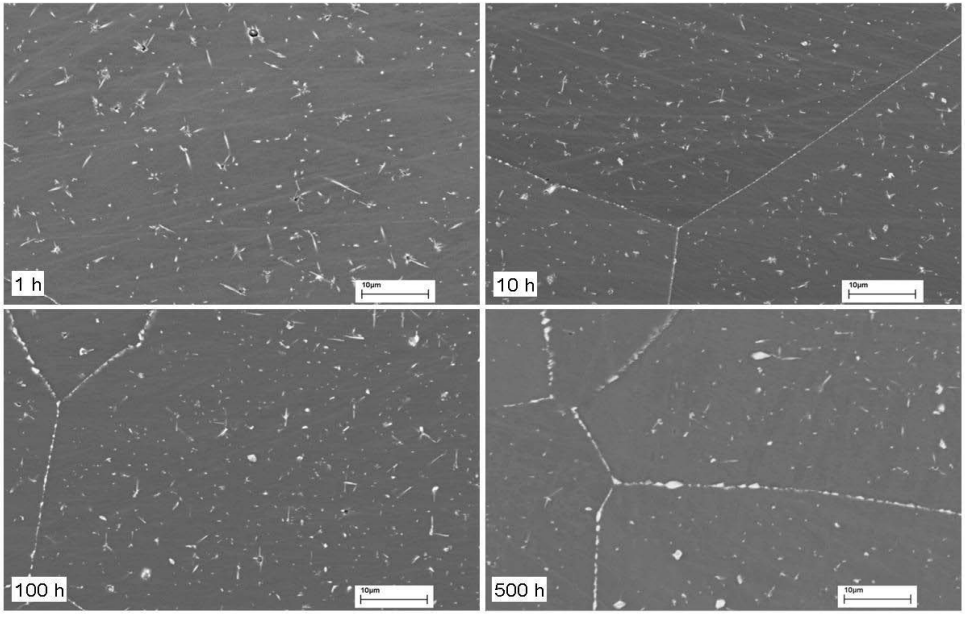

Figure 5.5: SEM/BSE images showing cross sections of the laboratory batch of Crofer 22 H (KUA) after solution annealing for 1 h at 1200 °C in static vacuum and subsequent vacuum heat treatment at 800 °C for various times.

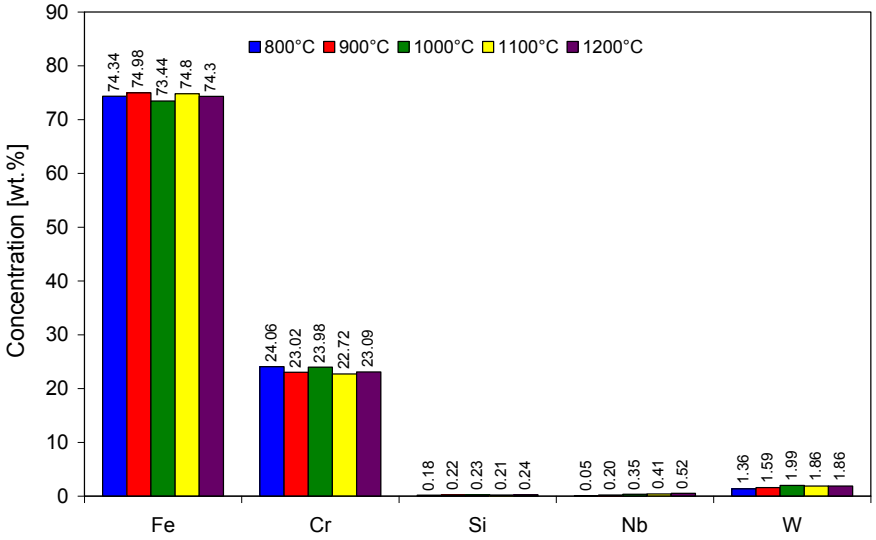

Figure 5.6: Chemical composition of the ferrite matrix in the laboratory batch of Crofer 22 H (KUA) after solution annealing for 1 h at 1200 °C in static vacuum and subsequent vacuum heat treatment at various temperatures for 24 hours as determined by WDX.

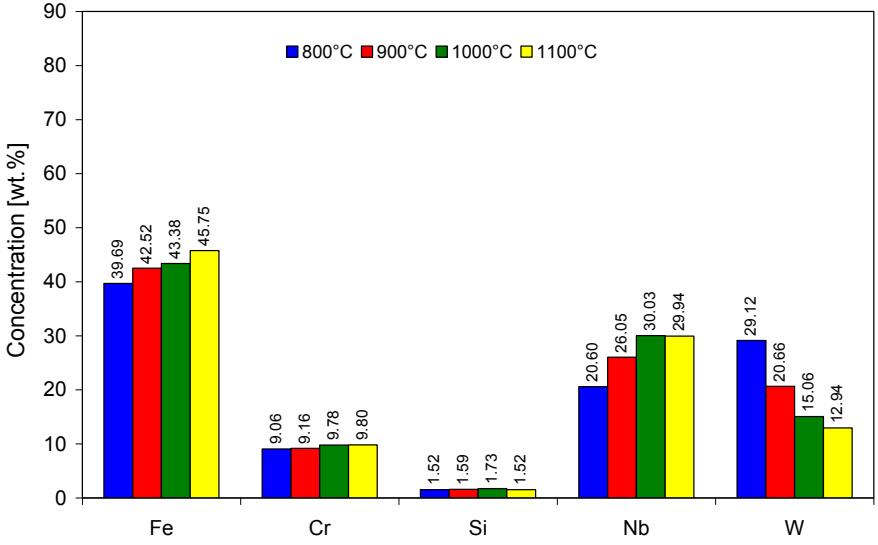

Figure 5.7: Chemical composition of Laves phase in the laboratory batch of Crofer 22 H (KUA) after solution annealing for 1 h at 1200 °C in static vacuum and subsequent vacuum heat treatment at various temperatures for 24 hours as determined by WDX.

5.1.3 Microstructure of laves phase containing model steel

In a further series of experiments the model steel "High Nb/Si" (LWU) was annealed at 800°, 900° and 1000 °C for 50 h, 100 h, 500 h or 1000 h. The results of these studies in respect to phase composition changes were very similar (Figures 5.8-10) to those observed for the laboratory batch of Crofer 22 H (KUA). The higher Nb content in steel LWU results in formation of coarser laves phase precipitates, which allows, as mentioned in the previous section, a more precise WDX analysis of their composition (Figures 5.11-12). Although the results are not identical to those of Crofer 22 H, the data confirm the tendencies in respect to time and temperature dependent changes of the phase compositions.

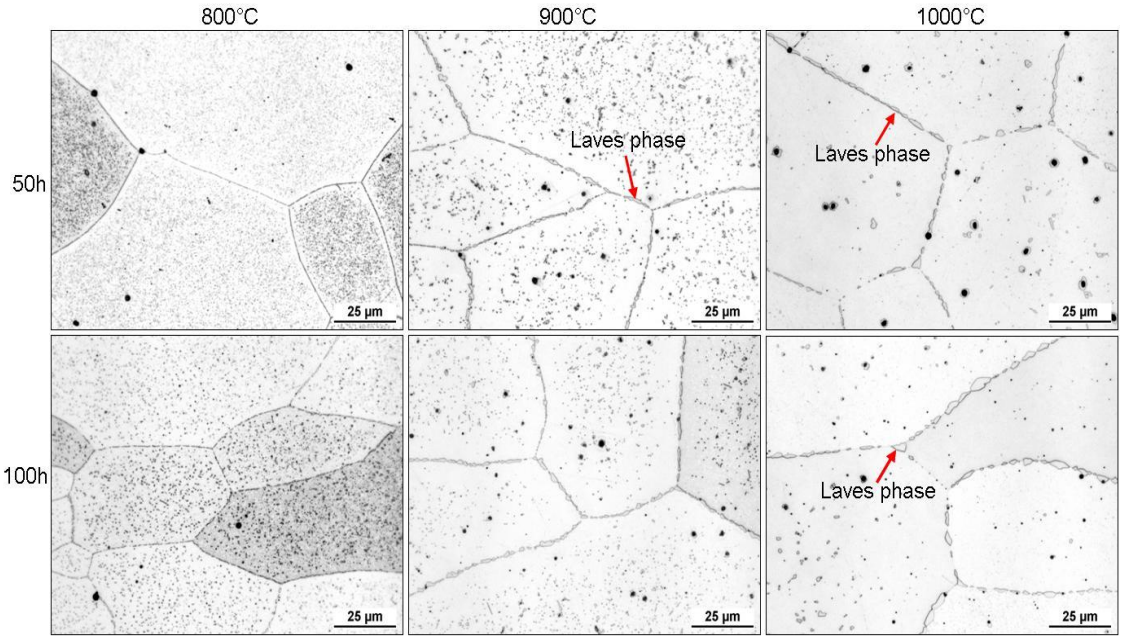

Figure 5.8: Optical micrographs showing cross sections of the "High Nb/Si" model alloy (LWU) after heat treatments in static vacuum for various times at different temperatures.

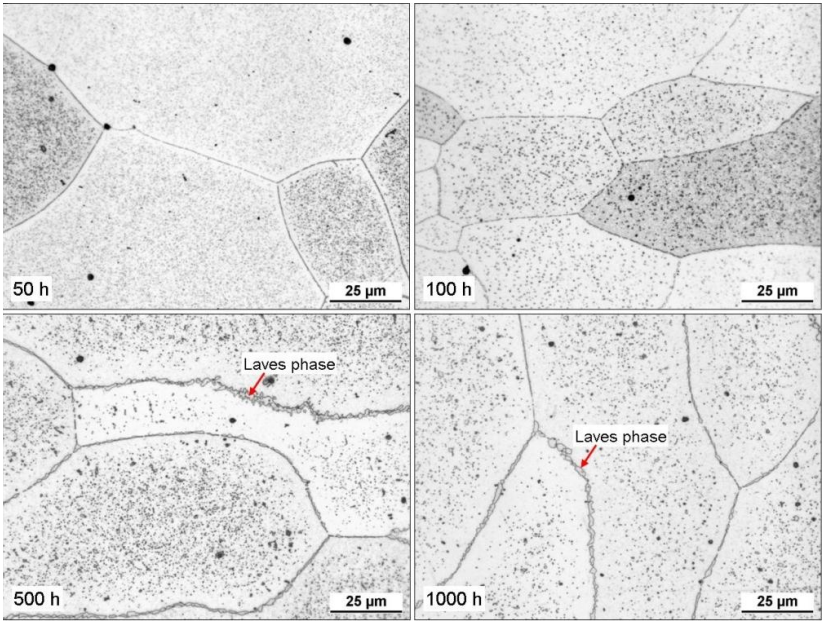

Figure 5.9: Optical micrographs showing cross sections of the "High Nb/Si" model alloy (LWU) after various heat treatment times at 800 °C in static vacuum.

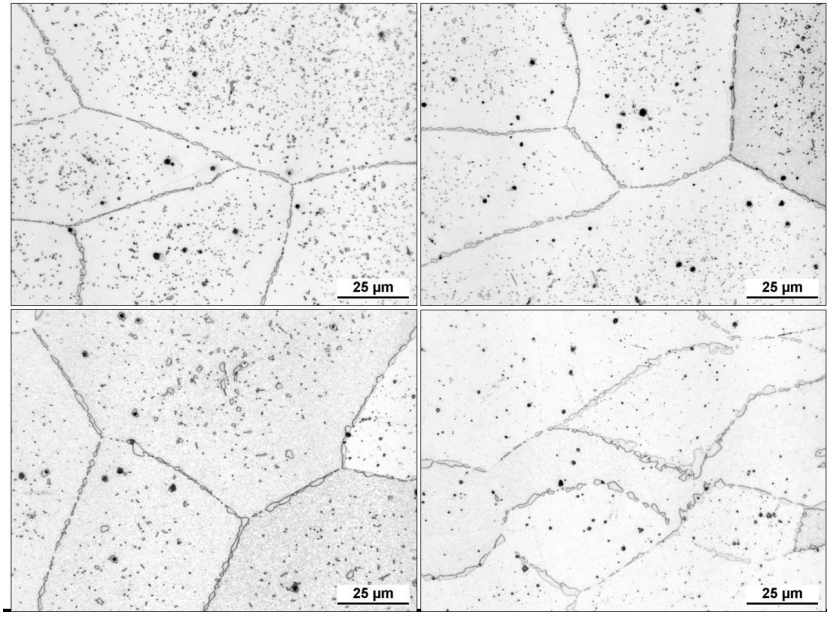

Figure 5.10*:* Optical micrographs showing cross sections of the "High Nb/Si" model alloy (LWU) after various heat treatment times at 900 °C in static vacuum.

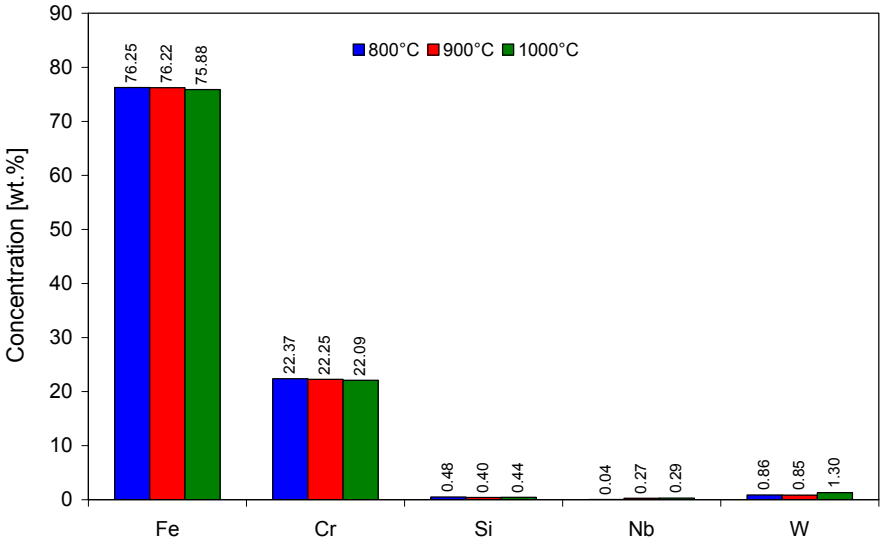

Figure 5.11: Chemical composition of the ferrite matrix in the "High Nb/Si" model alloy (LWU) after annealing at various temperatures for 1000 h determined by WDX.

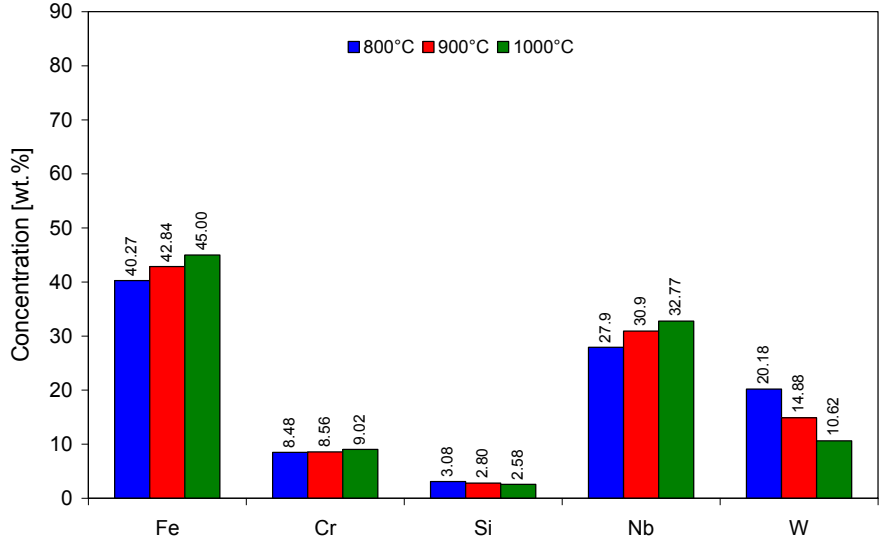

Figure 5.12: Chemical composition of Laves phase in the "High Nb/Si" model alloy (LWU) after annealing at various temperatures for 1000 h determined by WDX.

5.1.4 Microstructure of commercial steel Crofer 22 H

Figures 5.13-14 show microstructures of the commercial steel Crofer 22 H (designations MEC, MDP, MDT, MED) after various exposure times at 800 °C. The results show that the microstructural changes were similar to those observed during annealing of the laboratory heat KUA and that of the model steel LWU described in the previous sections, The Laves phase precipitates tend to coarsen and to become enriched at the grain boundaries with increasing exposure time.

Figure 5.15 illustrates that the oxidation induced composition change in the subsurface zone of the specimen clearly affects the Laves phase distribution. In the subsurface zone the Laves phase precipitates are more extensively coarsened and exhibit a more pronounced concentration at the grain boundaries than in the non-effected, centre part of the specimen.

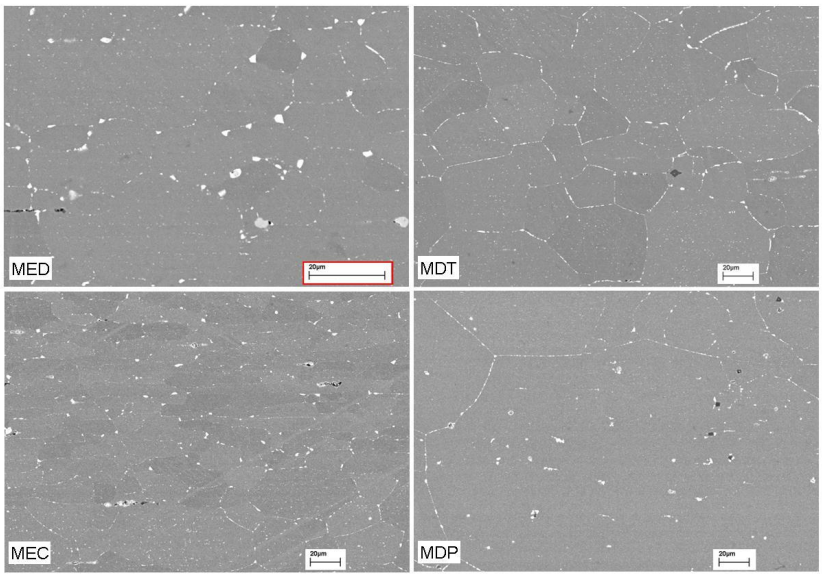

Figure 5.13*:* Cross sections (SEM/BSE) of commercial batch of Crofer 22 H after 1000 h exposure at 800 °C in air. MED–0.3 mm; MDT–0.5 mm; MEC–1 mm; MDP–2.5 mm. Sections were taken from the respective centres of the specimens so that the observed microstructures were not affected by oxidation induced depletion processes.

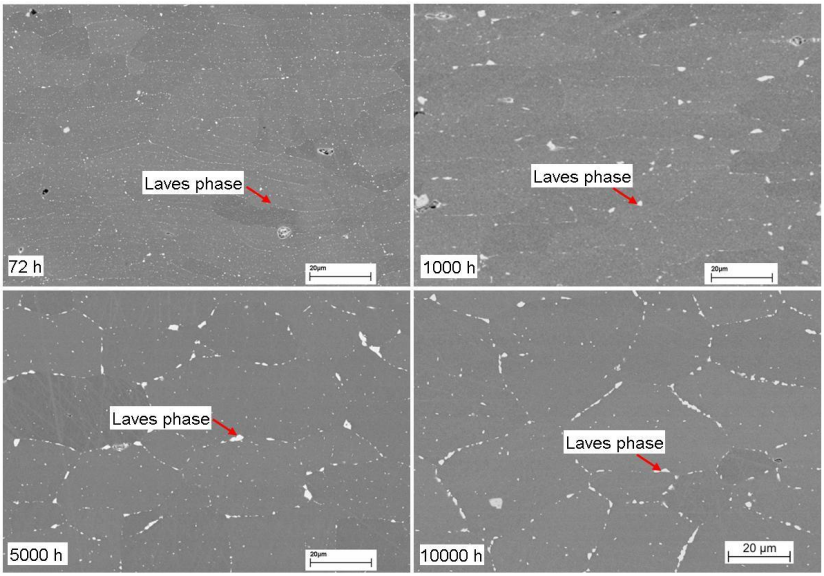

Figure 5.14: Cross sections (SEM/BSE) of 1 mm thick specimens of commercial batch of Crofer 22 H after various exposure times at 800 °C in air. Sections were taken from the respective centres of the specimens so that the observed microstructures were not affected by oxidation induced depletion processes.

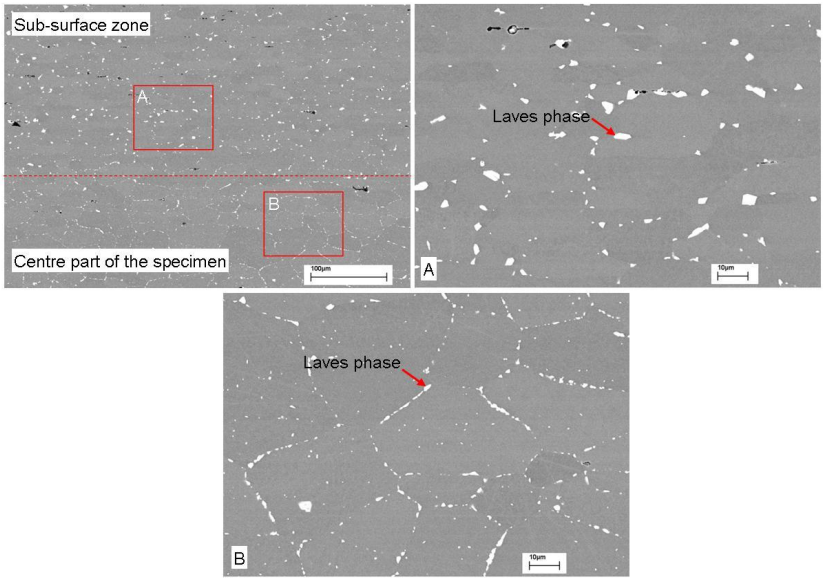

Figure 5.15: Microstructure of 1 mm thick specimen of commercial batch of Crofer 22 H (MEC) after 10000 h oxidation at 800 °C in air, illustrating effect of oxidation induced subsurface changes on Laves phase distribution. Fig. A shows microstructure in subsurface zone, Fig. B corresponds to the centre of the specimen.

5.2 Oxidation behaviour of Crofer 22 H

5.2.1 Temperature dependence of oxidation behaviour

Thermo gravimetric analyses at different temperatures were carried out to investigate the temperature dependence of the air oxidation behavior for getting more insight into the prevailing rate laws during isothermal exposure for the laboratory (KUA) and the commercial (MEC) batch of Crofer 22 H.

Figures 5.16-17 show weight changes as a function of time for the two batches during isothermal oxidation at various temperatures in synthetic air. The commercial batch MEC shows a slightly higher weight change than the laboratory batch. In general, the measured curves obey a near parabolic time dependence (an example for a data evaluation is given in Figure 5.18), that allows the calculation of the parabolic rate constant (K_w) values from each curve as a function of temperature (Figure 5.19). It can be seen that batch MEC shows a more pronounced temperature dependence than KUA, therefore, the commercial batch reveals a slightly higher oxidation rate than the laboratory batch at higher temperatures.

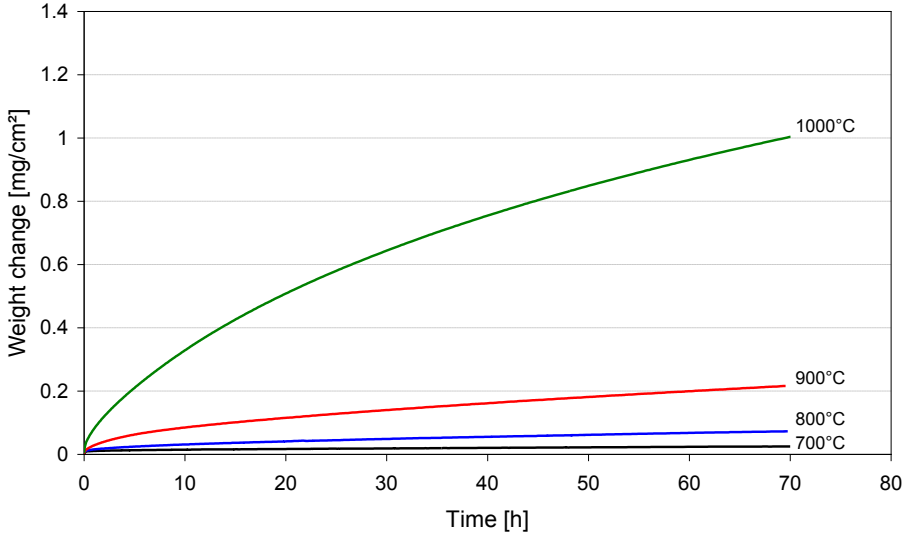

Figure 5.16: Weight change as a function of time during isothermal oxidation of the laboratory batch of Crofer 22 H (KUA) in air at different temperatures.

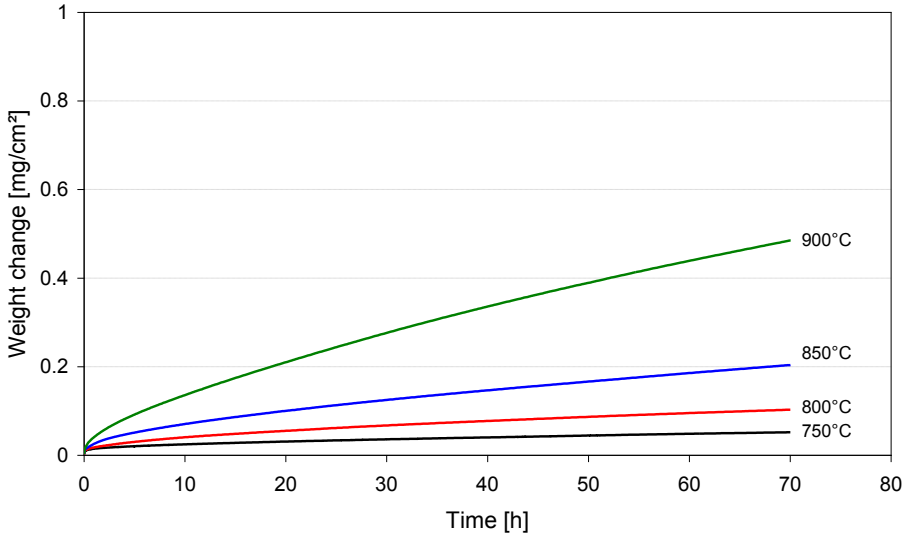

Figure 5.17: Weight change as a function of time during isothermal oxidation of the commercial batch of Crofer 22 H (MEC) in air at different temperatures.

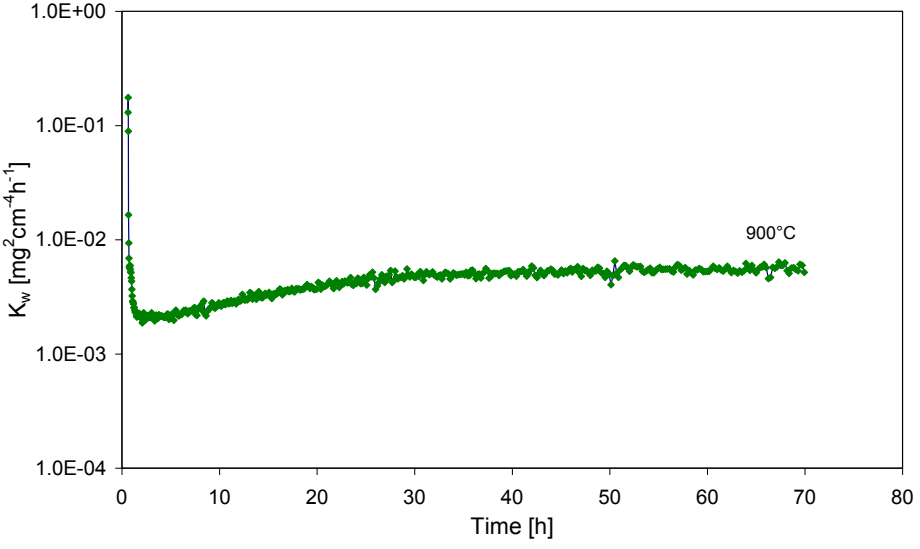

Figure 5.18: Instantaneous parabolic rate constant K_w as a function of exposure time for the commercial Crofer 22 H (MEC) at 900 °C during 72 h oxidation in air. The curve shows that the oxide scale growth obeys a near parabolic time dependence.

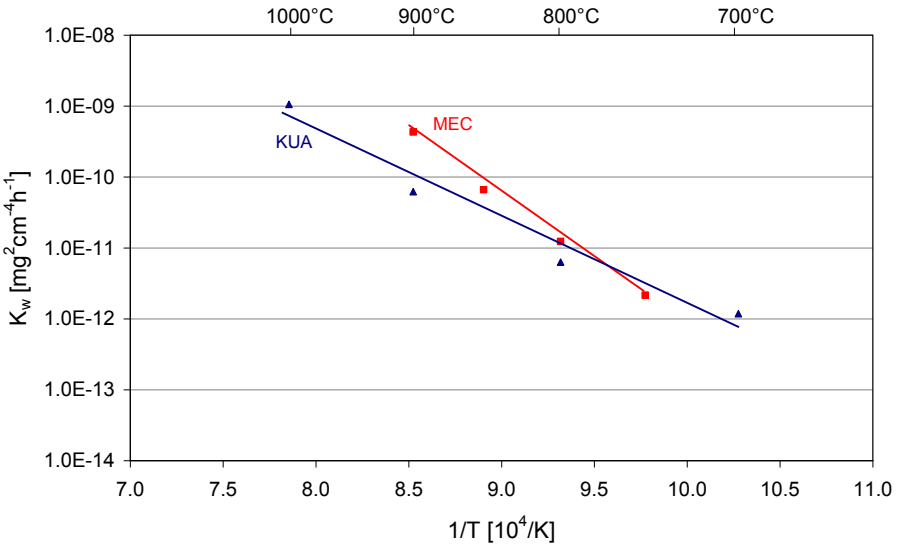

Figure 5.19: Parabolic rate constant K_w as a function of reciprocal temperature for the laboratory batch of Crofer 22 H (KUA) in comparison with that of the commercial batch of Crofer 22 H (MEC), oxidized isothermally for 72 h in synthetic air. K_w values calculated from TG curves in figures 5.16-17.

The laboratory (KUA) and the commercial batch (MEC) of Crofer 22 H exhibit after isothermal oxidation for 72 h at temperatures between 700 and 1000 °C in air a duplex oxide scale consisting of an outer layer of $(Mn,Cr)_3O_4$ and an inner layer of Cr_2O_3 (Figure 5.20-21). The internal oxidation zone in the laboratory batch of Crofer 22 H (KUA) consists of fine and randomly dispersed titanium oxide precipitates (Figure 5.21).

The commercial batch of Crofer 22 H (MEC) shows a slightly different appearance of the internal oxidation zone morphology. After oxidation at 750 °C virtually no internal titanium oxide particle formation is seen. At 900 °C after the same exposure time, the Ti-oxide precipitates can be found mostly on ferrite grain boundaries but not within the ferrite grains (Figure 5.20). The explanation for this difference in the morphology of the internal oxidation zone may be due to the impurities of C and N (see Table 4) present in higher amount in the commercial batch (MEC) than in the laboratory batch of Crofer 22 H (KUA).

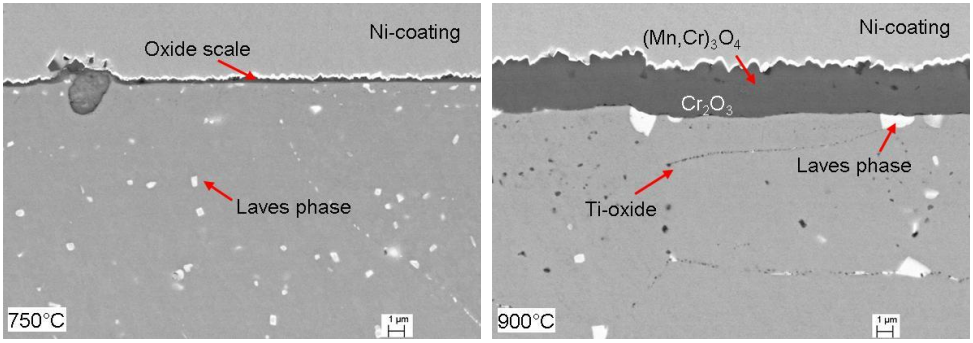

Figure 5.20: SEM/BSE images of cross sections of the oxide scales formed on the commercial batch of Crofer 22 H (MEC) during 72 h isothermal oxidation at 750 °C and 900 °C in synthetic air.

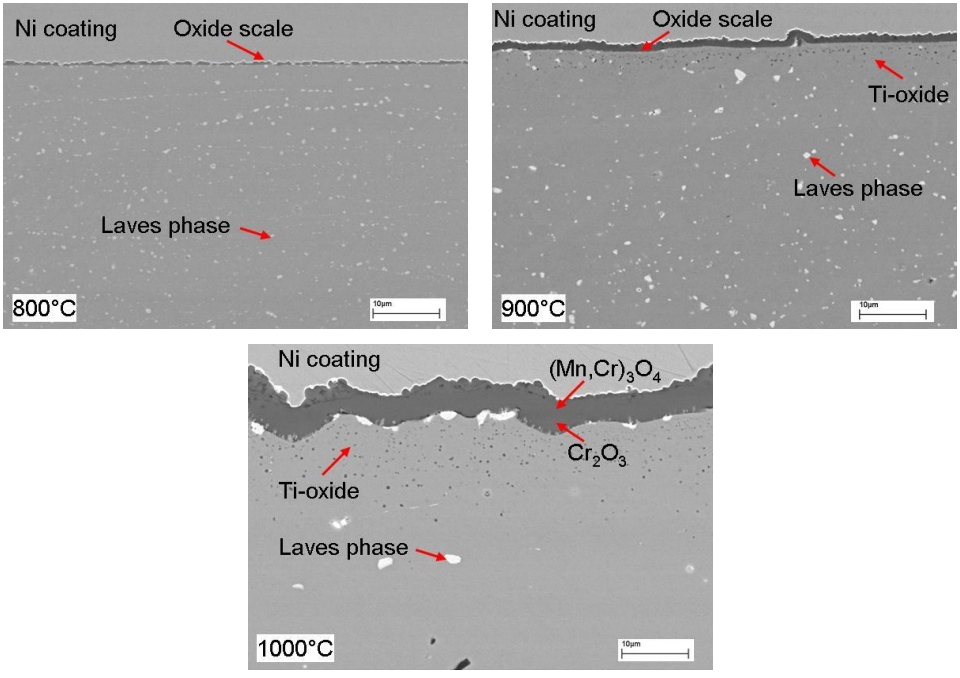

Figure 5.21: SEM/BSE images of cross sections of the oxide scales formed on the laboratory batch of Crofer 22 H (KUA) during 72 h isothermal oxidation at different temperatures in synthetic air.

5.2.2 Scale formation in air

For getting further information on the mechanisms of oxidation, the oxide scales on Crofer 22 H in air were investigated by Plasma-SNMS. Figures 5.22-29 show element

distributions in the oxide scale and the subscale zone after various oxidation times in case of the laboratory batch of Crofer 22 H (KUA) oxidized at 800 °C in air. All the specimens used in these tests had a thickness of 2 mm. Already after 1 h of oxidation the oxide scale grown on the steel consists of an outer layer enriched in manganese and an inner chromia layer. After 24 h of oxidation the surface concentration of Mn and Cr are virtually equal, after 70 h of oxidation the Mn concentration in the outer part of the oxide scale is higher than the Cr concentration. The Cr/Mn ratio in the outer part of the oxide scale after 70 h oxidation is approximately 3:4. It is unclear whether the Cr/Mn ratio is typical for the spinel in equilibrium with air [101] or whether it is partially Cr-depleted by formation of volatile chromium species.

As illustrated in section 4.1, Crofer 22 H possesses in the as-received condition a nearly single phase microstructure virtually free of Laves phase precipitates. But the exposure of the alloy at 800 °C results in changes of the microstructure. The primary change is formation of Laves phase precipitates from the oversaturated ferrite. The secondary change is coarsening of Laves phase precipitates. A further change is the redistribution of Laves phase precipitates caused by oxidation induced changes in the subscale zone of the alloy. During the oxidation process, especially chromium and manganese are consumed from the steel by the growing oxide scale. As a result, chemical activity gradients of those elements are developed in the Mn-and Cr-depleted zone. The gradients may be responsible for dissolution and re-precipitation of Laves phase in the depletion zone.

The plasma-SNMS profiles (Figures 5.30-36) show that the re-distribution process starts during the early stages of oxidation and occurs parallel to the above described primary and secondary processes. These processes will more extensively be discussed in section 5.3. Interesting to note is the fact that after 1 h of oxidation a sharp silicon peak near the oxide/metal interface is present (Figures 5.34 and 5.35). It is supposed that during the early stages of oxidation (“transient oxidation stage”) all elements which posses a high oxygen affinity, including silicon, are able to form their oxides.

Figure 5.37 shows the oxide scale formed on the laboratory batch of Crofer 22 H (KUA) after exposure for 70 h oxidation in air. A two-layered scale is formed consisting of an outer $(Cr,Mn)_3O_4$ layer and a inner Cr_2O_3 layer. The interface between the inner chromia and the outer spinel layer can only be seen due to a slight difference in brightness of the two phases in the backscattered electron image. The outer spinel layer formed during air exposure exhibits a morphology of faceted crystals and the oxide scale formed shows a smooth appearance. Titanium is frequently present in the scale [102]: that is, dissolved in the chromia near the scale/alloy interface and in form of titania particles at the scale/gas interface (Figure 5.33). In the alloy matrix and in some areas beneath the oxide scale, Laves phase precipitates can be also found.

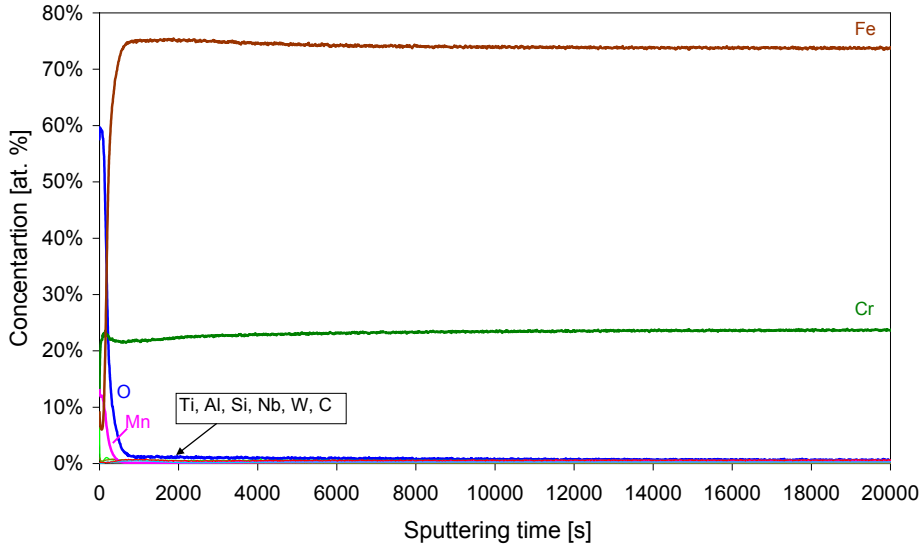

Figure 5.22: Plasma-SNMS (linear scale) element concentration profiles measured on the laboratory batch of Crofer 22 H (KUA) after 1 h oxidation at 800 °C in laboratory air.

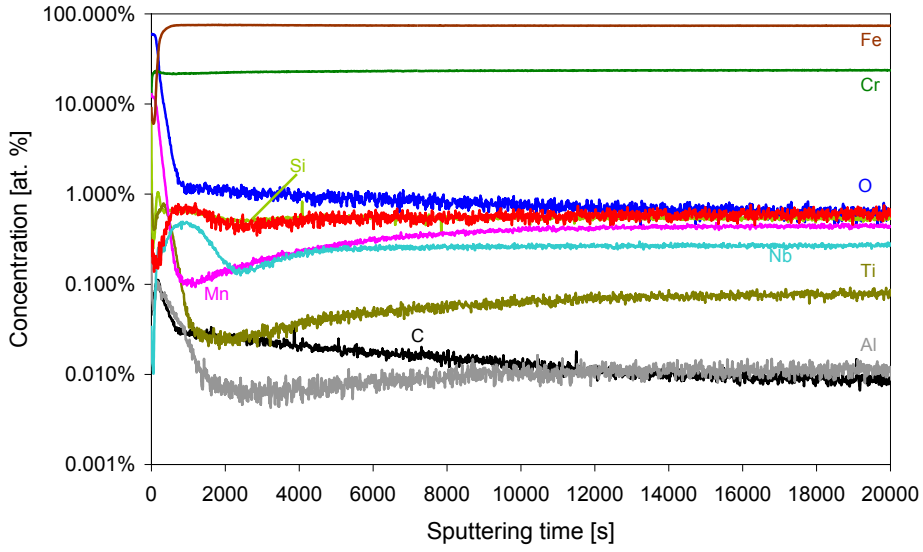

Figure 5.23: Plasma-SNMS (logarithmic scale) element concentration profiles measured on the laboratory batch of Crofer 22 H (KUA) after 1 h oxidation at 800 °C in laboratory air.

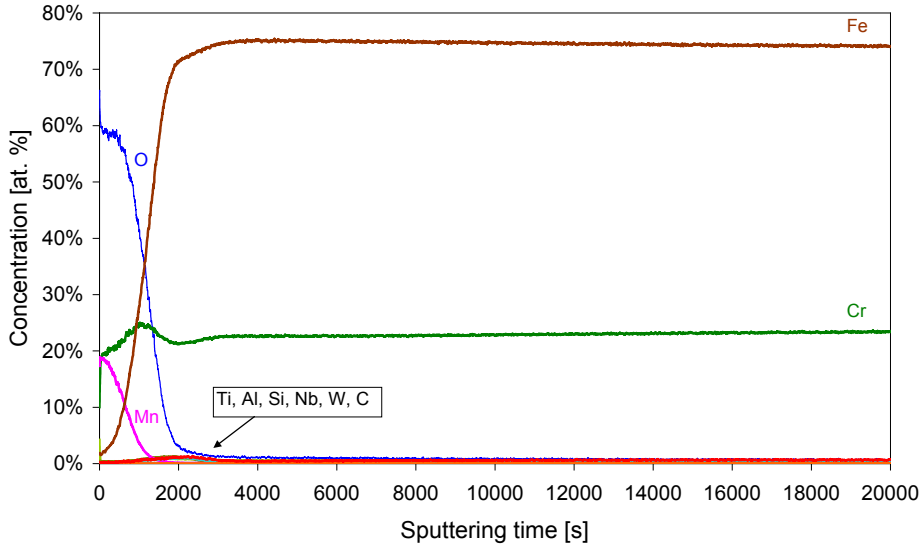

Figure 5.24: Plasma-SNMS (linear scale) element concentration profiles measured on the laboratory batch of Crofer 22 H (KUA) after 24 h oxidation at 800 °C in laboratory air.

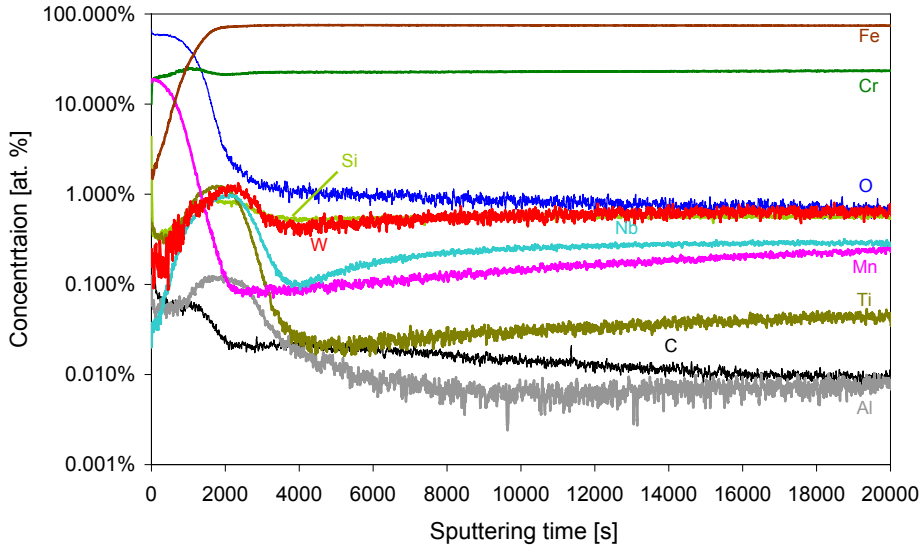

Figure 5.25: Plasma-SNMS (logarithmic scale) element concentration profiles measured on the laboratory batch of Crofer 22 H (KUA) after 24 h oxidation at 800 °C in air.

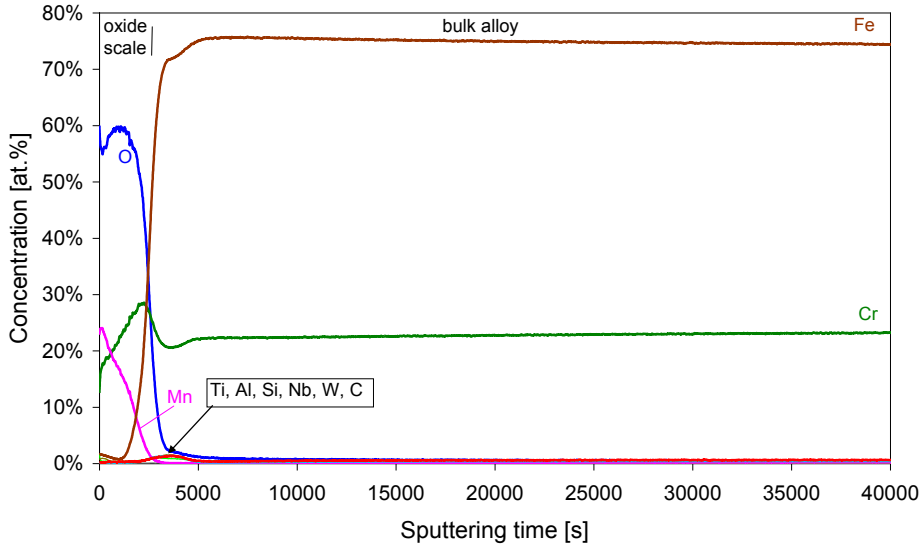

Figure 5.26: Plasma-SNMS (linear scale) element concentration profiles measured on the sample KUA after 70 h oxidation at 800 °C in laboratory air.

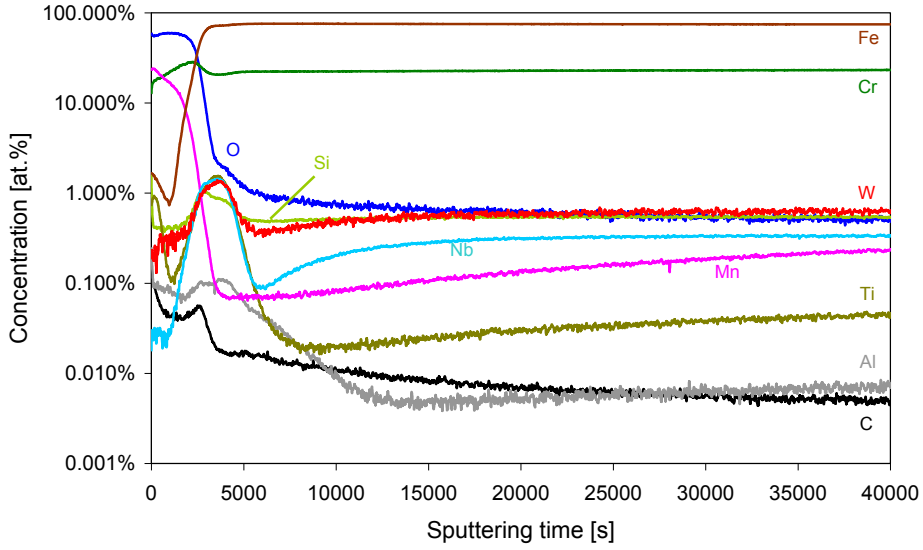

Figure 5.27: Plasma-SNMS (logarithmic scale) element concentration profiles measured on the laboratory batch of Crofer 22 H (KUA) after 70 h oxidation at 800 °C in air.

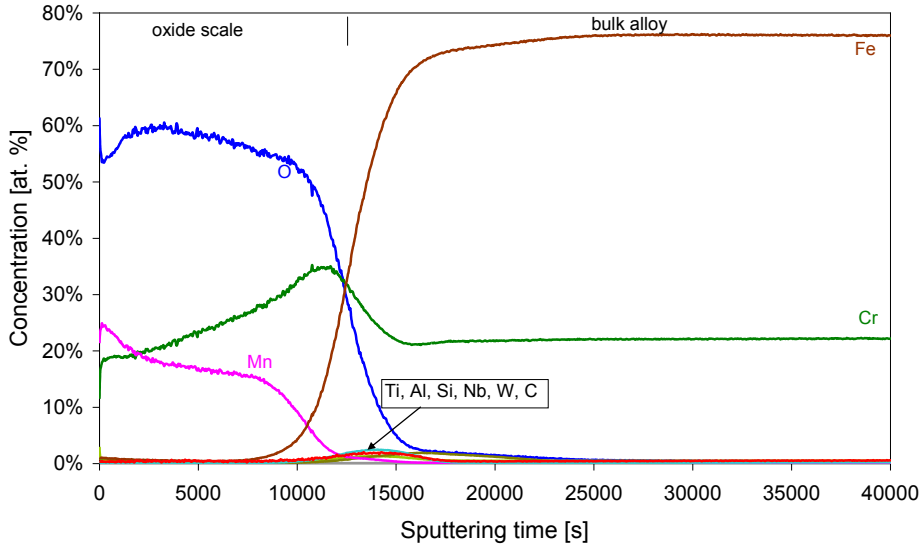

Figure 5.28: Plasma-SNMS (linear scale) element concentration profiles measured on the sample KUA after 1500 h oxidation at 800 °C in laboratory air.

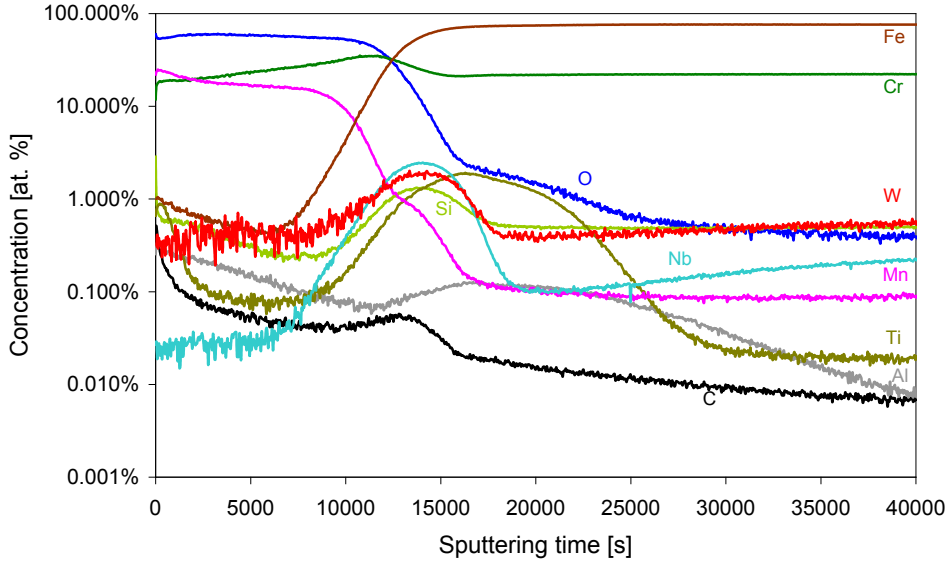

Figure 5.29: Plasma-SNMS (logarithmic scale) element concentration profiles measured on the laboratory batch of Crofer 22 H (KUA) after 1500 h oxidation at 800 °C in laboratory air.

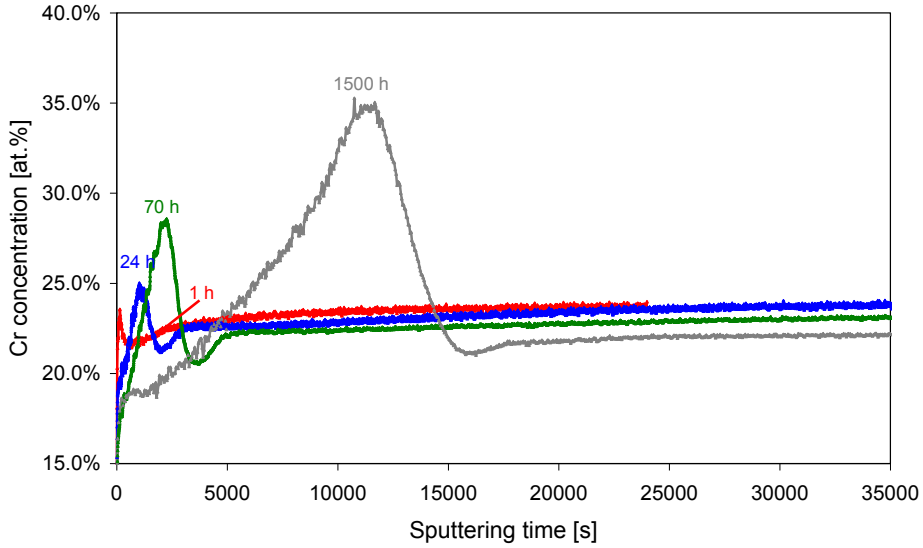

Figure 5.30: Chromium distribution (linear scale) in the laboratory batch of Crofer 22 H (KUA) oxidized for various times at 800 °C in air (measured with Plasma-SNMS).

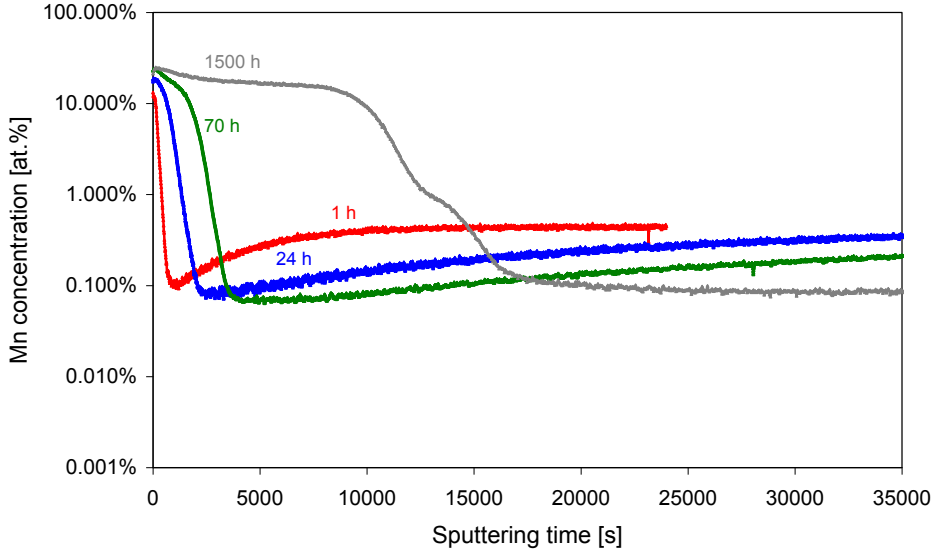

Figure 5.31: Manganese distribution (logarithmic scale) in the laboratory batch of Crofer 22 H (KUA) oxidized for various times at 800 °C in air (measured with Plasma-SNMS).

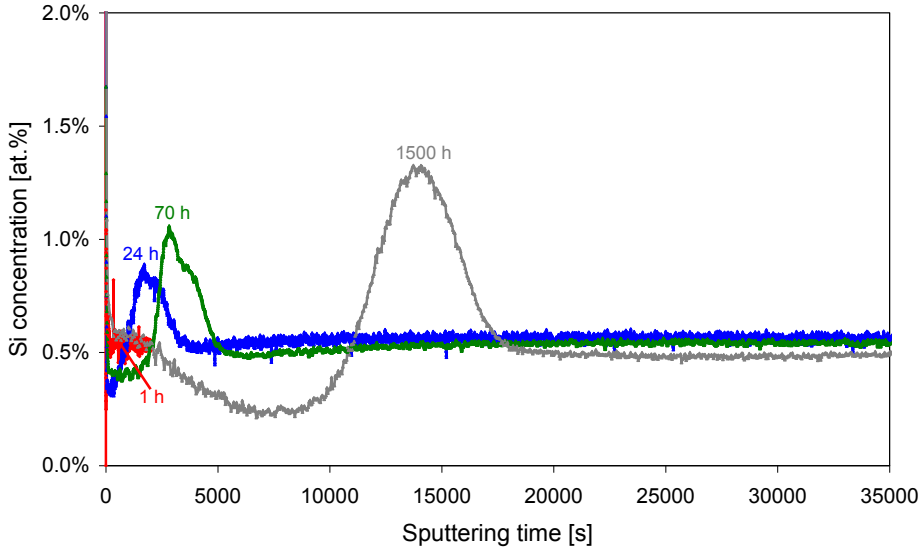

Figure 5.32: Silicon distribution (linear scale) in the samples of the laboratory batch of Crofer 22 H (KUA) oxidized for various times at 800 °C in air (measured with Plasma-SNMS).

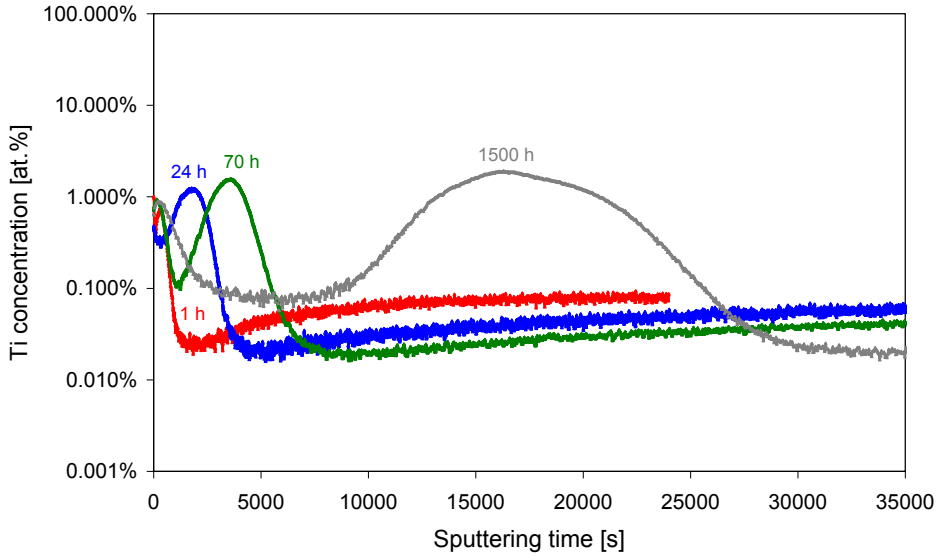

Figure 5.33: Titanium distribution (logarithmic scale) in the laboratory batch of Crofer 22 H (KUA) oxidized for various times at 800 °C in air (measured with Plasma-SNMS).

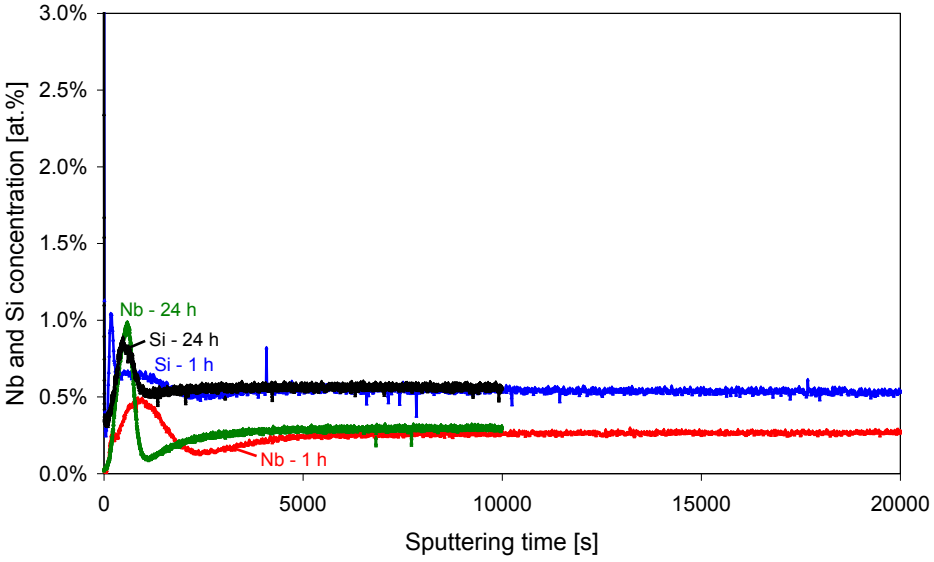

Figure 5.34: Nb and Si distribution (linear scale) in the samples of the laboratory batch of Crofer 22 H (KUA) oxidized for various times at 800 °C in air (measured with Plasma-SNMS). Short term tests.

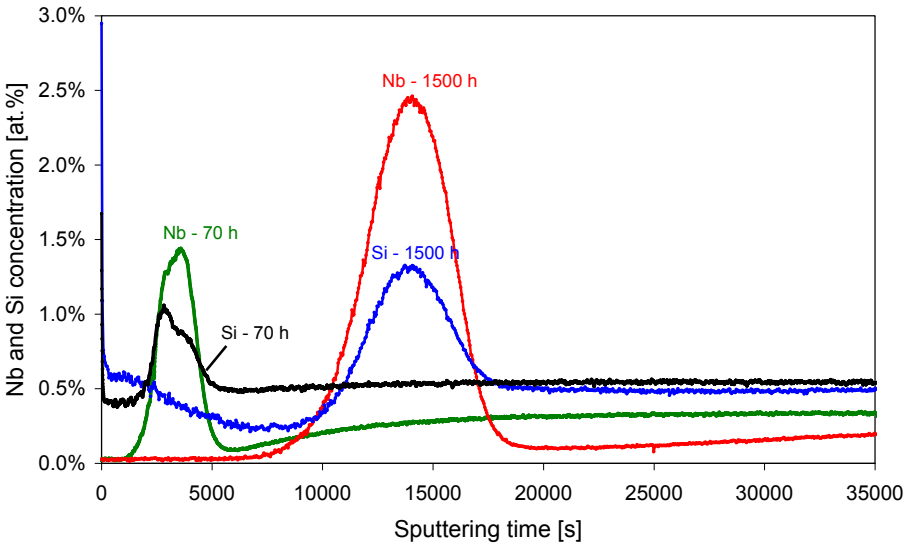

Figure 5.35: Nb and Si distribution (linear scale) in the laboratory batch of Crofer 22 H (KUA) oxidized for various times at 800 °C in air (measured with Plasma-SNMS). Longer term tests

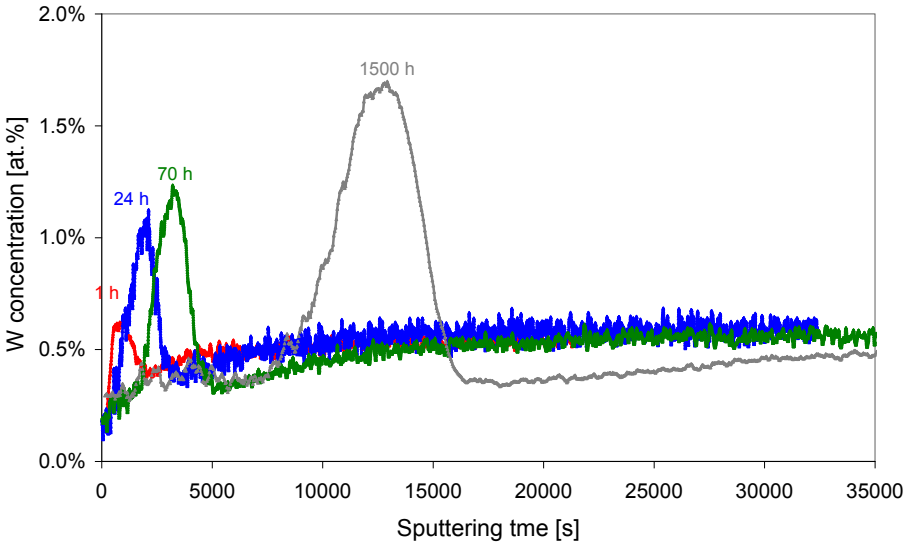

Figure 5.36: Tungsten distribution (linear scale) in the samples of the laboratory batch of Crofer 22 H (KUA) oxidized for various times at 800 °C in air (measured with Plasma-SNMS).

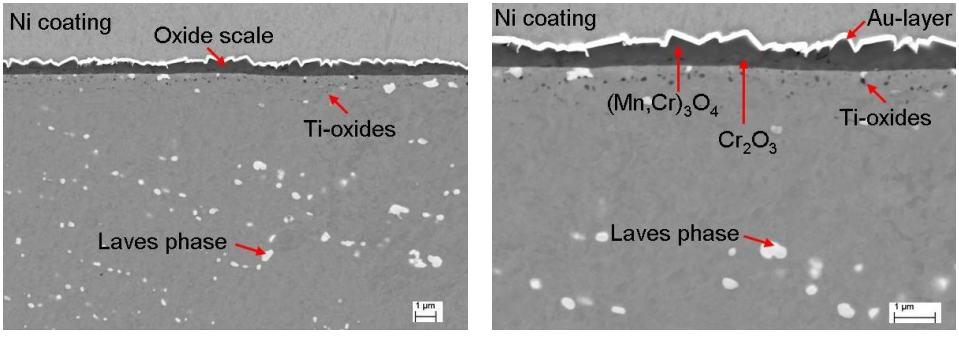

Figure 5.37: SEM/BSE images showing cross sections of oxide scale formed on laboratory batch of Crofer 22 H (KUA) during 70 h oxidation at 800 °C in air.

5.2.3 Scale formation in Ar-H_2-H_2O

Similar as described for the air exposure in section 5.2.2, also the scale formation in Ar-H_2-H_2O at 800 °C was studied in detail as function of exposure time. Figures 5.38-45 show the Plasma-SNMS profiles of the samples exposed for 1 h, 24 h, 70 h and 1000 h in

Ar-H_2-H_2O. The manganese concentration in the outer part of the scale increases with increasing oxidation time so that after 24 h the Cr/Mn ratio reaches a value of approximately 3:2 (Figure 5.40). An important difference between oxidation in air and Ar-H_2-H_2O is that in the latter gas a relative Mn-enrichment appears in the inner part of oxide scale. Already after 1 h oxidation, a Mn-enrichment near the oxide/metal interface is visible (Figure 5.38). The Mn-enrichment seems to be time independent and even after 70 h of oxidation it remains at a level of approximately 2 %. The differences in Mn distribution in case of exposures in air and simulated anode gas will be described in more detail in section 5.4.

The titanium distribution in the samples oxidized in simulated anode gas exhibits enrichment in the subscale zone, which reflects the formation of internal Ti-oxides. No surface enrichment of titanium in the oxide was observed. Lack of titanium in the outer part of the oxide scale suggests a low solubility in the $MnCr_2O_4$ spinel layer which is consistent with literature data on phase equilibria in the Ti-Mn-Cr-O system [101].

Niobium enrichment at the oxide/steel interface caused by Laves phase re-distribution formed during air exposure also appears during oxidation in simulated anode gas. However, contrary to the air experiments the maximum Nb-enrichment seems to become already very pronounced after shorter exposure times. Further details about this effect will be described in section 5.3.

The silicon distributions measured after oxidation in simulated anode gas are similar to those measured after air oxidation. However, formation of transient silica (after 1 h oxidation) seems to be less pronounced in simulated anode gas than in air (Figures 5.46-51).

Figure 5.52 shows the oxide scale formed in the laboratory batch of Crofer 22 H (KUA) after exposure for 70 h oxidation in Ar-4%H_2-2%H_2O. The outer part of the scale consists of Cr/Mn-spinel on top of an inner Cr_2O_3 layer. The oxide scale formed during simulated anode gas exposure shows a blade and whisker like morphology [103-105].

The scale exhibits a band of pores at the interface between the chromia and the spinel layer. Beneath the oxide scale an internal oxidation zone of small spherical titanium oxide particles can be seen. In the alloy matrix and in some areas beneath the oxide scale Laves phase precipitates can be found.

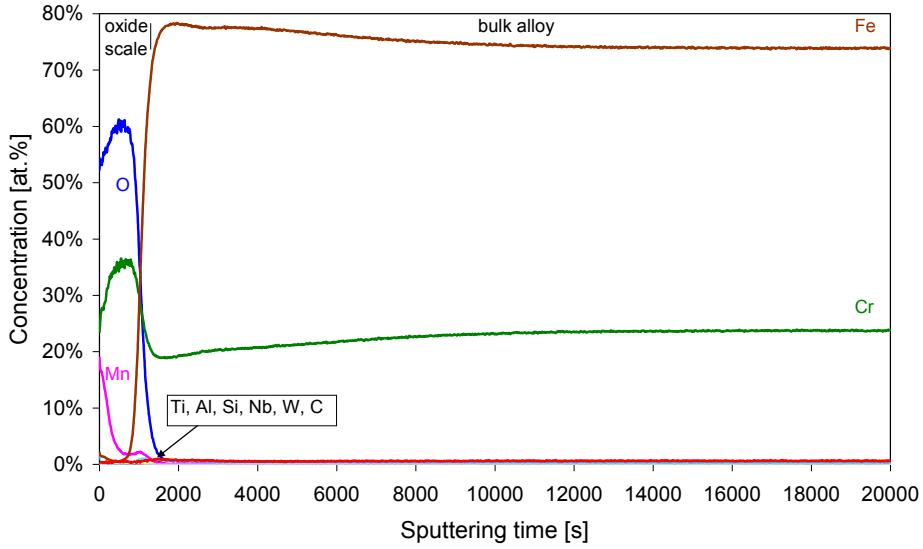

Figure 5.38: Plasma-SNMS (linear scale) element concentration profiles measured on the laboratory batch of Crofer 22 H (KUA) after 1 h oxidation at 800 °C in Ar-4%H_2-2%H_2O.

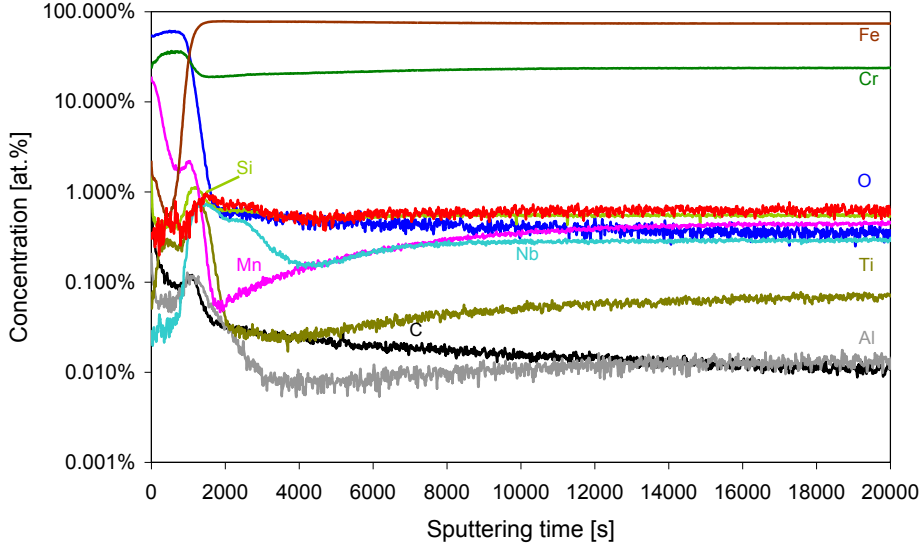

Figure 5.39: Plasma-SNMS (logarithmic scale) element concentration profiles measured on the laboratory batch of Crofer 22 H (KUA) after 1 h at 800 °C in Ar-4%H_2-2%H_2O.

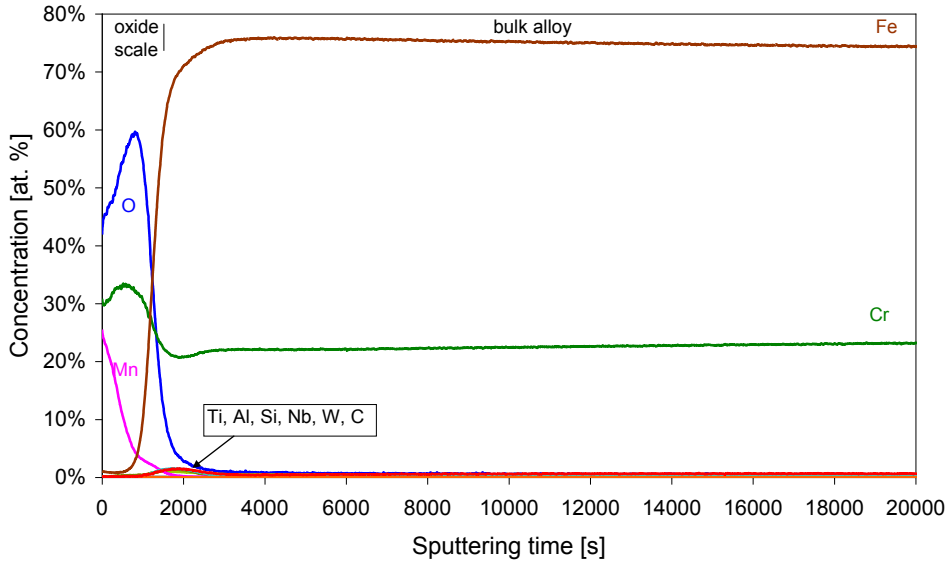

Figure 5.40: Plasma-SNMS (linear scale) element concentration profiles measured on the laboratory batch of Crofer 22 H (KUA) after 24 h oxidation at 800 °C in Ar-4%H_2-2%H_2O.

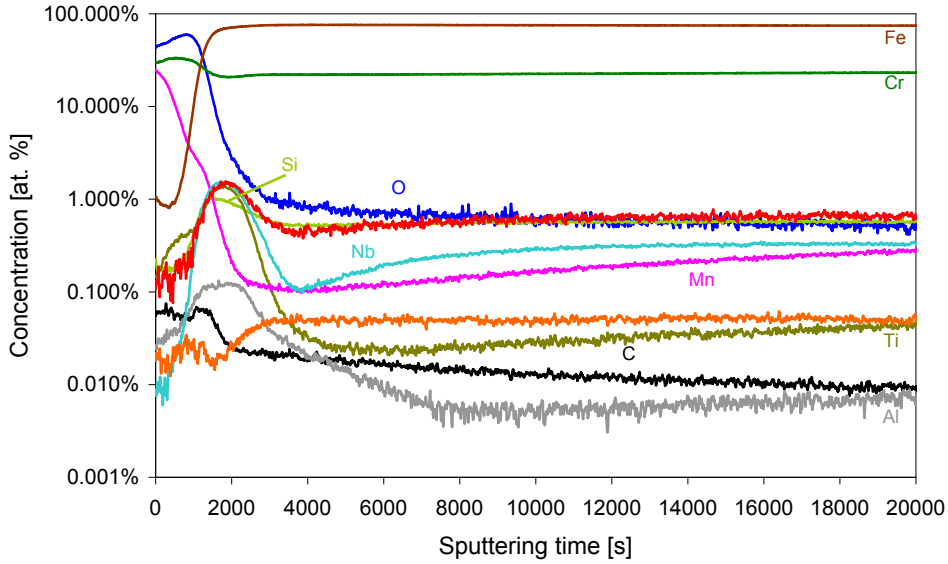

Figure 5.41: Plasma-SNMS (logarithmic scale) element concentration profiles measured on the laboratory batch of Crofer 22 H (KUA) after 24 h oxidation at 800°C in Ar-4%H_2-2%H_2O.

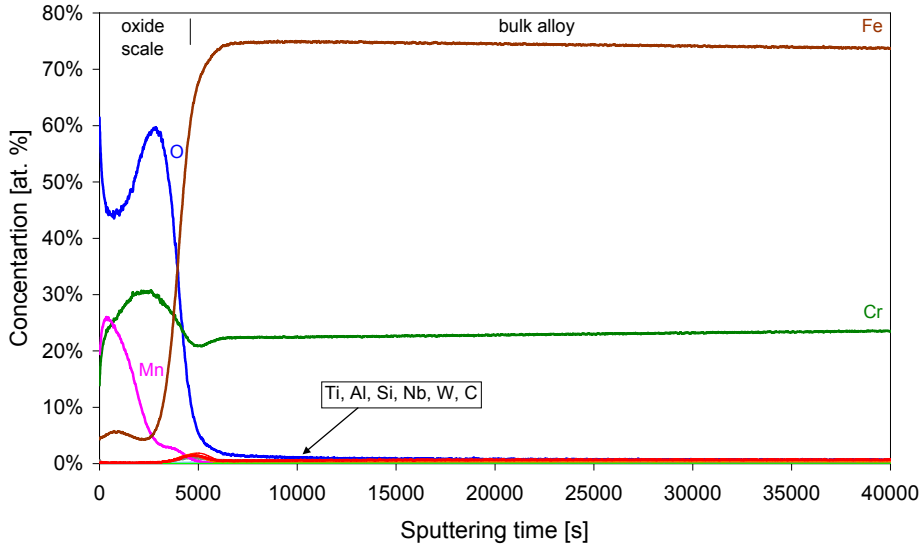

Figure 5.42: Plasma-SNMS (linear scale) element concentration profiles measured on the laboratory batch of Crofer 22 H (KUA) after 70 h at 800 °C in Ar-4%H_2-2%H_2O.

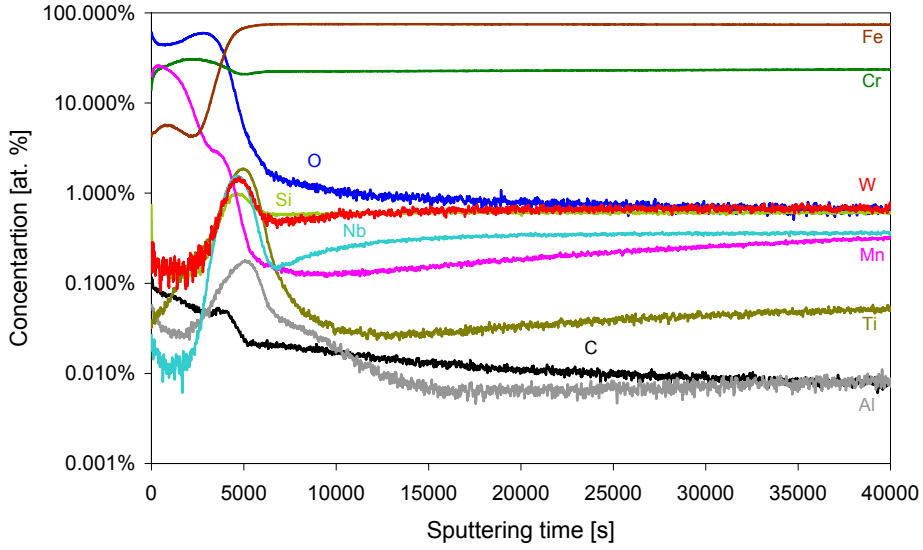

Figure 5.43: Plasma-SNMS (logarithmic scale) element concentration profiles measured on the laboratory batch of Crofer 22 H (KUA) after 70 h at 800 °C in Ar-4%H_2-2%H_2O.

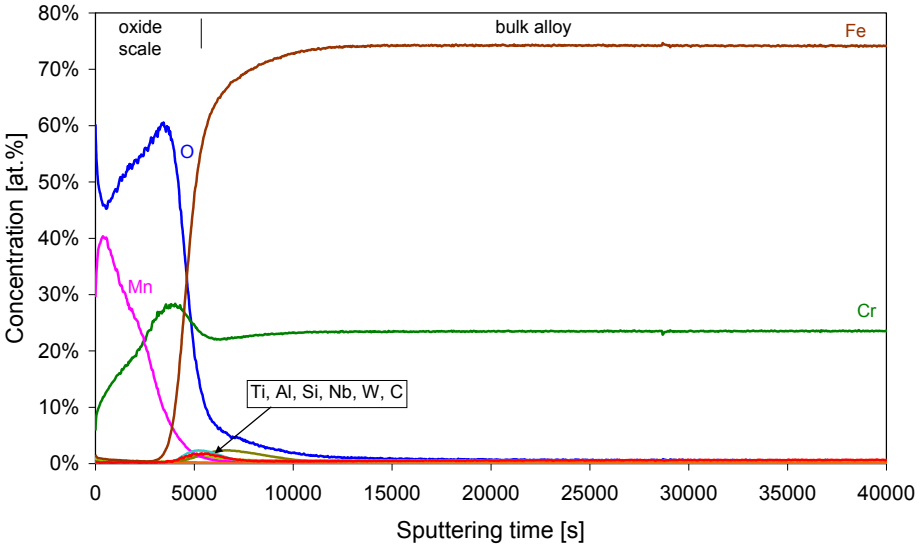

Figure 5.44: Plasma-SNMS (linear scale) element concentration profiles measured on the laboratory batch of Crofer 22 H (KUA) after 1000 h at 800 °C in Ar-4%H_2-20%H_2O.

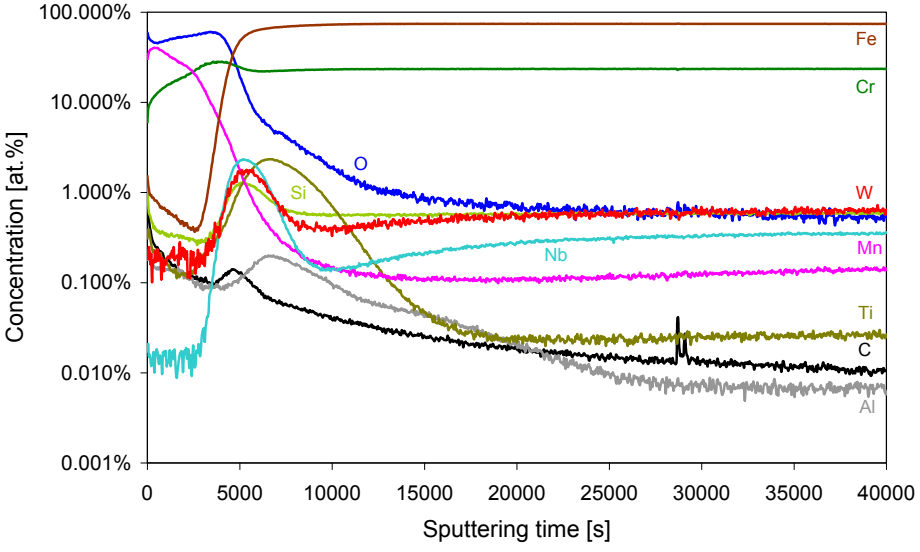

Figure 5.45: Plasma-SNMS (logarithmic scale) element concentration profiles measured on the laboratory batch of Crofer 22 H (KUA) after 1000 h at 800 °C in Ar-4%H_2-20%H_2O.

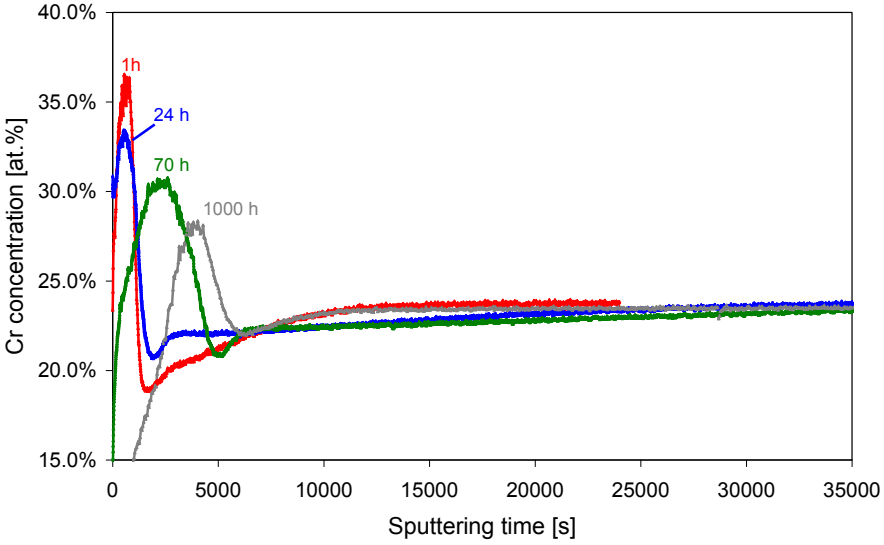

Figure 5.46: Chromium distribution (linear scale) in the laboratory batch of Crofer 22 H (KUA) oxidized for various times at 800 °C in Ar-H_2-H_2O (measured with Plasma-SNMS).

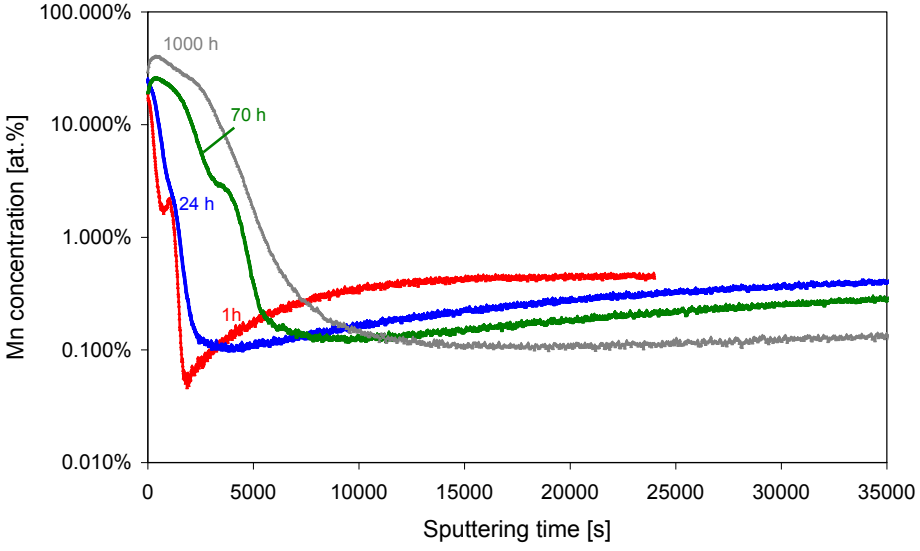

Figure 5.47: Manganese distribution (logarithmic scale) in the laboratory batch of Crofer 22 H (KUA) oxidized for various times at 800 °C in Ar-H_2-H_2O (measured with Plasma-SNMS).

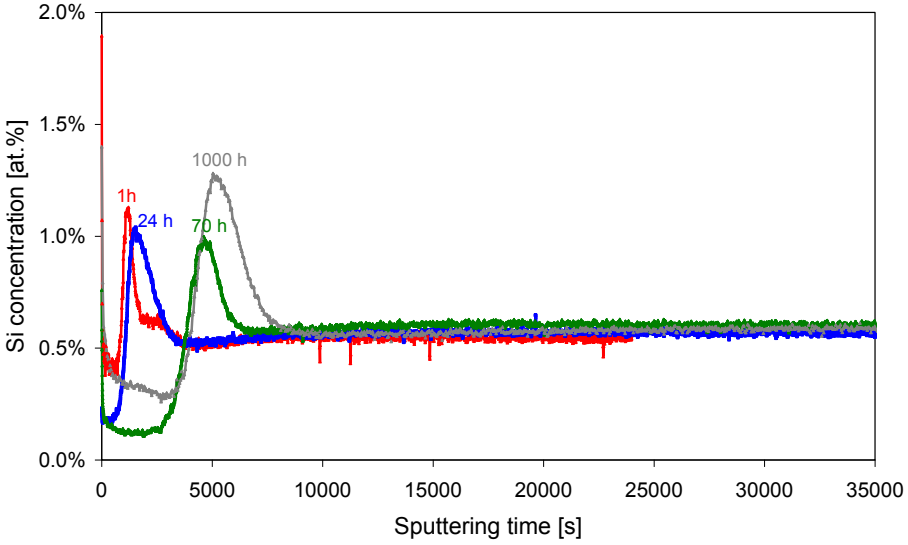

Figure 5.48: Silicon distribution (linear scale) in the laboratory batch of Crofer 22 H (KUA) oxidized for various times at 800 °C in Ar-H_2-H_2O (measured with Plasma-SNMS).

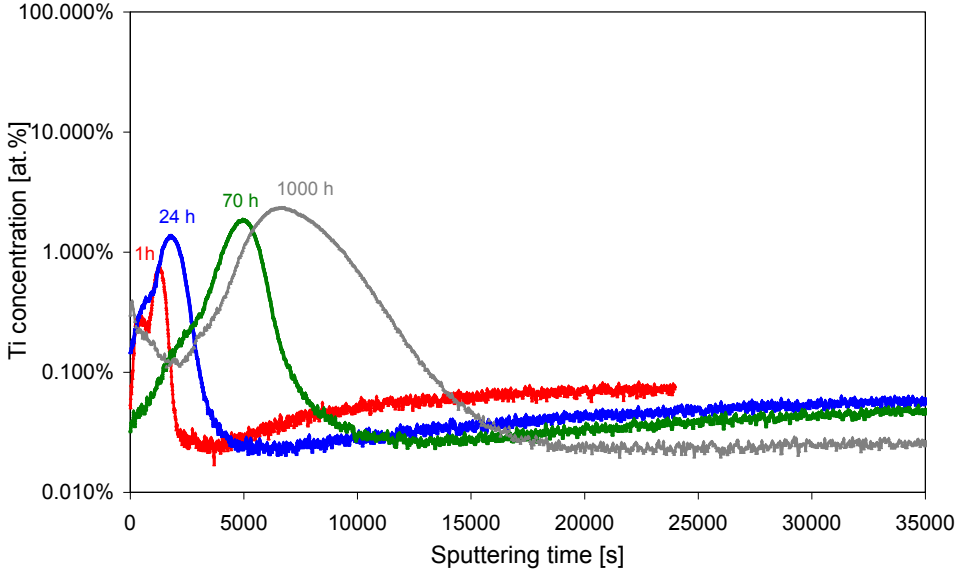

Figure 5.49: Titanium distribution (logarithmic scale) in the laboratory batch of Crofer 22 H (KUA) oxidized for various times at 800 °C in Ar-H_2-H_2O (measured with Plasma-SNMS). Short term tests.

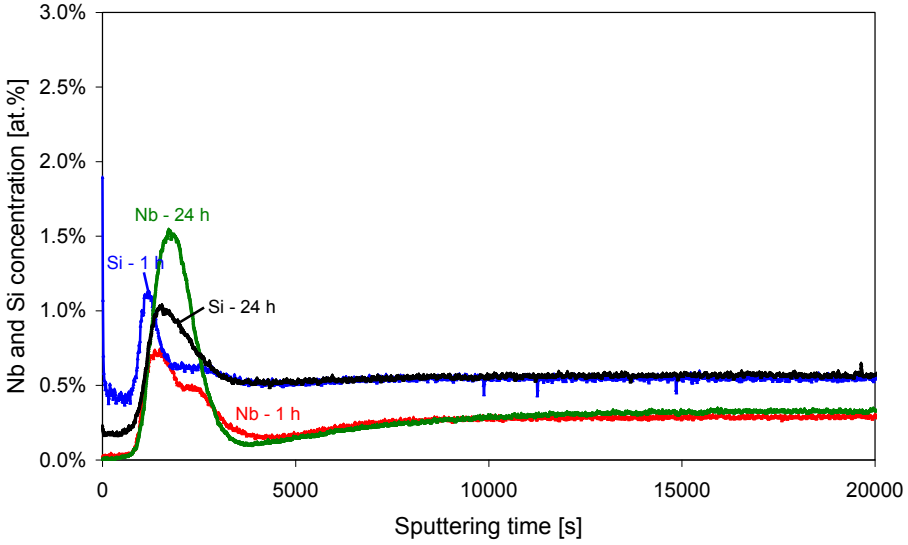

Figure 5.50: Niobium and silicon distribution in the laboratory batch of Crofer 22 H (KUA) oxidized for various times at 800 °C in Ar-H_2-H_2O (measured with Plasma-SNMS). Longer term tests.

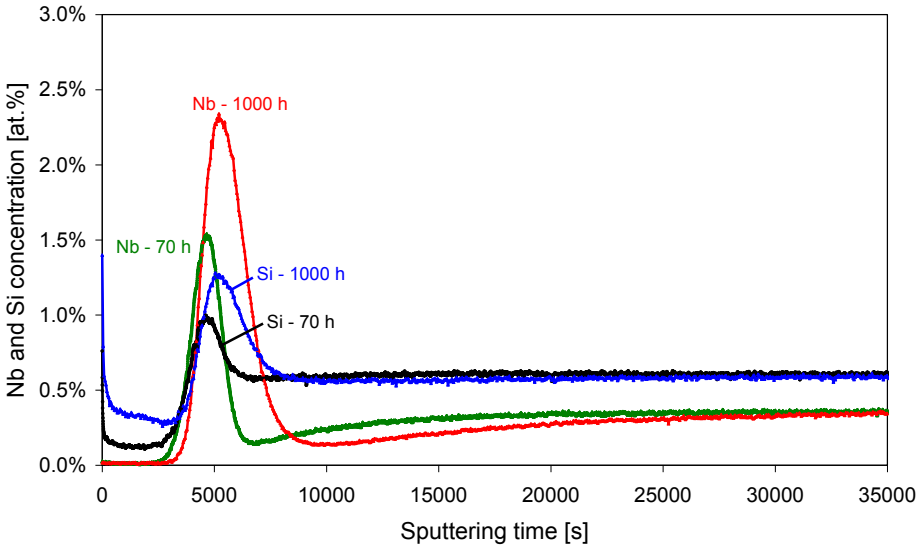

Figure 5.51: Niobium and silicon distribution in the laboratory batch of Crofer 22 H (KUA) oxidized for various times at 800 °C in Ar-H_2-H_2O (measured with Plasma-SNMS).

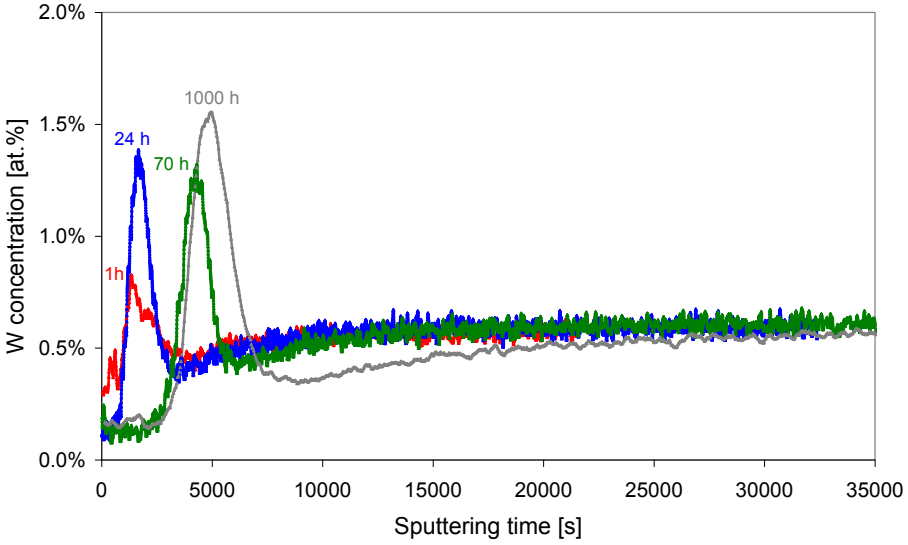

Figure 5.52: Tungsten distribution (linear scale) in the laboratory batch of Crofer 22 H (KUA) oxidized for various times at 800 °C in Ar-H_2-H_2O (measured with Plasma-SNMS).

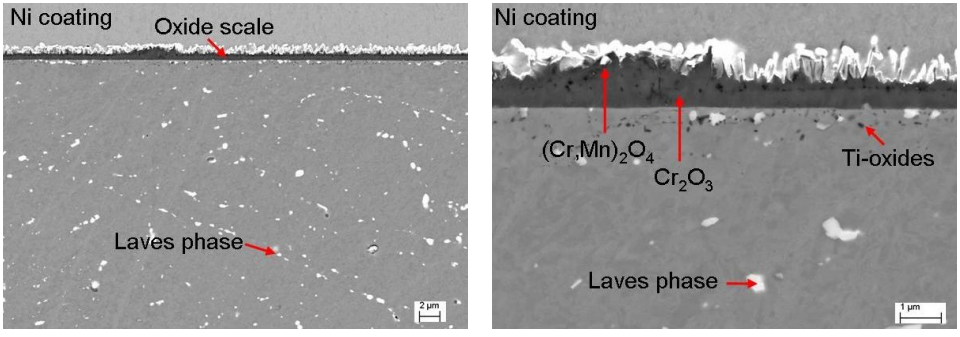

Figure 5.53: SEM/BSE images showing cross-sections of oxide scale formed on the laboratory batch of Crofer 22 H (KUA) during 70 h oxidation at 800 °C in Ar-4%H_2-2%H_2O.

5.2.4 Mechanisms of spinel formation

In evaluating the growth rates and the electronic properties of the surface scales of metallic interconnects, it has to be borne in mind that parts of the interconnectors are exposed on one side to the oxidant gas (mostly air) and on the other side to moist

hydrogen-based environments [30]. The results in the previous sections show that in both gases a two-layered scale is found to be formed consisting of Cr_2O_3 and an outer Cr/Mn-spinel. During air exposure the spinel is present in the form of well developed crystals, whereas in Ar-H_2-H_2O it possesses a blade/whisker like morphology. Another important difference between the oxide scale morphology in air and simulated anode gas is the formation of voids at/near the interface between the chromia and the spinel layer in low-pO_2 gas (Figure 5.53). On the basis of the phase diagrams of Naoumidis et al. [101] the spinel phase formed in the low-pO_2 gas is $MnCr_2O_4$ whereas in high-pO_2 gas it is $Mn_{1+x}Cr_{2-x}O_4$. This is confirmed by the results in Figure 5.54 showing Raman spectra which were measured on the outer layer of the oxide scales of Crofer 22 APU samples oxidized for 10 000 h in air and in simulated anode gas. The spectrum shows one distinct peak corresponding to $MnCr_2O_4$ at 685 cm^{-1}. This peak fits with the peak found in the anode gas exposure, so the spinel formed is $MnCr_2O_4$. However, the main peak found in air oxidation does not correspond with the peak of $MnCr_2O_4$. These differences in peak shape might be related to the differences in spinel type formed, i.e. $Mn_2Cr_2O_4$ in Ar-H_2-H_2O and $Mn_{1+x}Cr_{2-x}O_4$ in air, i.e. during air oxidation the spinel is stable in a wide range of compositions.

During long time exposure in Ar-H_2-H_2O, the formation and growth double-layered oxide structure would require a balanced flux of Cr and Mn ions through the oxide scale. The flux of Mn is reduced after longer exposure time due to depletion of the low Mn concentration in the alloy (Figure 5.44) and thus a Mn deficit is expected to occur in the spinel layer [85]. Due to the pO_2 gradient existing in the scale, a vacancy flux will prevail from the spinel surface towards the spinel-chromia interface. Here these vacancies tend to condense and result in void formation (Figure 5.53). In air, the Mn deficit in the spinel may be compensated by Cr cations from the inner chromia layer. This would result in an enhanced outward flux of Cr, which could explain why during air exposure the presence of Mn in the alloy increases not only the overall thickness of oxide but also that of the inner chromia scale [106]. The high Mn/Cr ratio found after longer time exposure in Ar-H_2-H_2O (Figures 5.44, 45) is likely related to formation of MnO next to spinel [107]. It should be mentioned that the rapid incorporation of Mn into the oxide layer may easily

lead to complete exhaustion of the Mn reservoir in the test specimen. This effect, which will be especially pronounced at high oxidation temperatures and/or when using thin components, will obviously alter the described effect of Mn additions on the gas composition dependence of the oxide growth kinetics.

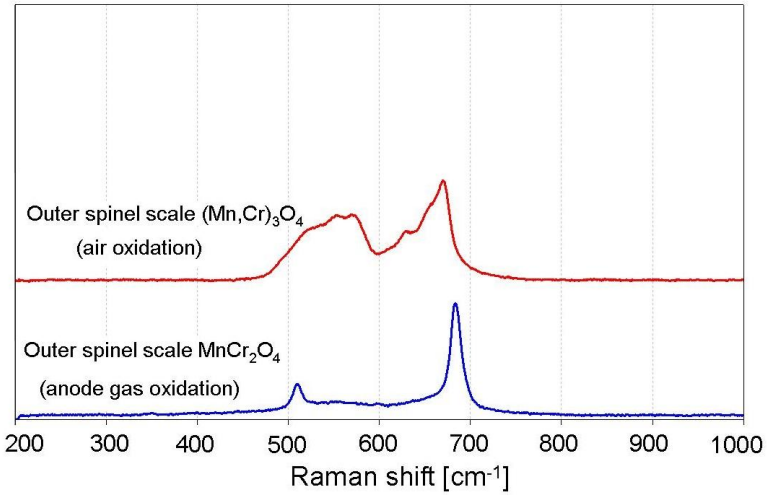

Figure 5.54: Raman spectra taken from outer layer of oxide scale on Crofer 22 APU oxidized for 10 000 h at 800 °C in laboratory air or in Ar-4%H_2-20%H_2O gas.

5.3 Oxidation induced phase changes in the subsurface depletion zone

5.3.1 General remarks

The SNMS studies in the previous sections revealed that during oxidation at 800 °C, a significant redistribution of the Laves phase forming elements (Nb, W, Si) occurs in the subscale layer. The occurrence of this effect and the underlying mechanisms will be further investigated in this section.

As Crofer 22 H, the vast majority of heat-resistant metallic materials developed for application at high temperatures in oxidizing environments rely for their oxidation resistance on the formation of a dense, well-adherent, protective chromium rich oxide layer on the alloy surface. Apart from the high chromium ferritic steels discussed in this thesis, examples of such materials are nickel base alloys or austenitic steels which contain typically chromium contents in the range 18–25 %. The high temperature (creep) strength is based on a combination of solid solution and precipitate strengthening [108]. For most of the austenitic steels and nickel base alloys the main strengthening precipitates are chromium base carbides, e.g. of the type $M_{23}C_6$ [109-110]. The formation and continuing growth of the chromia base surface oxide scales during high temperature service results for these alloys in a subscale chromium depletion and consequently in dissolution of the chromium rich carbide precipitates in the surface-near zone of the component [111-112]. Detailed quantitative knowledge of this effect is not only of great importance for the long term oxidation resistance but per definition also for the mechanical properties of the materials [111]. Numerous experimental data and several mathematical models which describe the subscale depletion phenomena [113-116] including dissolution of the carbide precipitates are available in literature [112, 117].

The strengthening mechanism by finely dispersed chromium base carbide precipitates is not technologically feasible for high chromium ferritic steels, because of the extremely low solubility for carbon in the ferrite lattice. As explained in section 2.11 the increase in creep strength of Crofer 22 H compared to Crofer 22 APU relies on additional solid

solution strengthening by tungsten addition but mainly on the formation of Laves phase precipitates of the type Fe_2M (M is mainly Nb and W) which form in the steel matrix during service at the typical application temperatures in the range 600–800 °C [94].

The subsurface depletion processes and corresponding phase transformations as a result of chromia surface scale formation occurring in Crofer 22 H will fundamentally differ from those of the above mentioned, more commonly used chromium carbide strengthened austenitic steels and nickel base alloys because, as shown in section 2.15.2, chromium is only a minor constituent of the Laves phase precipitates. As far as known to the author, hardly any quantitative experimental data and no mathematical modeling related to subscale depletion processes of Laves phase strengthened ferritic steels are available in literature.

In the following sections, the subscale depletion/enrichment processes occurring during oxidation of Crofer 22 H at 800 °C will be described and the experimental results will be discussed using the ThermoCalc and DICTRA software [118].

5.3.2 Experimental details

The material used for the investigations was the same laboratory batch of Crofer 22 H (KUA) as described in section 4.1. The used specimens all had a size of 20 x 10 x 2 mm. Some of the SNMS results presented here, refer to the same specimens as described already in section 5.2.

Especially for the quantitative modeling, a second alloy was used in these investigations in addition to Crofer 22 H. It had a composition (in mass.-%) of Fe–22.7Cr–2W–0.5Nb–0.26Si–0.13La–0.09Ti, (batch MKS-1 mm thickness, compare data from section 4.1). The composition was thus similar to that of Crofer 22 H, however, without Mn addition. Removal of Mn had the advantage that single-phase chromia surface scales rather than the double layered scales consisting of chromia and Cr/Mn spinel are expected to be formed. This allowed an easier quantification of the time dependent chromium loss by oxide scale formation. Most of the experiments with this model steel were carried out in Ar-4%H_2-20%H_2O gas. This atmosphere was used because it allows growth of a chromia base oxide

scale without substantial interference of formation of volatile Cr oxides and/or oxyhydroxides which is known to occur when exposing Cr-rich steels in laboratory air [119].

5.3.3 Subsurface phase transformations during oxidation of Crofer 22 H

Figures 5.55 to 5.60 show SEM images of metallographic cross sections of a commercial batch of Crofer 22 H (MDP, MDO, MEC, MDT) after various times of oxidation at 800 °C. The figures clearly show the Laves phase precipitates within the grains and the grain boundaries whereby coarsening tends to occur after longer times, as already more extensively explained in section 5.1. As mentioned in the section 5.3.1, formation of a classical subscale Laves phase depletion layer beneath the oxide scale is not expected because chromium, which is consumed from the alloy by the scale growth process, is not a major constituent of the Laves phase. In spite of that, the figures indicate formation of a subsurface zone in which the Laves phase, especially in the bulk grains, is partially or completely depleted compared to the microstructure of the unaffected part of the specimen.

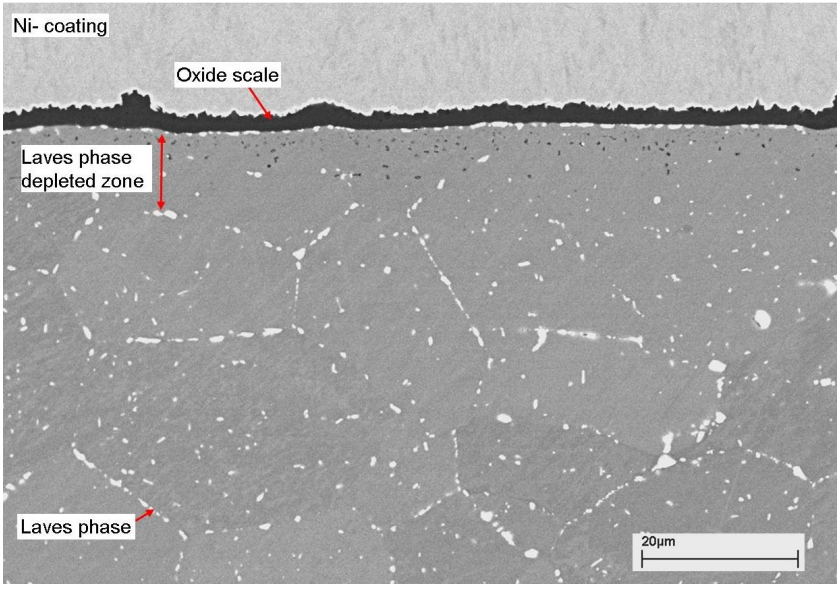

Figure 5.55: Cross section of the commercial batch of Crofer 22 H (MDT-0.5 mm thickness) after 1000 h oxidation at 800 °C in air.

Additionally, a slight Laves phase enrichment seems to prevail in the immediate vicinity of the scale/steel interface. This parallel depletion and enrichment of Laves phase in the subsurface zone is e.g. clearly visible in Figures 5.56-58, 5.60 and is in agreement with the SNMS data shown in section 5.2. However, in other cases (see e.g. Figures 5.55 and 5.59) the effect is far less pronounced.

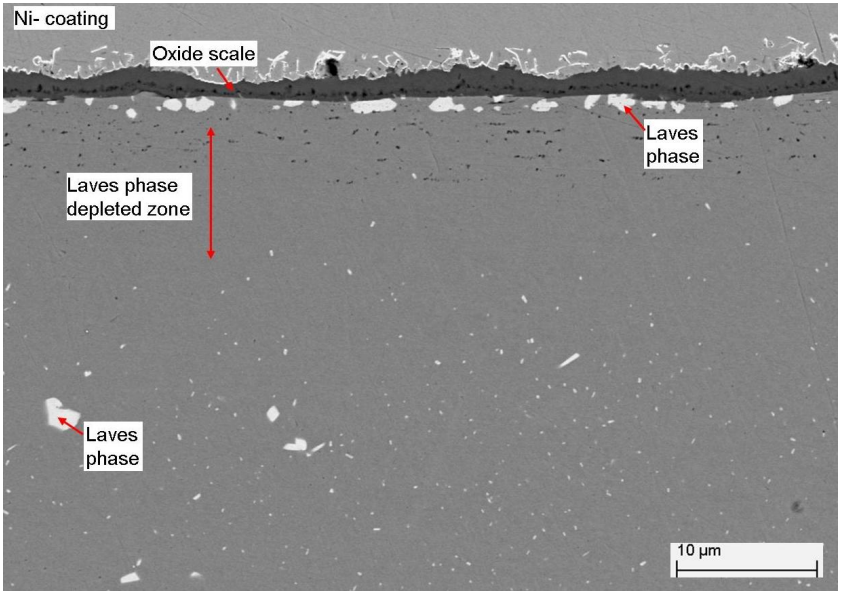

Figure 5.56: Cross section of the commercial batch of Crofer 22 H (MDO-2 mm thickness) after 1000 h oxidation at 800°C in Ar-4 % H_2-20 % H_2O.

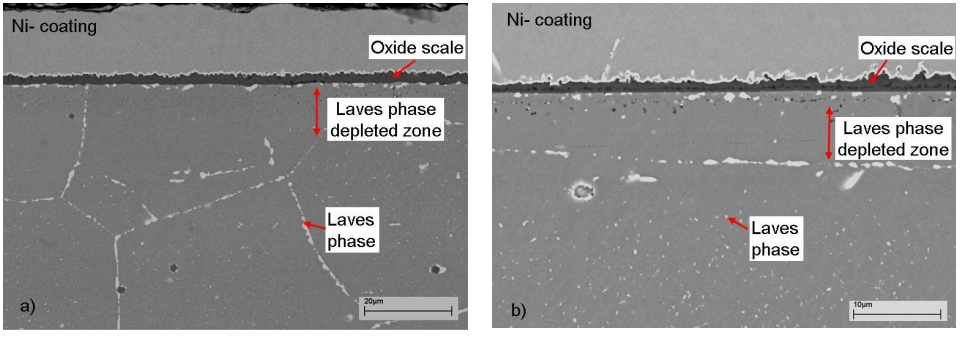

Figure 5.57: Cross section of the commercial batch of Crofer 22 H (MDP-2.5 mm thickness) after 1000 h oxidation at 800 °C in a) air and in b) Ar-4 % H_2-20 % H_2O (mark the different magnifications).

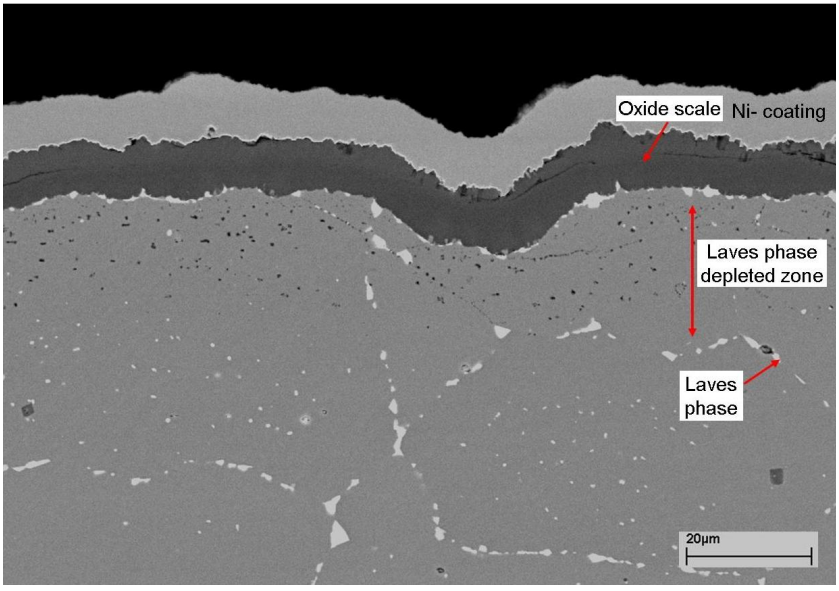

Figure 5.58: Cross section of the commercial batch of Crofer 22 H (MDP-2.5 mm thickness) after 10 000 h oxidation at 800 °C in air

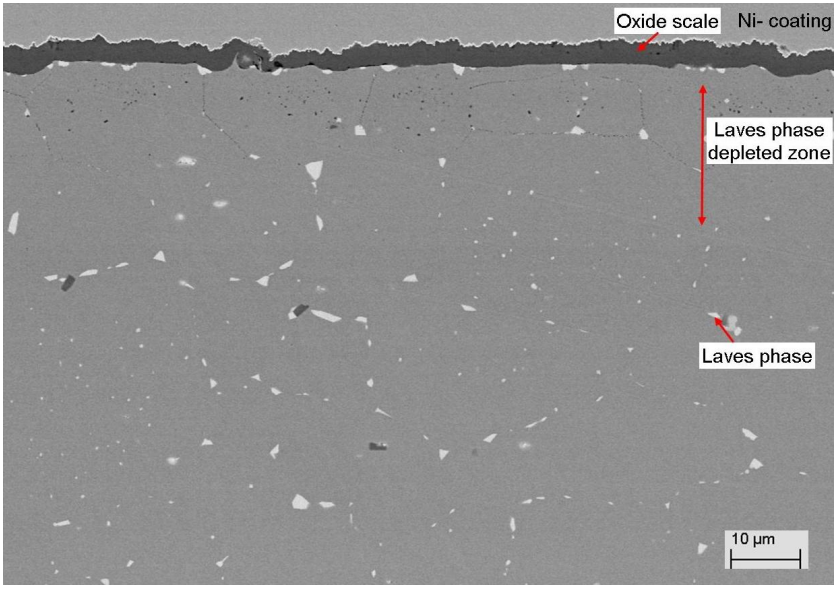

Figure 5.59: Cross section of the commercial batch of Crofer 22 H (MEC-1 mm thick-ness) after 72 h oxidation at 900 °C in air.

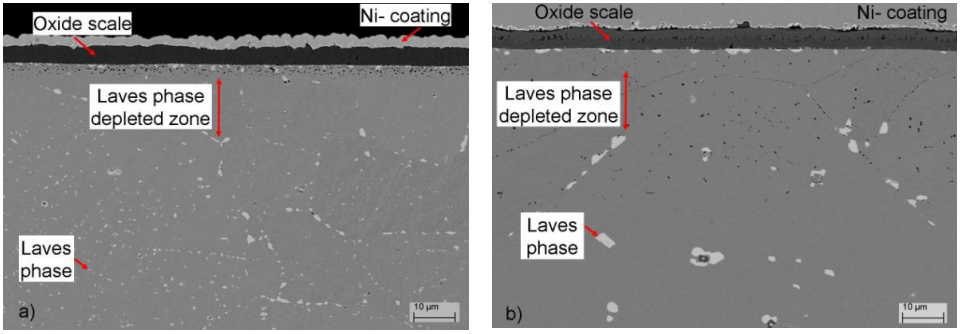

Figure 5.60: Cross section of the commercial batch of Crofer 22 H (MDP-2.5 mm thickness) after 1000 h oxidation at 900 °C in a) air and b) Ar-4%H_2-20%H_2O.

5.3.4 Time dependence of subscale phase transformations

Typical features occurring as a result of the oxidation process in air and simulated anode gas were already discussed in section 5.2:

- Formation of a double layered oxide consisting of chromia and Cr/Mn-based spinel.
- The spinel phase formed in air clearly differs from that in simulated anode gas.
- Internal oxidation of Ti
- A minor tendency for C-enrichment at the scale/steel interface
- A Ti enrichment at the outer oxide surface, especially after air exposure

Figures 5.61a, b-64a, b and Figures 5.65a, b-68a, b show the results of the depth profiling after various oxidation times in air and in simulated anode gas, whereby special emphasis is put on the subscale depletion of Cr and on the distribution of the alloying additions which are major constituents of the Laves phase, i.e. Nb, W and Si.

After air oxidation for 1, 24 and 70 hours, a clear depletion of Cr is visible in the subsurface zone. After 1500 h (Figure 5.64a) this effect seems to be less pronounced. This may be related to an analysis issue, i.e. the real depth up to which Cr is depleted is larger than the maximum sputter depth. However, a less pronounced Cr depletion might also be the result of the fact that the Cr consumption by scale growth obeys a sub-parabolic rather than a

parabolic time dependence [120-121]. In that case the Cr-concentration at the scale/steel interface is expected to increase with increasing exposure time.

After 1 hour air oxidation the Si profile exhibits three peaks, i.e. one very sharp one at the oxide/gas interface and a second one in the inner part of the oxide scale, the latter likely being related to internal oxidation of Si (compare section 5.2). A third, shallow peak is visible in the subscale layer and is locally correlated with enrichment of Nb and W (Figure 5.61b). In this enrichment zone the concentration of W and Si is higher than that of Nb. Beneath this enrichment zone, a slight depletion of Si, W and Nb is observed. Increasing the exposure time to 24 or 70 h results in a stronger enrichment of Nb and W relative to Si near the scale/steel interface. The Si enrichment near the scale/gas interface decreases with increasing oxidation time. The enrichment of the three alloying elements near the scale/steel interface increases if the time is extended to 1500 h (Figure 5.64b). Compared to their initial concentrations in the alloy, Nb exhibits the most pronounced relative enrichment, Si the lowest. It is interesting to see that after these longer exposure times, Si does, different from W and especially Nb, not show a depletion profile in the alloy beneath the enrichment layer (Figure 5.64b).

Qualitatively very similar features were found after various times of oxidation in simulated anode gas (Figures 5.65a, b-68a, b). Considering the composition of the Nb/W/Si enriched zone in the alloy beneath the oxide scale after longer exposure times clearly reveals that this effect is caused by Laves phase formation in the immediate vicinity of the scale alloy interface, observed in the SEM cross sections (Figures 5.69-70). The effect already starts to occur after very short exposure time of only 1 hour, whereby then the composition in the enrichment layer does not yet exactly correlate with that of the Laves phase. The reason for this effect is that in the early stages of exposure only minor Laves phase enrichment is present and thus the depth profiles reveal the average over an area consisting of ferrite as well as Laves phase. Additionally, the non-even alloy/steel interface affects the quantitative analysis by depth profiling. After longer exposure time this is still the case, however, the amount of Laves phase seems to increase so that the measured average composition in the SNMS depth profile comes nearer to the composition of the Laves phase.

Figures 5.69-70 show SEM cross sections after various oxidation times in air and in simulated anode gas. The microstructures clearly reveal for both gases the formation of the double-layered oxide scale, the internal oxidation zone as well as coarsening and re-distribution of Laves phase.

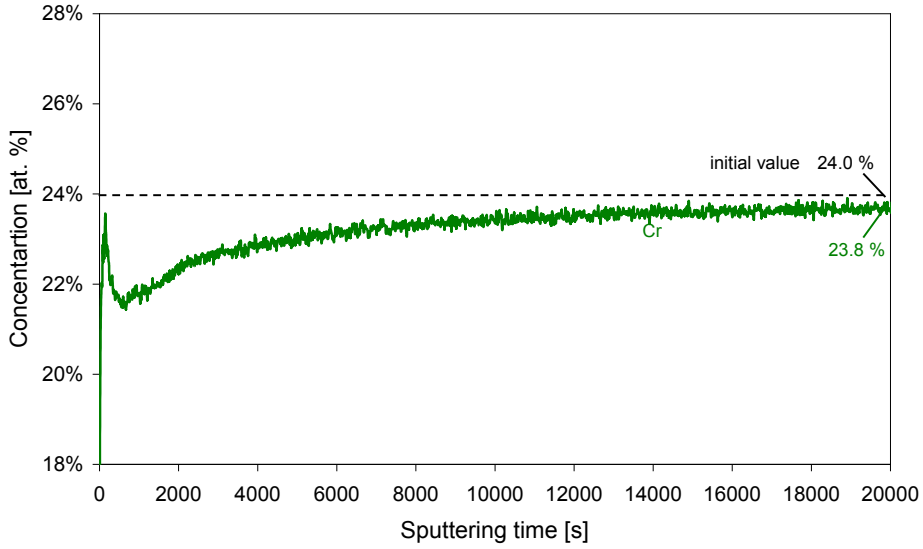

Figure 5.61a: SNMS depth profile showing the subscale depletion of Cr in the laboratory batch of Crofer 22 H (KUA) after 1h oxidation at 800 °C in air.

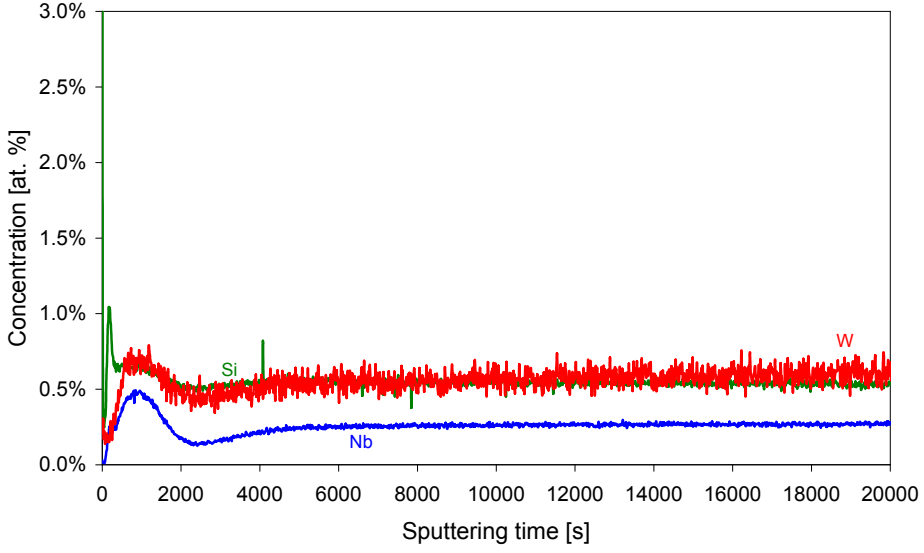

Figure 5.61b: SNMS depth profile showing distribution of Nb, Si and W in the subsurface zone of the laboratory batch of Crofer 22 H (KUA) after 1 h oxidation at 800 °C in air.

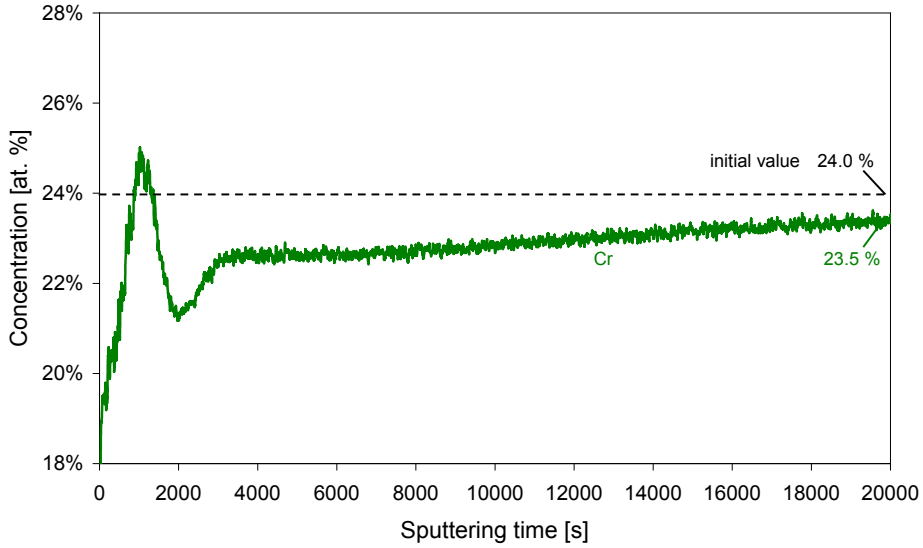

Figure 5.62a: SNMS depth profile showing the subscale depletion of Cr in the laboratory batch of Crofer 22 H (KUA) after 24 h oxidation at 800 °C in air.

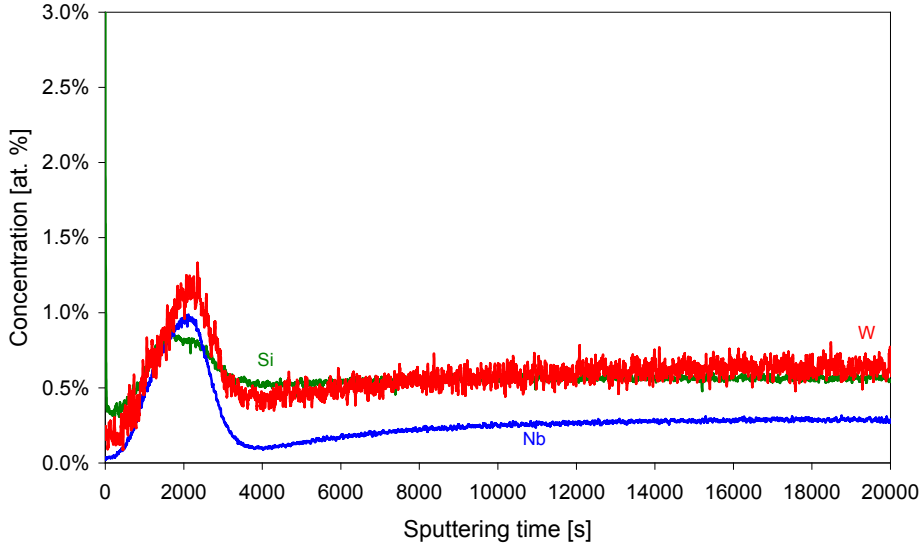

Figure 5.62b: SNMS depth profile showing distribution of Nb, Si and W in the subsurface zone of the laboratory batch of Crofer 22 H (KUA) after 24 h oxidation at 800 °C in air.

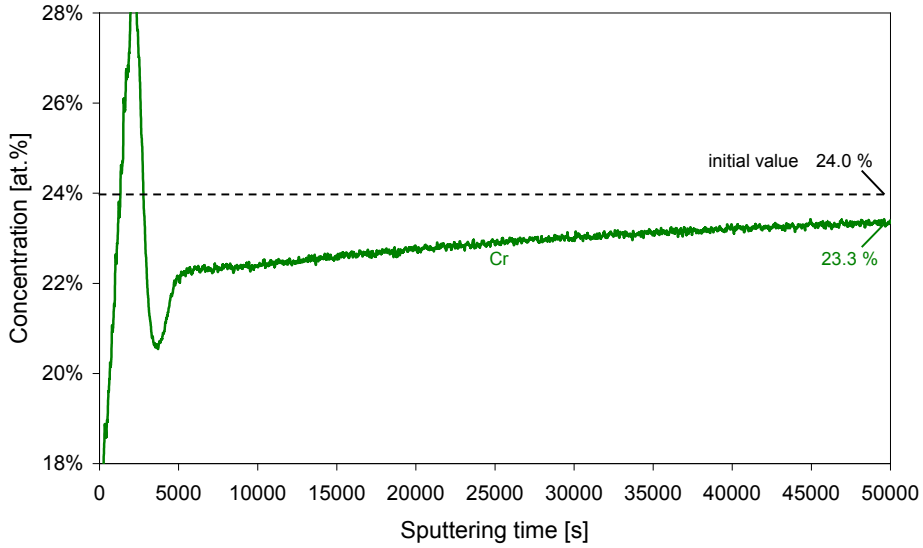

Figure 5.63a: SNMS depth profile showing the subscale depletion of Cr in the laboratory batch of Crofer 22 H (KUA) after 70 h oxidation at 800 °C in air.

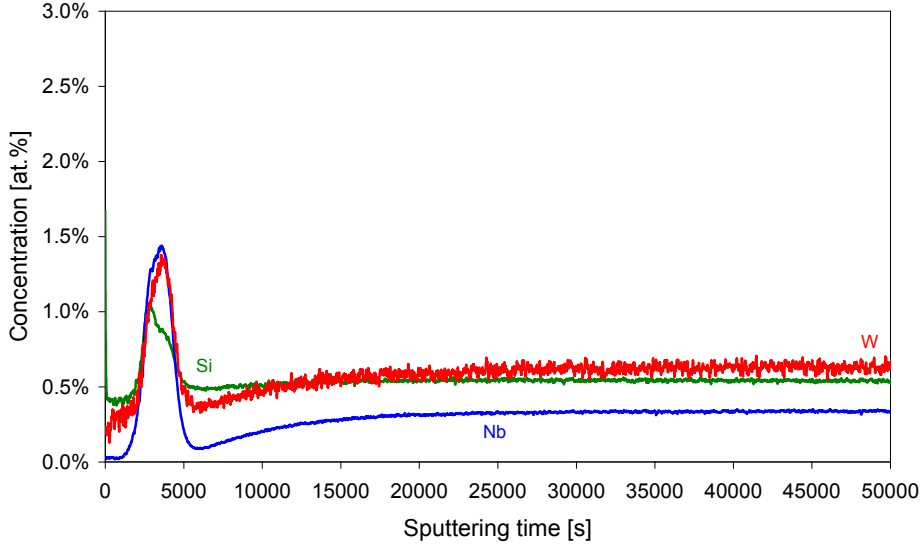

Figure 5.63b: SNMS depth profile showing distribution of Nb, Si and W in the subsurface zone of the laboratory batch of Crofer 22 H (KUA) after 70 h oxidation at 800 °C in air.

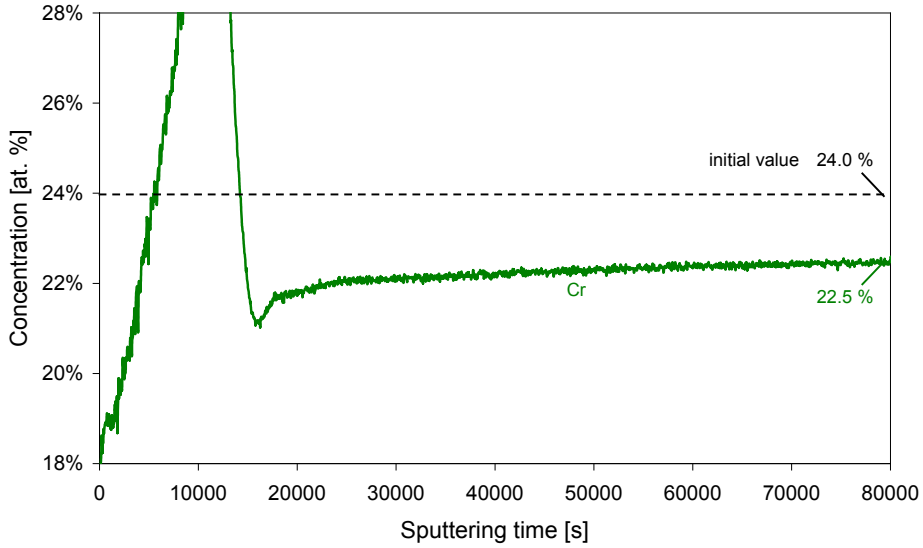

Figure 5.64a: SNMS depth profile showing the subscale depletion of Cr of the laboratory batch of Crofer 22 H (KUA) after 1500 h oxidation at 800 °C in air.

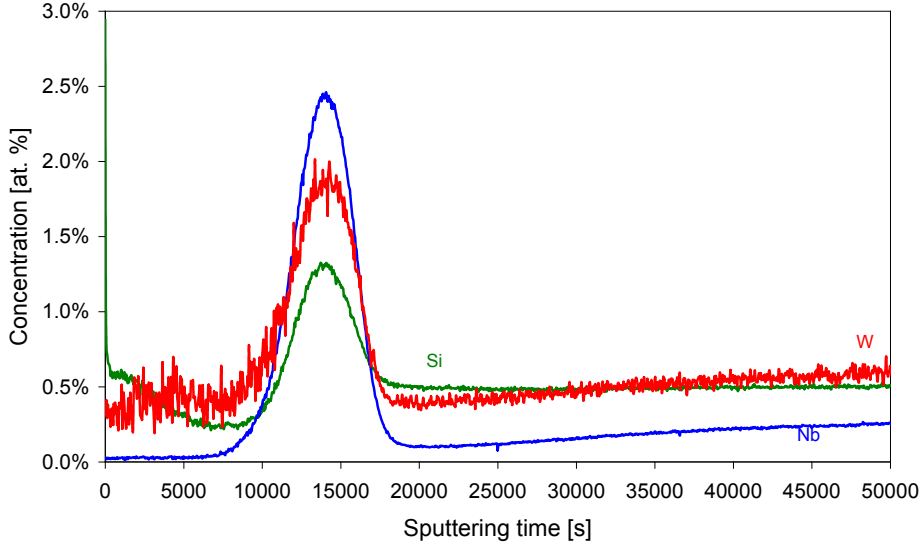

Figure 5.64b: SNMS depth profile showing distribution of Nb, Si and W in the subsurface zone of the laboratory batch of Crofer 22 H (KUA) after 1500 h oxidation at 800 °C in air.(Mind different horizontal axis compared to Figure 5.64a).

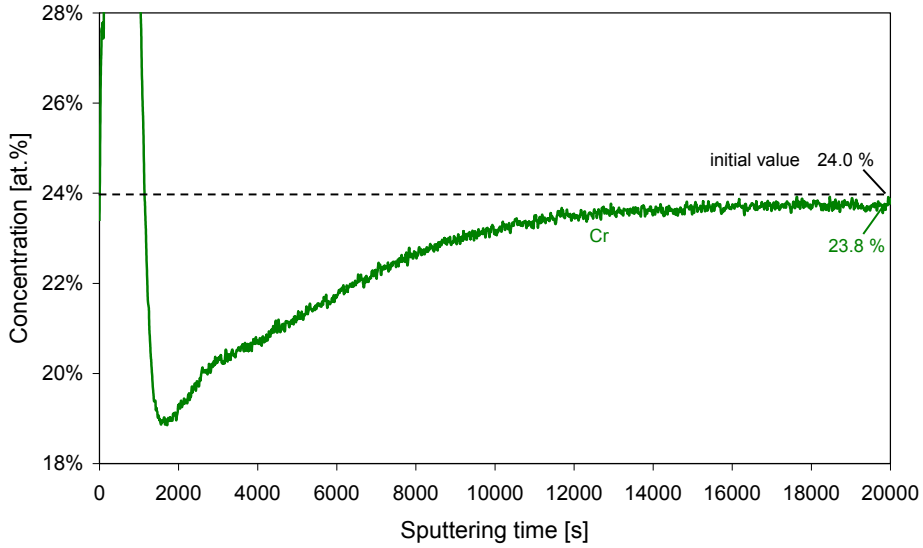

Figure 5.65a: SNMS depth profile showing the subscale depletion of Cr of the laboratory batch of Crofer 22 H (KUA) after 1 h oxidation at 800 °C in Ar-4%H_2-2%H_2O.

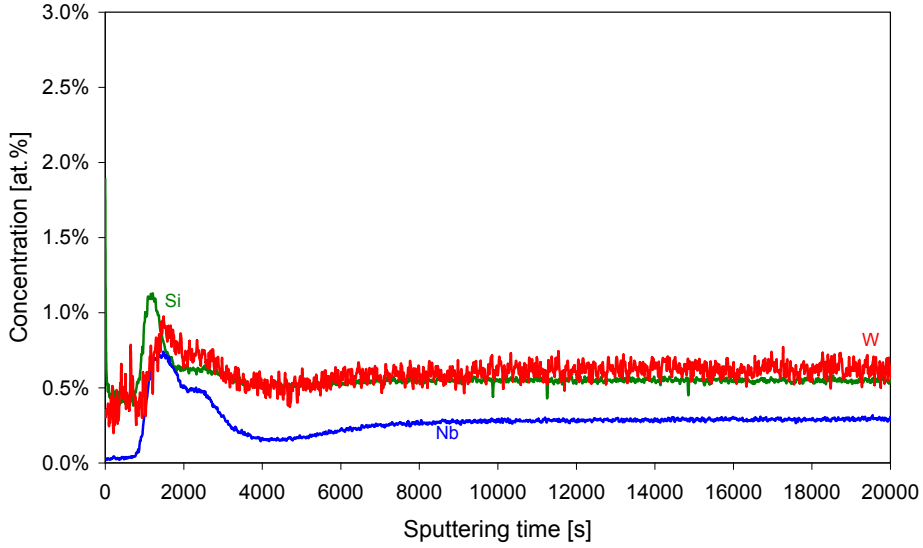

Figure 5.65b: SNMS depth profile showing distribution of Nb, Si and W in the subsurface zone of the laboratory batch of Crofer 22 H (KUA) after 1h oxidation at 800 °C in Ar-4%H_2-2%H_2O.

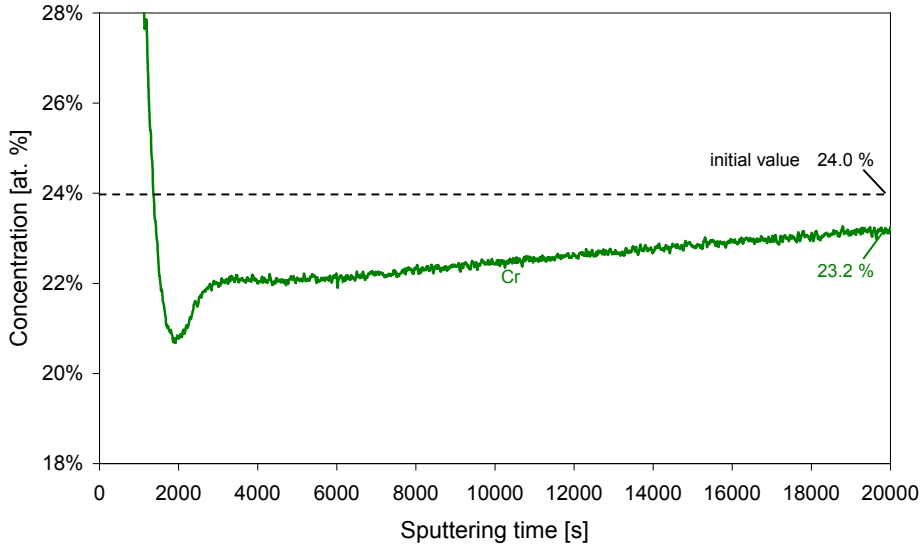

Figure 5.66a: SNMS depth profile showing the subscale depletion of Cr of the laboratory batch of Crofer 22 H (KUA) after 24 h oxidation at 800 °C in Ar-4%H_2-2%H_2O.

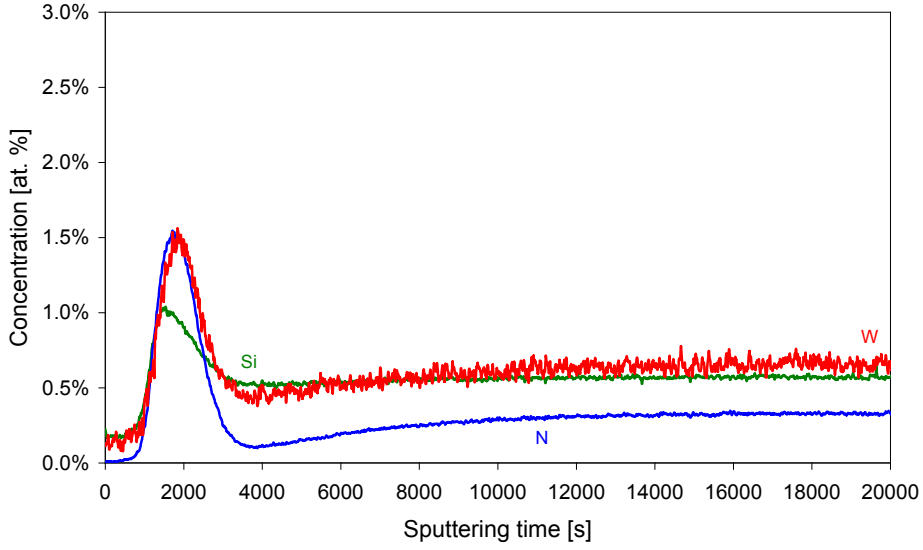

Figure 5.66b: SNMS depth profile showing distribution of Nb, Si and W in the subsurface zone of the laboratory batch of Crofer 22 H (KUA) after 24 h oxidation at 800 °C in Ar-4%H_2-2%H_2O.

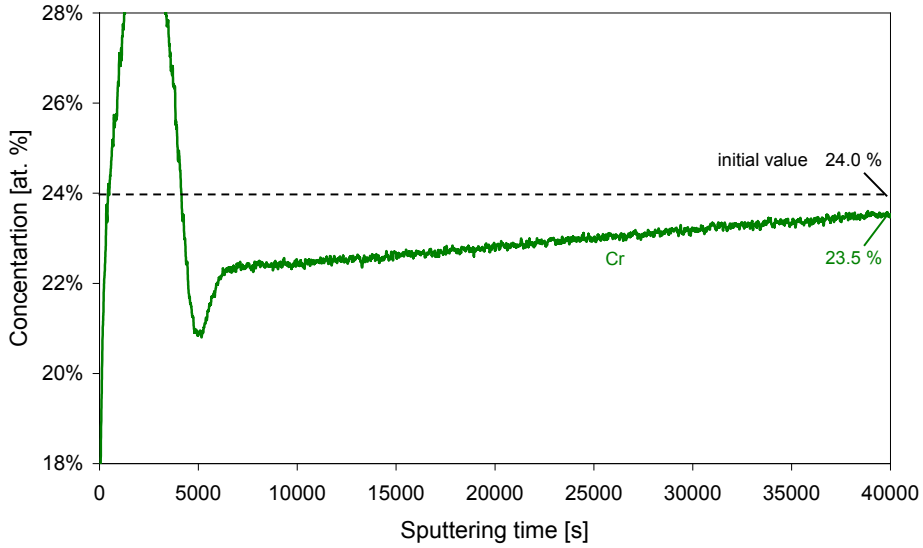

Figure 5.67a: SNMS depth profile showing the subscale depletion of Cr of the laboratory batch of Crofer 22 H (KUA) after 70 h oxidation at 800 °C in Ar-4%H_2-2%H_2O.

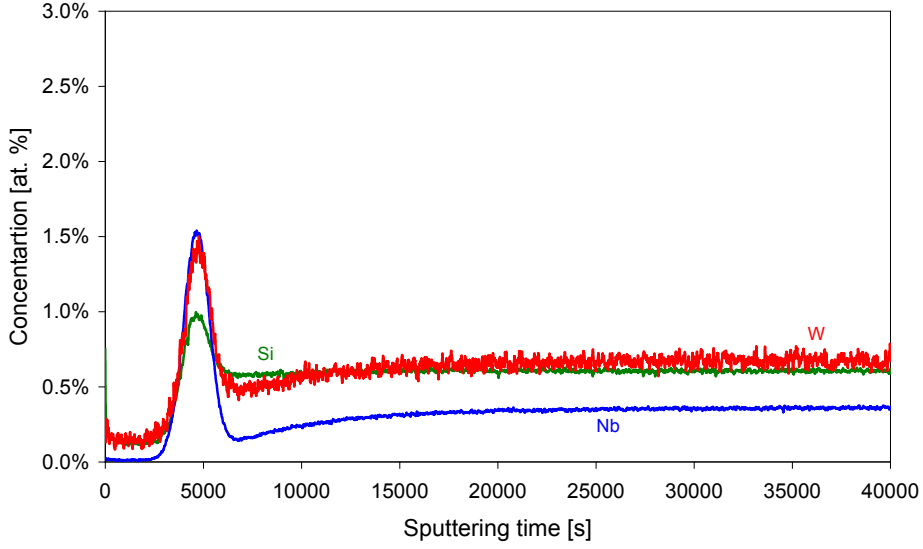

Figure 5.67b: SNMS depth profile showing distribution of Nb, Si and W in the subsurface zone of the laboratory batch of Crofer 22 H (KUA) after 70 h oxidation at 800 °C in Ar-4%H_2-2%H_2O.

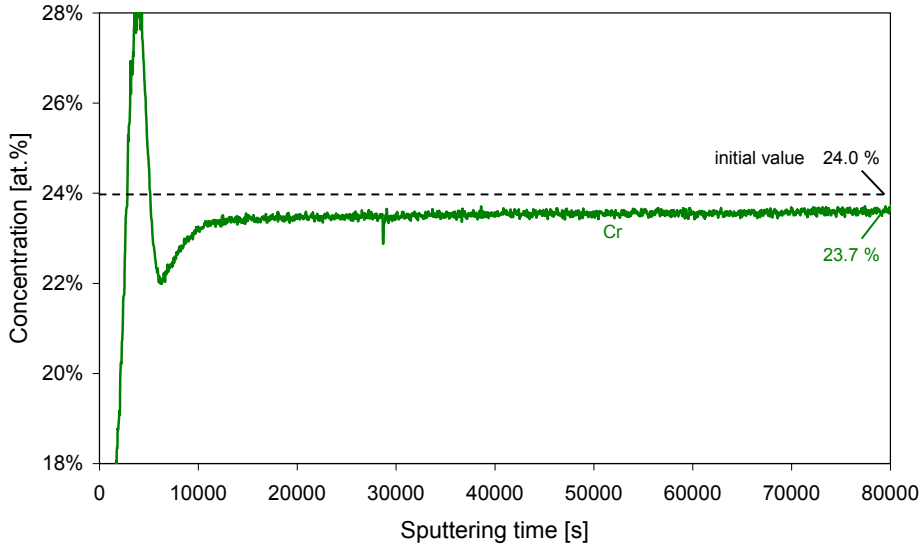

Figure 5.68a: SNMS depth profile showing the subscale depletion of Cr of the laboratory batch of Crofer 22 H (KUA) after 1000 h oxidation at 800 °C in Ar-4%H_2-20%H_2O.

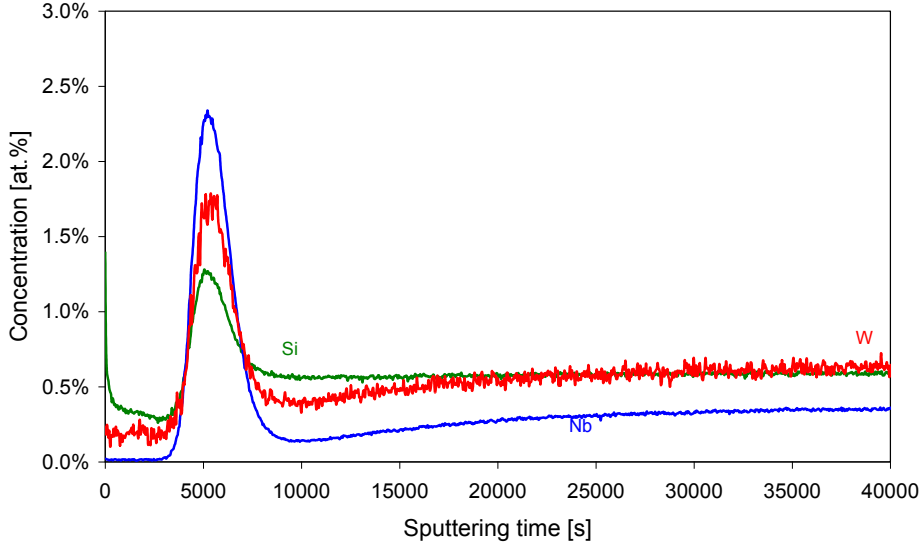

Figure 5.68b: SNMS depth profile showing distribution of Nb, Si and W in the subsurface zone of the laboratory batch of Crofer 22 H (KUA) after 1000 h oxidation at 800 °C in Ar-4%H_2-20%H_2O. (Mind different scale of horizontal axis compared to Figure 5.68a)

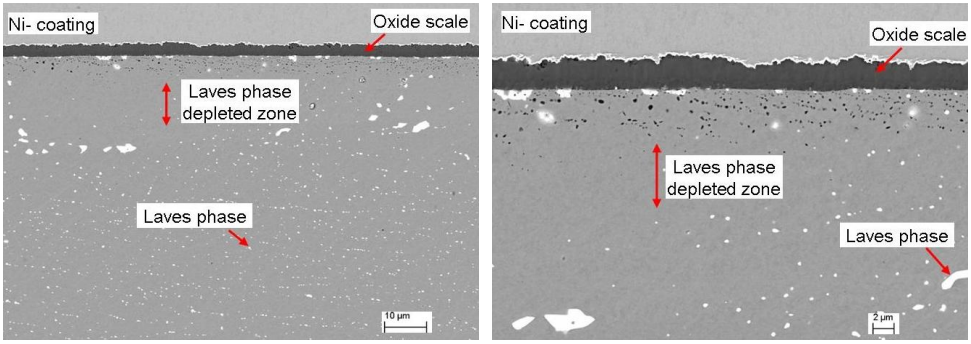

Figure 5.69: SEM/BSE images showing cross-sections of oxide scale formed on laboratory batch of Crofer 22 H (KUA) during 1500 h oxidation at 800 °C in air.

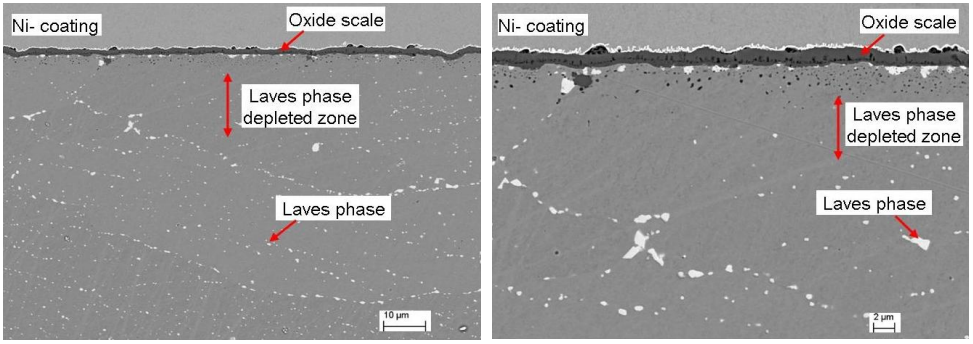

Figure 5.70: SEM/BSE images showing cross-sections of oxide scale formed on laboratory batch of Crofer 22 H (KUA) during 1000 h oxidation at 800 °C in Ar-4%H_2-20%H_2O.

5.3.5 Subsurface phase transformations during oxidation of Mn-free steel in simulated anode gas

Details of the surface scale formation of the Mn-free version compared to the standard Crofer 22 H in air and simulated anode gas will be described in section 5.4. Here, only selected results after exposure in Ar-H_2-H_2O will be illustrated, thereby concentrating on the subscale depletion-/enrichment processes of the Laves phase forming elements Nb, W and Si. Figure 5.71 shows SEM/BSE cross-sections of oxide scales formed after 100 h exposure at 800 °C. The images clearly show the presence of Laves phase in the bulk specimen. WDX analyses revealed for this phase a composition which was similar to that previously observed (in wt.-% 21Nb, 29W, 9Cr, 1.5Si, 40Fe) in Crofer 22 H (section 5.1.2). The surface oxide consists

virtually exclusively of chromia and only a minor amount of internal Ti oxide precipitates is present.

In the subsurface zone the amount and distribution of the Laves phase precipitates clearly differs from that in the bulk alloy. A zone of approximately 10 μm in width exists in which the precipitates are virtually completely absent. On the contrary, the Laves phase is still present and apparently even enriched in the immediate vicinity of the metal/oxide interface, as confirmed by the GDOES depth profile in Figure 5.72. This behaviour is in qualitative agreement with that shown in section 5.3.4 for the Mn containing laboratory batch of Crofer 22 H. The elements Nb, W and Si, which are constituents of the Laves phase, are clearly enriched in a narrow zone next to the oxide/steel interface. Beneath this zone W and Si are slightly depleted compared to their original concentrations in the steel. As for the Mn containing Crofer 22 H (section 5.3.4) the strongest concentration gradients (depletion/enrichment) were observed for Nb. This type of microstructural features as shown in Figure 5.71 and the enrichment/depletion effects measured by GDOES were found in all specimens up to exposure times of 3000 h (Figures 5.72-5.75). During the oxidation process the Cr concentration was found to decrease from 24 at. % in the bulk alloy to values of approximately 22.5 at. % (depending on exposure time) near the oxide/steel interface (Figures 5.76-77).

Previous studies [79] revealed that thermodynamic equilibrium calculations using ThermoCalc correctly predicted the Laves phase to coexist with the ferrite matrix at 800 °C. However, the calculated composition revealed the Nb solubility in the α-Fe matrix to be substantially higher than the actually measured values. Also it was found, that ThermoCalc does not correctly describe the solubility of Si in the Laves phase [79].

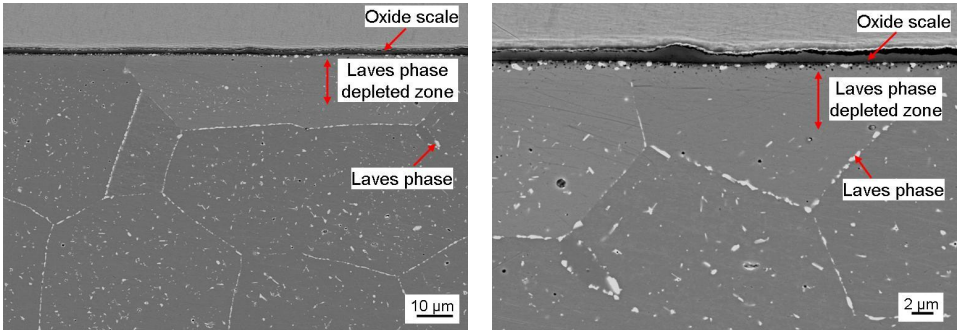

Figure 5.71: SEM/BSE images showing chromium oxide scales and Laves phase precipitates in Mn-free variant of Crofer 22 H (batch MKS) after 100 h exposure in Ar-4%H_2-20%H_2O at 800 °C.

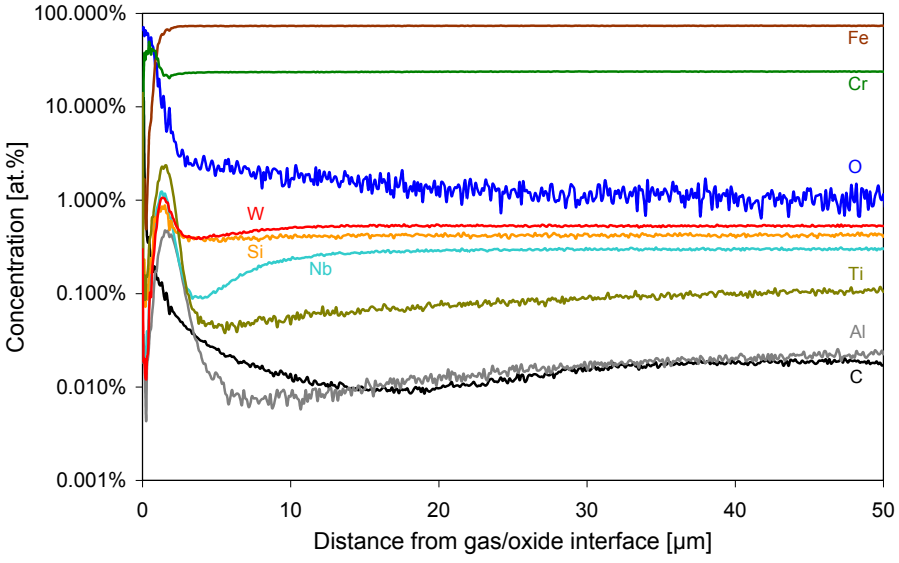

Figure 5.72: GDOES depth profile of Mn-free variant of Crofer 22 H (MKS) after 100 h oxidation at 800 °C in Ar-4%H_2-20%H_2O.

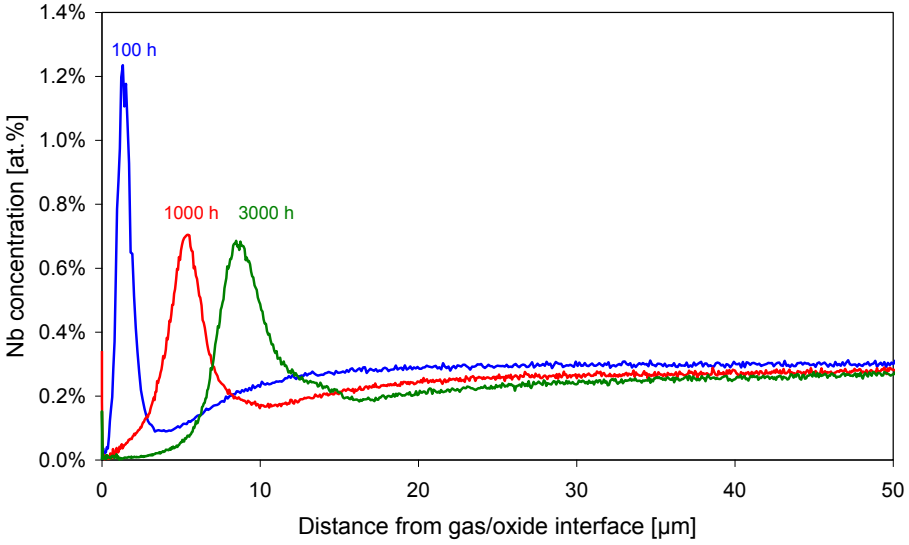

Figure 5.73: Niobium depth profiles after various oxidation times for the Mn-free variant of Crofer 22 H (MKS) at 800 °C in Ar-4%H_2-20%H_2O (taken from GDOES profiles).

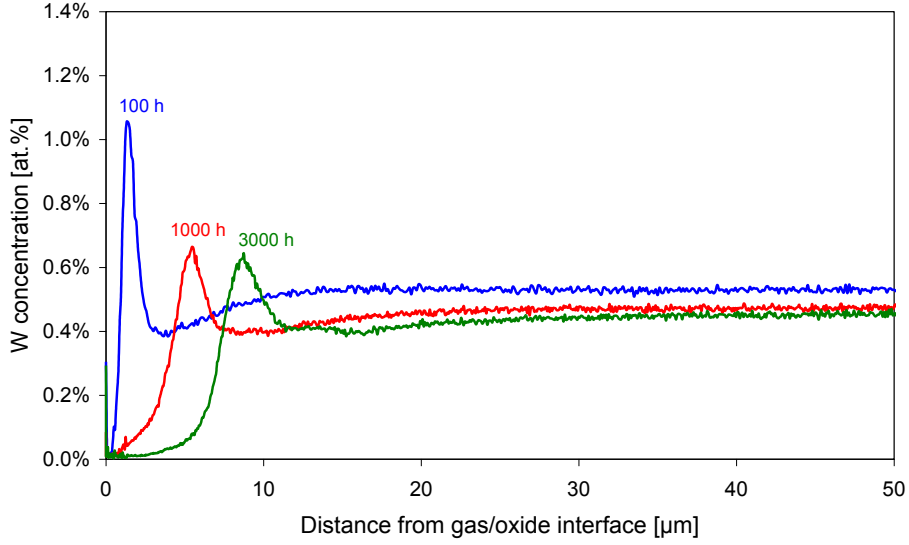

Figure 5.74: Tungsten depth profiles after various oxidation times for the Mn-free variant of Crofer 22 H (MKS) at 800 °C in Ar-4%H_2-20%H_2O (taken from GDOES profiles) .

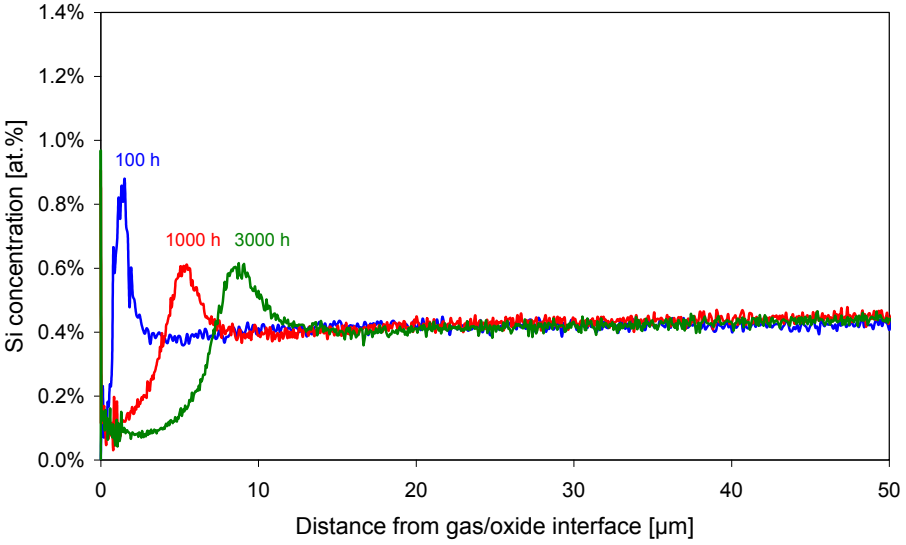

Figure 5.75: Silicon depth profiles after various oxidation times for the Mn-free variant of Crofer 22 H (MKS) at 800 °C in Ar-4%H_2-20%H_2O (taken from GDOES profiles).

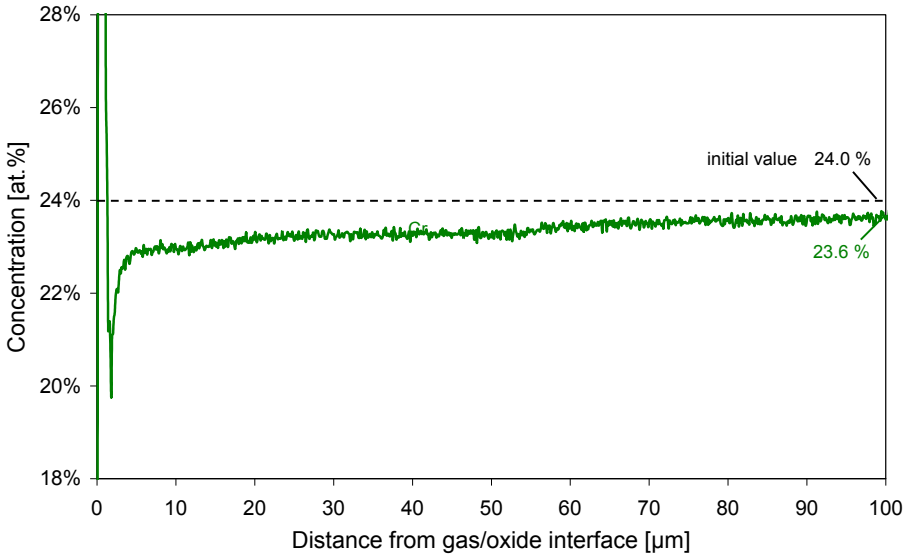

Figure 5.76: GDOES depth profile showing the subscale depletion of Cr for the Mn -free Crofer 22 H (MKS) after 100 h oxidation at 800 °C in Ar-4%H_2-20%H_2O.

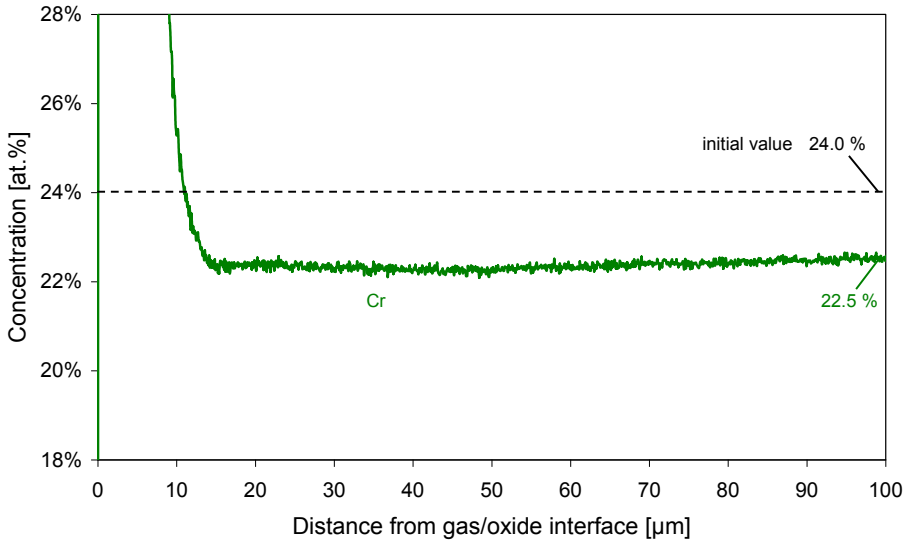

Figure 5.77: GDOES depth profile showing the subscale depletion of Cr for the Mn-free variant of Crofer 22 H (MKS) after 3000 h oxidation at 800 °C in Ar-4%H_2-20%H_2O.

The formation of a Laves phase depleted subscale zone (Figure 5.71) as a result of oxidation induced Cr depletion may at first sight be a surprising result because the main constituents of the Laves phase are Fe, Nb and W whereas only a minor amount of chromium is present. In parallel with the depleted layer, however, a very thin Laves phase enriched zone is present in the immediate vicinity of the scale/alloy interface (Figure 5.71). The quantitative information from the GDOES depth profiles, in agreement with the SNMS data from the Mn containing Crofer 22 H (section 5.3.4), might be interpreted as if initially present Laves phase precipitates in a zone at a depth of 15 to 35 µm (depending on exposure time) dissolve and then re-precipitate at/near the scale/steel interface.

If chromium is depleted during oxidation of the Mn-free Crofer 22 H, the concentrations of the other alloy constituents (mainly Fe, Nb, W, Si) in the subsurface zone should increase because the sum of all elements naturally will remain 100 % (Figure 5.78). The GDOES profiles of Nb, W and Si (Figure 5.79) exhibit a sharp increase in concentration of these elements near the oxide/steel interface which obviously is not caused by a "100 % effect", i.e. a normalization of the element concentrations after chromium depletion. The sharp

enrichment in concentration of the mentioned elements could be detected up to the maximum test times of 3000 hours (Figures 5.80). Apparently, a real diffusion of Nb, W and Si occurs from the bulk alloy in direction of the scale/steel interface, as confirmed by the depletion of Nb and W, just beneath the enrichment zone. The relative enrichment of Nb is more pronounced for Nb than for W or Si, in agreement with the relative concentration ratio's of the elements in the Laves phase.

According to the results shown in Figures 5.79-80, the enrichment in concentration of Nb, W and Si decreases with time. A possible reason for that may be a subparabolic oxidation behaviour which can be observed in the subscale depletion of Cr profiles (Figures 5.76-77) because this element is the only significant metallic constituent consumed in the Mn-free alloy due to growth of the surface oxide scale. The Cr gradient decreases with time, i.e. the driving force for enrichment of Nb/W/Si is also decreased and the profiles become flatter with time.

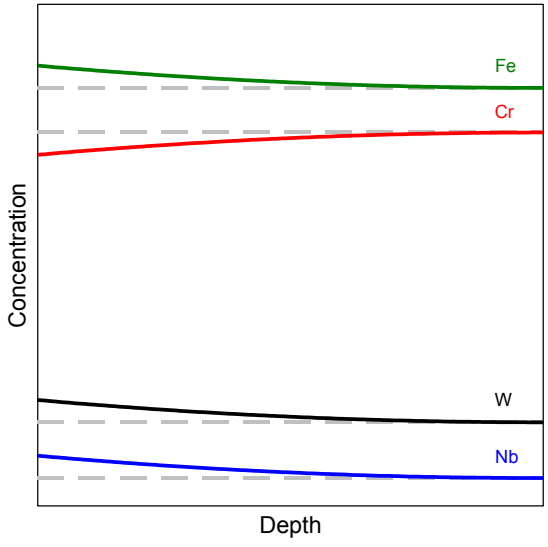

Figure 5.78: Graph showing the qualitative change of element concentration profiles as a result of oxidation induced Cr depletion in subscale zone of FeCrNbW alloy, if, apart from Cr, no diffusion of alloying elements would occur.

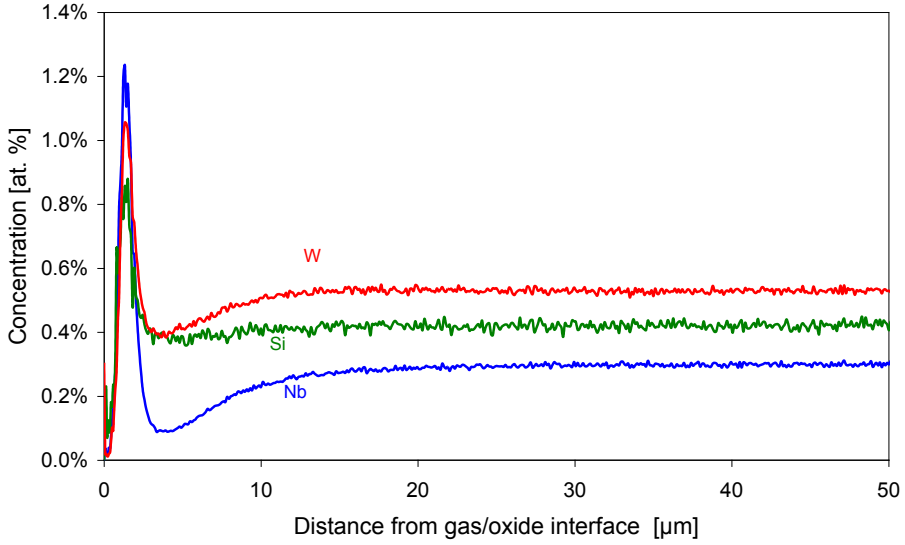

Figure 5.79: GDOES depth profile showing distribution of Nb, Si and W in the subsurface zone for the Mn-free variant of Crofer 22 H (MKS) after 100 h oxidation at 800 °C in Ar-4%H_2-20%H_2O.

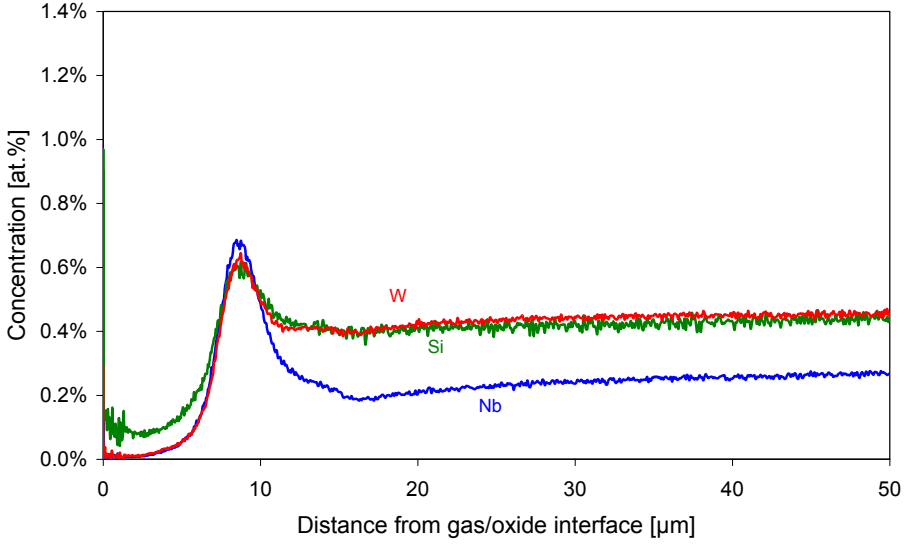

Figure 5.80: GDOES depth profile showing distribution of Nb, Si and W in the subsurface zone for the Mn-free variant of Crofer 22 H (MKS) after 3000 h oxidation at 800 °C in Ar-4%H_2-20%H_2O.

5.3.6 Mechanisms of subsurface enrichment/depletion

Subsurface phase transformations during oxidation are commonly directly or indirectly related to the depletion of the oxide scale forming element(s). In case of the Mn containing batch of Crofer 22 H (e.g. KUA) these are especially manganese and, in case of the Mn-free variant (MKS), only chromium. The observed depletion of intermetallic precipitates and the parallel enrichment at the scale/alloy interface was recently observed for a niobium containing nickel base alloy [122] and was described by considering activity gradients of the precipitate forming elements in the sub scale chromium concentration gradient. The subscale enrichment/depletion process of the intermetallic phase, in the prevailing case Fe/Nb-base Laves phase, might, however, also be affected by preferential nucleation of the precipitate at the scale/steel interface. For that case, the scale/steel interface would act in a similar manner on the intermetallic phase nucleation and growth as an alloy grain boundary.

In the following sections these two possibilities for the experimentally observed sub scale Laves phase depletion/enrichment processes will be considered i.e.

- Effect of an oxidation induced chromium depletion profile and
- Oxide/steel interface as preferential nucleation site for Laves phase precipitates.

5.3.6.1 Modeling of subsurface depletion/enrichment as a result of Cr depletion

Considering the composition of the Laves phase, the main requirement which must be fulfilled for preferential precipitation of this phase near the scale/alloy interface is a driving force for Nb (and/or W, Si) to diffuse from the bulk alloy towards the scale/alloy interface. The establishment of such a driving force must be indirectly caused by the subscale depletion of the alloying elements which are the main constituents of the surface oxide scale. For alloying an easier correlation between the amount of scale forming element(s) incorporated in the scale with that depleted from the alloy, the following treatment relate to the Mn-free version of Crofer 22 H (MKS).

Comparing the Laves phase composition and the initial concentrations of Nb, W and Si in the alloy, it is apparent that the element which exhibits the most substantial relative enrichment

at the scale/alloy interface is Nb (Figure 5.7). Its concentration increases from 0.48 % in the bulk alloy to approximately 21 % in the Laves phase. The respective concentrations for W are 2 % and 29 %; for Si they are 0.24 % and 1.5 %.
To establish, whether the Laves phase formation at the scale alloy interface may be a natural consequence of the oxidation induced subscale chromium depletion, a number of model calculations were carried out utilizing the software packages DICTRA and ThermoCalc [69, 118]. As described in section 5.3.5, the underlying thermodynamic database does not quantitatively correctly describe the experimentally observed Laves phase composition. Therefore, the modeling calculation was carried out using a simplified ternary Fe–Cr–Nb system as Nb exhibits, relative to the original alloy composition, the strongest depletion/enrichment process in the subsurface layer (Figure 5.64b).

For the DICTRA modeling an "imaginary diffusion couple", [122] was used as input whereby one part of the couple was the model steel Fe–22Cr–0.4Nb and the other part was vacuum. Then the boundary conditions were set in such a way that a preset chromium flux (J in mol·cm^{-2}·s^{-1}) occurs from the alloy in direction of the vacuum to simulate the chromium loss as a result of surface oxide formation. Thereby

$$J = \frac{(2k_p)^{1/2}}{\overline{V}_{Cr_2O_3}} \cdot t^{-1/2} \qquad (5.1)$$

in which $\overline{V}_{Cr_2O_3}$ is the molar volume of chromium oxide in cm^3·mole^{-1}, t the time in s and k_p the parabolic oxidation rate constant in terms of oxide scale thickness (thus $X^2 = 2k_p' t$) which was experimentally determined to be 1×10^{-14} cm^2·s^{-1} (see data in following section).

The phase distribution calculated using DICTRA for an oxidation time of 100 hours in Figure 5.81 shows formation of a Laves phase depleted zone and, in parallel, an enrichment of Laves phase in the immediate vicinity of the scale/alloy interface in qualitative agreement with the experimental observations. Although the alloy composition used in the calculation is, for the reason mentioned above, not identical to that of the experimentally studied alloy, the calculated results in Figure 5.81 clearly reveal that the combined depletion/enrichment in

the subscale zone of a Laves phase containing alloy may occur as a natural result of the oxidation induced chromium depletion.

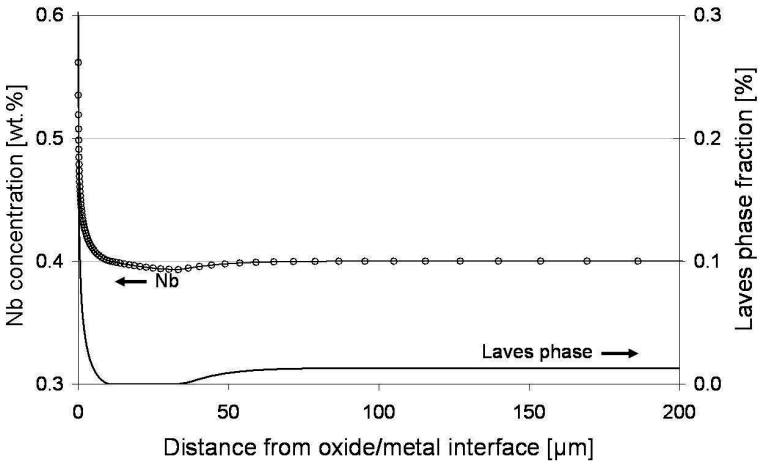

Figure 5.81: Distribution of the Nb and Laves phase in the subsurface region of model alloy Fe–22%Cr–0.4%Nb after 100 h oxidation at 800 °C calculated using DICTRA [118] with the parabolic oxidation rate constant $k_p' = 1\times10^{-14}$ cm^2·s^{-1} as input parameter.

The question which remains to be answered is what the thermochemical background is for the formation of the calculated subscale phase changes shown in Figure 5.81. From diffusion theory [123], the flux J_k of species k can be explicitly defined as a function of the chemical potential gradient

$$J_k = -\frac{1}{\overline{V}_m} \cdot M_k x_k \frac{\partial \mu_k}{\partial z} \tag{5.2}$$

in which M_k is the mobility of species k, $\overline{V}_m$ the molar volume, x_k the molar fraction of species k, μ_k the chemical potential, and z the spatial coordinate (in case of oxidation, the distance from the oxide/steel interface). If the chemical potentials of the element Nb would increase along the chromium depletion profile from the scale/alloy interface in direction of the bulk alloy and thus the flux would be negative, Nb will tend to diffuse in the opposite direction downhill the activity gradient, i.e. towards the oxide/alloy interface.

To check this possibility, Figure 5.82 shows the effect of chromium content in the base composition of the model Fe-22Cr-0.4Nb steel on the chemical potential of Nb, using the data base TCFE4 coupled to the ThermoCalc software [69]. The data shows an influence of alloy chromium content on the chemical activity of niobium whereby decreasing chromium content decreases the niobium activity, although the change in Nb activity is relatively small.

Based on these data the oxidation induced chromium depletion as a result of oxide scale formation and growth results in a decrease of the niobium activity in the subsurface zone. Due to the chromium depletion induced niobium activity gradient, diffusion of niobium is expected to occur from the inner part of the chromium depletion zone towards the scale/steel interface. This is a possible explanation for the formation of the observed Laves phase depleted subscale zone (Figure 5.71). Additionally, this process leads to Nb enrichment in the area of the lowest chromium concentration, i.e. in the immediate vicinity of the oxide/alloy interface, with the result that Laves phase formation becomes favored. The substantial solubility of the Laves phase for W and Si then provides a driving force for these two other Laves phase constituents in direction of the scale/alloy interface. These processes qualitatively explain the experimental observations (Figures 5.79-80) i.e. an enrichment of the Nb/W/Si rich Laves phase at the scale/alloy interface and beneath that formation of a zone of approximately 10 μm wide (after 100 h exposure at 800°C) in which the Laves phase is depleted.

This mechanism for the oxidation induced phase changes in the subscale chromium depleted layer is qualitatively similar to that very recently described for the chromia forming nickel base alloy INCONEL 625 [122]. In that alloy a similar depletion/enrichment process was found for the δ-Ni_3Nb phase during oxidation at 900 and 1000 °C. However, for the Ni base alloy the effects were far more pronounced than for the ferritic steel used in the present investigation, i.e. a near continuous band of the δ-Ni_3Nb phase was formed at the scale/alloy interface.

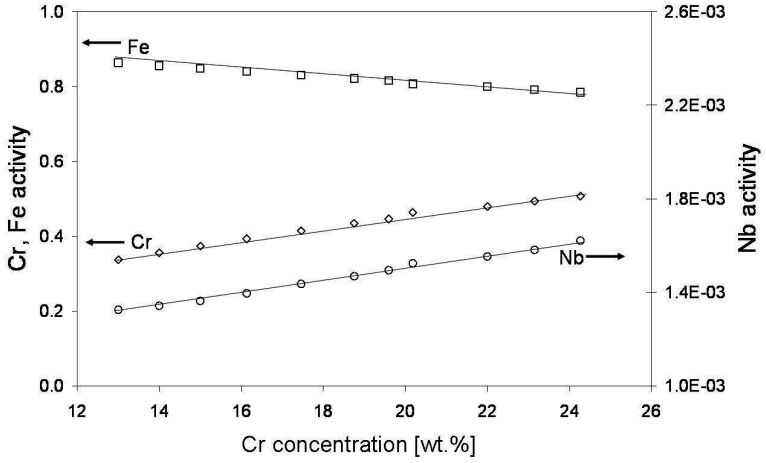

Figure 5.82: Chemical activities of Fe, Cr and Nb in Fe-Cr-0.4Nb alloys at 800 °C as a function of chromium content calculated in ThermoCalc using the TCFE4 [69].

This quantitative difference between the Laves phase strengthened ferritic steel and the nickel base alloy 625 is mainly related to the fact that, compared to the ferritic steel, the Ni-base alloy exhibits:

1) a substantially lower chromium diffusion coefficient in the alloy, or more precise, a substantially larger ratio between the oxidation rate k_p and the chromium diffusion coefficient D in the alloy. This results in a lower Cr concentration at the scale/alloy interface of the Ni-base alloy than in case of the ferritic steel
2) a higher Nb content
3) a far more pronounced effect of Cr content on Nb activity [123].

The experimental results and theoretical considerations thus show that the phase transformations in the subscale chromium depletion zone of a Laves phase strengthened ferritic 22 % Cr steel during oxidation at 800 °C substantially differ from those in Cr carbide strengthened chromia forming materials such as conventional austenitic steels and Ni base alloys. Although the Laves phase contains only minor amounts of chromium, consumption of this element from the alloy as a result of chromia surface scale formation may result in formation of a subsurface layer in which the Laves phase is depleted. However, this occurs in parallel with formation of a thin zone near the scale/steel interface in which the phase is

enriched. Modeling the diffusion processes and the precipitate dissolution using the DICTRA and ThermoCalc software revealed that this depletion/enrichment process can be explained by the influence of chromium concentration on the niobium activity in the alloy matrix. This process provides a driving force, though small, for diffusion of niobium in the chromium depleted zone towards the area of lowest chromium concentration, i.e. the scale/alloy interface. The enrichment of W and Si is then a consequence of their solubility in the Laves phase.

5.3.6.2 Preferential nucleation at steel/oxide interface

Although the establishment of an oxidation induced Cr concentration gradient may fundamentally explain the observed Laves phase depletion/enrichment process (see previous sections) it cannot be excluded that the mechanism is at least partially affected by preferential nucleation at the scale/alloy interface. A possibility to check whether the steel/oxide interface might be a preferential site for Laves phases precipitation would be to compare the behaviour of solution annealed and pre-aged material. If the scale/steel interface would be a preferential precipitate nucleation site, the exposure of solution annealed Crofer 22 H in air at e.g. 800 °C is expected to result in preferential Laves phase precipitates at the scale/steel interface in a similar manner as would be the case for a steel grain boundary. If pre-aged material would be subjected to the mentioned oxidation exposure, the extent of Laves phase precipitation at the scale/steel interface should be less pronounced because the ferritic steel matrix would already be depleted in respect to the Laves phase forming alloying elements, mainly Nb, W and Si, up to an equilibrium level and thus subsequent precipitation at the scale/steel interface would be expected to be less pronounced than in case of the solution annealed material.

Pre-ageing could principally be accomplished by straightforward heat treatment at high temperatures e.g. 800 or 900 °C (section 5.5.4). However, a heat treatment of specimens commonly used for oxidation test might already result in oxidation and subscale depletion processes even if the treatment would be carried out in a so-called inert environment. Environments such as e.g. pure argon or vacuum are characterized by a low pO_2 but for steels containing minor amounts of oxygen active elements such as Si, Ti, La

or Nb, such environments cannot be considered as being really inert. Therefore, a different experimental approach was used to produce aged material in which Laves phase was precipitated in a near equilibrium state. A Crofer 22 H batch which prevailed in form of 16 mm plate was used as test material (batch NEC, Tables 3 and 4). Specimens of 2 mm thickness were machined from one part of the plate. A second part of the 16 mm thick plate was encapsulated in silica glass capsules evacuated down to 10^{-5} mbar vacuum and subsequently exposed for 500 hours at 900 °C, i.e. a heat treatment which is known (section 5.5.4) to result in a substantial, near equilibrium Laves phase precipitation. The third part of the plate was aged in a similar manner for 2000 hours at 800 °C. Subsequently, specimens of different thickness were spark eroded from the centre of the thick, aged plate. In this way oxidation test specimens with an aged microstructure were obtained which were not affected by external or internal oxidation processes. The experimental approach was similar to that which will be described in more detail in section 5.5.4 and which was used for a study of the specimen thickness dependence of oxidation behaviour.

Figure 5.83 shows metallographic cross sections of Crofer 22 H bactch NEC after oxidation at 800 °C in air for 4000 hours. The figures compare the oxide scale formation and sub scale depletion/enrichment processes of solution annealed material with that of material in the mentioned two different ageing conditions. The figures reveal that the thickness, morphology and composition of the surface oxide scales are hardly affected by the ageing treatment. However, it is apparent that the formation of Laves phase precipitates at the scale/steel interface in case of the aged materials is less pronounced than in case of the solution annealed material.

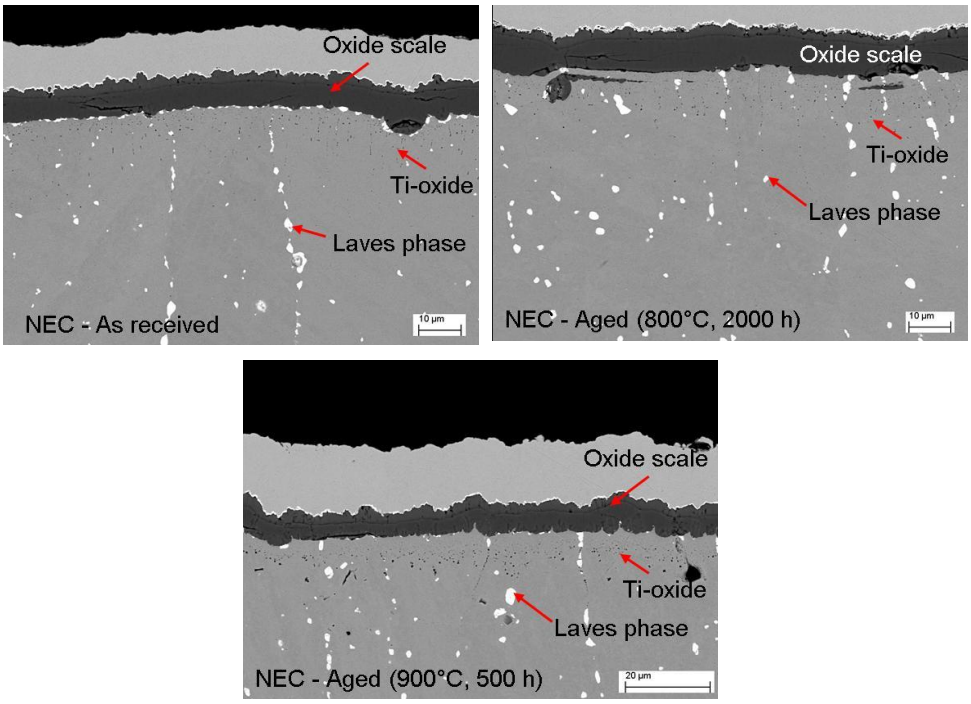

Figure 5.83: SEM images showing cross sections of oxide scales formed on Crofer 22 H batch NEC during 4000 h oxidation at 800 °C in air: a) as received material; b) aged (800 °C, 2000 h, vacuum) c) aged (900 °C, 500 h, vacuum). Figures illustrate results obtained for specimen with the same thickness of 0.25 mm.

These results provide a strong indication that the experimentally observed sub surface Laves phase depletion/enrichment process is only partly governed by the theoretical considerations in section 5.3.6.1 related to an activity gradient of Nb in the chromium concentration gradient. The process is at least partly affected by the preferential nucleation of Laves phase at the scale/steel interface, i.e. this interface acts in respect to Laves phase precipitation in a similar manner as a grain boundary in the bulk alloy.

5.4 Significance of Mn for oxide scale properties

5.4.1 Introductory remarks

In the development of the interconnector steels Crofer 22 APU and Crofer 22 H it was decided to define an addition of Mn of 0.4 mass.-% [5, 30] .As explained in sections 2.12 and 2.13, the reason for the Mn addition was that in this way the steel formed during exposure at typical SOFC service temperatures around 800 °C a double-layered surface scale consisting of chromia plus Cr/Mn-spinel, rather than a pure chromia scale. The presence of the outer spinel layer was shown to reduce the formation of volatile Cr-oxides and -oxyhydroxides during exposure in air[5, 76, 124-125] especially if substantial amounts of water vapour were present [126]. A disadvantage of the Mn addition was that the oxidation rate during air exposure was increased by the Mn addition [106, 127]. This in contrary to the anode side gas exposure in which the Mn addition had hardly any effect or even tended to decrease the scale growth rate [106]. Whereas in a number of studies the effect of Mn on formation of volatile species in cathode gas is claimed to be substantial, some of the recent studies indicate [76], that the reduction in formation of volatile Cr species by presence of Mn during air exposure is only marginal. Therefore, the aim of the studies in the following sections was to evaluate, whether the addition of Mn had a significant effect on the oxidation behaviour and especially on the formation of volatile Cr species in case of the Laves phase strengthened steel of the type Crofer 22 H. For this purpose, a model steel with the same type and amount of alloying additions as in Crofer 22 H was produced, however without addition of manganese. Details of the steel manufacturing were already described in the previous section. The detailed chemical composition of the investigated alloy is given in Table 7 and 8.

Table 7: Chemical composition in wt. % of Mn-free variant of Crofer 22 H measured by ICP-OES in the central division of analytical chemistry (ZCH) at FZJ.

Designation	Thickness	Cr	Mn	La	Ti	Nb	W	Al	Si
MKT	2 mm	22.66	<0.01	0.13	0.09	0.51	2.06	0.018	0.26
MKS	1 mm								
MKU	0.5 mm								
MKW	0.3 mm								

Table 8: Impurities in wt. % of the Mn-free variant of Crofer 22 H according to hot gas extraction IR spectroscopy measured in the central division of analytical chemistry (ZCH) at FZJ.

Designation	Thickness	C	S	N	O
MKT	2 mm	0.0032	0.0014	0.006	0.003
MKS	1 mm				
MKU	0.5 mm				
MKW	0.3 mm				

5.4.2 Oxidation behaviour at 800°C

Figure 5.84 shows weight changes for the investigated steel for specimens of different thickness after 1000 h discontinuous oxidation at 800 °C in air and in Ar-4%H_2-20%H_2O. The weight changes measured after exposure in simulated anode gas were almost two times higher than those after air exposure. Thereby, no effect of specimen thickness on the oxidation rate was observed during exposure in both atmospheres. The Mn-free steel forms on its surface a virtually pure chromia scale (Figures 5.85-86). Beneath the oxide layer an internal oxidation zone consisting of Ti-oxides was formed, similar to that found for Crofer 22 H (Figure 5.87).

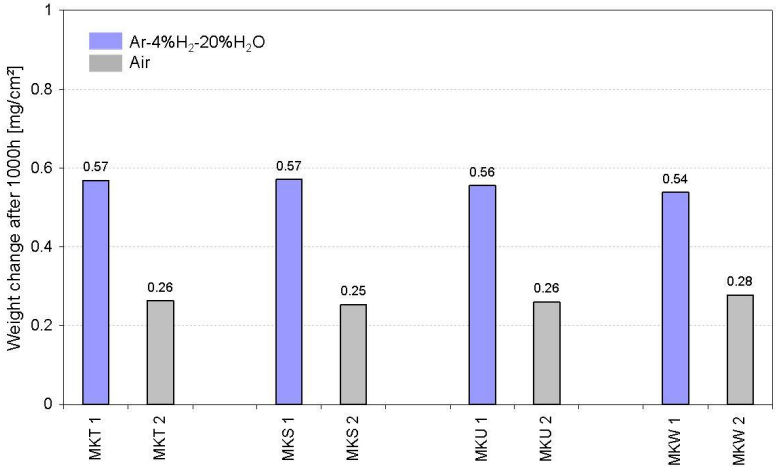

Figure 5.84: Weight changes after 1000 h discontinuous oxidation at 800 °C in air and in Ar-4%H_2-20%H_2O for samples of the Mn-free variant of Crofer 22 H with different thicknesses (MKT-2 mm; MKS-1 mm; MKU-0.5 mm; MKW-0.3 mm).

Different from the observations for Crofer 22 H (section 5.2), the air formed scale consists after 1000 h exposure of a layer with a thickness of approximately 2 µm, with large, outward growing, quasi free standing crystals which possess a height up to approximately 4 µm. This type of scale morphology was previously observed during long term air exposure of Cr-base ODS alloys [128] and was attributed to the formation and parallel re-deposition of volatile Cr species.

The scales formed on the Mn-free steel in simulated anode gas are thicker than those formed in air. This is in agreement with the previous findings for various types of chromia forming alloys [5] as explained in the introductory remarks (section 5.4.1). The anode gas formed scales of the Mn-free variant are thicker than those formed on Crofer 22 H, thus confirming previous findings that in this gas the addition of Mn reduces the oxidation rate (Figure 5.88).

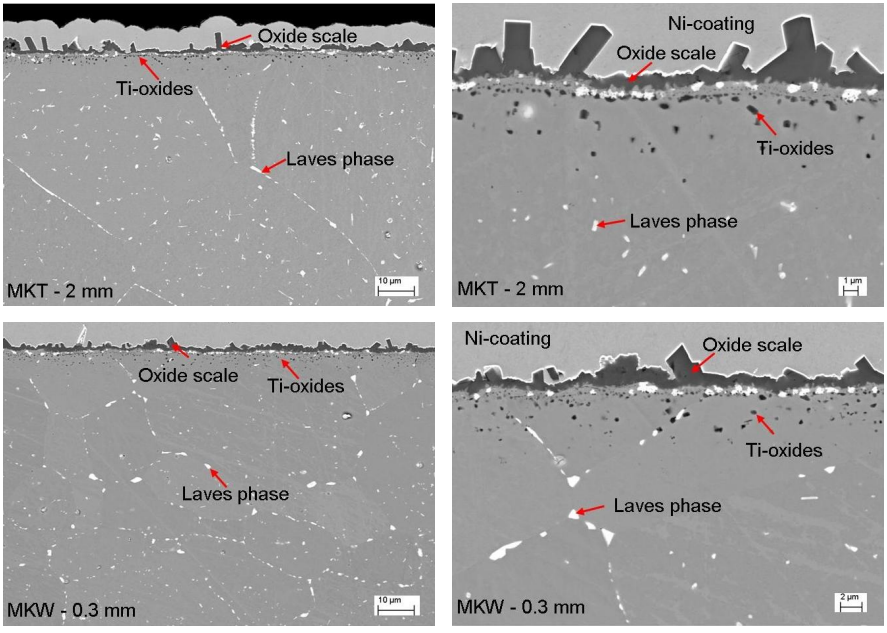

Figure 5.85: SEM/BSE images showing cross sections of oxide scale formed on Mn-free variant of Crofer 22 H during 1000 h discontinuous oxidation at 800 °C in air. Figures illustrate results obtained for specimens of different thickness (MKT-2 mm; MKW-0.3 mm).

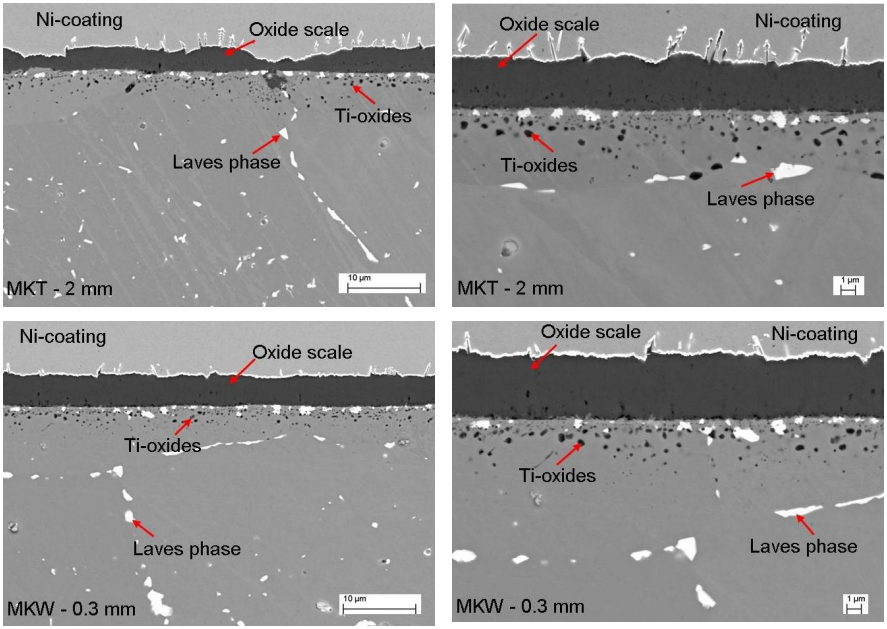

Figure 5.86: SEM/BSE images showing cross sections of oxide scale formed on Mn-free variant of Crofer 22 H during 1000 h oxidation at 800 °C in Ar-4 % H_2-20 % H_2O. Figures illustrate results obtained for specimens of different thickness (MKT-2 mm; MKW-0.3 mm).

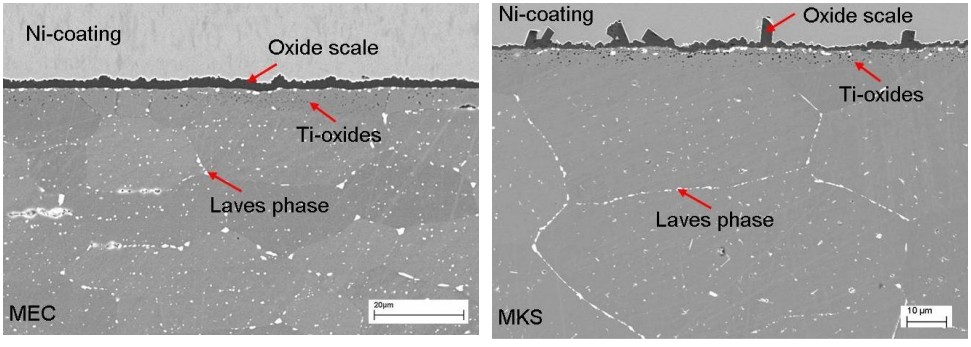

Figure 5.87: SEM/BSE images of cross sections comparing oxide scales formed on Crofer 22 H (batch MEC: 1 mm) and Mn-free variant of Crofer 22 H (MKS) during 1000 h oxidation at 800 °C in air.

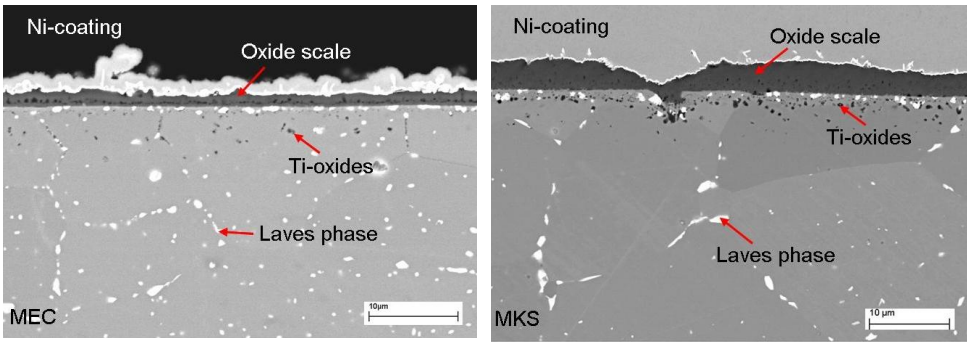

Figure 5.88: SEM/BSE images of the cross sections comparing oxide scales formed on Crofer 22 H (batch MEC: 1 mm) and Mn-free variant of Crofer 22 H (MKS) during 1000 hours oxidation at 800°C in Ar-4%H_2-20%H_2O.

A proposal for the positive effect of Mn on the growth rates in simulated anode gas was described in reference [129]. The authors found Mn addition in a NiCr alloy to enhance the oxidation rate and decrease the scale adherence during Ar-O_2 exposure, but it decreased the growth rate in Ar-H_2-H_2O. Similar low oxidation rates were found for the Mn-containing alloys during exposure in Ar-CO-CO_2 [130], thus the mechanism seems to be primarily related to the low pO_2 rather than the presence of water vapor and/or hydrogen in the simulated anode gas. The NiCrMn alloy exhibited a double-layered surface oxide consisting of a thin layer of Cr/Mn spinel on top of the inner chromia scale. In the case of Ar-4%H_2-7%H_2O exposure, the spinel layer was slightly thicker than that formed in Ar-20%O_2. These results indicate that in the ternary NiCrMn alloy the atmosphere dependence of the oxidation rate is related to the formation of the Cr/Mn spinel in the outer part of the scale. Manganese has a lower solubility in Cr_2O_3 at low oxygen potential than at high pO_2 (Figure 5.89) [101]. It was argued [129] that in the low pO_2 gas Mn prevents inward oxygen transport by segregating at the oxide grain boundaries. This effect has, however, not been studied widely and there is no unequivocal evidence which could be derived from previous work. Considering the large size of the Mn^{2+} ion compared to that of Cr^{3+} it is likely that grain boundary segregation of Mn in the scale formed may occur in the low pO_2 gas. Based on the phase diagrams (Figure 5.89) estimated by Naoumidis et al. [101], the spinel phase formed in the low pO_2 gas is stoichiometric $MnCr_2O_4$ while in high pO_2 gas it is stable in a wide range of

compositions, in other words, it may be designated as $Mn_{1+x}Cr_{2-x}O_4$. This was confirmed by SNMS results [131] showing a change of the Cr/Mn ratio in the outer part of the oxide scale formed in air and almost constant Cr/Mn ratio after exposure in Ar-H_2-H_2O. If the flux of Mn is reduced after longer exposure times due to the low Mn concentration in the alloy, a Mn deficit will occur in the spinel layer. Because of the pO_2 gradient existing in the scale, there will be a vacancy flux from the spinel surface towards the spinel-chromia interface where the vacancies will tend to condense resulting in void formation. The reason why during air exposure the presence of Mn in the alloy increases not only the overall thickness of the oxide but also that of the inner chromia scale could be explained by the fact that in air, the Mn deficit in the spinel can be compensated by Cr cations from the inner chromia layer resulting in an enhanced outward flux of Cr [106].

A rapid incorporation of Mn into the oxide scale could lead to complete exhaustion of the Mn reservoir in the specimen because of the low Mn concentration. This effect might modify the described effect of Mn additions on the dependence of the gas composition of the oxide growth kinetics in very thin components.

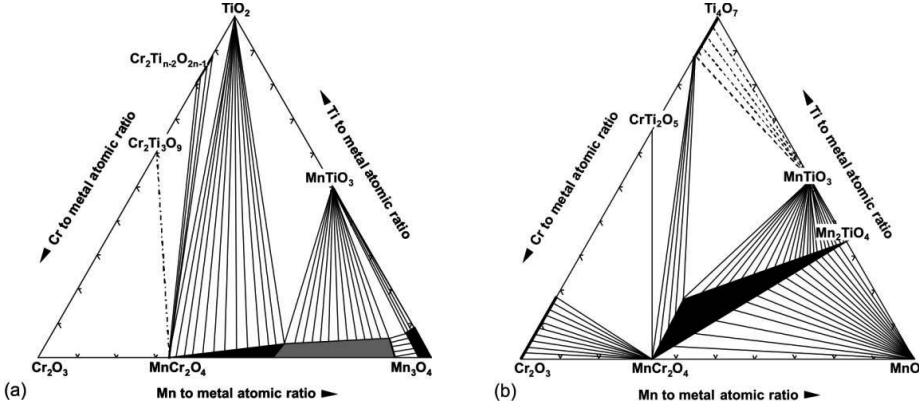

Figure 5.89: Phase equilibria in the quasi-ternary system: (a) Cr_2O_3-Mn_3O_4-TiO_2 after annealing at 1000 °C in air; (b) Cr_2O_3-MnO-Ti_4O_7 after annealing at 1000 °C in a gas with a pO_2 of 10^{-21} bar [101].

The difference in spinel composition in low and high pO_2 gas also explains the different shapes of the oxygen profiles after oxidation of Crofer 22 H in air and Ar-H_2-H_2O as measured by SNMS (sections 5.2.2 and 5.2.3) and Figure 5.90. If the Mn concentration in

the outer scale increases after longer times to a level such that the Mn/Cr ratio is larger than that in the stoichiometric spinel Cr_2MnO_4, this results during air exposure to formation of a Mn rich $(Cr,Mn)_3O_4$ whereas in Ar-H_2-H_2O additional Mn-oxide (MnO) is formed [132] (Figure 5.91).

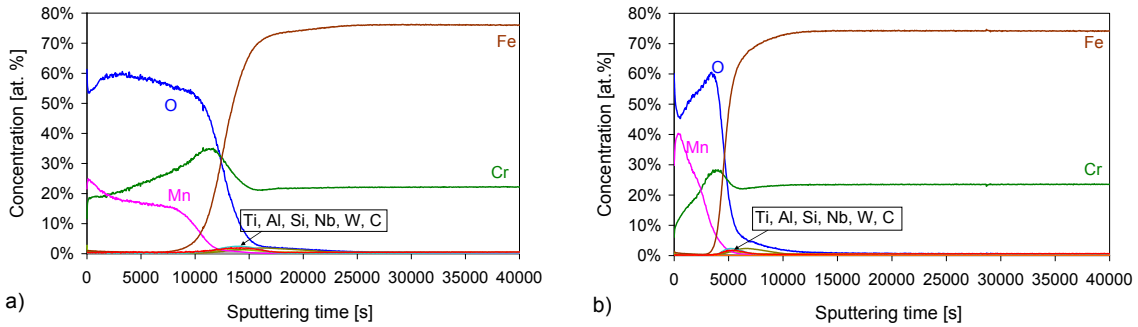

Figure 5.90: Plasma-SNMS element concentration profiles measured on the laboratory batch of Crofer 22 H (KUA) after 1000 h oxidation at 800 °C in a) air and b) Ar-4%H_2-20% H_2O.

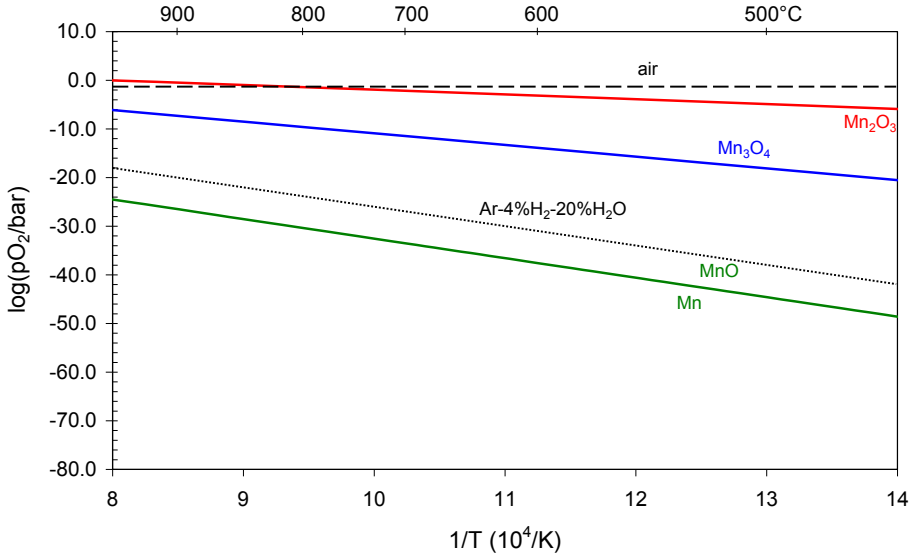

Figure 5.91: Dissociation pressure of manganese oxides as a function of reciprocal temperature compared with equilibrium oxygen partial pressure in air and in Ar-4%H_2-20%H_2O. Calculation carried out with FactSage software [133].

Figure 5.92 shows weight changes of the 1 mm thick specimens of the Mn-free variant of Crofer 22 H (MKS) during 3000 h discontinuous oxidation at 800°C in air and in Ar-4%H_2-20%H_2O. The data qualitatively confirm the results obtained during the 1000 h oxidation experiments (Figure 5.84). However, an important finding is that, during the air exposure a clear weight decrease becomes apparent after exposure times beyond approximately 1000 h of oxidation. The cross-sections in Figures 5.91-98 show that during air exposure only a minor thickness change with increasing oxidation time occurs. These findings clearly illustrate, that the oxidation kinetics can in first approximation be described by a para-linear rate law [35-36]. Characteristic for this type of oxidation kinetics is an initial net weight increase and a subsequent net weight loss after longer exposure time. The scale thickness initially increases and then reaches a near constant value. Para-linear oxidation kinetics prevail if scale growth is governed by solid state diffusion through the scale in parallel with formation of volatile species, here $CrO_3^{(g)}$ and especially Cr-oxyhydroxide $CrO_2(OH)_2^{(g)}$ [36, 73] The oxide scales grown in Ar-4%H_2-20%H_2O show a steadily increasing thickness with increasing oxidation time, as expected, if the scale formation is not affected by volatile species (and/or scale spallation).

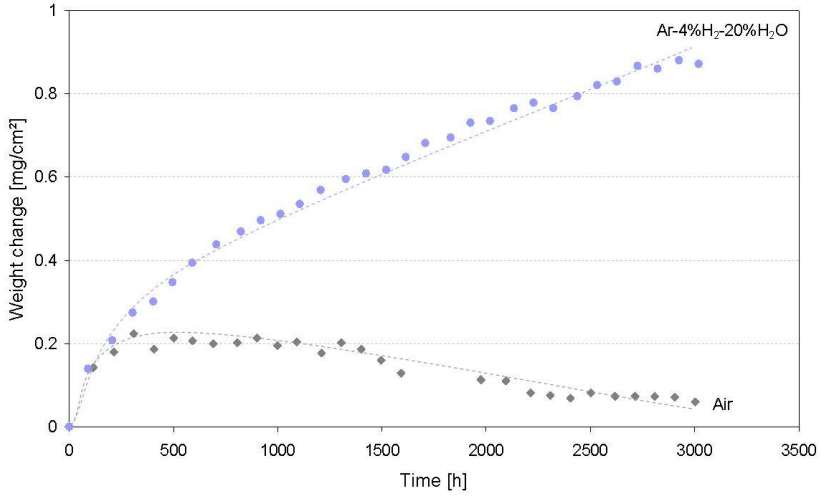

Figure 5.92: Weight change as a function of oxidation time during discontinuous oxidation of Mn-free variant of Crofer 22 H (MKS; specimen thickness 1 mm) at 800 °C in air and in Ar-4%H_2-20%H_2O.

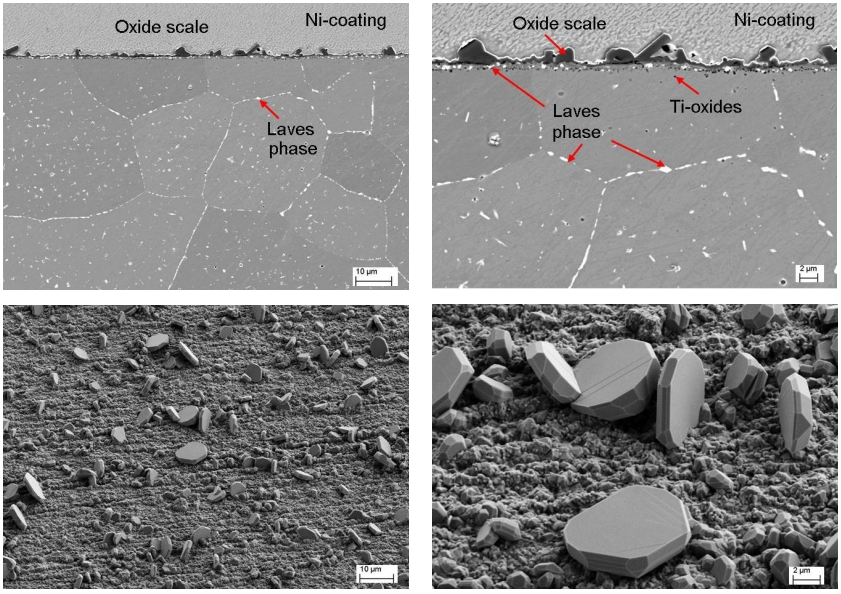

Figure 5.93: SEM/BSE images showing cross sections (upper pictures) and surface morphologies (bottom pictures) of oxide scale formed on Mn-free variant of Crofer 22 H (MKS; specimen thickness 1 mm) during 100 h discontinuous oxidation at 800 °C in air.

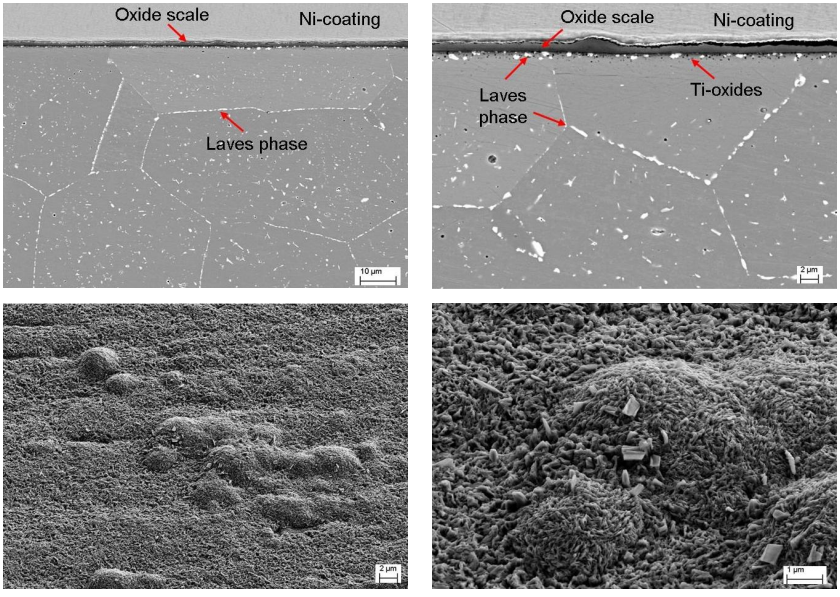

Figure 5.94: SEM/BSE images showing cross sections (upper pictures) and surface morphologies (bottom pictures) of Mn-free variant of Crofer 22 H (MKS; specimen thickness 1 mm) during 100 h oxidation at 800 °C in Ar-4%H_2-20%H_2O.

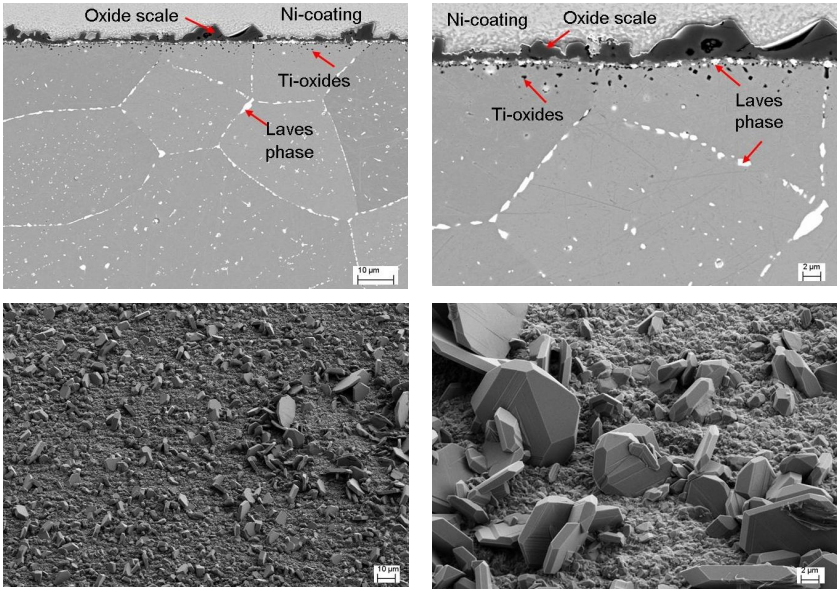

Figure 5.95: Cross sections (upper pictures) and surface morphologies (bottom pictures) of Mn-free variant of Crofer 22 H (MKS-1 mm) during 500 h oxidation at 800 °C in air.

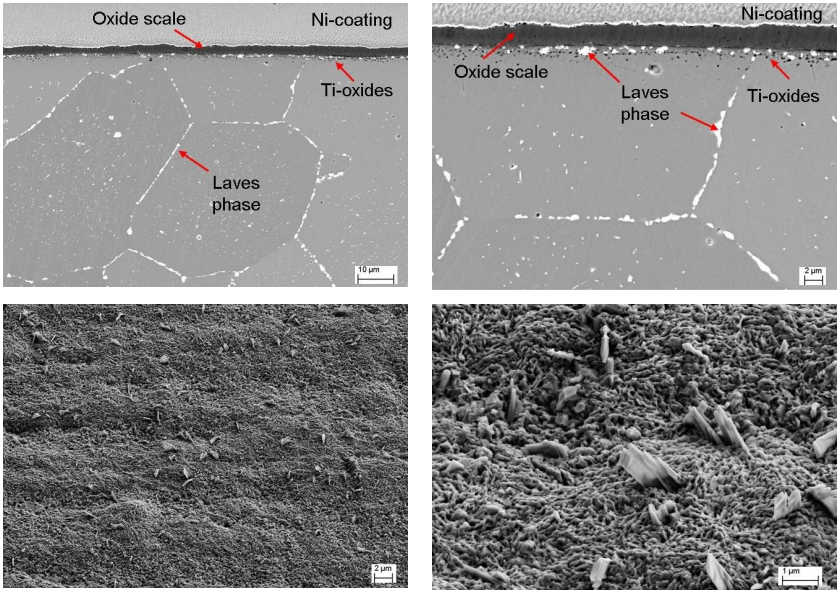

Figure 5.96: Cross sections (upper pictures) and surface morphologies (bottom pictures) of Mn-free variant of Crofer 22 H (MKS, specimen thickness 1 mm) during 500 h oxidation at 800 °C in Ar-4%H_2-20%H_2O.

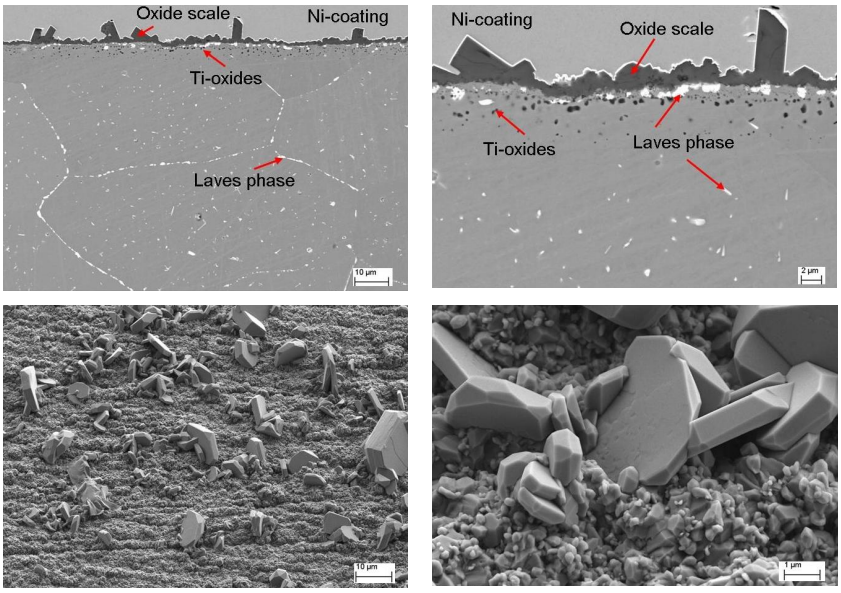

Figure 5.97: Cross sections (upper pictures) and surface morphologies (bottom pictures) of Mn-free variant of Crofer 22 H (MKS-1 mm) during 1000 h oxidation at 800 °C in air.

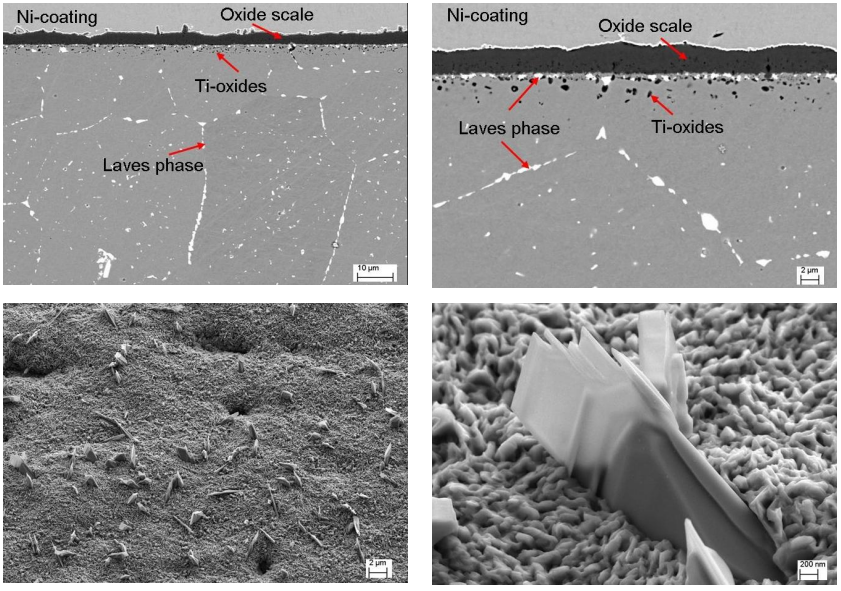

Figure 5.98: Cross sections (upper pictures) and surface morphologies (bottom pictures) of oxide scale formed on Mn-free variant of Crofer 22 H (MKS; specimen thickness 1 mm) during 1000 h oxidation at 800°C in Ar-4%H_2-20%H_2O.

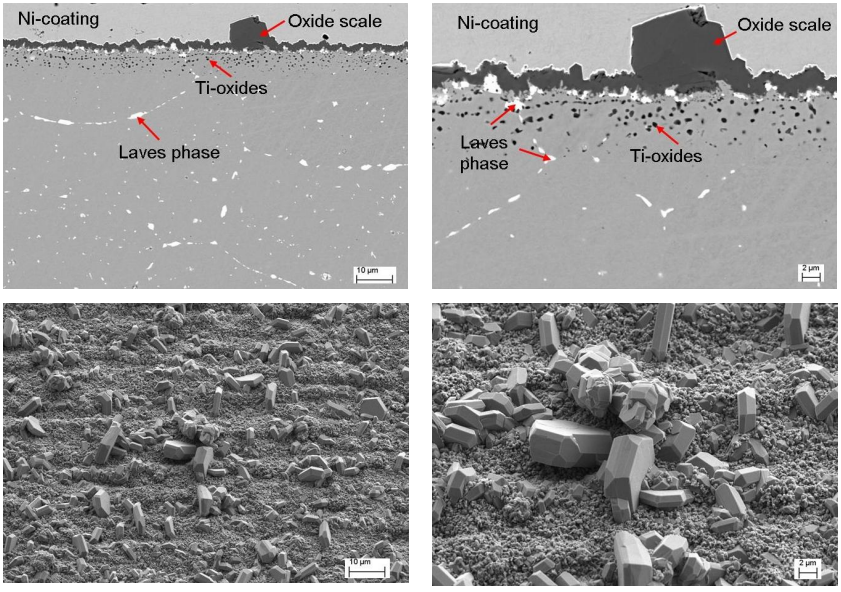

Figure 5.99: SEM/BSE images showing cross sections (upper pictures) and surface morphologies (bottom pictures) of oxide scale formed on Mn-free variant of Crofer 22 H (MKS; specimen thickness 1 mm) during 3000 h discontinuous oxidation at 800 °C in air.

Figure 5.101 shows GDOES profiles of the Mn-free variant of Crofer 22 H after 1000 h oxidation in air and in Ar-H_2-H_2O. From the metallographic cross sections (Figure 5.97) it is obvious that the depth profiles of the air exposed samples cannot be used for a quantitative estimation of the subscale depletion/enrichment process. The layer of outwardly growing Cr_2O_3 crystals on the surface results in a substantial roughness of the oxide surface. Therefore, the sputtering process during the GDOES analysis will not provide reliable, quantitative results. This is apparent from the shallow profiles resulting in not well-defined interfaces in the GDOES profiles (Figure 5.101).

Figure 5.102 shows that the enrichment in the concentrations of Nb, W and Si at the scale/steel interface decreases during exposure in Ar-H_2-H_2O with time. A possible reason for this behaviour may be a subparabolic oxidation behaviour of the Mn-free Crofer 22 H (MKS) which can be observed in the subscale depletion of Cr profiles (Figure 5.103). Chromium is the only significant metallic constituent consumed in the alloy due to growth of the surface oxide scale. As the Cr gradient virtually vanishes after

longer time (Figure 5.103), the driving force for Nb to diffuse towards the oxide/steel interface gradually decreases.

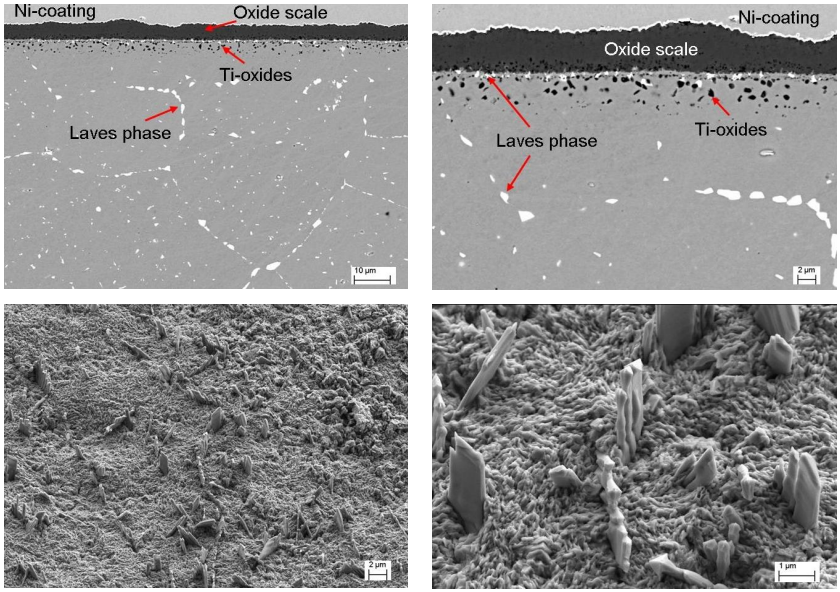

Figure 5.100: SEM/BSE images showing cross sections (upper pictures) and surface morphologies (bottom pictures) of oxide scale formed on Mn-free variant of Crofer 22 H (MKS; specimen thickness 1 mm) during 3000 h discontinuous oxidation at 800 °C in Ar-4%H_2-20%H_2O.

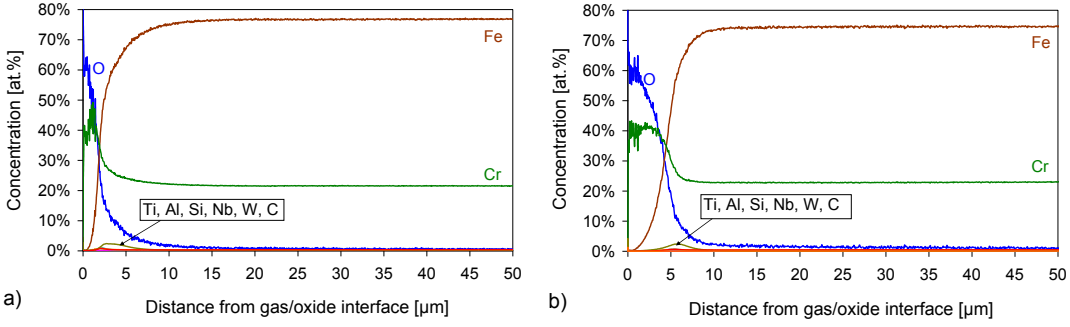

Figure 5.101: GDOES element concentration depth profiles measured on Mn-free variant of Crofer 22 H (MKS; specimen thickness 1 mm) after 1000 h oxidation at 800 °C in a) air and b) Ar-4%H_2-20%H_2O.

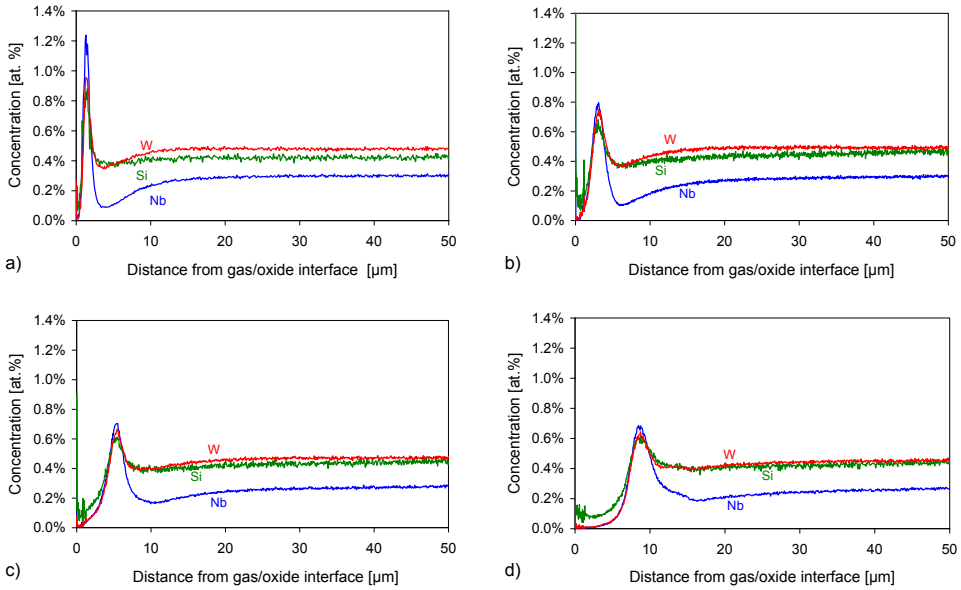

Figure 5.102: GDOES depth profile showing distribution of Nb, Si and W in the subsurface zone for the Mn-free variant of Crofer 22 H (MKS) after a) 100 h, b) 500 h, c) 1000 h, d) 3000 h oxidation at 800 °C in Ar-4%H_2-20%H_2O.

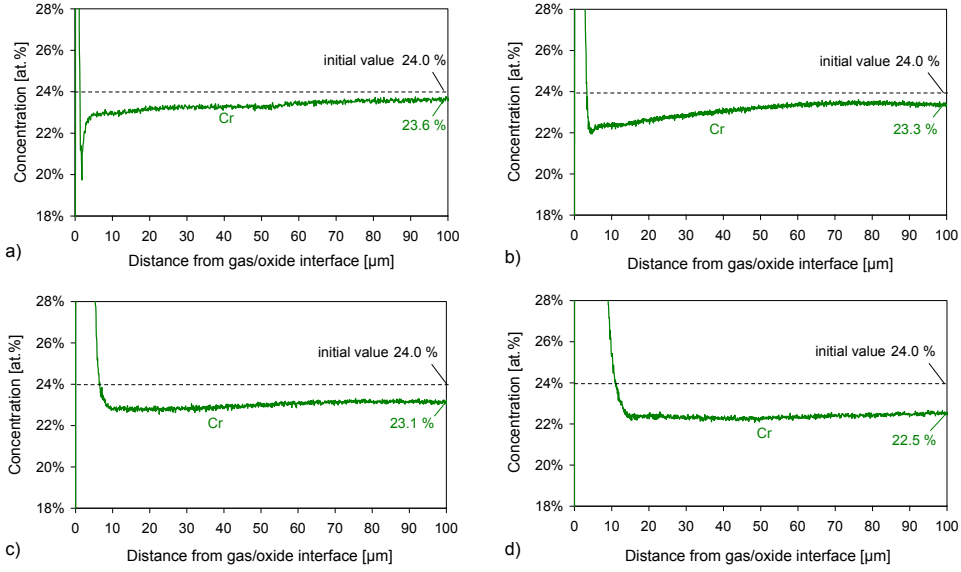

Figure 5.103: GDOES depth profile showing the subscale depletion of Cr for the Mn-free variant of Crofer 22 H (MKS) after a) 100 h, b)500 h, c) 1000 h, d) 3000 h oxidation at 800 °C in Ar-4%H_2-20%H_2O.

Summarizing it can be said that a small amount (approx. 0.4 %) of manganese added to the Crofer 22 type steels reduces the growth rate of the chromia scale in the low pO_2 environment (simulated anode gas). Manganese increases the growth rate of the chromia based scale in high pO_2 environments (air) especially during the early states of oxidation [5, 106] but in parallel, it forms on top of the inner Cr_2O_3, a layer of $(Mn,Cr)_3O_4$ which substantially reduces the formation of volatile Cr species which is of great significance for application of the steel in SOFC application [5, 124].

5.5 Effect of specimen thickness on the oxidation behaviour of Laves phase strengthened ferritic steel

5.5.1 General remarks

As explained in section 2.13, the first group of high-chromium ferritic steels, such as Crofer 22 APU, which were especially designed for SOFC applications, were optimised mainly with respect to electrical conductivity of the surface oxide scales, reduced Cr evaporation and improved workability [30]. This could be achieved by specifying steel compositions with careful control of minor alloying additions and impurities. Especially, the concentrations of the commonly used de-oxidants aluminium and silicon were specified at very low levels beneath 0.1 % to prevent the formation of electrically insulating sub layers of alumina and/or silica beneath the surface chromia scale during high temperature service [30]. Also it was found that the internal oxidation which occurs in steels containing Si and/or Al in concentrations in the order of 0.1 %, adversely affects the external scale growth by formation of outwardly protruding metallic nodules in the scale [30]. One of the disadvantages of the high purity steels is that they possess a relatively poor creep resistance at the high SOFC operating temperatures in the range 600 to 900 °C. In reference [88, 134] it was proposed that the poor creep resistance is the main reason for the observation that the oxidation rates of the steels tend to increase with decreasing component/specimen thickness [86-87]. The latter effect has as result, that thin specimens/components (of a few tenths of a mm thickness) form during a certain service time, thicker oxide scales than would be expected on the basis of results derived from standard laboratory test specimens of a few mm thickness. If the mentioned considerations for the reason of this effect would be correct, then the scale growth rates for the Laves phase strengthened steel Crofer 22 H [9, 91] should exhibit no, or at least a less pronounced specimen thickness dependence than the high purity steels such as Crofer 22 APU.

The following sections will concentrate on the effect of specimen thickness and intrinsic creep strength on the oxidation rate of Laves phase strengthened steel of the type Crofer 22 H, whereby main emphasis is put on the behaviour at 800 °C.

5.5.2 Experimental details

Commercial batches of the ferritic steels Crofer 22 APU (batches LXF, LXE, LXD) and Crofer 22 H (batches MDP, MEC, MDT, MED) were used in the oxidation tests. Generally, Crofer 22 APU and Crofer 22 H (after the heat treatments mentioned in section 4.1) possess a single-phase microstructure, apart from minor amounts of Ti-rich carbonitride precipitates. The detailed compositions of the used batches are given in table 9 and 10. For the oxidation experiments specimens of 20 mm×10 mm in size and varying in thickness between 0.25 and 2.5 mm were machined from the prevailing sheets and subsequently ground down to 1200 grit surface finish (further details were given in section 4.2).

Table 9: Chemical composition in wt. % of the commercial materials measured by ICP-OES in the central division of analytical chemistry (ZCH) at FZJ.

Steel	Designa-tion	Thickness	Cr	Mn	La	Ti	Nb	W	Al	Si
Crofer 22 APU	LXF	2.5 mm								
Crofer 22APU	LXE	1 mm	22.9	0.45	0.066	0.062	-	-	0.006	0.019
Crofer 22 APU	LXD	0.5 mm								
Crofer 22 H	MDP	2.5 mm								
Crofer 22 H	MEC	1 mm								
Crofer 22 H	MDT	0.5 mm	22.9	0.43	0.08	0.07	0.51	1.94	0.02	0.21
Crofer 22 H	MED	0.3 mm								
Crofer 22 H	NEC	16 mm								

Table 10: Impurities in wt. % of the commercial materials measured by hot gas extraction IR spectroscopy in the central division of analytical chemistry (ZCH) at FZJ.

Steel	Designation	Thickness	C	S	N	O
Crofer 22 APU	LXF	2.5 mm				
Crofer 22 APU	LXE	1 mm	0.001	0.0035	0.004	0.006
Crofer 22 APU	LXD	0.5 mm				
Crofer 22 H	MDP	2.5 mm				
Crofer 22 H	MEC	1 mm				
Crofer 22 H	MDT	0.5 mm	0.007	<0.002	0.015	0.006
Crofer 22 H	MED	0.3 mm				
Crofer 22 H	NEC	16 mm				

Figure 5.104 shows weight change data for specimens of different thickness of the investigated steels Crofer 22 APU and 22 H during discontinuous oxidation at 800 °C in laboratory air up to an exposure time of 1000 h. Figure 5.105 shows the oxide scale

morphologies and alloy microstructures of Crofer 22 H after 1000 h discontinuous oxidation at 800 °C. As already found for Mn containing high-Cr alloys in earlier studies [18] the oxidation rates for both steels were higher in air than in simulated anode gas (Figure 5.106). In all cases the oxide scales consisted of an outer Mn/Cr-spinel layer and an inner chromia scale. Also an internal oxidation zone of fine Ti oxide precipitates was visible in both alloys. In case of Crofer 22 H indications for enrichment of Laves phase at the scale/alloy interface were found (compare section 5.2). Details of the microstructural features of oxide scale morphologies of Crofer 22 APU were extensively described in references [18, 30, 85-87] and section 2.13 and will not be further discussed here.

In agreement with previous findings [87-88, 134] Crofer 22 APU exhibits during air oxidation a clear dependence of the oxidation rate on the specimen thickness, the thin specimens showing higher oxidation rates than the thick ones. This is not the case for Crofer 22 H; a specimen thickness variation from 0.3 to 2.5 mm did not substantially affect the oxidation rates (Figure 5.104). This is confirmed by the metallographic cross sections in Figure 5.105. The oxidation rate of the thickest specimen of Crofer 22 APU is similar to that of the corresponding Crofer 22 H sample.

Schütze [135] found that at high temperatures no substantial intrinsic plasticity can be expected in protective oxide scales. Nevertheless, there are suggestions in the literature that a mechanism of “pseudoplasticity” can be observed because the formation of microcracks in oxide scales due to growth stresses may be superimposed by healing process closing these microcracks by the formation of new oxide [135-136]. For NiO scales on Ni, Küppenbender et al. [137] observed that the pseudoplasticity mechanism was responsible for stress relief in growing oxide scales. In case of some of the Crofer 22 H samples, minor cracking was sometimes observed in the outer part of the oxide layer. It could not unequivocally be derived whether these microcracks were formed during exposure (e.g during temperature change) or during the preparation of the metallographic cross sections.

Also during exposure in simulated anode gas Ar-4%H_2-20%H_2O Crofer 22 H did not exhibit any indication for a specimen thickness dependence of the oxidation rate even up to exposure times of 10 000 h (Fig. 5.106). Important to note that, in accordance with previous results [18], also for Crofer 22 APU a specimen thickness dependence of the oxidation rate in simulated anode gas is hardly present or at least far less pronounced than during air exposure.

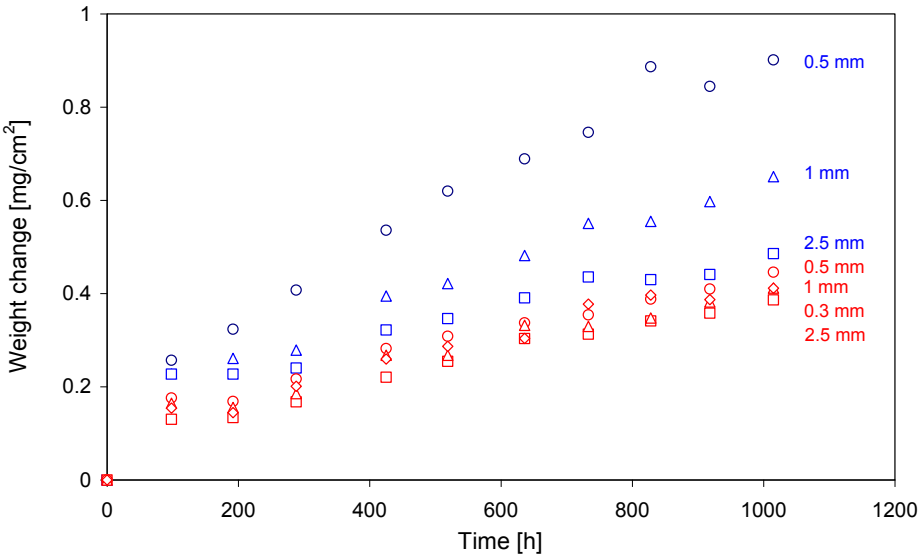

Figure 5.104: Weight change data for Crofer 22 APU (blue symbols, batches LXD-0.5 mm; LXE-1 mm; LXF-2.5 mm) and Crofer 22 H (red symbols, batches MDP-2.5 mm; MEC-1 mm; MDT-0.5 mm; MED-0.3 mm) during discontinuous oxidation at 800 °C in laboratory air showing effect of specimen thickness on oxidation rates.

Figure 5.107 shows weight change data of Crofer 22 H during exposure for 10 000 h at 800 °C in air. The specimens with a thickness ranging from 0.3–2 mm (Figure 5.108) showed no substantial differences in oxidation rate up to approximately 3500 h. However, after that time the oxidation rate of the thinnest specimen of 0.3 mm started to increase. This finding was reproduced by a second series of specimens which were only exposed up to 5000 h; also in that case a clearly visible increase in oxidation rate was observed after about 3500 h exposure. The substantially thicker oxide after 10 000 h

exposure of the thinnest specimen compared to that on the thicker specimens is clearly confirmed by the cross sections in Figure 5.109. This is in contrary to the scales formed in anode gas (Figure 5.110) in agreement with the weight change data in Figure 5.106.

5.5.3 Mechanisms for specimen thickness dependence on oxidation rates

The main findings of the experiments in the previous section using specimens with a thickness in the range 0.3-2.5 mm at 800 °C are:

- During air exposure Crofer 22 H exhibits, contrary to Crofer 22 APU, no specimen thickness dependence of the oxidation rate up to approximately 3500 h.
- After that time, the thinnest specimen (0.3 mm) of Crofer 22 H starts to exhibit a higher oxidation rate than the thicker ones.
- In simulated anode gas hardly any effect of specimen thickness on the oxidation rate is found for both steels.

Huczkowski et al. [86-87] observed a specimen thickness dependence of the oxidation rate of Crofer 22 APU and a number of high purity, ferritic model steels during air exposure at 800 and 900 °C. The authors considered a number of possibilities for this effect and came to the conclusion that it is unlikely related to differences in minor alloying element depletion in thick and thin specimens. This is in agreement with the experimental observations made in the present study. Crofer 22 H and Crofer 22 APU form on specimens of a (few) mm thickness oxide scales which are very similar in thickness and composition. Accordingly it is expected, that the subscale depletion processes in both steels will be very similar. Huczkowski et al. [86-87] proposed that the specimens thickness dependence of the oxidation rate was probably related to differences in creep deformation of the metallic substrates by oxide growth stresses in specimens of different thickness. Zurek et. al. [88, 134] found a specimen thickness dependence of the oxidation rates during oxidation of NiCr-base alloys at temperatures in the range 1000°C showing that chromia growth rates tend to be higher on thin than on thick specimens. Echsler et al. [138] studied the stress generation and relaxation occurring during oxidation of Fe-Cr-Al alloys and the experiments revealed that the stress relaxation at

1200 °C and during cooling strongly depends on the creep strength of the specimen, which is affected by the specimen thickness and/or the type of material.

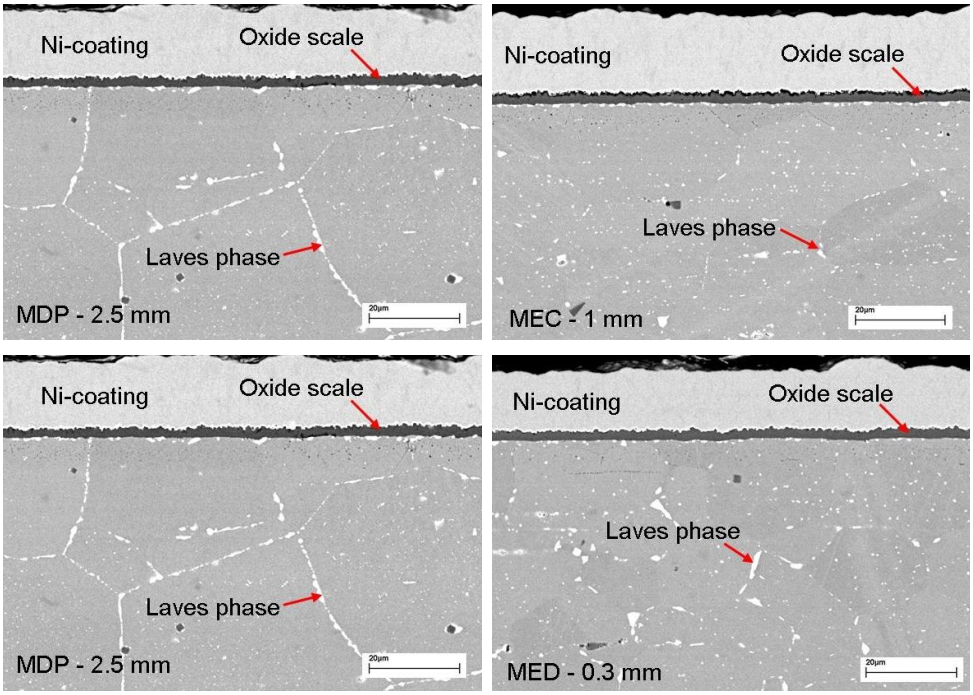

Figure 5.105: SEM/BSE images showing cross sections of oxide scales on Crofer 22 H (different specimen thickness) after 1000 h oxidation at 800 °C in air.

Based on literature data Zurek et al. [88, 134] proposed that a compressive oxide growth stress is initiated during growth of the chromia base surface scales, although the absolute values of the reported growth stress exhibit a large variation. This compressive stress affects the growth rate by decreasing the concentration and/or the rate of transport of diffusing ionic species in the oxide layer whereby this effect was assumed to be more likely due to an effect of stress on the concentration of point defects in the oxide than on the diffusion coefficient of the ionic species [88].

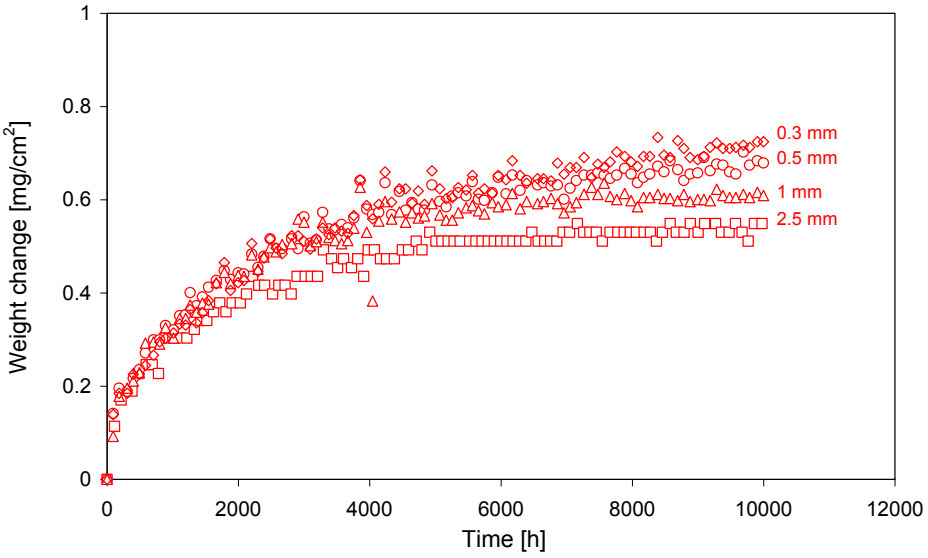

Figure 5.106: Weight changes during discontinuous oxidation of Crofer 22 H (batch MDP-2.5 mm; MEC-1 mm; MDT-0.5 mm; MED-0.3 mm)) for 10 000 h at 800 °C in Ar-4 % H_2-20 % H_2O showing effect of specimen thickness.

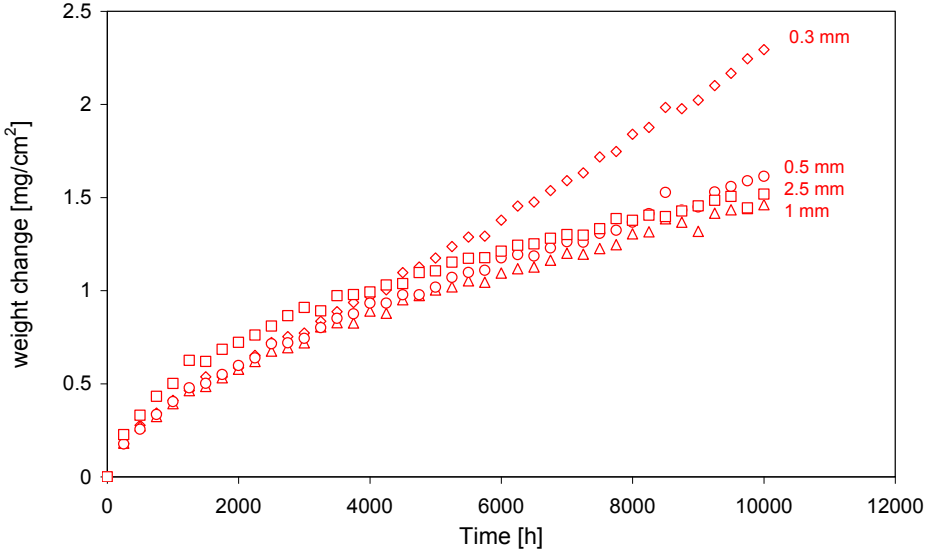

Figure 5.107: Weight changes as function of time during discontinuous oxidation of Crofer 22 H (batch MDP-2.5 mm; MEC-1 mm; MDT-0.5 mm; MED-0.3 mm) during 10 000 h oxidation at 800 °C in air showing effect of specimen thickness.

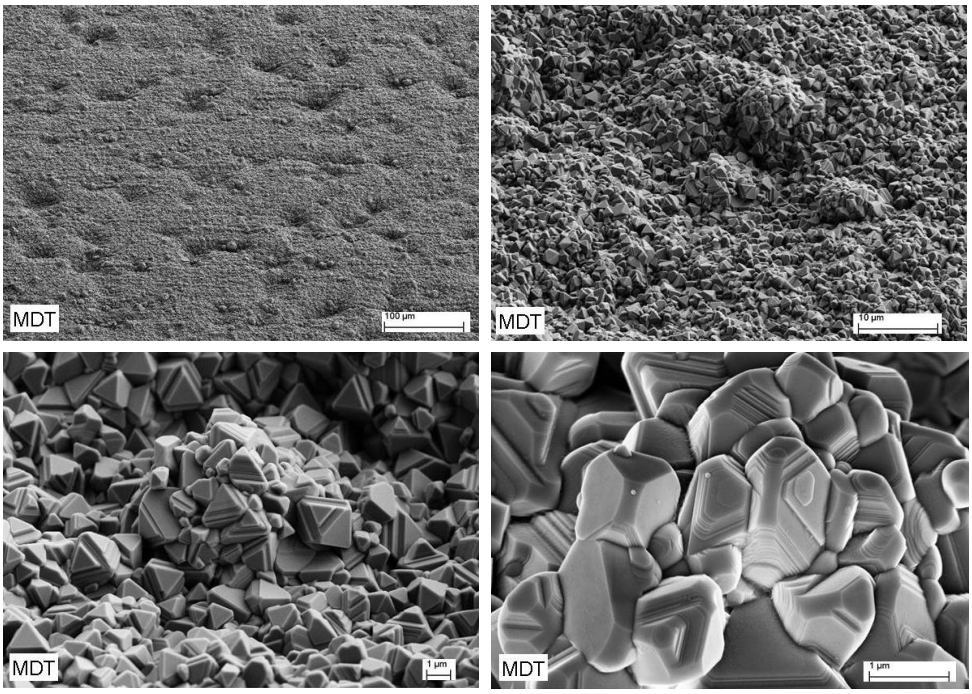

Figure 5.108: Surface morphology of oxide scale formed on steel Crofer 22H (batch MDT-0.5 mm) during 10 000 h oxidation at 800 °C in air.

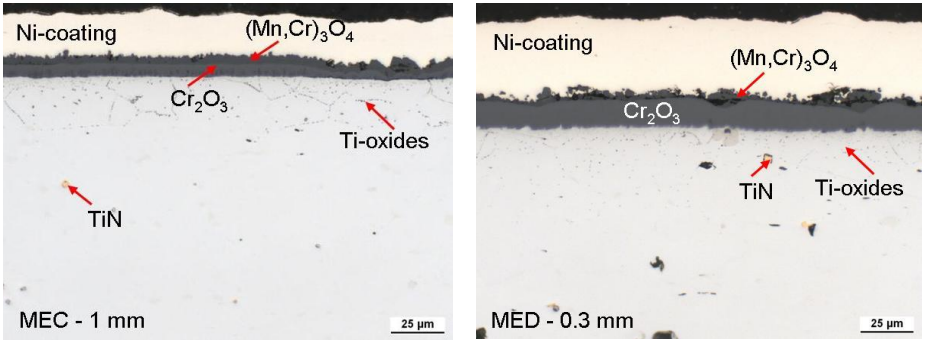

Figure 5.109: Optical micrographs showing cross sections of oxide scales on Crofer 22 H after 10 000 h oxidation at 800 °C in air, illustrating effect of specimen thickness on oxide scale formation.

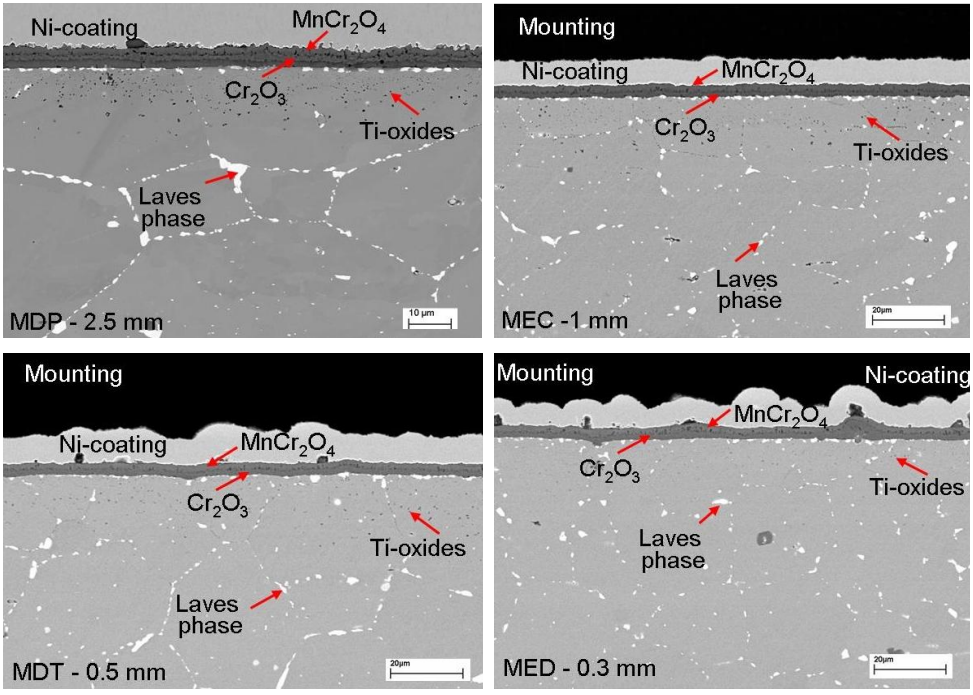

Figure 5.110: SEM images of cross sections of oxide scales on Crofer 22 H (batch MDP, MEC, MDT, MED) after 10000 h oxidation at 800 °C in Ar-4 % H_2-20 % H_2O showing oxide scale formation on specimens of different thickness (mark differences in magnification)

In the case of an oxide under a biaxial compressive stress σ_{xx}, the diffusivity may be written as [88, 139]

$$D = A\exp\left(\frac{\Delta S^*}{R}\right)\exp\left(\frac{-\Delta H^*}{RT}\right)\exp\left(\frac{\frac{2}{3}\Delta V^*\sigma_{xx}}{RT}\right) \tag{5.3}$$

where ΔH^* and ΔS^* are the activation enthalpy and entropy respectively; ΔV^* is the activation volume and A is a pre-exponential constant. Additionally, there is the possibility of a stress gradient over the oxide scale. In these cases both cations and anions are transported from regions where the stress is compressive to regions where the stress is tensile resulting in a net transport of oxide into the tensile regions. The creep rate is determined by the rate of diffusion of the slower ion. However, in the case of oxidation

the rate is controlled by the faster diffusing ion. If, for example, the oxide ions are the slower species and move by oxygen vacancies, the effect of the stress is to increase the vacancy concentration in the tensile regions and decrease it in the compressive regions according to:

$$C_V = C_V^o \exp\left(\frac{\sigma_h \Delta V^F}{RT}\right) \tag{5.4}$$

where C_V^o is the equilibrium concentration of vacancies in the unstressed state and ΔV^F is the volume change associated with the formation of the relevant point defect. Based on results in reference [88] the effect of stress on the diffusion processes in the scale seems to be more related to the stress-dependent defect concentration than to diffusivity [88]. Thus, based on these theoretical considerations, Zurek et al. [88, 134] proposed that differences in growth stress relief by plastic deformation of the thick and thin metallic substrate are responsible for the differences in oxidation kinetics. Asuming growth stress in anode gas side scales to differ from that in air formed oxides, this also explains the observation that the specimen thickness dependence of the oxidation rate depends on the atmosphere, for instance, it is far less pronounced in anode than in cathode gas [85]. The explanation would imply that an increase in creep strength of the ferritic steel may be a solution to decrease the tendency that the oxidation rate increases with decreasing component thickness (Figure 5.111) as actually experimentally observed in the present studies.

This assumption will now be used to explain the experimental observations described in the previous section.

A compressive growth stress (σ_{ox}) which is built-up in the oxide scale will generate a tensile stress (σ_M) in the metallic substrate

$$\sigma_M = 2\sigma_{ox} \cdot \frac{x}{d} \tag{5.5}$$

where x is the thickness of the oxide layer formed on both sides of a flat substrate of thickness d. Consider as example an oxide formed on a thick and a thin specimen of a given alloy whereby it is assumed for simplicity that at a given time the oxide thicknesses and the growth stresses in the oxide layers are independent of the specimen thickness.

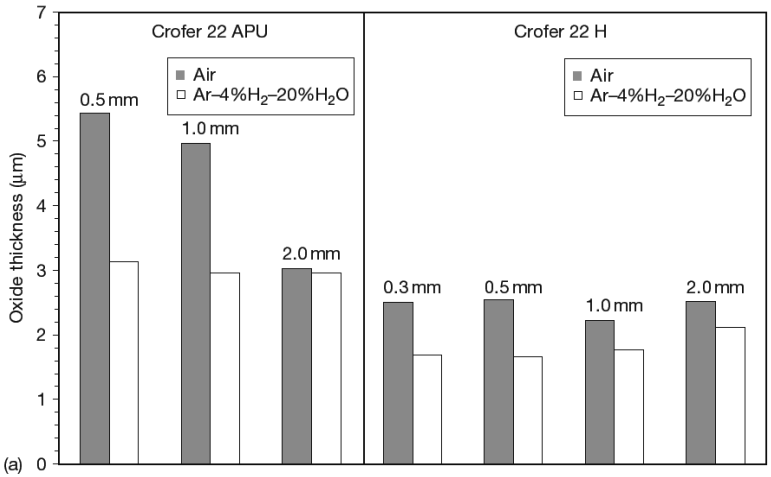

Figure 5.111*:* Oxide thicknesses on Crofer 22 APU and Crofer 22 H after 1000 h discontinuous oxidation at 800 °C in different atmospheres [79].

The tensile stress in the thin metallic substrate will then, due to equation 5.5, be larger than that in the thick specimen. Consequently, the creep rate induced in the metallic substrate will be higher in the thin than in the thick specimen. We assume in first approximation a power law stress dependence of the creep rate in the metal on the applied stress as described in section 2.15.1 [140],

$$\frac{d\varepsilon}{dt} = k \cdot \sigma_M{}^n \tag{5.6}$$

Here ε is the creep strain, k is for a given alloy at a given temperature a constant and n is the creep exponent commonly used when describing an exponential stress dependence of the secondary creep rate by Norton's law [140].

The (secondary) creep rate in the metallic substrate due to the induced tensile stress caused by the compressive growth stress in the oxide can then be described as

$$\frac{d\varepsilon}{dt} = k\left(2\sigma_{ox} \cdot \frac{x}{d}\right)^n \tag{5.7}$$

It is apparent, that a substantial decrease of growth stress will only occur if the creep rate of the metallic substrate exceeds a certain minimum value [141-142], because at very low creep rates the build-up of growth stress is expected to be faster than its relaxation by creep deformation of the metallic substrate.

It is at present not possible to give exact quantitative numbers related to these processes. The literature data [88] on growth stresses in chromia base surface scales vary from high values in the GPa range down to values of less than 100 MPa. A similar variation in the growth stresses was also observed in oxide scales on e.g. TiAl alloys [143]. This large variation in growth stress data may be related to the fact that differences in stress relaxation effects in thin and thick specimens might have affected the reported growth stress results. Additionally, the build-up of growth stresses in the oxide scales is governed by the transport processes in the oxide which are known to be strongly affected by minor alloying elements and impurities, especially oxygen active elements. The build-up of oxide growth stress will thus likely differ from alloy to alloy and is likely affected by the atmosphere. The following treatment can thus only describe the possible processes in respect to specimen thickness dependence of the oxidation rates in a qualitative rather than a quantitative manner.

Consider two specimens of alloy Crofer 22 APU with different thicknesses (d_1 and d_2). For a given oxide thickness with corresponding growth stress on both specimens, the creep rate in the substrate will, due to equation 5.7, differ by a factor $(d_1/d_2)^n$. In recent studies with Crofer 22 APU [91] n was found to be in the range 4-8 and consequently minor changes in specimen thickness will, for a given oxide growth stress, result in substantial changes in creep rate in specimen of different thickness. For instance, a

reduction in specimen thickness and growth stress by a factor of two will, for a given oxide thickness result in an increase of the creep rate by a factor of 2^4 - 2^8.

Figure 5.112 schematically illustrates the effect of specimen thickness on creep rate (in arbitrary units) in the metallic substrate for a given constant oxide growth stress at constant temperature for Crofer 22 APU and H assuming for the creep exponent n=6. For qualitatively explaining the effect of specimen thickness on growth stress relaxation, it is arbitrarily assumed that the critical creep rate of the metallic substrate for obtaining substantial growth stress relaxation to be 0.1 (indicated by the green arrow in Figure 5.112).

For the chosen values, substantial growth stress relaxation would neither for Crofer 22 APU nor for Crofer 22 H occur in case of a specimen with a thickness of 2 mm. For Crofer 22 APU substantial growth stress relaxation would occur if the specimen thickness is decreased beneath approximately 1 mm. So, if the above considerations concerning the specimen thickness dependence of the oxidation rate are correct, Crofer 22 APU should start to exhibit enhanced oxidation rates if the specimen thickness is thinner than approximately 1 mm, as experimentally observed during early stages of exposure (Figure 5.104).

For Crofer 22 H no effect of specimen thickness on the oxidation rate should be observed, even if the thickness would be as low as 0.3 mm. However, during long term exposure at 800 °C, the Laves phase coarsening will result in a decrease of the intrinsic creep strength of the steel [91], resulting in a gradual shift of the red line in Figure 5.112 as indicated by the red arrows. If the precipitate coarsening after a given oxidation time would have increased the k-value in equation (5.7) e.g. by a factor of 10, then an effect of specimen thickness on oxidation should start to occur for specimens with a thickness of less than 0.4 mm.

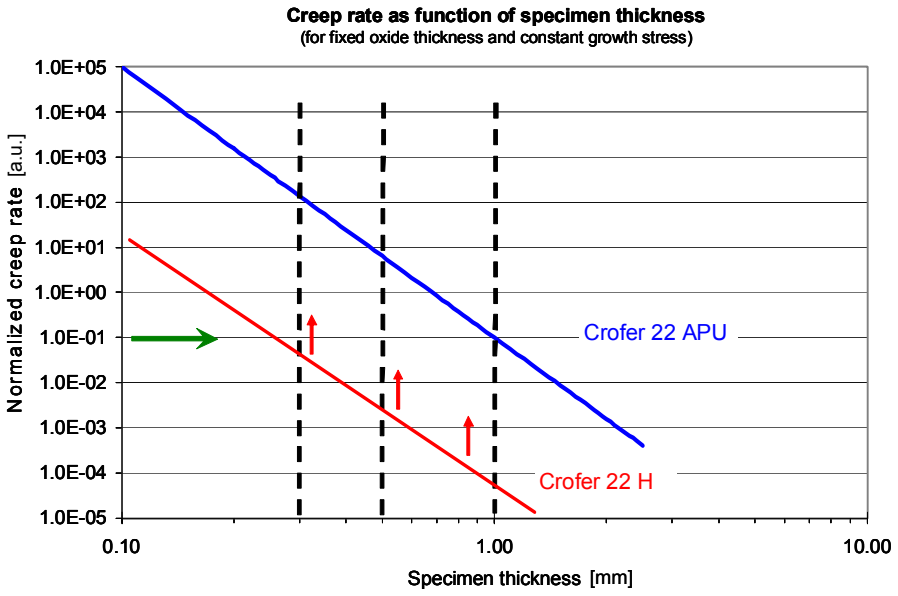

Figure 5.112: Schematic illustration showing semi-quantitative effect of specimen thickness on creep rate (in arbitrary units) for a given constant oxide growth stress at constant temperature for two materials (Crofer 22 APU and H) with different intrinsic creep strength (assuming for the creep exponent n=6). Green arrow indicates arbitrary chosen minimum creep rate required for obtaining substantial growth stress relaxation by creep of the metallic substrate. Red arrows indicate effect of decrease in steel creep strength as a result of precipitate coarsening.

Clear indications for a substantial loss in creep strength of Crofer 22 H as a result of precipitate coarsening were obtained by Kuhn et al. [91] confirmed by recent studies of Chiu et al. [144]. During constant load creep testing at 800 °C Crofer 22 H did not exhibit a classical time period in which a constant secondary creep rate is observed. Rather, a slow, continuous increase in creep rate was found after initial establishment of a very low minimum creep rate. The gradual increase of the secondary creep rate might be described by a k-value in the power law creep equation (5.5) which increases with increasing exposure time. At 800 °C and an applied load of 7 MPa the creep rate between 1000 h and 10 000 h was found to increase by a factor of 10 to 100 [91]. Newer results revealed that pre-ageing at 900 °C substantially decreased the creep strength of Crofer 22 H (see Figure 113)

The semi-quantitative treatment illustrated by Figure 5.112 explains the main experimental findings described in the previous sections for the air exposure tests:

- Already during the early stages of exposure, Crofer 22 APU exhibits a clear effect of specimen thickness on the oxidation rate when using specimens with a thickness range between 0.5 and 2.5 mm (Figure 5.104).
- Crofer 22 H does not show this effect up to exposure times of at least 3000 h, even if the specimen thickness is decreased to 0.3 mm (Figure 5.107).
- The 0.3 mm specimen of Crofer 22 H starts to exhibit an increased oxidation rate after approximately 3500 h.

The weight change curves for Crofer 22 H specimens of different thickness (Figure 5.108) can be explained by the fact that initially the creep strength of Crofer 22 H at 800 °C is sufficiently high to prevent establishment of a critical creep rate of the metallic substrate required to induce substantial growth stress relaxation, even for the thinnest specimen of 0.3 mm. The gradual decrease in creep strength as a result of precipitate coarsening has as consequence, that after a given exposure time (apparently approximately 3500 h, Figure 5.107) the creep rate in the thinnest specimen of 0.3 mm becomes sufficiently high for significant growth stress relaxation to occur, resulting in an increase of the oxide growth rate.

The above considerations can for a number of reasons only give a semi-quantitative description of the actually prevailing mechanism. First, because of the above mentioned lack of experimental data on growth stresses in chromia scales and, second because a number of simplifying assumptions are being made in the considerations:

- The creep induced in the metallic substrate as a result of oxide growth stress is being described by equation (5.7) which was formulated to treat secondary (or steady state) creep. In the prevailing case, the creep processes in the metallic substrate will, however not solely be related to secondary creep processes.
- The growth stress is in reality not a constant value but is likely to be time dependent [142].

- The tensile stress generated in the metallic substrate is not constant over the whole specimen thickness. Rather, a stress gradient establishes from the scale/alloy interface towards the specimen centre. The stress is also influenced by the fact that the scale/alloy interface is not ideally flat.

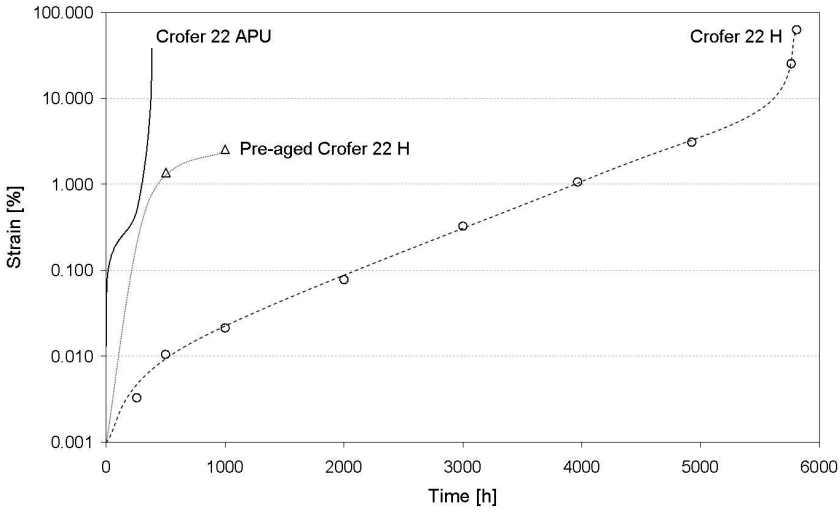

Figure 5.113: Strain versus time for solution annealed and pre-aged (500 h, 900 °C) Crofer 22 H during creep test at 800 °C at an applied stress of 10MPa. Data are compared with results of Crofer 22 APU. The test for the latter material and that of solution annealed Crofer 22 H was extended till occurrence of rupture. The data points of the aged Crofer 22 H specimen relate to an ongoing experiment. (Creep experiments carried out by B. Kuhn, Forschungzentrum Jülich, 2011)

It is, however, believed that these simplifying assumptions affect the above considerations in a quantitative but not a qualitative manner.

An interesting observation is that, a specimen thickness dependence of the oxidation rate is virtually absent during exposure in the simulated anode gas, even for the thinnest specimens of Crofer 22 APU (Figure 5.111). An obvious reason might be that the oxide scales formed in this gas are thinner than those formed during air oxidation (Figure 5.111). For a given exposure time and prevailing growth stress the tensile stress initiated in the metallic substrate (Equation 5.7) would thus be smaller in case of the simulated

anode gas than during air exposure. However, using the measured oxidation data in Figure 5.107 in combination with the approach used above reveals that in case of the thinnest specimens of Crofer 22 APU a thickness dependence of the oxidation rate should occur, although less pronounced than in air, after long term exposure. Observations concerning chromia growth on pure chromium [129], NiCr alloys [88] and ferritic steels [18] lead to the conclusion that the growth mechanism as well as the microstructure of chromia scales formed in air substantially differ from those in simulated anode gas. Therefore it is quite likely that the growth stresses in the latter oxide scales substantially differ from those in air formed chromia base oxide scales. In case of the Crofer type materials an additional source for differences in growth stresses are possibly the different compositions of the Cr/Mn-spinel type oxide in the two environments, as discussed in section 5.2.

A further parameter which may affect the oxide scale formation, is the generation and relaxation of thermally induced stresses upon heating and cooling during a long term, discontinuous oxidation test. Cooling from oxidation temperature will in case of the investigated ferritic steels result in initiation of a compressive stress in the oxide and a tensile stress in the metallic substrate. It has been shown for various alloy types, that the stress may partly be relaxed during the cooling process by creep of the metallic substrate [145-146]. The thermal stress in oxide and substrate are thus lower than the values calculated assuming full elastic materials behaviour. For a given oxide thickness, the tensile stress in the metallic substrate, will increase with decreasing specimen thickness. Additionally, the creep relaxation is expected to be more substantial in a thin than in a thick specimen. During subsequent heating this phenomenon will for a short time result in initiation of a tensile stress in the oxide scale initiating microcrack formation in the scale, resulting in access of gas molecules leading enhanced oxidation. Due to the above considerations related to reference [86, 137, 147], the enhanced oxidation would be expected to be more pronounced in specimens with a poor resistance against creep, i.e. due to a limited thickness and/or low intrinsic creep strength of the alloy.

Important to mention that these considerations are only applicable if the oxide exhibits perfect adherence to the metallic substrate. If this would not be the case, the thermal stress initiated in the oxide during cooling are expected to be relaxed by cracking and/or spallation. The mechanisms which determine the spallation behaviour of oxide scales and models describing this behaviour have been discussed by several authors [141, 148-149].

5.5.4 Effect of pre-ageing on specimen thickness dependence of oxidation rates

The above considerations provide a suitable explanation for the differences in specimen thickness dependence of the air oxidation rates for the steels Crofer 22 APU and Crofer 22 H, i.e. the different behaviour is related to differences in intrinsic creep strength of the two steels. This being a suitable explanation, it is, however, not an unequivocal proof that the specimen thickness dependence of the oxidation rate finds its cause in growth stress relaxation by substrate creep. The oxide scales formed on Crofer 22 APU and H are very similar but are certainly not 100 % identical. Very small amounts of the minor alloying additions (Nb, Si, W) in Crofer 22 H might become incorporated into the oxide scale and modify e.g. the defect structure of the chromia and/or the spinel phase. Differences in depletion of these elements in the subscale layer of thin and thick specimens might lead to different effects of specimen thickness on oxide growth rate compared to the case of the near single phase alloy Crofer 22 APU. Also, the tendency for Laves phase enrichment at the scale/alloy interface (section 5.5.3) might somehow affect the differences in behaviour between Crofer 22 APU and H. An unequivocal test of the above theory could thus only be obtained if a single material would prevail in form of batches with different creep strength. Then, a possible effect of alloy composition differences on the specimen thickness dependence of the oxidation rate could be ruled out.

An attempt was made to obtain these experimental starting conditions in the following additional experimental procedure:

A commercial batch of Crofer 22 H (designation NEC) was used as test material (see composition in section 4.1 and 5.5.2). Different from the previously used batches, this material prevailed in form of a 16 mm thick plate. Three pieces (approximately 200 x 50 mm) were cut from the large plate. From the first piece common rectangular specimens (20 x 10 mm) with a thickness of 0.25, 0.5, 1 and 2 mm were prepared using spark erosion, in a similar manner as described in section 4. The second piece was exposed in an evacuated quartz capsule for 500 h at 900 °C, the third piece for 2000 h at 800 °C. Aim of these two heat treatments was to enhance Laves phase formation and especially coarsening prior to the actual, subsequent oxidation test. Specimens with thicknesses of 0.25, 0.5, 1 and 2 mm were cut from the centre part of the two pieces after the heat treatments at 800 and 900 °C respectively. In this way, samples of one and the same batch of Crofer 22 H were obtained which possess identical chemical composition and are not affected by oxidation induced subsurface depletion processes during the ageing treatment. However, the samples made from the three different pieces differ in strength due to different states of Laves phase precipitation and coarsening. The specimens obtained in this way were ground and degreased in the same way as described for other oxidation tests, i.e. as described in section 4. Subsequently, specimens from the three heat treatment variants were exposed at 800 °C in laboratory air, whereby all specimens were present in the same furnace at the same time. This prevented possible effects of very minor variations in experimental parameters (e.g. moisture content in laboratory air) on the actual results. The oxidation tests were discontinuous, i.e. every 200 h the specimens were cooled to room temperature with 2 °C per minute for weight measurements. The aim of this slow cooling was to reduce a possible influence of thermal mismatch stresses between metallic substrate and oxide scale caused by rapid heating and/or cooling.

Figure 5.114 shows weight change data of the non-aged specimens of the Crofer 22 H batch NEC during air exposure at 800 °C up to 2000 h. The data show excellent reproducibility between the four test specimens, i.e. the specimen thickness does not have an effect on the oxidation rates in agreement with the observations for the other Crofer 22 H batches (see section 5.5.2) up to the exposure time of 2000 h.

Commonly oxidation kinetics can suitably be described by a parabolic time dependence of the oxide scale thickening (see section 2.9.2). This is related to the fact that, if solid state diffusion in the scale is the rate determining step for the oxide scale growth, the increase rate of the scale thickness at a given time is inversely proportional to the prevailing oxide thickness.

In terms of area specific weight gain (Δm e.g. in mg cm^{-2}) the parabolic oxidation kinetics can (as already explained in section 2.9.2) be expressed as

$$(\Delta m)^2 = K_w \cdot t + C' \tag{5.8}$$

in which K_w is the parabolic rate constant. If C'=0, the equation can be written in its most simple form, i.e.

$$(\Delta m)^2 = K_w \cdot t \tag{5.9}$$

The rate constant K_w is commonly derived by differentiation of plots of $(\Delta m)^2$ as function of t or Δm as function of $t^{1/2}$ [35]. If C'=0, then both ways of plotting reveal the same value of K_w. If C' does not equal 0, then the K_w values determined by the two methods are not identical [35]. This situation prevails if e.g. the actual parabolic oxidation on a chromia forming alloy is preceded by a transient oxidation stage in which the base metal oxides substantially affect the overall oxidation process [35].

Figures 5.114-116 show plots of the weight change data of the non-aged NEC specimens as function of $t^{1/2}$ as well as a plot of $(\Delta m)^2$ as function of t. Both ways of plotting reveal that the gravimetric data can with very reasonable accuracy be described by a parabolic oxidation over the whole time period. The K_w values determined by the two methods for the various specimens show only very minor differences thus indicating that the value of C' in equation 5.8 is close to zero.

Figures 5.117-118 show the measured weight changes during oxidation up to 2000 h of the specimens manufactured from the pre-aged Crofer 22 H (batch NEC) compared with those for the non-aged material. The data shows that for the materials after both ageing treatments the weight changes are already during quite short oxidation times of a few hundred hours slighly higher than those of the non-aged material. For both pre-aged materials the weight changes of the thinnest specimens of 0.25 and 0.5 mm are, within the accuracy and reproducibility of measurement, higher than those of the specimens of 1 and 2 mm thickness. This is especially the case for the specimens which were pre-aged at 900 °C.

After these findings, it was decided to extend the exposures for the pre-aged NEC specimens. From the non-aged materials only the exposure of the thinnest specimen (0.25 mm) was extended because no increased oxidation rates of the thicker specimens would be expected, based on the results for the experiments with the Crofer 22 H batches MEC, MED and MDP shown in the previous section (Figure 5.107).

Figures 5.119 and 5.120 show plots of $(\Delta m)^2$ as function of time for the NEC specimens including the data obtained during extended exposure up to 4000 h. This way of data presentation illustrates that the data for the thick specimens (1-2.5 mm) can with reasonable accuracy be fitted by straight lines thus indicating that the oxidation kinetics exhibit a near parabolic time dependence of the scale thickness.

Comparing extrapolated parabolic oxidation data with the actually measured results illustrate, that the 0.25 mm specimen of the non-aged Crofer 22 H batch NEC starts to exhibit a clear deviation from parabolic behaviour, i.e. an enhanced oxidation rate, after approximately 2500 h exposure (Figures 5.119-120). This is a shorter time than that observed for the 0.3 mm specimen of the Crofer 22 H batch MED discussed in the previous section, where start of an enhanced oxidation rate was found after approximately 3500 h (Figure 5.107).

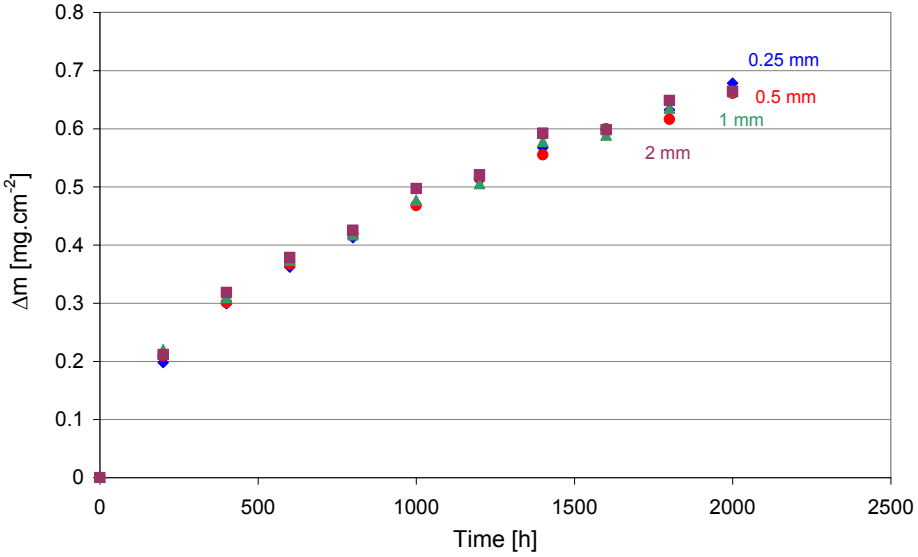

Figure 5.114: Weight change data of non-aged Crofer 22 H batch NEC during 800 °C air oxidation up to 2000 h, showing effect of specimen thickness on oxidation.

If the 10 000 h data presented in the previous section (Figure 5.107) are also plotted in form of $(\Delta m)^2$ as function of time (Figure 5.121), it is found that the data for the thick specimens (1 and 2.5 mm) can over the whole test period with reasonable accuracy be described by a parabolic time dependence of the scale thickness. The absolute values of K_w only slightly differ from those derived for batch NEC (Figures 5.114-116). This way of plotting clearly confirms that the specimen with a thickness of 0.3 mm starts to exhibit enhanced oxidation after approximately 3500 h, as already seen from the linear plots of Δm as function of t (Figure 5.107). The plot of $(\Delta m)^2$ as function of time (Figure 5.121) indicates that also the 0.5 mm specimen starts to exhibit enhanced oxidation after approximately 6000 h, whereby exact determination of this time is hampered by the limitations in accuracy and reproducibility of measurement.

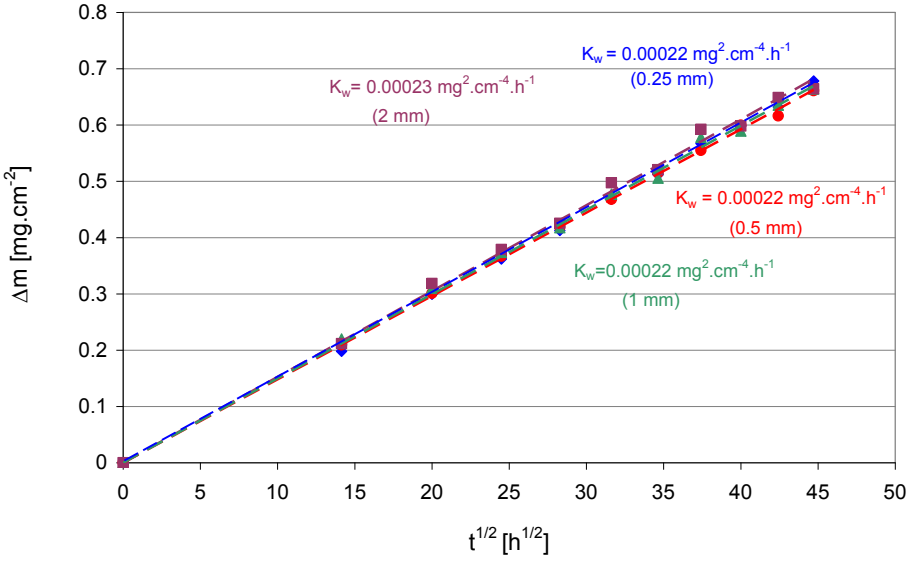

Figure 5.115: Weight change data from figure 5.98 (non-aged Crofer 22 H batch NEC during 800 °C air oxidation up to 2000 h), plotted as Δm ($t^{1/2}$) showing K_w (in $mg^2.cm^{-4}.h^{-1}$) values for specimens of different thickness.

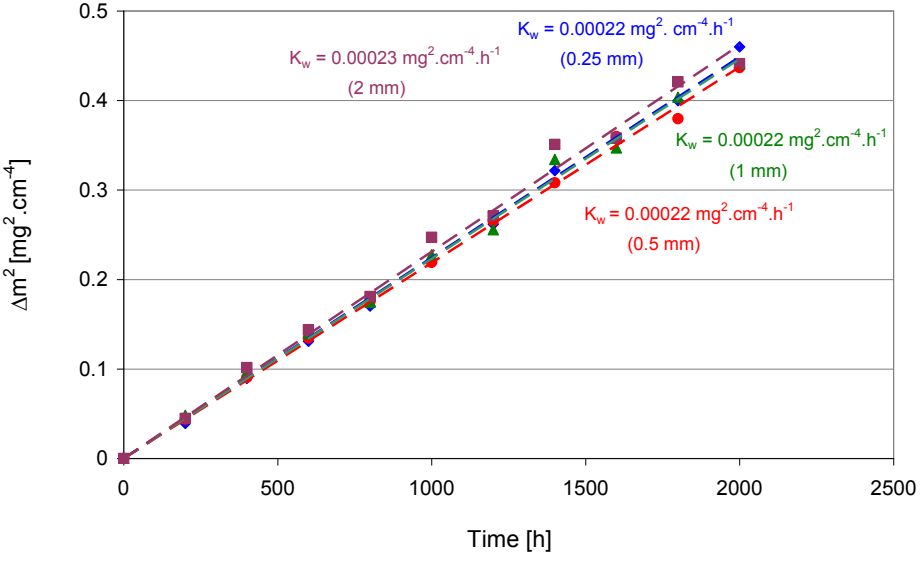

Figure 5.116: Weight change data from figure 5.108 (non-aged Crofer 22 H batch NEC during 800 °C air oxidation up to 2000 h, plotted as Δm^2 (t) showing K_w (in $mg^2.cm^{-4}.h^{-1}$) values for specimens of different thickness.

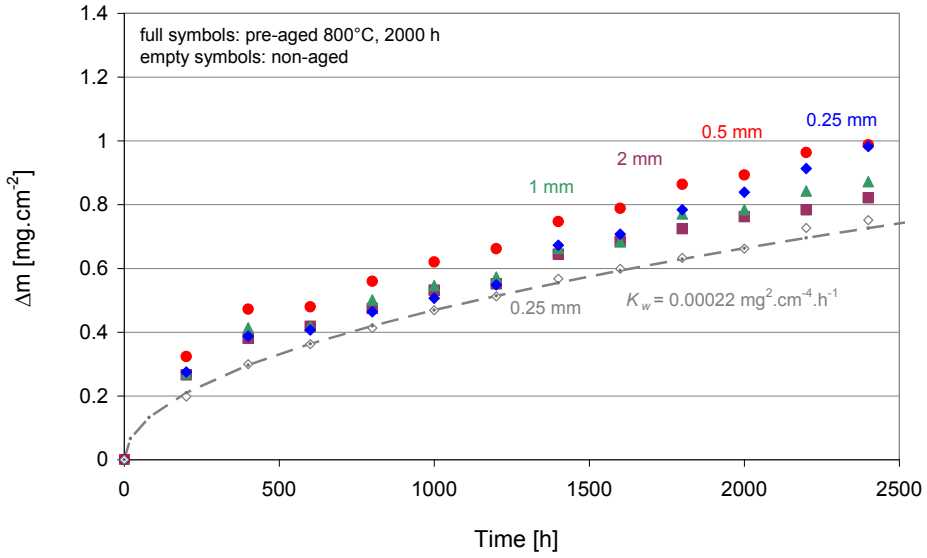

Figure 5.117: Weight change data of pre-aged (800 °C, 2000 h) Crofer 22 H batch NEC during 800 °C air oxidation up to 2000 h, showing effect of specimen thickness on oxidation. The data are compared with the thinnest specimen of the non-aged material (see Figure 5.114). Also inserted is a calculated weight change curve assuming parabolic oxidation using the K_w value derived in Figures 5.115 and 5.116 for the non-aged material.

Due to the limited accuracy of the experimental weight change data the exact times at which the enhanced oxidation occurs is subject to substantial error. However, the data in Figures 5.119-120 comparing the results for batch NEC in the as-received condition with that of pre-aged samples clearly show that:

1) for the samples pre-aged at 800 or 900 °C the weight changes are already during short term oxidation slightly higher than those for the non-aged samples,
2) For the aged samples the oxidation rates for the thin specimens are higher than those of the thick ones. The time at which enhanced oxidation rates (i.e. clear deviation from parabolic behaviour) are observed for the thin samples (0.5 and especially 0.25 mm) is substantially shorter than that observed for the non-aged samples.

The first mentioned observation may be related to the fact that the oxides formed in the early stages of oxidation on the various materials are not completely identical. The non-

aged material is upon start of the oxidation process single phase and it is therefore expected that already after quite short oxidation times the oxide consists of a laterally homogeneous layer, mainly consisting of Cr-oxide and Cr/Mn-spinel (see section 5.2). The aged materials will logically contain (coarse) precipitates of Nb-rich Laves phase. In the early stages of oxidation it is expected that this material will, next to the chromia/spinel layer, locally form Nb-rich oxide nodules [150]. These will not dominate the oxidation process during longer term exposure, however they are expected to result in a "doping" of the transient oxide scale e.g. with niobium, an element which was shown [9] to enhance chromia growth. This may be a possible explanation for the observation that all aged specimens, also the thicker ones, show already during short term oxidation of a few hundred hours slightly higher oxidation rates than the non-aged material.

The above mentioned second finding, i.e. gradually enhancing oxidation rates during long term exposure of the thinnest aged samples, cannot only be explained by this effect. The ageing treatment at 800 and 900 °C and the subsequent specimen preparation was accomplished in such a way that the various specimens shown in Figures 5.119-120 did not differ in (subsurface) chemical composition. The above mentioned oxidation of Laves phase in aged materials will be limited to the very early stages of oxidation and will not differ for thick and thin specimens.However, the steady increase of the oxidation rate after an initial stage of near-parabolic oxidation starts to occur after long time exposure in the range of a few thousand hours. Thereby the time for the onset of the effect decreases with decreasing specimen thickness and it is shorter for aged than for non-aged specimens. Figure 5.121 shows the cross sections of oxide scales on non-aged Crofer 22 H (batch NEC-0.25 mm) during 800 °C air oxidation up to 4000 h. More Laves phase precipitates beneath the oxide scale appear to be present in case of non-aged Crofer 22 H (Figure 5.123) than in pre-aged samples (Figures 5.124 and 5.125).

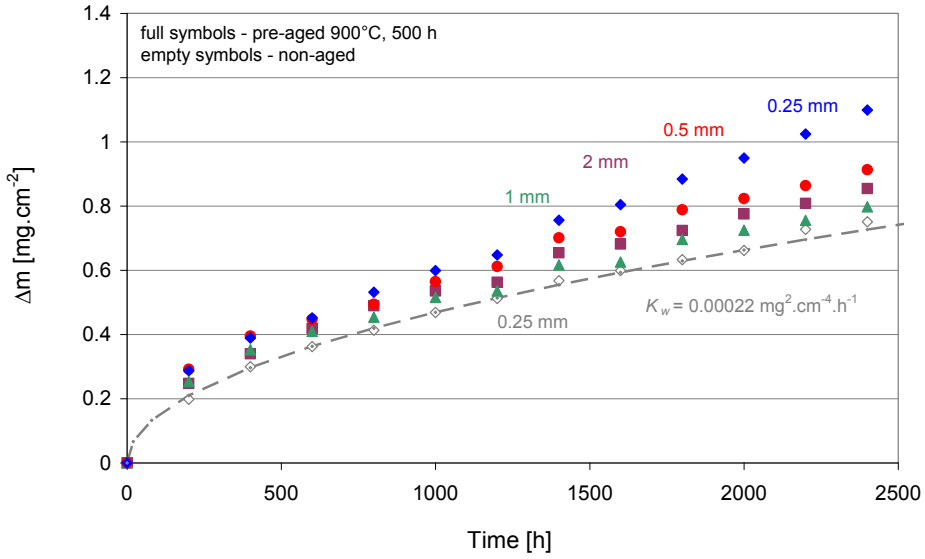

Figure 5.118: Weight change data of pre-aged (900 °C, 500 h) Crofer 22 H batch NEC during 800 °C air oxidation up to 2000 h, showing effect of specimen thickness on oxidation. The data are compared with the results obtained for the thinnest specimen (0.25 mm) of the non-aged material (see Figure 5.114). Also inserted is a calculated weight change curve assuming parabolic oxidation using the K_w value derived in Figures 5.115 and 5.116 for the non-aged material.

In some cases cracks are generated by presence of stress in the oxide scale (Figures 5.123-125) and in some cases, as in Figure 5.125 for the sample of 2 mm thickness, some Mn-rich regions were found where due to cracks, the oxygen can penetrate the oxide scale and oxidize the Mn.

The cross sections in Figures 5.123-125 show that the different weight changes are really correlated with differences in scale thickness.

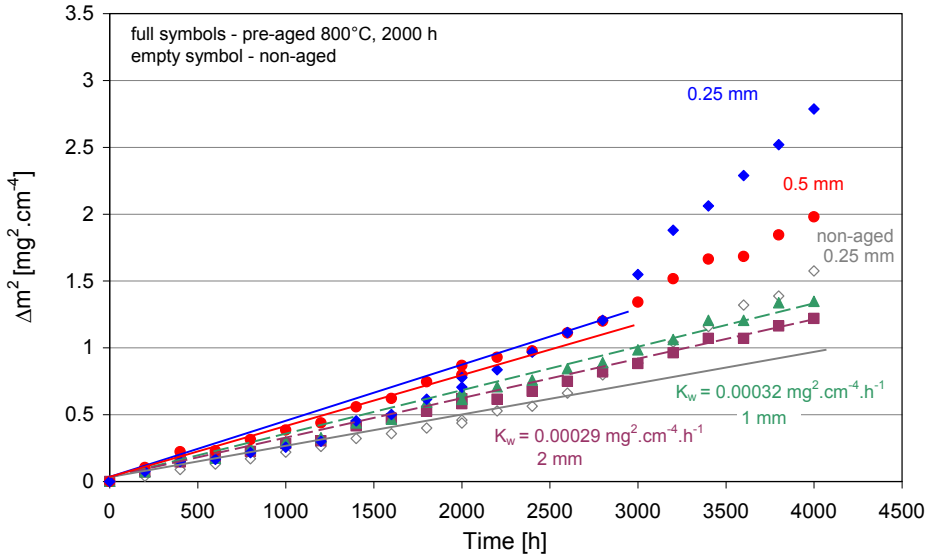

Figure 5.119: Weight change data plotted as $\Delta m^2(t)$ showing K_w values for different Crofer 22 H specimens, illustrating effect of specimen thickness on oxidation of pre-aged (800 °C, 2000 h) material of batch NEC. Data are compared with those for 0.25 mm specimen of non-aged material.

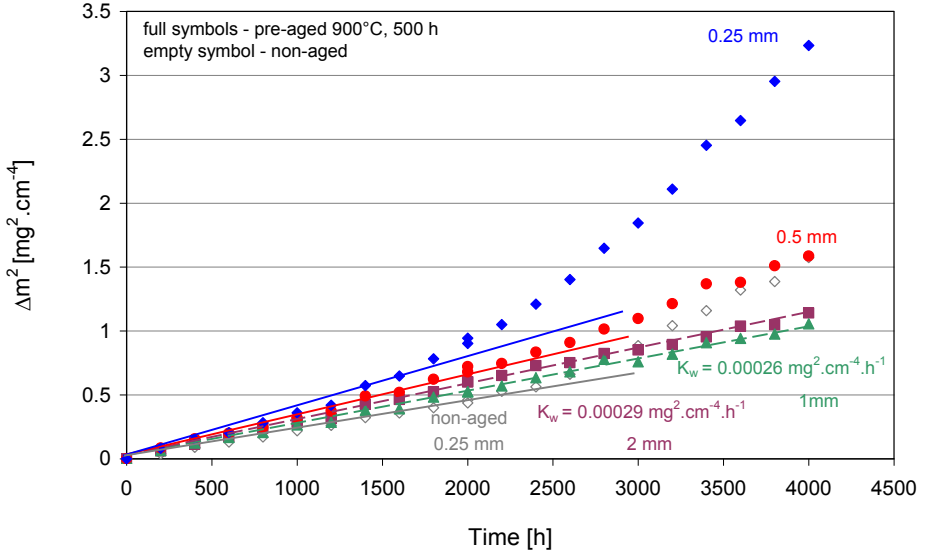

Figure 5.120: Weight change data plotted as $\Delta m^2(t)$ showing K_w values for different Crofer 22 H specimens, illustrating effect of specimen thickness on oxidation of pre-aged (900 °C, 500 h) material of batch NEC. Data are compared with those for 0.25 mm specimen of non-aged material.

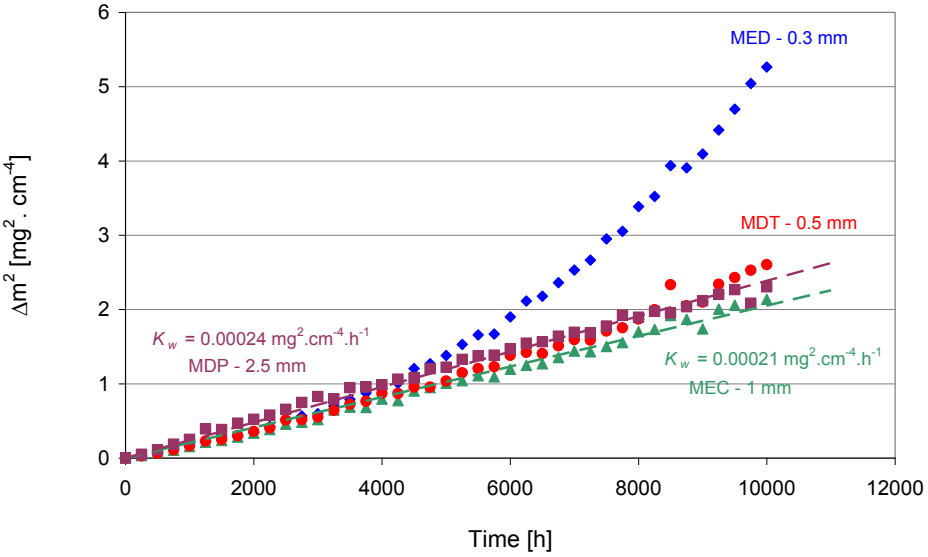

Figure 5.121: Weight change data from Figure 5.107 (non-aged Crofer 22 H batches MED-0.3 mm, MEC-1 mm, MDT-0.5 mm, MDP-2.5 mm;) plotted as $\Delta m^2(t)$ illustrating effect of specimen thickness on oxidation rates at 800 °C in air. Inserted are K_w values and fit lines derived fromr data of the two thickest specimens.

In conclusion it can be said, that, based on the experimental results and the theoretical considerations it can unequivocally be derived that the oxidation behaviour of chromia forming ferritic steels is affected by the creep resistance of the actual component. Differences in creep resistance of the component may be related to differences in component thickness and/or intrinsic creep properties of the prevailing alloy. This technologically important observation was shown to be likely related to relaxation of oxide growth stress by creep of the metallic substrate which results in an enhancement of the oxidation rate.

The critical creep rate required for obtaining substantial growth stress relaxation is, for a given oxide thickness and a given growth stress, more easily obtained with poor creep resistance of the metallic substrate. Poor creep strength can prevail because of the limited thickness of the substrate material and/or because of the poor intrinsic creep resistance of the alloy.

The latter is e.g. responsible for the fact that Crofer 22 APU specimens even with a substantial thickness of e.g. 1 mm may exhibit enhanced oxidation rates during air exposure at 800 °C already during the early stages of oxidation (see section 5.5.2). For the more creep resistant steel Crofer 22 H this is not the case. Even specimens of only 0.3 mm thickness of as-received material do at 800 °C not exhibit enhanced oxidation even up to exposure times of several thousand hours. Only if Laves phase coarsening, either during the actual oxidation experiment or during a pre-ageing treatment, has resulted in a substantial decrease in intrinsic creep strength of the alloy, the resistance of the thinnest samples (e.g. 0.25-0.5 mm) against substantial creep deformation becomes gradually too small to prevent substantial relaxation of oxide growth stress, resulting in enhanced oxidation rates.

The specimen thickness dependence of the oxidation rate does not occur during exposure in anode gas. This is partly caused by the slower oxidation rates compared to air exposure, but more important seems to be a lower oxide growth stress as a result of the different oxide microstructures [129]. The lower, or even non-existing growth stresses in anode gas formed oxide scales is confirmed by the observation [85, 129] that oxide scales formed on thick specimens in this type of gases exhibit a far smaller tendency to buckling than air grown oxides.

For a full confirmation of the above proposed mechanism, a further direct experimental method would be required to measure the differences in growth stress in oxides formed in air and simulated anode gas.

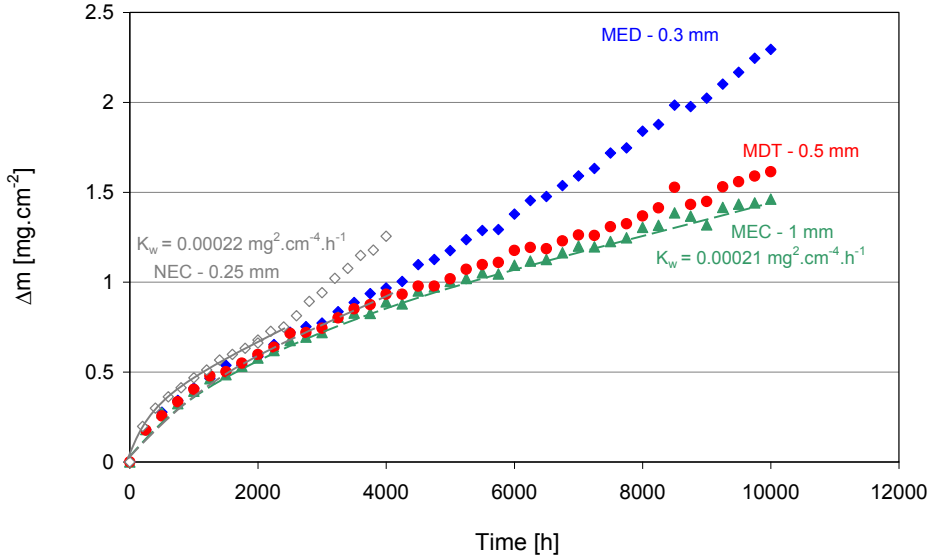

Figure 5.122: Comparison of oxidation behaviour of selected specimens of studied non-aged Crofer 22 H (batches MED-0.3 mm, MEC-1 mm, MDT-0.5 mm, MDP-2.5 mm) (data taken from Figures 5.107 and 5.119) at 800 °C in air. Inserted are calculated values assuming parabolic oxidation behaviour taking data given in Figures 5.117-119. The data illustrate earlier onset of enhanced oxidation for 0.25 mm thick specimen (batch NEC) compared to 0.3 mm specimen (batch MED, see Figure 5.107) and especially 0.5 mm specimen (MDT, see Figure 5.107).

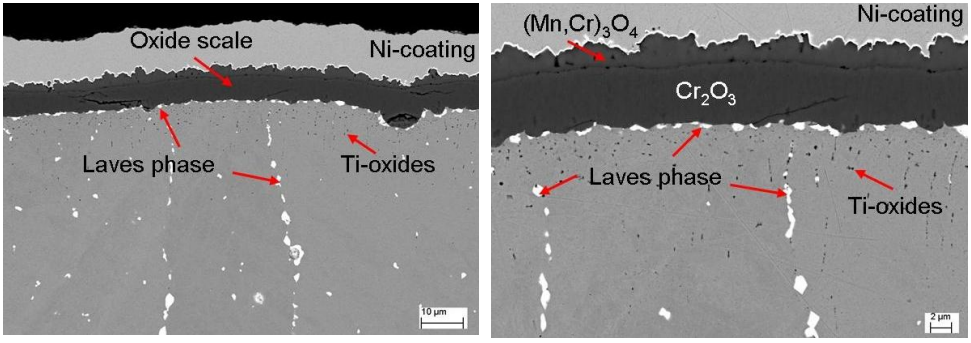

Figure 5.123: SEM images of cross sections of oxide scales on non-aged Crofer 22 H (batch NEC-0.25 mm) after 800 °C air oxidation up to 4000 h.

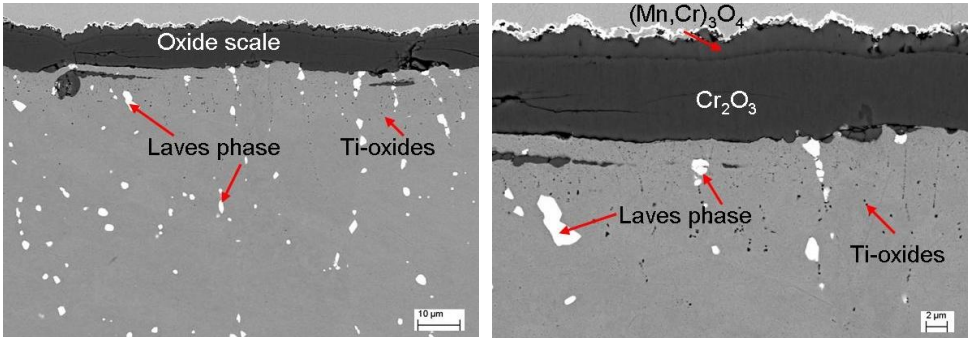

Figure 5.124: SEM images of cross sections of oxide scales on pre-aged (800 °C, 2000 h) Crofer 22 H (batch NEC-0.25 mm) after 800 °C air oxidation up to 4000 h.

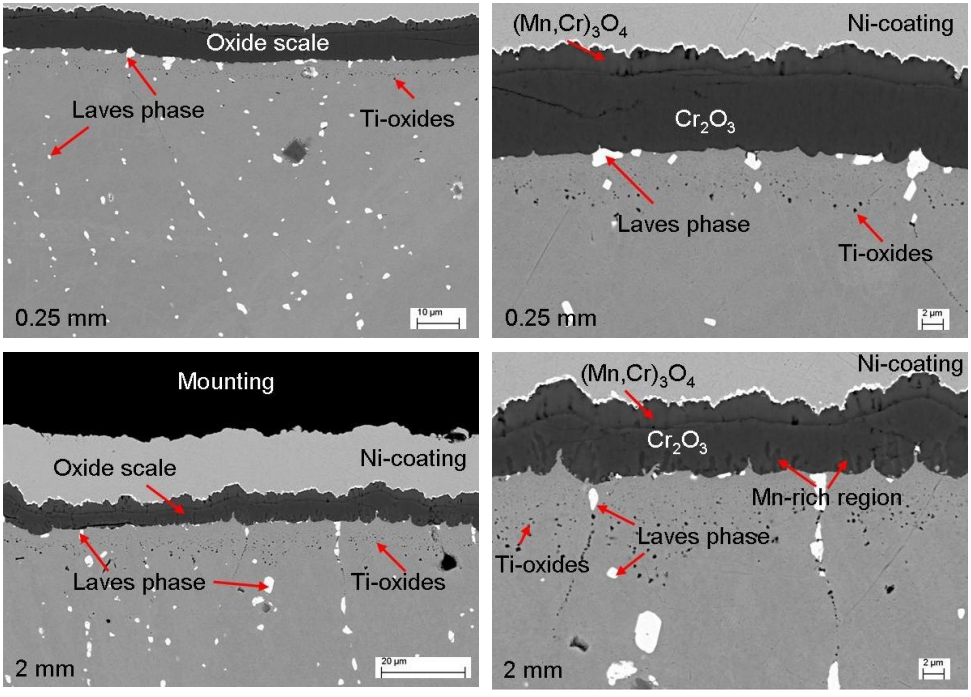

Figure 5.125: SEM images of cross sections on oxide scales on pre-aged (900 °C, 500 h) Crofer 22 H (batch NEC-2 mm and 0.25 mm) after 800 °C air oxidation up to 4000 h, showing effect of specimen thickness on oxidation.

5.6 Microstructure and oxidation behavior of niobium-free steels

5.6.1 Background of the investigations

Taking the composition of Crofer 22 APU as a basis, the development of Crofer 22 H was based on the following philosophy [9]:

- Addition of Nb (0.5 wt. %) for obtaining strengthening by Laves-phase precipitates of the type Fe_2Nb.
- Choosing an optimized Nb/Si-ratio to obtain a dissolution of Si in the Laves phase up to such a level that the formation of Si-and/or Nb-base oxides beneath the external chromia base oxide scale during high temperature service is prevented.
- Addition of W (2 wt. %) to obtain solid solution strengthening in addition to the precipitate strengthening by Laves phase.

From the binary alloy phase diagram Fe-W in Figure 5.126 it is apparent, that in principle it should be possible to obtain precipitate plus solid solution strengthening by adding only W to the steel, i.e. without any Nb addition. Due to the high solubility of W in ferrite, however, the amount of W should then be substantially higher than that of Nb in Crofer 22 H.

Replacing Nb by W would have a substantial advantage. The most metal-rich Nb-oxide NbO possesses a dissociation pressure which is lower than that of chromia. This implies that Nb will tend to oxidize beneath external chromia scales and a possible occurrence of microcracks in the protective layer may result in rapid Nb-oxide formation thus deteriorating the oxidation resistance of the material. This was shown in reference [9] to be the case in Fe-Cr-Nb model alloys during oxidation at 900 °C. In Crofer 22 H this effect is suppressed by the carefully adjusted addition of Si (see section 2.13), however, in case of manufacturing related changes in Nb/Si ratio, the danger of undesired subscale oxidation of Nb is potentially possible. This effect is less likely if only W would be added as strengthening element in the steel as the most metal rich W-oxide i.e. WO_2, possesses a dissociation pressure which is substantially higher than that of chromia.

Therefore, in the following sections the effect of variation in W addition on the microstructural features and oxidation properties of Nb-free Crofer type steels is being investigated. First, as reference, the behaviour of W containing steels, without any Si- or Nb addition is evaluated. Investigations using these alloys should give insight in a possible effect of W on the intrinsic oxidation properties and on the possible effect imparted by solid solution strengthening in suppressing the specimen thickness dependence of the oxidation rates. A second aim of the investigations was to estimate, whether Fe-W base intermetallic compounds are able to dissolve Si in a similar manner as the Fe_2Nb base Laves phase with the aim to suppress silica subscale formation during high temperature oxidation.

For this purpose, three types of Nb-free tungsten containing alloy variants were produced, using again Crofer 22 APU as base composition:

- Tungsten alloyed steels “1W” (KCW) and “3W” (KDN) with 0.9 or 2.7 wt. % of W respectively
- Tungsten and silicon alloyed steel (“5W-0.24Si-0.03La-0.04Ti”) LFK and LJF (“5W-0.3Si”) with approximately 5 wt. % of W and 0.25 wt. % of Si and thus, one of them (batch LFK) having low amounts of La and Ti
- Tungsten and silicon alloyed steel batches (“7W-0.25Si-0.03La-0.04Ti”) LFN and (“7W-0.25Si”) LJH with approximately 7 wt. % of W and 0.25 wt. % of Si, one of them (batch LFN) having low amounts of La and Ti

Table 11 and 12 show the chemical compositions of the investigated tungsten and tungsten plus silicon containing steels. The oxidation tests were carried out as described in section 4 whereby, unless indicated differently, specimens with a thickness of 2 mm were used.

First studies on microstructural properties and oxidation behaviour of these alloys were already presented in reference [79]. However, a number of open questions had to be clarified:

- More detailed analysis and verification of phase composition in high-W steels.

- More detailed composition of oxide scales and subsurface depletion layer.
- Long term behaviour of W+Si alloys.
- Specimen thickness dependence of oxidation behaviour at 800°C.
- Oxidation induced plastic deformation of the steel substrate.

For a better readibility the new results will be presented in combination with some of the data in reference [79]. Data obtained from that publication are explicating quoted in the figure captions.

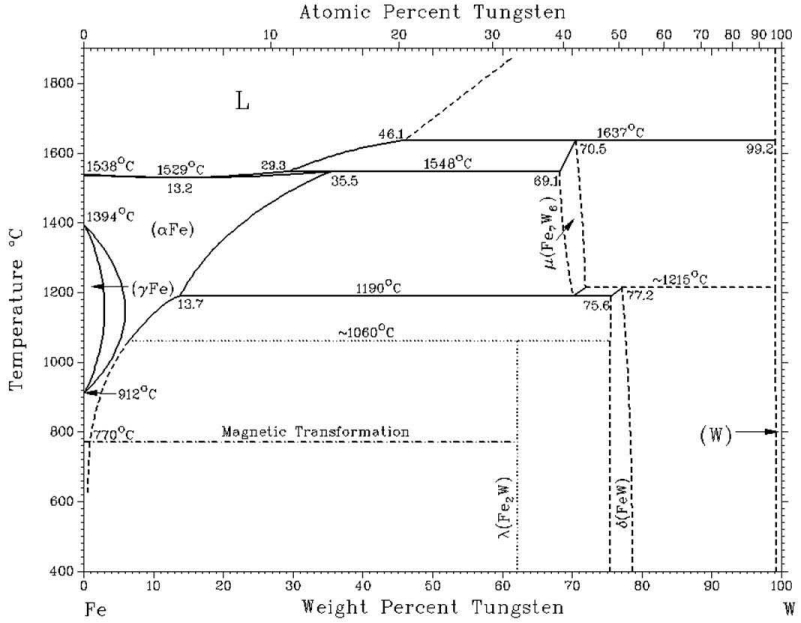

Figure 5.126: Binary phase diagram Fe-W [70].

Table 11: Chemical compositions in wt. % of the investigated Nb-free, W and W+Si alloyed steels as determined by ICP-OES in the central division of analytical chemistry (ZCH) at FZJ.

Batch	"1W" (KCW)	"3W" (KDN)	"5W-0.24Si-0.03La-0.04Ti" (LFK)	"5W-0.3Si" (LJF)	"7W-0.25Si-0.03La-0.04Ti" (LFN)	"7W-0.25Si" (LJH)
Fe	75.9	75.8	71.9	71.5	69.6	69.4
Cr	22.3	20.7	22.5	22.56	22.7	22.7
Mn	0.51	0.53	0.45	0.46	0.45	0.47
Ti	0.09	0.09	0.04	0.07	0.04	0.06
La	0.12	0.13	0.03	0.09	0.03	0.14
Nb	-	-	-	-	-	-
W	0.95	2.7	4.79	4.91	6.98	6.98
Al	0.01	0.01	0.01	0.01	0.01	0.01
Si	0.06	0.04	0.24	0.28	0.25	0.25

Table 12: Impurities in wt. % in the investigated Nb-free, W and W+Si alloyed steels according to hot gas extraction IR spectroscopy measured in the central division of analytical chemistry (ZCH) at FZJ.

Batch	"1W" (KCW)	"3W" (KDN)	"5W-0.24Si-0.03La-0.04Ti" (LFK)	"5W-0.3Si" (LJF)	"7W-0.25Si-0.03La-0.04Ti" (LFN)	"7W-0.25Si" (LJH)
C	0.013	0.009	0.0030	0.0015	0.0030	0.0010
S	0.002	0.002	0.0020	0.0005	0.0021	0.0011
N	0.0151	0.0056	0.010	0.0036	0.006	0.0050
O	0.0067	0.0049	0.0070	0.0071	0.0070	0.0071

5.6.2 Microstructure of W containing Nb-free steels

Figure 5.127 shows a 900 °C section of the ternary phase diagram Fe-Cr-W system [151]. In addition to the phases known from the binary phase diagrams, the ternary diagram assumes the existence of two ternary phases, i.e. $Cr_9Fe_{10}W$ and $Cr_7Fe_{10}W_3$. Comparing the diagram with the data in Table 11 and 12, the Nb/Si-free, low W steels "1W" (KCW) and "3W" (KDN) should possess a single phase microstructure. SEM/WDX investigations of model steels "5W-0.24Si-0.03La-0.04Ti" (LFK) and "7W-0.25Si-0.03La-0.04Ti" (LFN) revealed that an increase of the tungsten addition up to 5 or 7 wt. % W results in formation of two precipitate phases with compositions close to $Cr_7Fe_{10}W_3$ and λ-$(Fe,Cr)_2W$ after 10 000 h at 800 °C (Figure 5.128). According to WDX

analyses these phases possess hardly any solubility for Si. Detailed chemical compositions of all discussed phases are given in table 13. These analyses relate to exposures at 800 °C and, unfortunately, no complete 800 °C section of the ternary Fe-Cr-W diagram could be found in literature. Because of that the actually determined accurate phase composition data measured after 10 000 h at 800 °C (red triangle) are inserted into the 900 °C section of the Fe-Cr-W system. The measured phase compositions are qualitatively in reasonable agreement with those from the presented phase diagram. The maximum measured tungsten solubility in the ferrite matrix at the prevailing Cr content of 22 % was approximately 0.8 at. % (2.6 wt. %) at 800 °C.

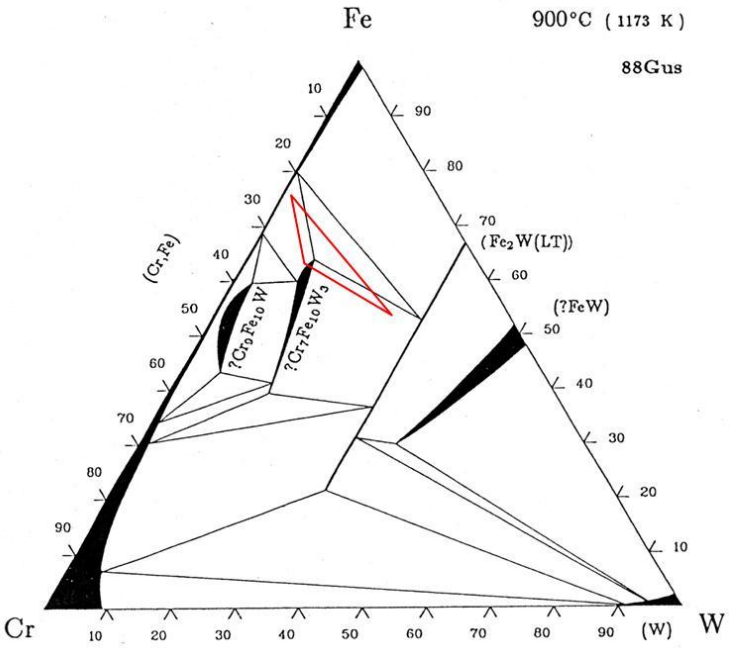

Figure 5.127: 900 °C section of ternary Fe-Cr-W phase diagram [151] with inserted red marked three-phase field at 800 °C derived from the present investigations.

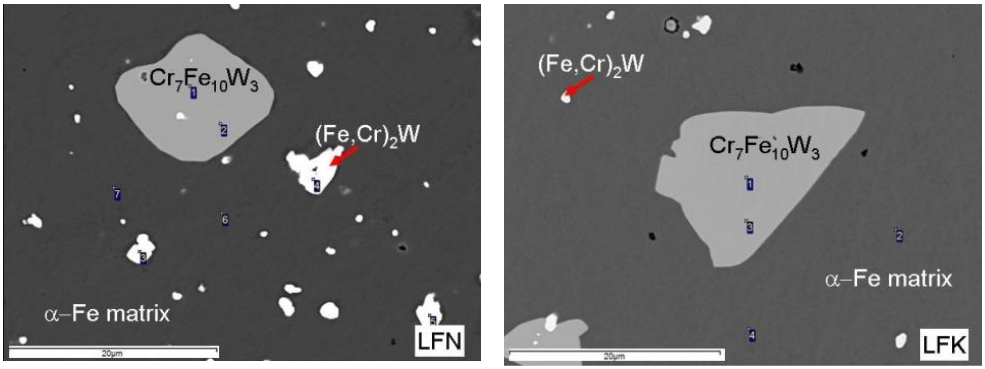

Figure 5.128: SEM/BSE images of model steels"5W-0.24Si-0.03La-0.04Ti" (LFK) and "7W-0.25Si-0.03La-0.04Ti" (LFN) after 10 000 h exposure at 800 °C in air showing the formation of two precipitate phases with compositions close to χ-$Cr_7Fe_{10}W_3$ and λ-$(Fe,Cr)_2W$

Table 13: WDX data of chemical compositions in at. % for phases identified in samples "5W-0.24Si-0.03La-0.04Ti" (LFK) and "7W-0.25Si-0.03La-0.04Ti" (LFN) after 1000 h at 900 °C and 10 000 h at 800 °C.

Sample	Phase	Fe	Cr	W	Mn	Si
900 °C, 1000 h LFK	χ-$Cr_7Fe_{10}W_3$	62	26.6	11.4	---	---
	Ferrite	74.3	24.2	1.2	0.1	0.2
900 °C, 1000 h LFN	χ-$Cr_7Fe_{10}W_3$	62.7	25.9	11.3	0.1	---
	λ-$(Fe,Cr)_2W$	52.2	18.6	28.9	---	0.3
	Ferrite	75.5	23.1	1.2	0.1	0.2
800 °C, 10 kh LFK	χ-$Cr_7Fe_{10}W_3$	61.5	27.6	10.8	0.1	---
	λ-$(Fe,Cr)_2W$	52.1	17.7	30	0.2	---
	Ferrite	74.6	24.2	0.7	0.2	0.3
800 °C, 10 kh LFN	χ-$Cr_7Fe_{10}W_3$	61.6	27.6	10.5	0.2	---
	λ-$(Fe,Cr)_2W$	52.5	18	29.4	0.1	---
	Ferrite	74.4	24.3	0.8	0.1	0.4

SEM/EBSD measurements confirm that the crystal symmetries of both intermetallic phases correspond to the λ and χ (chi) phase respectively (Figure 5.129-130). Thermodynamic calculations of the phase composition of the model steel Fe-22%Cr-7% W-0.25%Si using ThermoCalc [69] revealed that the χ phase should be stable at temperatures above approximately 580°C. It was found that these calculations underestimate the stability of the λ-Laves phase (Figure 5.131).

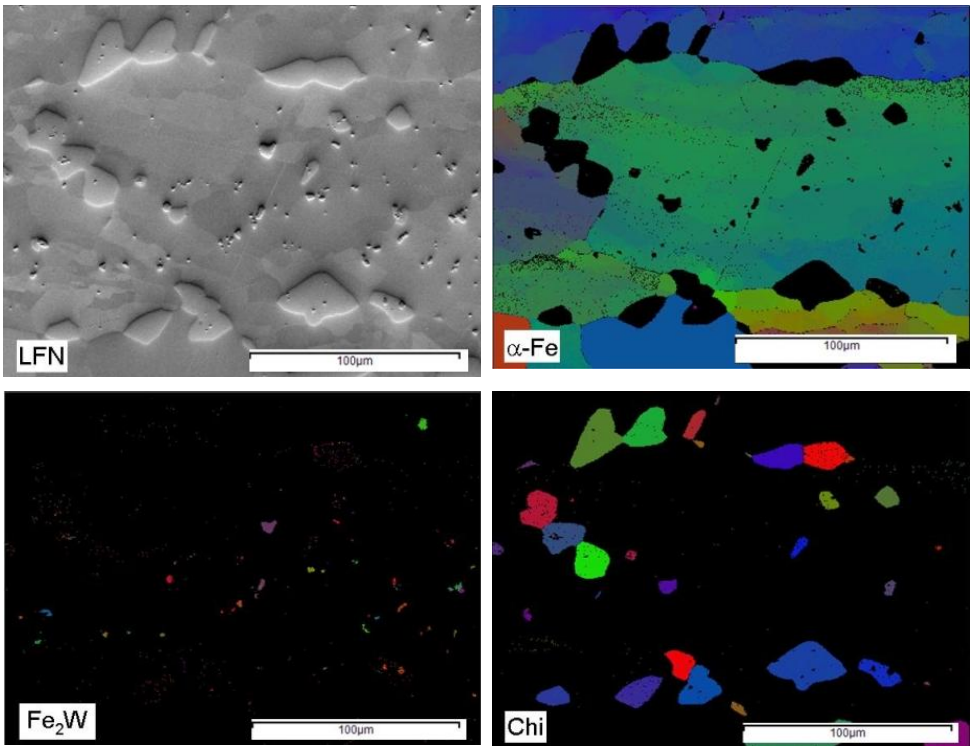

Figure 5.129: SEM/EBSD mapping showing phase distribution in centre of the sample of "7W-0.25Si-0.03La-0.04Ti" (LFN) after 10 000 h exposure at 800 °C in air.

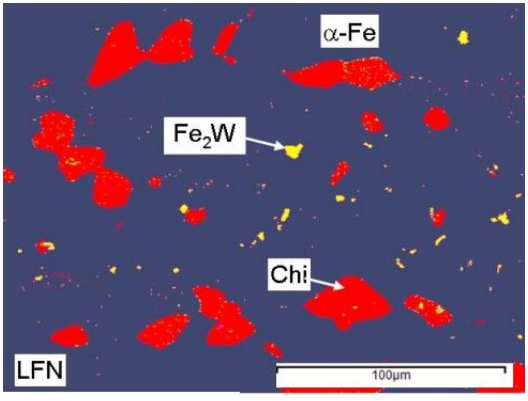

Figure 5.130: SEM/EBSD mapping showing phase distribution in sample"7W-0.25Si-0.03La-0.04Ti" (LFN) after 10 000 h exposure at 800 °C in air.

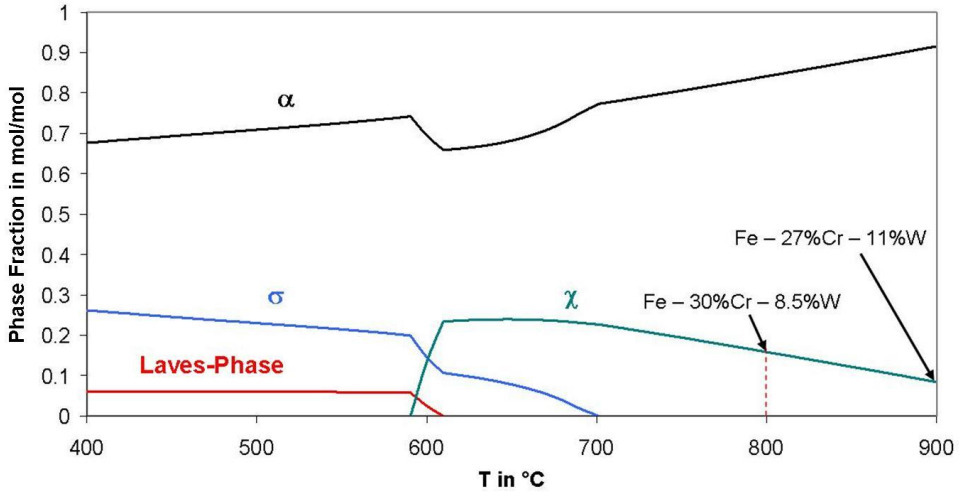

Figure 5.131: Calculated mol fraction of the different phases as a function of temperature for alloy "7W-0.25Si-0.03La-0.04Ti" (LFN) calculated with ThermoCalc [69] (all compositions in wt. %).

The maximum solubility of tungsten in the ferrite matrix at 800 °C is approximately 1.2 at. % which corresponds to about 3.9 wt. %. The data presented in Table 13 shows that the $(Fe,Cr)_2W$ phase dissolves only very minor amounts of silicon.

5.6.3 Oxidation behaviour: steels without Si addition

Figures 5.132-133 show weight changes as a function of time for the two W-containing, Si-free steels during isothermal oxidation at various temperatures in synthetic air. Generally, all measured curves obey a near parabolic time dependence of the scale thickness. This allows the reliable calculation of a k_w value from each curve. Figure 5.134 shows the dependence of the parabolic rate constant for the two materials k_w as a function of reciprocal temperature. The data show that the oxidation rates are very similar to those of a high purity version of Crofer 22 APU (batch KCR). The steels oxidized for 72 h at 1000 °C in air exhibit the typical duplex oxide scales consisting of outer $(Mn,Cr)_3O_4$ and inner Cr_2O_3. The internal oxidation zone in the steels consists of fine, randomly dispersed Ti-oxide precipitates. Figure 5.135 shows the oxide scale microstructures and the measured XRD patterns (Figures 5.136 and 5.137).

Figure 5.138 and 5.139 show the weight changes during 1000 h discontinuous oxidation at 800 °C in air for the two steels “1W”(KCW) and “3W”(KDN) and for the Crofer 22 APU batch KCR, and the corresponding oxide scale microstructures after 1000 h exposure.

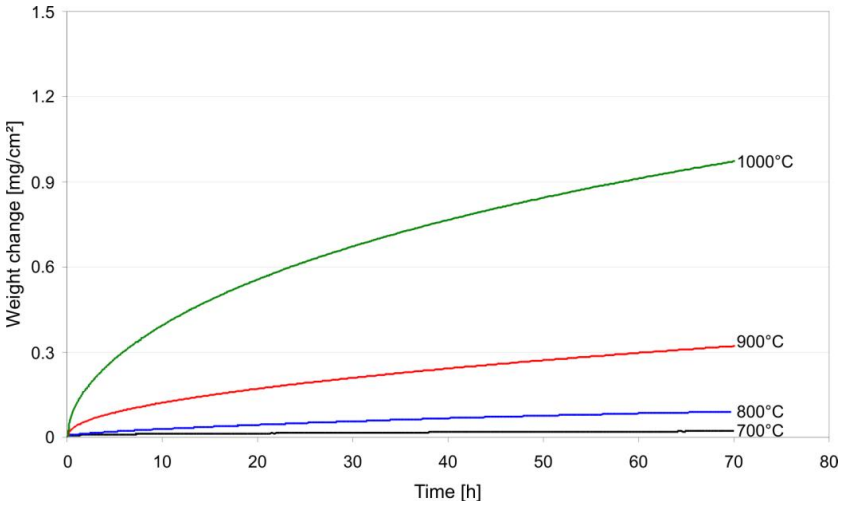

Figure 5.132: Weight change as a function of time during isothermal oxidation of steel “1W” (KCW) at various temperatures in synthetic air. (Specimen thickness 2 mm).

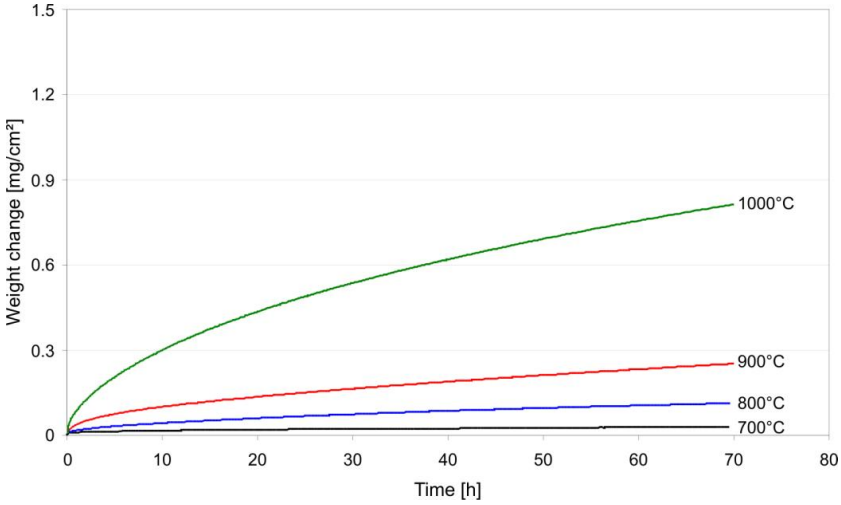

Figure 5.133: Weight change as a function of time during isothermal oxidation of steel “3W” (KDN) at various temperatures in synthetic air. (Specimen thickness 2 mm).

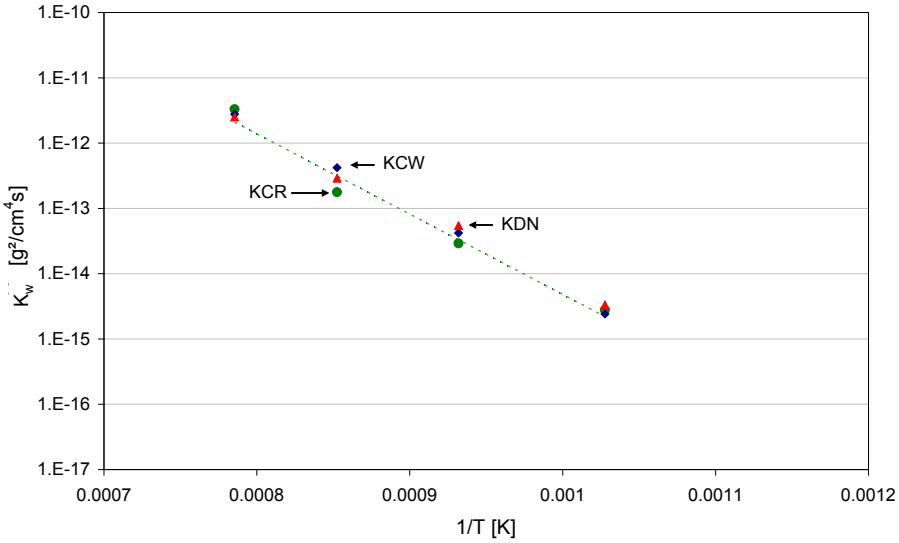

Figure 5.134: Parabolic rate constant k_w as a function of reciprocal temperature for "1 W" (KCW) and "3W" (KDN) and Crofer 22 APU (KCR) based on isothermal oxidation 72 h in synthetic air. K_w values calculated from TG curves in figures 5.132 and 5.133.

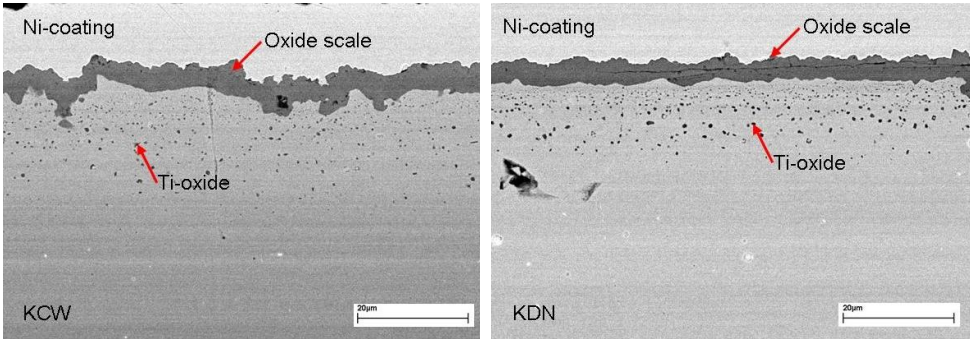

Figure 5.135: SEM/BSE images of the cross sections of oxide scales formed on model steels "1W" (KCW) and "3W" (KDN) during 72 h isothermal oxidation at 1000 °C in synthetic air. (Specimen thickness 2 mm).

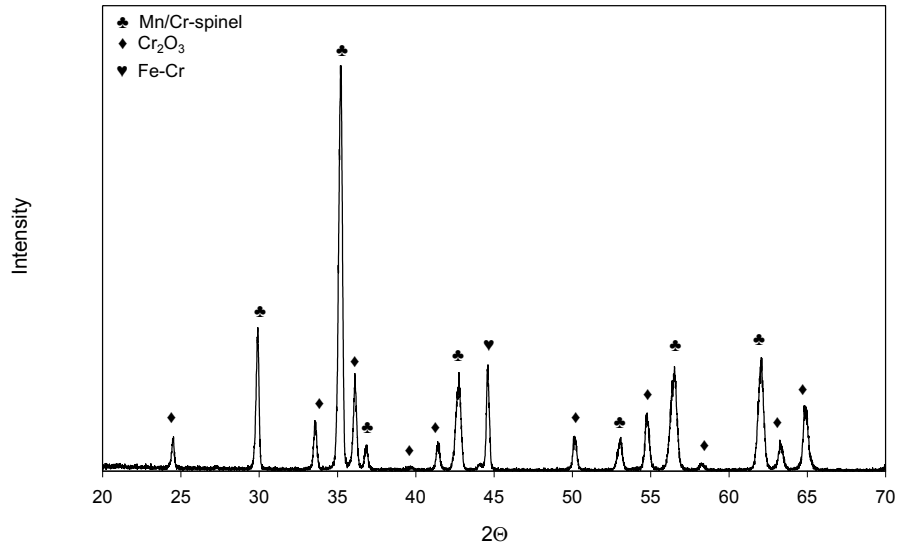

Figure 5.136: XRD pattern taken from sample "1W" (KCW) after 72 h isothermal oxidation at 1000 °C in synthetic air.

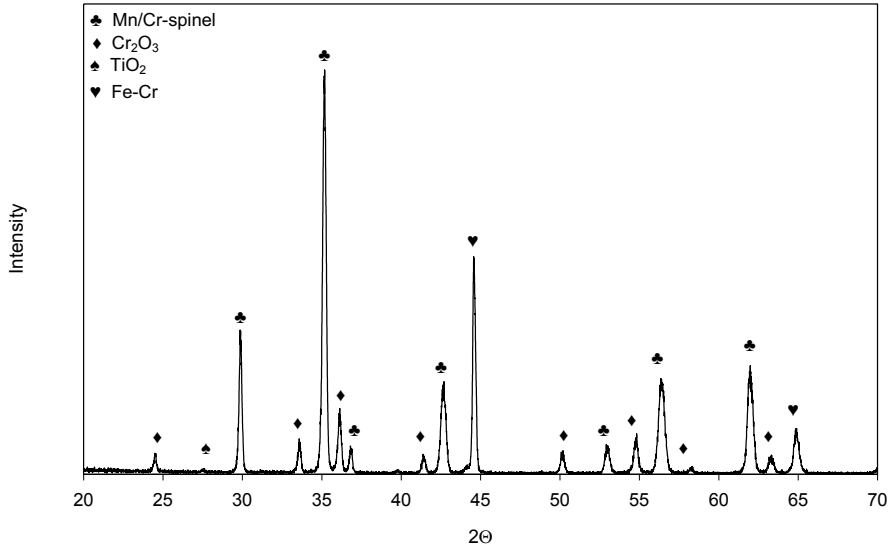

Figure 5.137: XRD pattern taken from sample "3W" (KDN) after 72 h isothermal oxidation at 1000 °C in synthetic air.

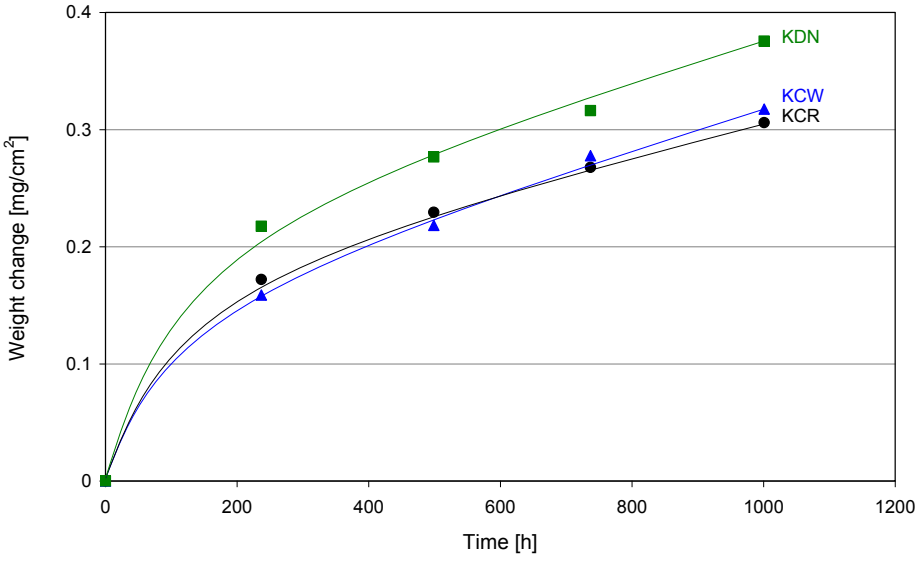

Figure 5.138: Weight changes during 1000 h discontinuous oxidation for steels "1W" (KCW) and "3W" (KDN) (250 h cooling intervals) at 800 °C in laboratory air (Specimen thickness 2 mm).(Data taken from reference [79]).

Figures 5.140 and 5.141 show backscattered electron images of "3W" (KDN) steel after 5000 and 10 000 h exposure at 800 °C. The morphological features of the surface oxide and the internal oxidation zone are very similar to those commonly found for Crofer 22 APU (see section 2.13, figure 2.9).

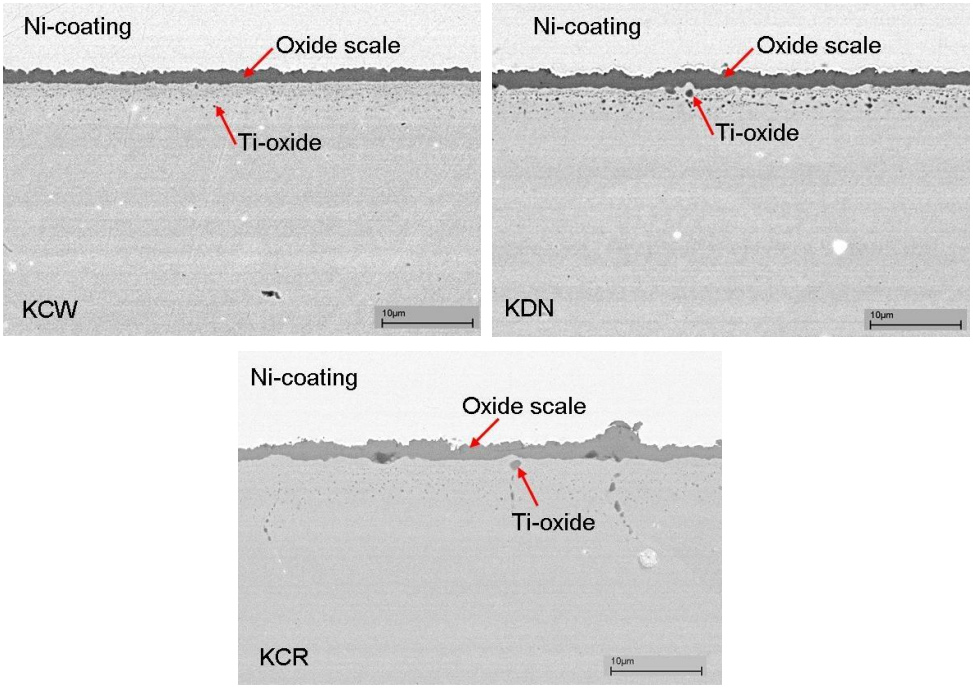

Figure 5.139: SEM/BSE images of cross sections comparing oxide scales formed on model steels "1W" (KCW) and "3W" (KDN) and Crofer 22 APU (KCR) during 1000 h discontinuous oxidation at 800 °C in laboratory air. (Specimen thickness 2 mm).(Data taken from reference [79]).

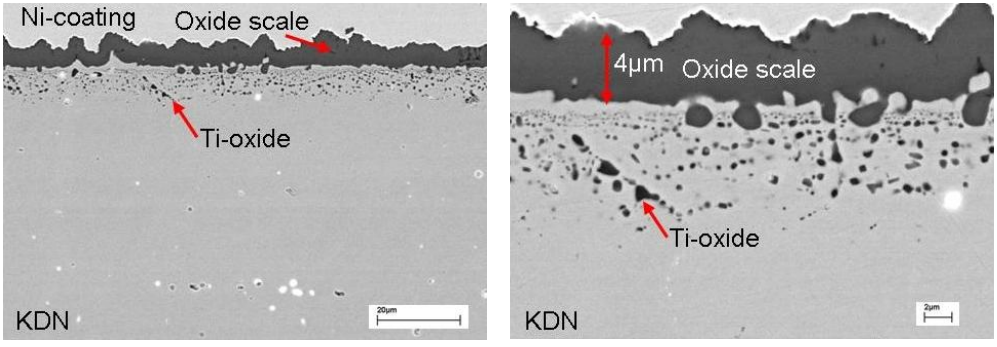

Figure 5.140: SEM/BSE images of the cross sections of the oxide scales formed on steel "3W" (KDN) during 5000 h discontinuous oxidation at 800 °C in laboratory air. (Specimen thickness 2 mm).

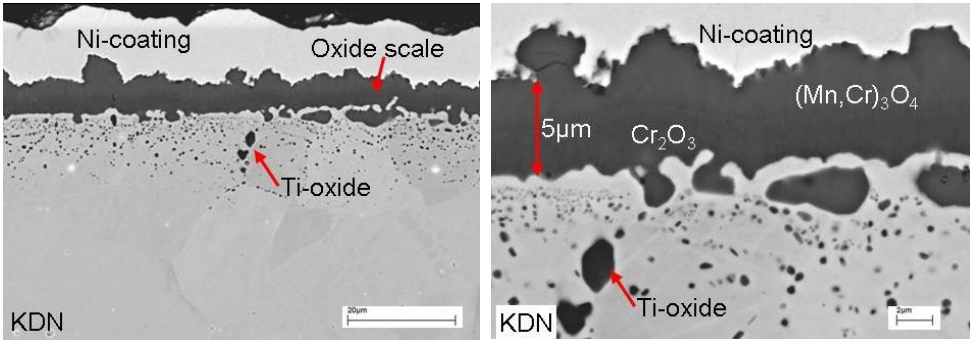

Figure 5.141: SEM/BSE images of the cross sections of the oxide scales formed on steel“3W” (KDN) during 10 000 h discontinuous oxidation at 800 °C in laboratory air. (Specimen thickness 2 mm).(Micrograph -on the left side- taken from reference [79]).

5.6.4 Oxidation behaviour: W containing steels with Si addition

Figure 5.142 shows the weight changes during 1000 h discontinuous oxidation of the model steels containing W and Si additions (batches “5W-0.24Si-0.03La-0.04Ti” (LFK), “5W-0.3Si” (LJF), “7W-0.25Si-0.03La-0.04Ti” (LFN) and “7W-0.25Si” (LJH); the chemical compositions are shown in Table 11 and 12). The weight changes are found to be substantially higher than those of the Si-free batch “3W” (KDN).

Figure 5.143 shows weight changes during long term exposure confirming this observation.

The increased weight changes compared to batch KDN mainly result from a silica sub-layer which forms near the metal/oxide interface (Figure 5.144).The GDOES profiles (Figure 5.145 and 5.146) confirm the strong Si enrichment near the scale alloy interface. Si is also enriched in a very thin layer at the oxide/gas interface.

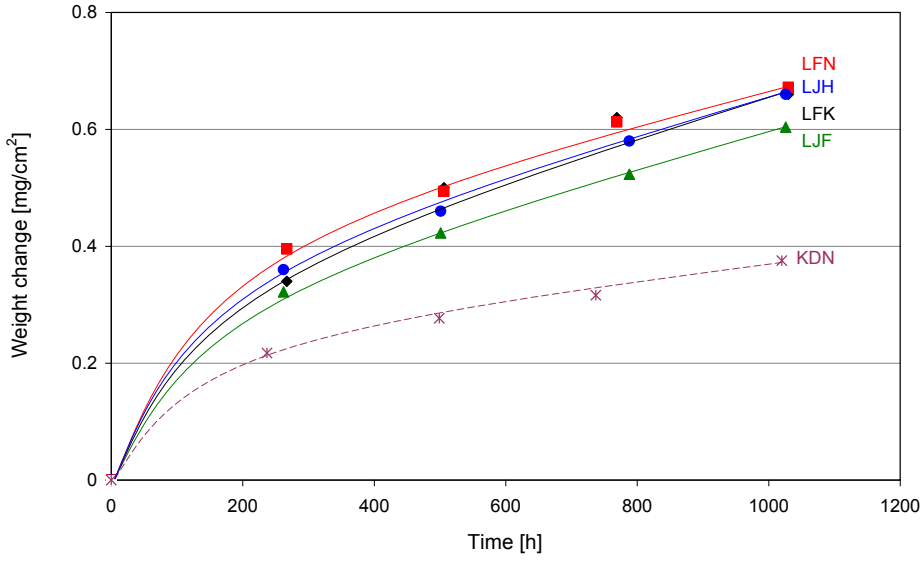

Figure 5.142: Weight changes during 1000 h oxidation for various model steels containing W and Si additions ("5W-0.24Si-0.03La-0.04Ti" (LFK), "5W-0.3Si" (LJF), "7W-0.25Si-0.03La-0.04Ti" (LFN), "7W-0.25Si" (LJH)) at 800 °C in laboratory air. (Specimen thickness 2 mm). Data are compared with results of Si-free, W-containing steel ("3W" (KDN)).

During exposure at 900 °C it may be possible to use the higher oxidation rates at relatively short times for the prediction of the long term oxidation behaviour at 800 °C. However, this approach is not in all cases reliable due to a possible change of the oxidation mechanism at higher temperature. An interesting observation is that the morphology of the subscale silica formation after 1000 h air oxidation at 900 °C differs from alloy to alloy. In one case the silica is in direct contact with the chromia scale (batch "5W-0.24Si-0.03La-0.04Ti" (LFK)), in other cases, the silica and the chromia scale are separated by a metallic region, free of precipitates (batch "7W-0.25Si" (LJH) and especially "5W-0.3Si" (LJF)). Considering the morphologies of the internal oxidation zones (Figures 5.147 and 5.148) and the batch compositions (Table 11 and 12) these differences in oxidation behaviour are likely related to differences in alloy titanium content. The internal oxidation of Ti, especially in the high-Ti batch "5W-0.3Si" (LJF), causes a volume increase in the subsurface layer imparting a compressive stress in the alloy. This results in an outward flow [85] of Ti and Si depleted metal.

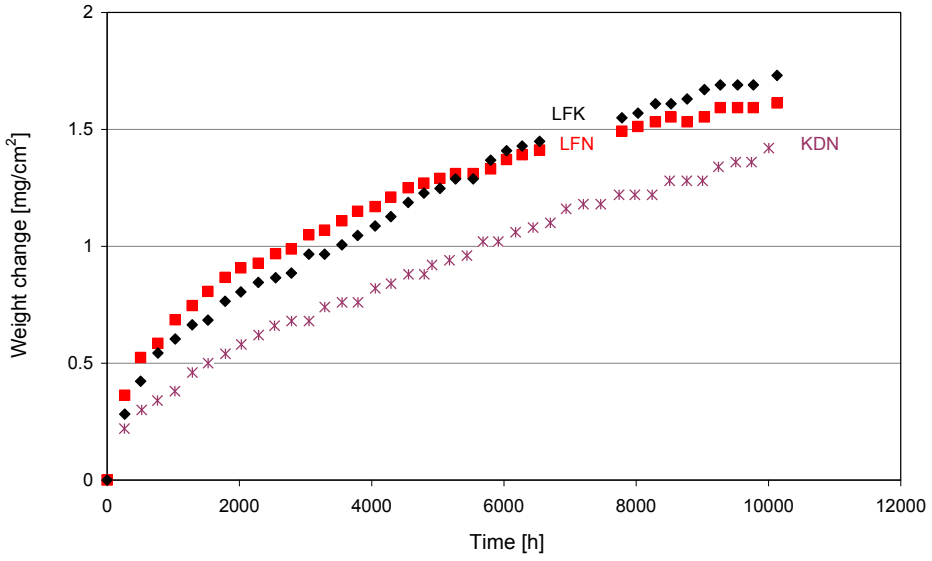

Figure 5.143: Weight changes during 10 000 h oxidation at 800 °C in air of W-variant ("5W-0.25Si-0.03La-0.04Ti" (LFK), "7W-0.25Si-0.03La-0.04Ti" (LFN)). Data are compared with Si-free, W-containing steel ("3W" (KDN)) (Specimen thickness 2 mm).

Figure 5.147 shows the XRD pattern of the sample "7W-0.25Si" (LJH) after 1000 h oxidation at 900 °C in air.

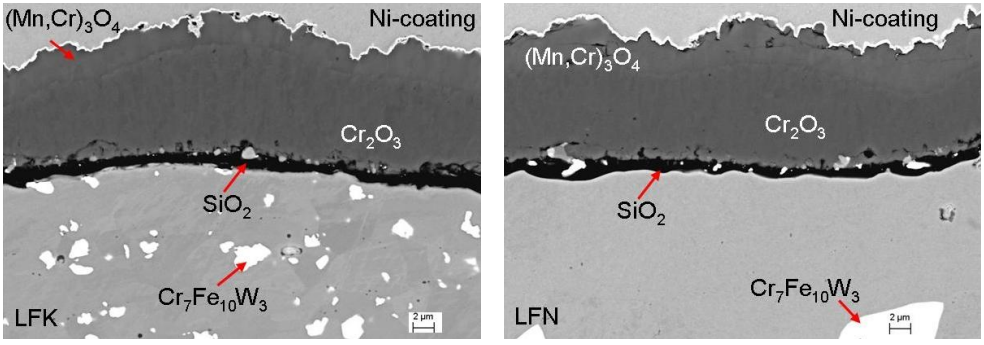

Figure 5.144: SEM images showing the cross sections of oxide scales formed on model steels "5W-0.24Si-0.03La-0.04Ti" (LFK), "7W-0.25Si-0.03La-0.04Ti" (LFN) during 10 000 h oxidation at 800 °C in air. (Specimen thickness 2 mm).

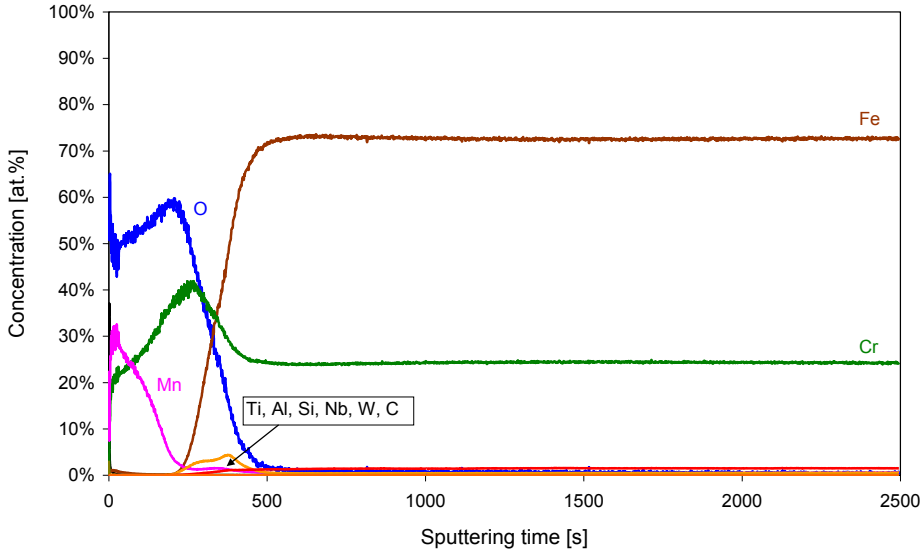

Figure 5.145: GDOES element concentration profiles measured on batch "5W-0.24Si-0.03La-0.04Ti" (LFK) after 10 000 h oxidation at 800 °C in air.

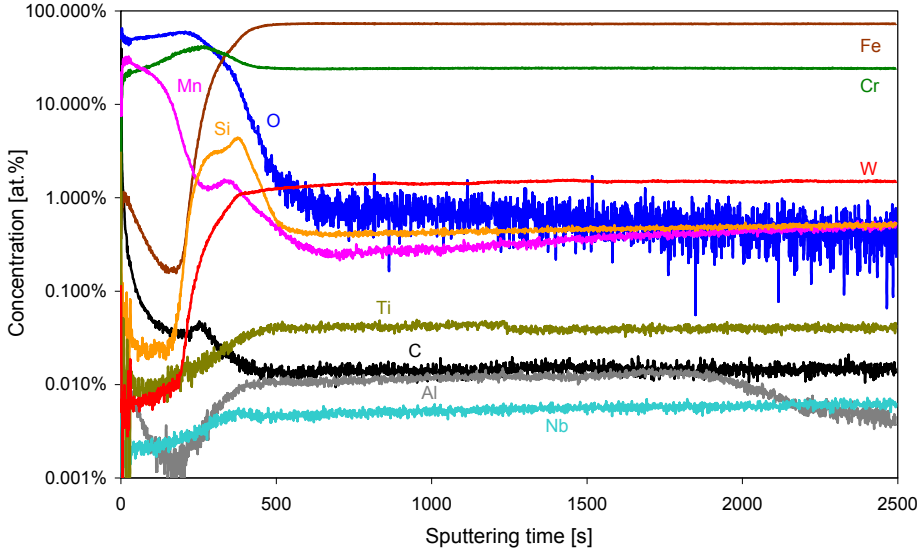

Figure 5.146: GDOES (logarithmic scale) element concentration profiles measured on batch "5W-0.24Si-0.03La-0.04Ti" (LFK) after 10 000 h oxidation at 800 °C in air.

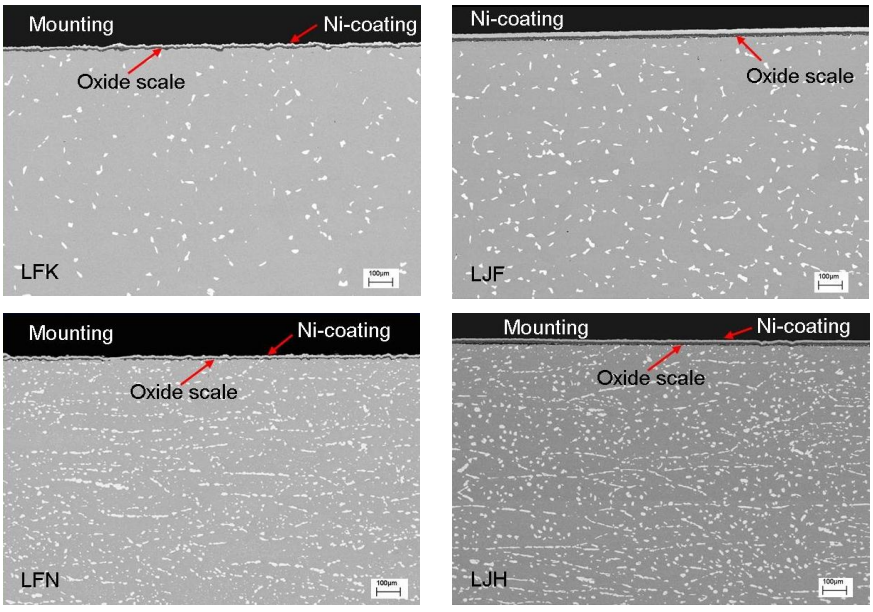

Figure 5.147: SEM images of cross sectioned alloys “5W-0.24Si-0.03La-0.04Ti” (LFK), “5W-0.3Si” (LJF), “7W-0.25Si-0.03La-0.04Ti” (LFN), “7W-0.25Si” (LJH) after 1000 h of oxidation at 900 °C in laboratory air.

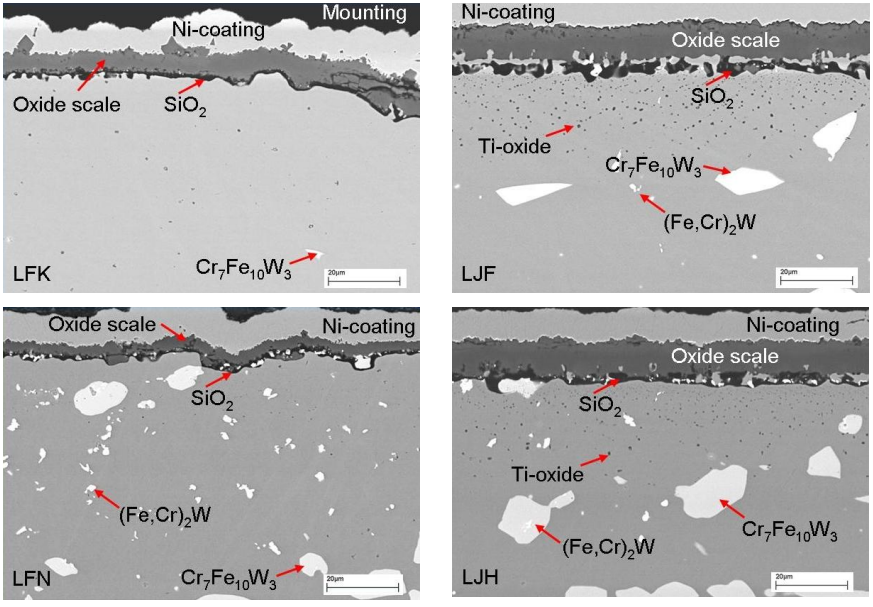

Figure 5.148: SEM images of cross sectioned alloys “5W-0.24Si-0.03La-0.04Ti” (LFK), “5W-0.3Si” (LJF), “7W-0.25Si-0.03La-0.04Ti” (LFN), “7W-0.25Si” (LJH) after 1000 h of oxidation at 900 °C in laboratory air.

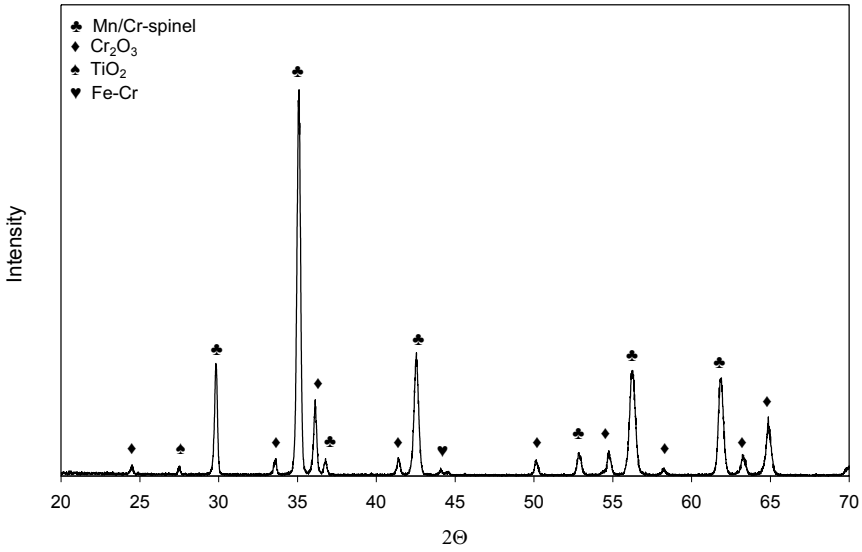

Figure 5.149: XRD pattern taken from sample "7W-0.25Si" (LJH) after 1000 h oxidation at 900 °C in air.

5.6.5 Specimen thickness dependence of the oxidation rate for Nb-free steels

Based on the theoretical considerations in section 5.6.4, addition of W may, even in Nb free alloys, affect the specimen thickness dependence of the oxidation rate because W is an efficient solid solution strengthener and an increase in creep strength by W addition in Crofer 22 APU type steel was illustrated in reference [9].

To check the effect of increased creep strength on the specimen thickness dependence of Nb-free alloys, a series of experiments was designed to study the oxidation behaviour of specimens with different thicknesses during oxidation up to 2000 h at 800 °C in laboratory air. Each 200 h, the specimens were cooled down to room temperature for weight change measurements. Cooling and heating rate were carefully controlled and set on 2 °C/min as used in section 5.5.4.

The experiments were only carried out with the Si-free steels to exclude a possible effect of the Si subscale oxidation on the oxidation behaviour and thus the specimen thickness

dependence of the oxide scale growth rate. The results of the two Nb/Si-free W containing steels “1W” (KDN) and “3W” (KCW) were compared with that of the Crofer 22 APU batch KCR. (Tables 14 and 15).

Table 14: Chemical compositions in wt. % of W alloyed steels and Crofer 22 APU by ICP-OES in the central division of analytical chemistry (ZCH) at FZJ.

Batch	“1W” (KCW)	“3W” (KDN)	Crofer 22 APU (KCR)
Fe	75.9	75.8	76.06
Cr	22.3	20.7	23.19
Mn	0.51	0.53	0.53
Ti	0.1	0.11	0.06
La	0.12	0.13	0.16
Nb	-	-	-
W	0.95	2.7	-
Al	0.01	0.01	0.006
Si	-	0.06	0.03

Table 15: Impurities in wt. % in the investigated W alloyed steels and Crofer 22 APU according to hot gas extraction IR spectroscopy measured in the central division of analytical chemistry (ZCH) at FZJ.

Batch	“1W” (KCW)	“3W” (KDN)	Crofer 22 APU (KCR)
C	0.013	0.009	0.01
S	0.002	0.002	0.001
N	0.0151	0.0056	0.0076
O	0.0067	0.0049	0.0046

Figure 5.150 shows the weight changes as function of time for steels “1W” (KCW) and “3W” (KDN) in comparison with those of Crofer 22 APU (KCR) during 2000 h discontinuous oxidation at 800 °C in air. The investigated tungsten alloyed steels show in the prevailing test a minor thickness dependence of the oxidation rate which is, however, substantially smaller than that for Crofer 22 APU batch KCR. The results thus show that the addition of W reduces the influence of substrate thickness on the oxidation rate at 800 °C compared to that observed for Crofer 22 APU. Cross sections of different specimens of “1W” (KCW) (see Figure 5.151) show qualitatively the same trend with respect to specimen thickness dependence observed for Crofer 22 APU (KCR) (Figure 5.152). The comparison of the scale thicknesses confirms the weight gain data: the scale

on the 0.25 mm sample is thicker than that on the other samples, however the difference in oxide thickness on thick and thin samples is smaller than that for Crofer 22 APU.

The change in oxidation rate with changing specimen thickness is likely related to oxide growth stress relaxation during the oxidation process, as explained in section 5.5.3. Interesting to note that eight of nine tested samples ("1W" (KCW) and "3W" (KDN) and Crofer 22 APU (KCR)) exhibited a secondary recrystallized microstructure after 2000 h of testing. (Figures 5.153 - 5.155).

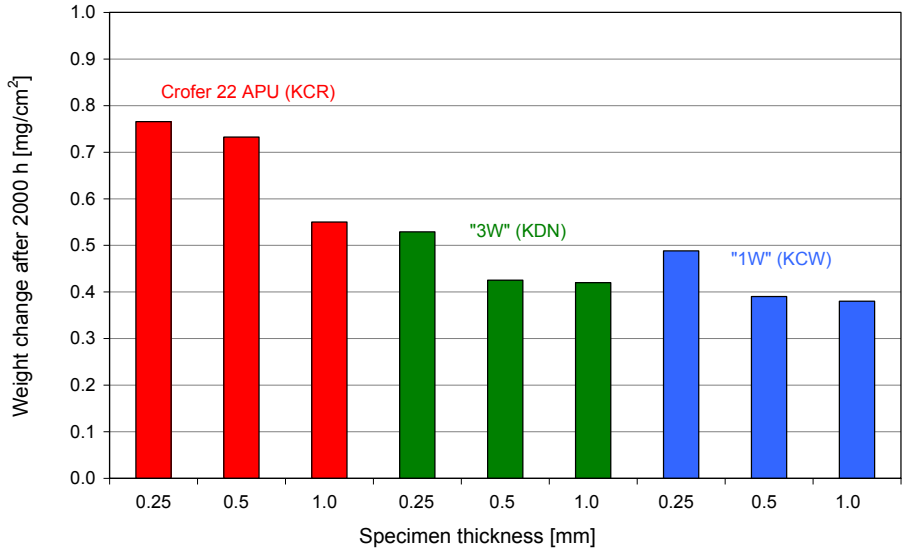

Figure 5.150: Weight changes after 2000 h as a function of specimen thickness for steels "1W"(KCW), "3W"(KDN) and Crofer 22 APU (KCR) discontinuously oxidised (200 h cooling intervals) at 800 °C in laboratory air.

For a more extensive evaluation of the specimen thickness dependence of the W containing steels, Figure 5.156 shows weight changes as a function of time for samples with various initial thicknesses for the Nb/Si-free, "3W" (KDN) steel during 1000 h cyclic oxidation at 900 °C in air. At this temperature a clear specimen thickness dependence of the oxidation rate is observed, thinner samples exhibiting higher oxidation rates than thicker samples. Contrary to Crofer 22 APU [152] (Figure 5.157) no indication

of breakaway oxidation was found up to exposure times of 1000 h, for the thinnest specimen.

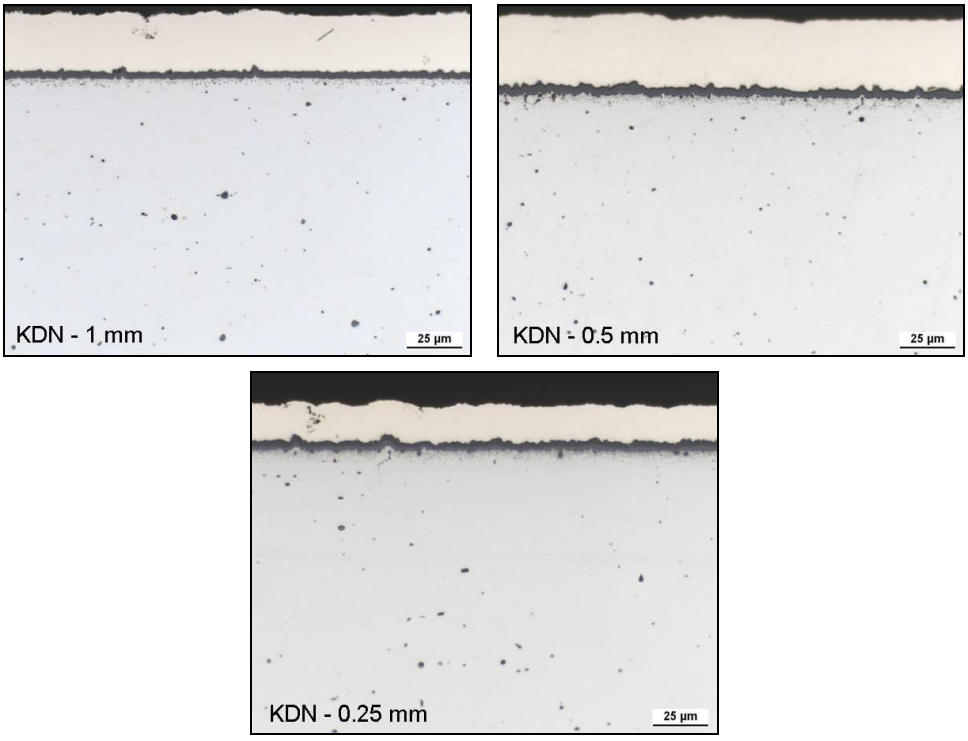

Figure 5.151: Specimens of different thicknesses of steel“3W” (KDN) after 2000 h discontinuous oxidation at 800 °C in air.

Comparing the behaviour of the Nb/Si-free steel, “3W” (KDN) at 800 °C and 900 °C, reveals that the specimen thickness dependence of the oxidation rate is less pronounced at 800 °C than at 900 °C, but is still clearly seen and of technical importance (Figure 5.158).

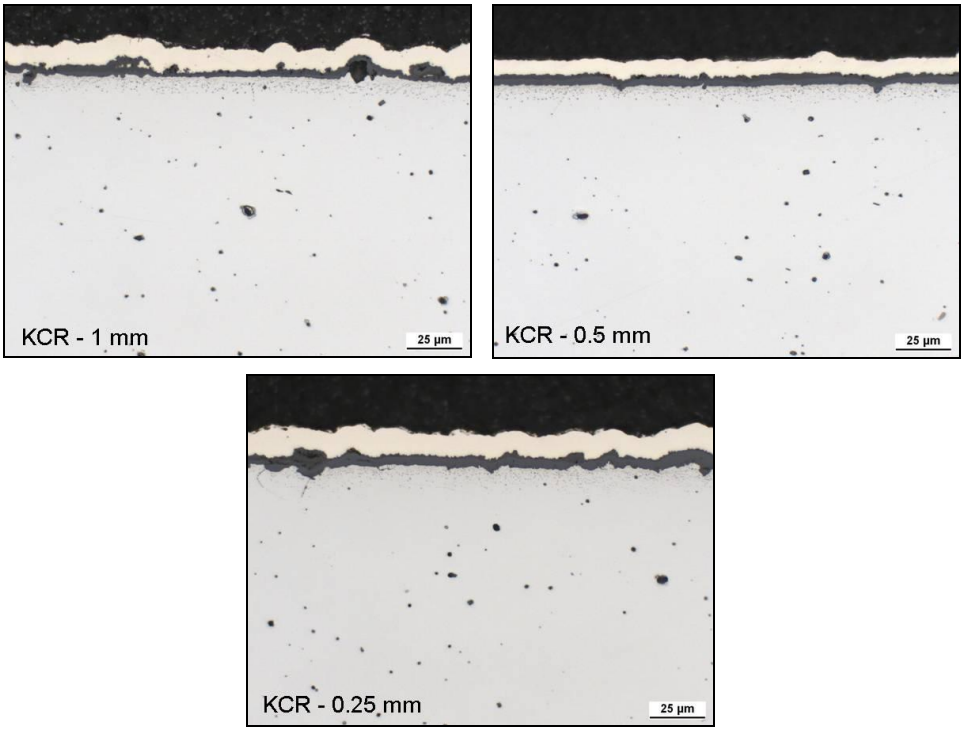

Figure 5.152: Specimens of different thicknesses of Crofer 22 APU (KCR) after 2000 h discontinuous oxidation at 800 °C in air.

Figure 5.153: Optical micrographs showing cross sections of steel“1W” (KCW) samples with different thicknesses after 2000 h oxidation at 800 °C in laboratory air. (Samples etched with 5%H_2SO_4).

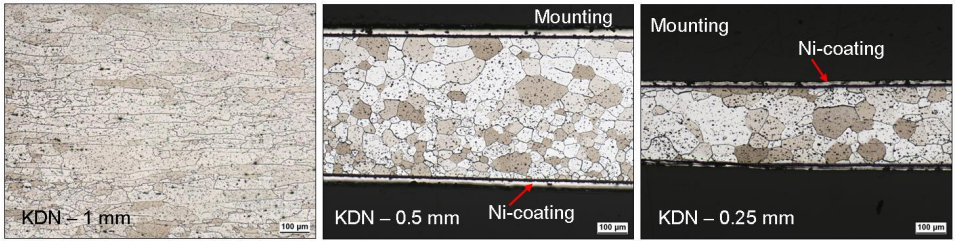

Figure 5.154: Optical micrographs showing cross sections of steel "3W" (KDN) samples with different thicknesses after 2000 h oxidation at 800 °C in laboratory air. (Samples etched with 5%H_2SO_4).

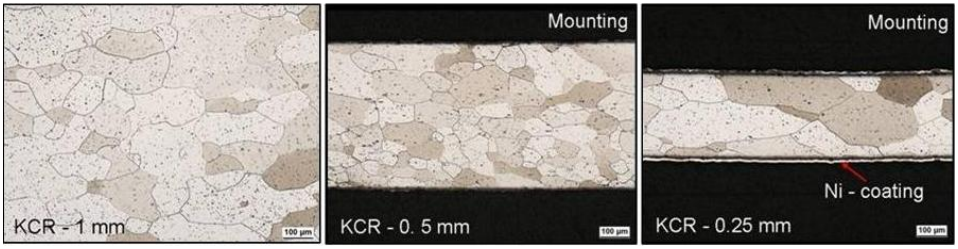

Figure 5.155: Optical micrographs showing cross sections of Crofer 22 APU (KCR) samples with different thicknesses after 2000 h oxidation at 800 °C in laboratory air. (Samples etched with 5%H_2SO_4).

The macro images shown for samples of steel "3W" (KDN) in Figure 5.159 indicate elongation of the thin samples due to creep of the substrate. The relative length change as function of the specimen thickness in Figure 5.160 shows that once the sample thickness falls below a critical value, small variations in thickness have a considerable impact on the oxidation induced deformation.

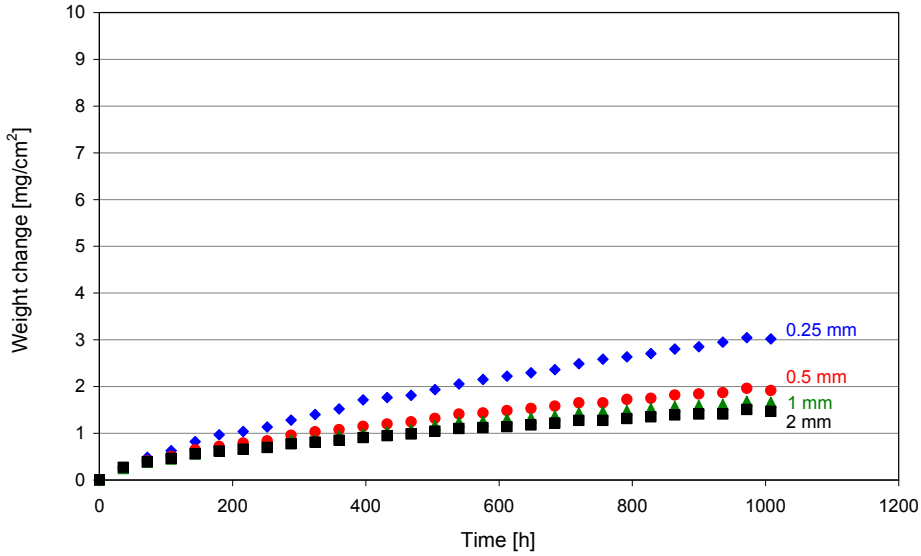

Figure 5.156: Weight changes as a function of time for samples of different thickness of steel“3W” (KDN) during 1000 h cyclic oxidation at 900 °C in laboratory air. (Data taken from reference [79]).

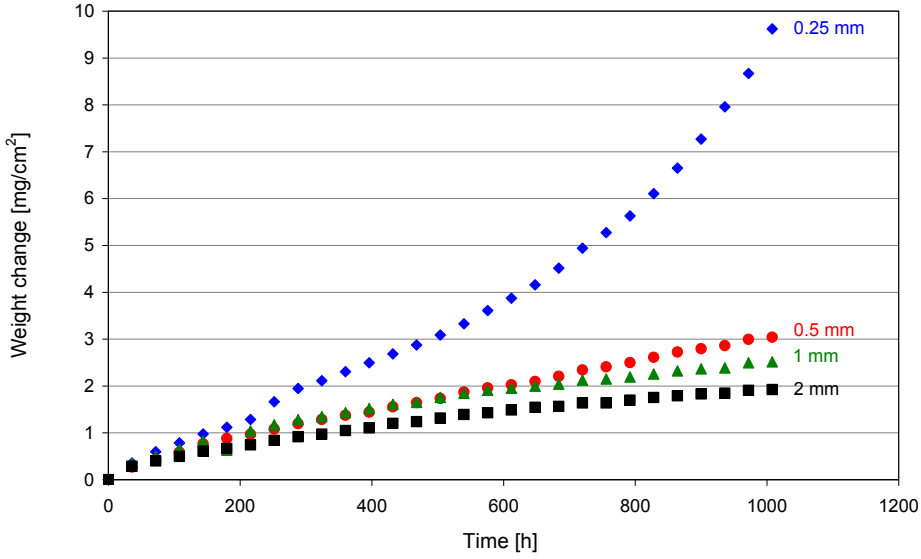

Figure 5.157: Weight changes as a function of time for samples of different thickness of Crofer 22 APU (KCB) during 1000 h cyclic oxidation at 900 °C in laboratory air. (Data taken from reference [79]).

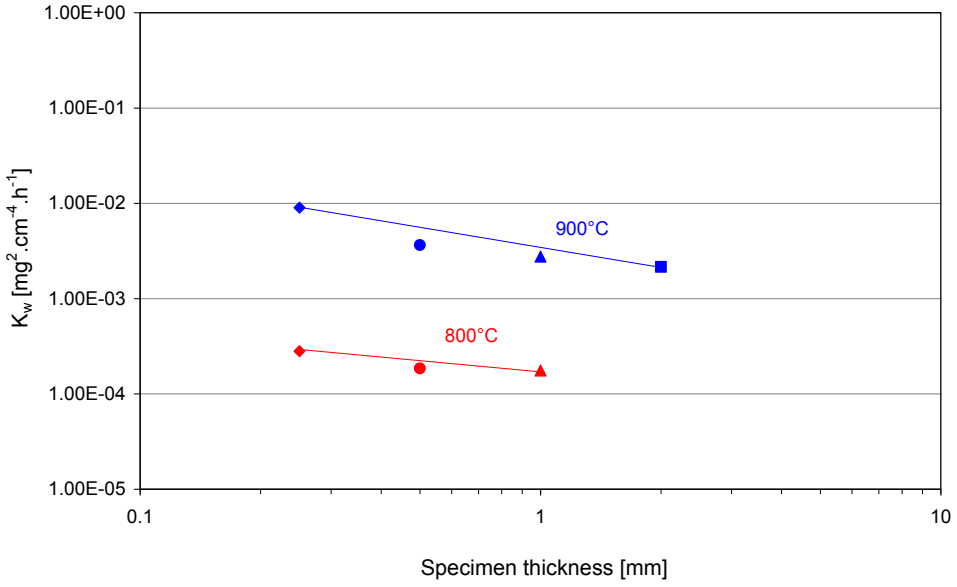

Figure 5.158: Measured K_w values during discontinuos oxidation of steel“3W” (KDN) in air.

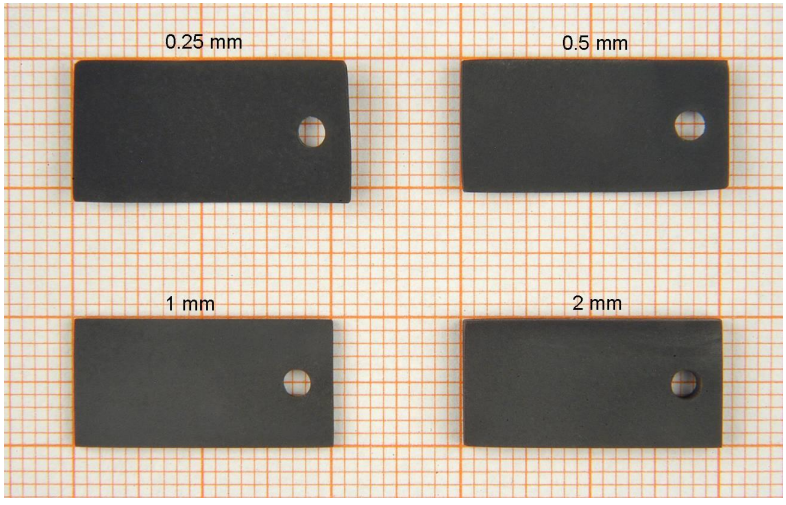

Figure 5.159: Macro images of Nb/Si-free, tungsten alloyed steel KDN during 1000 h cyclic oxidation at 900 °C in laboratory air. Initial sample size: 20 x 10 mm, with thicknesses varying between 0.25 and 2 mm.

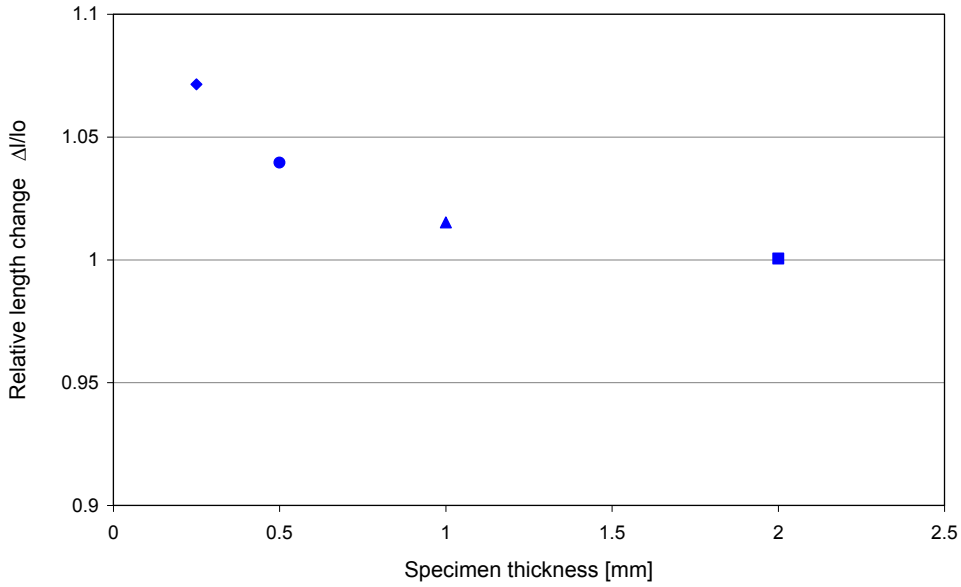

Figure 5.160: Relative length change as function of specimen thickness of steel"3W" (KDN) during 1000 h cyclic oxidation at 900 °C in air.

5.6.6 Oxidation behaviour of Nb-free steels in simulated anode gas

Figure 5.161 shows a comparison of weight change data for the Nb/Si-free steels "1W (KCW), "3W" (KDN) and Crofer 22 APU (KCR) after 1000 h exposure at 900 °C in air and in the simulated anode gas Ar-4%H_2-20%H_2O. The oxidation rate in Ar-H_2-H_2O is for all three steels found to be lower than that in air. The W addition does not seem to have a significant effect on the oxide growth rate.

Figure 5.162 shows cross-sections of samples of the alloys Nb/Si-free steels "1W" (KCW), "3W" (KCW) and Crofer 22 APU (KCR) after 1000 h oxidation at 900 °C in Ar-4%H_2-20%H_2O. In the oxide microstructure porosity is found at the interface between the outer $(Cr,Mn)_3O_4$ spinel and the inner Cr_2O_3 layer. The pore formation is a typical feature for Mn containing steels when oxidized in a low pO_2 environment [104]. The samples oxidized in Ar-H_2-H_2O show a plate like oxide morphology with whisker formation on the sample surface.

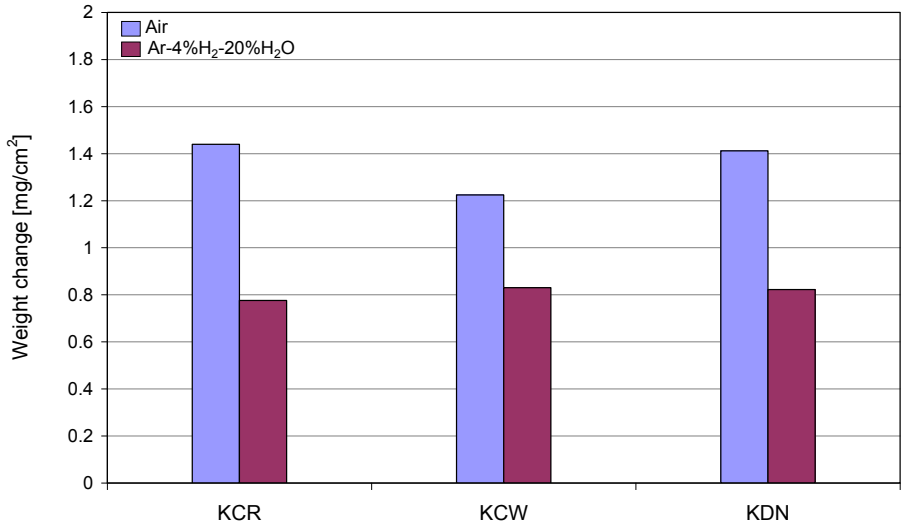

Figure 5.161: Weight change of the Nb/Si-free steels "1W" (KCW), "3W" (KDN) and Crofer 22 APU (KCR) after 1000 h oxidation at 900 °C in air and Ar-4%H_2-20%H_2O. (Data taken from reference [79]). Specimen thickness 2 mm.

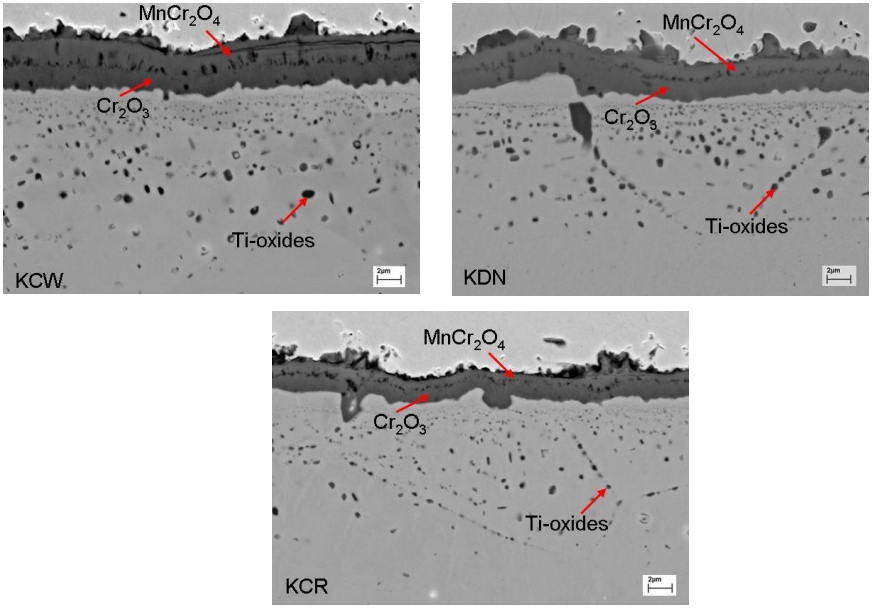

Figure 5.162: SEM images of Nb/Si-free steels ("1W" (KCW), "3W" (KDN)) and Crofer 22 APU (KCR) after 1000 h at 900 °C in Ar-4%H_2-20%H_2O. (Data taken from reference [79]).

5.6.7 Summary of behaviour of Nb-free, W-containing steels

The new findings in combination with the previously obtained results [79] allow the following conclusions:

Tungsten additions up to approximately 3 wt. % in Nb free, high Cr steels of the type Crofer 22 are an effective measure to increase the creep strength by solid solution strengthening. This tungsten addition has up to exposure times of 10.000 h no substantial influence on the intrinsic oxidation properties when considering samples of a few millimeter thickness in air and simulated anode gases in the temperature range 800 °C–900 °C. The dissociation pressure of WO_2 is several orders of magnitude higher than that of Cr_2O_3 so that internal oxidation of tungsten beneath an external chromia layer is, contrary to internal oxidation of niobium, not possible. An important finding is that tungsten addition improves the air oxidation resistance at 800 °C of thin ($d < 1$ mm) steel components. This effect can, in accordance with the theoretical considerations in section 5.6.1, be explained by the effect of increased alloy creep strength on the specimen thickness dependence of the oxidation rate. This positive effect of tungsten addition on the oxidation behaviour of thin-specimens is virtually lost at 900 °C because the creep resistance of the material is quite low at this temperature in spite of the W addition. This is clearly verified by the observed substantial elongation of the thinnest specimens during 900 °C air oxidation.

When added in large amounts (more than approximately 5 wt. %), tungsten addition results at 800 °C in formation of χ-$Cr_7Fe_{10}W_3$ and/or λ-$(Fe,Cr)_2W$ precipitates. This is in agreement with recent findings from Yun et al. [153] who found χ phase precipitates in a 22 % Cr ferritic steel with W additions of 4 % after exposure at 800 °C. The authors found precipitation of χ phase at the scale/steel interface if the W content was higher than 4 %. The finding of these authors differs in this respect from the present results due to the much lower Si content of the alloy used in reference [153].

A technologically very important finding from the results in the proceding sections is that, different from Nb addition, alloying with W does not substantially reduce the silicon

activity in the steel because of the low silicon solubility in the mentioned W-rich intermetallic phases. As a result W additions even as high as 7 wt. % do not suppress the formation of silica sub-layers beneath the external chromia base surface scale during oxidation of Crofer 22 type steels with typical silicon contents of approximately 0.25 wt. %.

5.7 Contact resistance of oxidized interconnect steels

5.7.1 General comments

A major property required for a metallic interconnect material is that it should possess a high electronic conductivity at the SOFC service temperature [2, 18, 23, 30]. For the ferritic steel matrix this requirement is fulfilled, however the oxide scales formed during the high temperature service possesses a far smaller electronic conductivity than the metallic substrate and may thus substantially decrease the overall electronic conductivity of the interconnect. This is mainly a concern at the cathode side of the cell because at the anode side the electrical contact between interconnect and anode is commonly achieved by spot-welding a nickel wire mesh to the interconnect [23]. Therefore the contact resistance measurements described in the following sections only relate to conditions relevant for the cathode side of the SOFC.

The experimental setup used for the measurements of the contact resistance was described in section 4.5. First, a test was carried out to check the long term stability of the experimental setup using rectangular samples (10 x 10 x 3 mm) of sintered $LaCrO_3$ ceramic. The $LaCrO_3$ material was selected for this purpose because it was previously proposed as possible interconnect material for SOFC's [2, 14, 18, 23, 30]. Figures 5.163 and 5.164 show that the measured ASR values at 800 °C vary between 110 and 180 $m\Omega \cdot cm^2$. The values increase with decreasing temperature, which is a typical behaviour known for semiconducting materials (Figures 5.163). The results illustrate an excellent long term stability of the test facility. The observed minor variations in ASR's between various specimens are probably related to non-ideal homogeneity of the Pt-contact layer and/or to sample porosity.

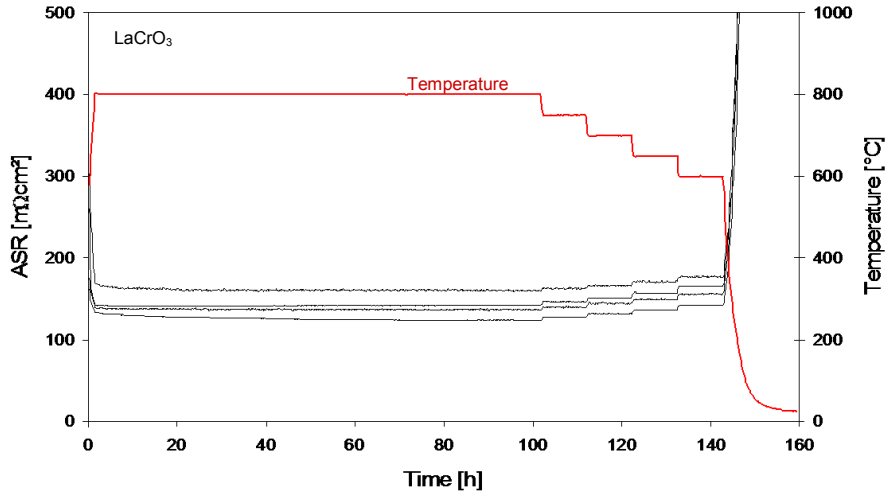

Figure 5.163: Area specific resistance (ASR) values for $LaCrO_3$ standard specimens (10 x 10 x 3 mm) measured at 800 °C in static air at an applied current of 0.1 A per specimen.

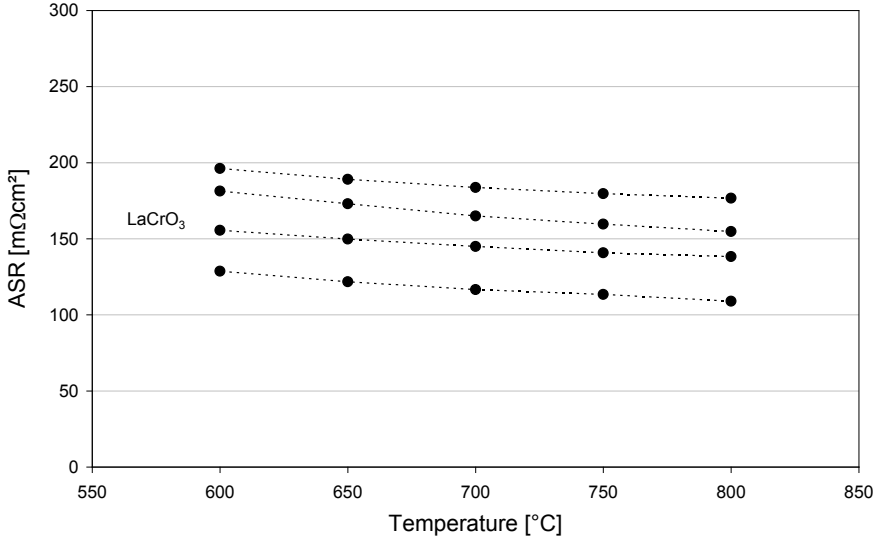

Figure 5.164: Area specific resistance as function of temperature (ASR) for $LaCrO_3$ standard specimens measured in static air at an applied current of 0.1 A. (Specimen thickness 3 mm).

5.7.2 Contact resistance of the Crofer 22 H type ferritic steels

The contact resistance measurements were carried out as described in section 4.5, i.e. the specimens were pre-oxidized in air at 800 °C before a Pt contact paste was applied to the specimen.

Using this experimental procedure, the measured ASR values were commonly found to decrease during the first 25-75 h of the experiment and then remained virtually constant before the final stepwise increase during cooling. As shown in reference [152] two factors are responsible for this typical behaviour and for the observed variation between various specimens, i.e. a poorly reproducible thickness/ morphology of the Pt-layer and reaction (dissolution) of the oxide scale in the Pt-layer.

The time dependences of the ASR values measured for all measured Crofer 22 type materials showed a clear increase of the ASR values during stepwise cooling which confirms the continuity of the oxide scales, i.e. the lack of short circuits.

Figure 5.165 shows the measured results for Crofer 22 APU at 800 °C. After the mentioned, initial slight decrease, the ASR-values after approximately 100 h are in the range 10 to 25 mΩ·cm²; they increase during the stepwise temperature decrease to 600 °C.

The average ASR-values derived from the five specimens are plotted in Figure 5.166 as function of temperature. It can be seen that they range between 7 and 19 mΩcm² at 800 °C to 15 and 34 mΩ·cm² at 600 °C.

The data in Figure 5.167 show that W additions to a Crofer 22 APU type steel do not have a detrimental effect on the ASR values. However, the variants containing Si in addition to W (“5W-0.3Si” (LJF) and “7W-0.25Si” (LJH)) exhibit substantially higher ASR values than the Si-free steels. This can easily be explained by formation of the silica sub-layer beneath the Cr-rich oxide scale observed in the oxidation tests (section 5.6.4).

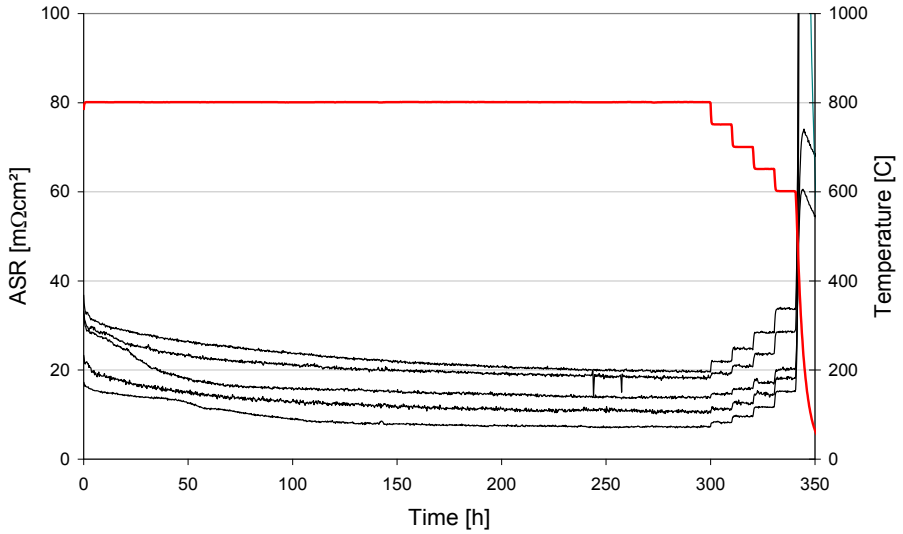

Figure 5.165: Area specific resistance (ASR) values for Crofer 22 APU (KCR) specimens measured at 800 °C in static air at an applied current of 0.1 A per specimen (pre-oxidation for 100 h, at 800 °C in air; specimen thickness 2 mm).

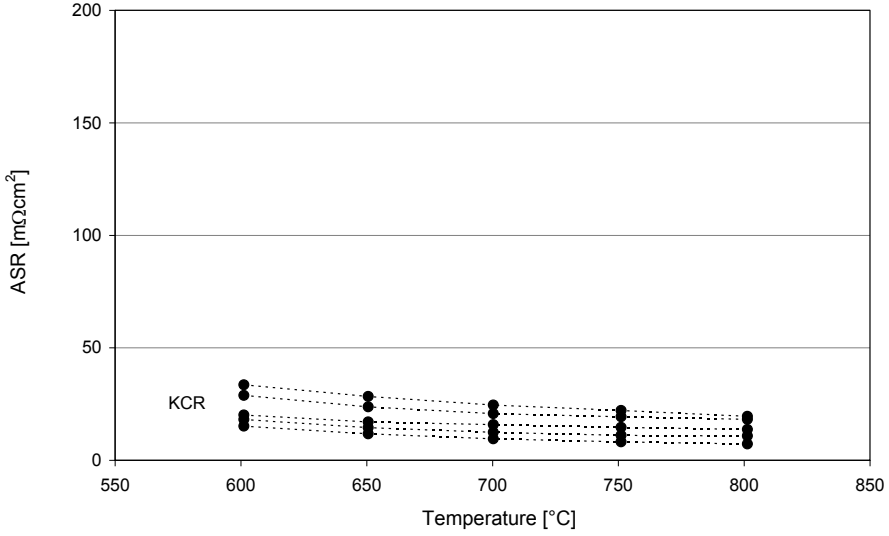

Figure 5.166: Area specific resistance (ASR) as function of temperature for Crofer 22 APU samples measured in static air at 800 °C and an applied current of 0.1 A per specimen. (Specimen thickness 2 mm). Data relate to stepwise temperature decrease after 300 h isothermal exposure.

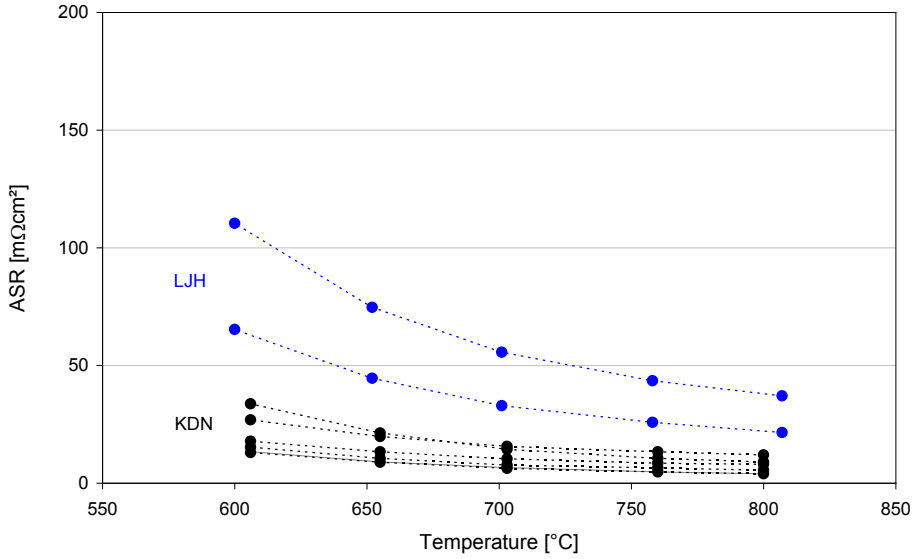

Figure 5.167: Area specific resistance (ASR) as function of temperature for Nb-free steels alloyed with W ("3W" (KDN)) or with W and Si ("5W-0.3Si"(LJF), "7W-0.25Si" (LJH)) measured in static air at 800 °C and an applied current of 0.1 A per specimen. (Specimen thickness 2 mm). Data relate to stepwise temperature decrease after 300 h isothermal exposure.

Figure 5.168 shows the ASR values for the laboratory batch of Crofer 22 H (KUA) as function of temperature. It can be seen that the ASR values for the three specimens are in the range between 11 and 18 mΩ·cm² at 800 °C and 26 and 39 mΩ·cm² at 600 °C. The recorded data is in the same margin as found for Crofer 22 APU (KCR) (Figure 5.166). For the commercial batch of Crofer 22 H (MDO) the measured ASR values vary between 19 and 23 mΩ·cm² at 800 °C and between 97 and 123 mΩ·cm² at 600 °C (Figures 5.169 and 5.170).

It can be seen that most of the samples exhibit at 800 °C ASR values in the range of 15-20 mΩ·cm² which is in agreement with the data presented in the literature [30, 154-155]for high purity, optimized interconnect steels.

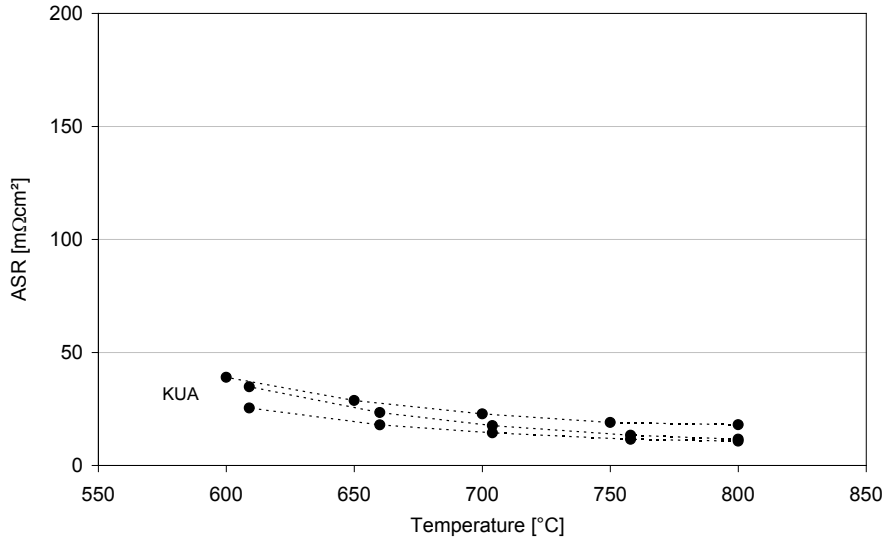

Figure 5.168: Area specific resistance (ASR) as function of temperature for laboratory batch of Crofer 22 H KUA) measured in static air at 800 °C and an applied current of 0.1 A per specimen. (Specimen thickness 2 mm). Data relate to measurement during stepwise temperature decrease after 300 h isothermal exposure.

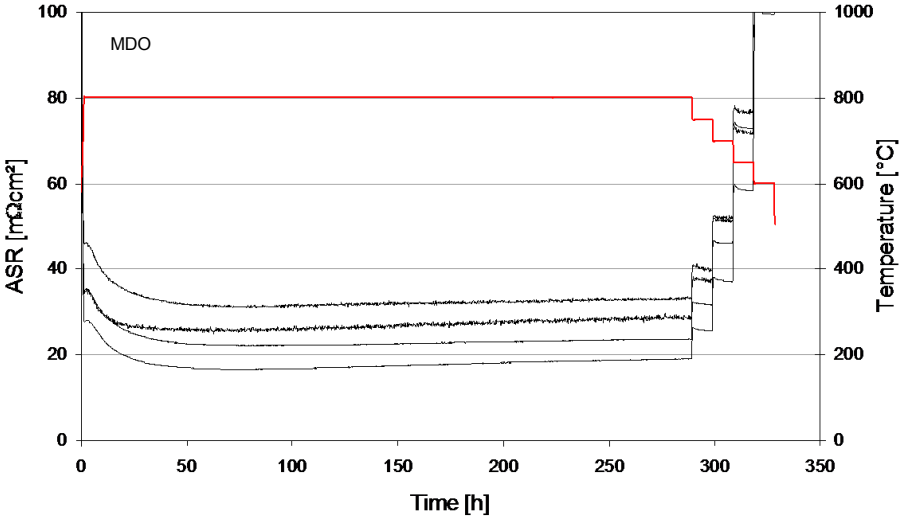

Figure 5.169: Area specific resistance (ASR) values for Crofer 22 H (MDO) specimens measured at 800 °C in static air at an applied current of 0.1 A per specimen (pre-oxidation for 100 h, at 800 °C in air; specimen thickness 2 mm).

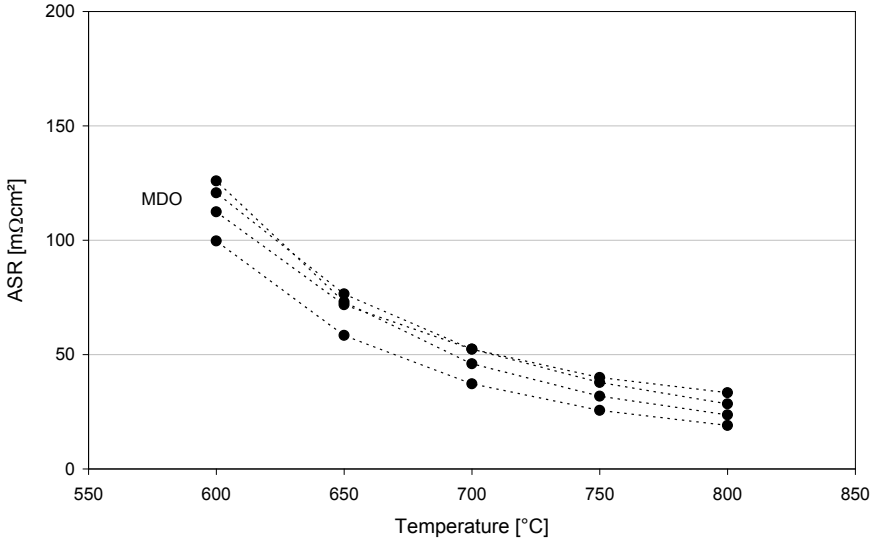

Figure 5.170: Area specific resistance (ASR) as function of temperature for Crofer 22 H (MDO) samples measured in static air at 800 °C and an applied current of 0.1 A per specimen. (Specimen thickness 2 mm). Data relate to measurement during stepwise temperature decrease after 300 h isothermal exposure.

6. Conclusions

The high-Cr, Laves phase strengthened ferritic steel Crofer 22 H, has recently been proposed as construction material for interconnects in solid oxide fuel cells (SOFC). Aim of the present investigation was to get more insight in the details of the oxidation mechanisms in SOFC relevant service environments as a function of time and temperature, with main emphasis on the most commonly used service temperature 800 °C. In these studies the following issues were addressed:

- time and temperature dependence of steel microstructure
- mechanisms of scale formation and subsurface depletion process
- significance of component thickness for oxidation behaviour
- effect of variations in alloy additions Nb, W and Si on microstructure and oxide scale formation
- effect of Mn on scale formation and Cr evaporation
- test of the area specific resistance for the commercial batch Crofer 22 H; effect of composition variation.

With increasing temperature and/or annealing time, a coarsening and redistribution of Laves-phase was found to occur. Precipitates initially located inside the ferrite grains, tend to vanish near the grain boundaries and increasing amounts of Laves phase become precipitated at the ferrite grain boundaries. These microstructural changes were observed for batches produced on a laboratory scale as well as for the commercially produced material.

Thermo gravimetric analyses at different temperatures were carried out to investigate the temperature dependence of the air oxidation behavior for getting more insight into the prevailing oxidation rate laws during isothermal exposure. It was found that the commercial batch of Crofer 22 H showed a slightly more pronounced temperature dependence of oxidation kinetics than the laboratory batches. This effect is likely related to different amounts of C/N-impurities which affects e.g. the internal oxidation of Ti.

As Crofer 22 H, the vast majority of heat-resistant metallic materials developed for application at high temperatures in oxidizing environments, rely for their oxidation resistance on the formation of a dense, well-adherent, protective chromium rich oxide layer on the alloy surface; examples of such materials are nickel base alloys or austenitic steels which contain typically chromium contents in the range 18–25 % and the main strengthening precipitates are chromium base carbides, e.g. of the type $M_{23}C_6$. The formation and continuing growth of the chromia base surface oxide scales during high temperature service results in a subscale chromium depletion and consequently in dissolution of the chromium rich carbide precipitates in the surface-near zone of the component. The creep strength of Crofer 22 H relies, apart from solid solution strengthening by W, on the formation of Laves phase precipitates of the type Fe_2M (M is mainly Nb, W and Si). The oxidation induced subsurface phase transformations occurring in Crofer 22 H fundamentally differs from those in the above mentioned austenitic steels and Ni base alloys because chromium is only a minor constituent of the Laves phase precipitates. The present studies showed that, in spite of this difference, formation of a subsurface layer occurs in which the Laves phase is depleted. However, different from the case for austenitic steels and Ni base alloys, depletion is accompanied by formation of a thin zone near the scale/steel interface in which the Laves phase is enriched. Modeling the diffusion processes and the precipitate dissolution using the DICTRA and ThermoCalc software revealed that this depletion/enrichment process can be explained by the influence of chromium concentration on the niobium activity in the alloy matrix. This effect results in diffusion of niobium in the chromium depleted zone towards the area of lowest chromium concentration, i.e. the scale/alloy interface. The solubility of W and Si in the Laves phase results in parallel diffusion of the element towards the scale/alloy interface. Although this mechanism explains the observed depletion/enrichment process, experiments with solution annealed and pre-aged materials showed, that the subsurface phase transformation processes are at least partially affected by preferential Laves-phase nucleation at the scale/steel interface.

In the development of the interconnector steels Crofer 22 APU it was previously decided to define a Mn addition of 0.4 mass.-% for obtaining at typical SOFC service

temperatures a double layered surface scale consisting of chromia plus Cr/Mn-spinel to reduce the formation of volatile Cr-oxides and -oxyhydroxides during exposure in SOFC cathode gas. In the present studies it was evaluated, whether the addition of Mn had a similar effect on the oxidation of Laves phase strengthened steels of the type Crofer 22 H. The experimented results revealed that a small amount (approx. 0.4 %) of manganese is beneficial because it substantially reduces the growth rate of the double-layered scale in the low pO_2 simulated anode gas. Manganese increases the growth rate in high pO_2 environment (air), but the outer layer of $(Mn,Cr)_3O_4$ was found to significantly reduce the formation of volatile Cr species.

One of the technologically important properties of quasi single phase, high purity steels such as Crofer 22 APU is that during 800 °C air oxidation they exhibit increasing oxidation rates with decreasing specimen thickness. In the present studies it was found that in case of Crofer 22 H this effect did not occur for specimen thicknesses varying between 0.25 and 2 mm up to exposure times of approximately 3000 hours. After that time, the thinnest specimen of 0.25 mm started to exhibit increased oxidation rates whereas indications were found that this occurred for the 0.5 mm specimen after approximately 9000 h.

Based on the experimental results and theoretical considerations it can be derived that the oxidation behaviour of chromia forming ferritic steels such as Crofer 22 APU and Crofer 22 H is affected by the creep strength of the actual component. Differences in creep strength of the component may be related to differences in component thickness and/or intrinsic creep properties of the prevailing alloy. The specimen/component thickness dependence of the oxidation rate is claimed to be related to relaxation of oxide growth stress by creep of the metallic substrate. The occurrence of oxidation induced creep of the thinnest specimens could inequivocally be demonstrated by the measured change in specimen dimensions after long term oxidation. The critical creep rate required for obtaining substantial growth stress relaxation is, for a given oxide thickness and a given growth stress, more easily obtained with poor creep resistance of the metallic substrate. Poor creep strength can either prevail because of the limited thickness of the substrate

material and/or the poor intrinsic creep resistance of the alloy. The latter is e.g. responsible for the fact that Crofer 22 APU specimens, even with a substantial thickness of e.g. 1 mm, exhibit enhanced oxidation rates during air exposure at 800 °C already during the very early stages of oxidation. For the more creep resistant steel Crofer 22 H this is not the case. Only if Laves phase coarsening, either during the actual oxidation experiment or during a pre-ageing treatment, results in a substantial decrease in intrinsic creep strength of the alloy, the resistance of the thinnest samples (e.g. 0.25-0.5 mm) against substantial creep deformation becomes gradually too small to prevent significant relaxation of oxide growth stress, resulting in enhanced oxidation rates.

Hardly any specimen/component thickness dependence of the oxidation rate was found to occur during exposure in anode gas. This is partly caused by the slower oxidation rates compared to air oxidation, but more important seems to be a lower oxide growth stress as a result of the different oxide microstructures compared to that of air formed oxides.

As explained above, the presence of Nb in Crofer 22 H is of major importance for obtaining increased creep strength due to formation of Laves phase precipitates. Also, the substantial solubility of the Nb-rich Laves phase for Si has an important consequence that this element does not internally oxidize if the Nb/Si-ratio in the steel is suitably adjusted. This concept to suppress internal oxidation of silicon has the disadvantage that Nb might internally oxidize and/or increase the chromia growth rate if the Nb/Si ratio would be slightly too low e.g. due to concentration variations in large-scale alloy manufacturing. These disadvantages would not exist if Nb could be replaced by W because the dissociation pressure of W-oxide is higher than that of chromia. From the binary alloy phase diagram Fe-W, it is apparent that in fact it should be possible to obtain precipitate plus solid solution strengthening by adding only W to the steel, i.e. without any Nb addition. The amount of W should then, however be substantially higher than that of Nb in Crofer 22 H, due to the high solubility of W in ferrite. Tungsten additions up to approximately 3 wt. % in Nb free high Cr steel of the type Crofer 22 were found to have no substantial influence on the intrinsic oxidation properties when considering samples of a few millimeter thickness in air and in simulated anode gas. However, tungsten addition

to Crofer 22 APU improves the air oxidation resistance at 800 °C of thin (d < 1 mm) specimens. This effect can, in accordance with the considerations described above, be explained by the increase in alloy creep strength.

This positive effect of tungsten addition on the oxidation behaviour of thin-specimens (typically a few tenths of a mm) is significantly smaller at 900 °C because the creep resistance of the material is quite low at this temperature in spite of the W addition.

The microstructural studies revealed that tungsten, when added in large amounts (more than approximately 4 wt. %) results at 800 °C in formation of χ-$Cr_7Fe_{10}W_3$ and/or λ-$(Fe,Cr)_2W$ precipitates. It was, however; found that tungsten additions do not substantially reduce the silicon activity in the steel because of the low silicon solubility in the mentioned phases. Therefore, W additions up to 7 wt. % do not suppress the formation of silica sub-layers in Crofer 22 type steels with typical silicon contents of approximately 0.25 wt. %.

A major property required for a metallic interconnect material is a suitable electronic conductivity of the surface oxide scales at the SOFC service temperature. This is mainly a concern at the cathode side of the cell because at the anode side the electrical contact between interconnect and anode is commonly achieved by spot-welding a nickel wire mesh to the interconnect. Therefore contact resistance measurements were carried out in the present investigation related to conditions relevant for the cathode side of the SOFC. The experimental results showed that the electrical conductivity of the oxide scales formed during air exposure of Crofer 22 H were in a similar range as the values measured for Crofer 22 APU. This was not the case for Nb-free model alloys with similar Si content as Crofer 22 H. In those materials formation of a near-continuous silica sub-layer adversely affected the oxide scale conductivity.

7. References

1. A. B. Stambouli, E. Traversa, "Solid oxide fuel cells (SOFCs): a review of an environmentally clean and efficient source of energy". Renewable and Sustainable Energy Reviews, vol. 6, pp. 22, 2002.
2. Z. Yang, "Recent advances in metallic interconnects for solid oxide fuel cells". International Materials Reviews, vol. 53, pp. 15, 2008.
3. W. J. Quadakkers, T. Malkow, J. Piron Abellan, U. Flesch, V. Shemet, L. Singheiser, “Suitability of ferritic steels application as construction materials for SOFC interconnects”, Proceeding 4th European Solid Oxide Fuel Cell Forum, J. McEvoy Edt. Oberrohrdorf, Switzerland, vol.2, pp.9, 2000.
4. T. Malkow, U. Crone, A. M. Laptev, T. Koppitz, U. Breuer, W. J. Quadakkers, "Thermal expansion characteristics and corrosion behaviour of ferritic steels for SOFC interconnects ". Solid oxide fuel cells (SOFC V), The Electrochemical Society Proceeding Series, vol. PV 97-18, pp. 8, 1997.
5. J. Piron Abellan, V. Shemet, F. Tietz, L. Singheiser, W. J. Quadakkers, “Ferritic steel interconnect for reduced temperature SOFC”, The Electrochemical Society Proceeding Series, vol. PV 2001-16, pp. 8, 2001.
6. K. Hilpert, W. J. Quadakkers, L. Singheiser, “Interconnects”, Handbook of Fuel Cells-Fundamentals, Technology and Applications, vol. 4, pp. 17, 2003.
7. R. Hojda, W. Heimann, W. J. Quadakkers, "Production-capable materials concept for high temperature fuel cells". ThyssenKrupp Techforum, pp. 3, 2003.
8. N.N, "Crofer 22 APU material data sheet 4046", ThyssenKrupp VDM, Werdohl, Germany, Dec 2006.
9. J. Froitzheim, G. H. Meier, L. Niewolak, P. J. Ennis, H. Hattendorf, L. Singheiser, W. J. Quadakkers, "Development of high strength ferritic steel for interconnect application in SOFCs". Journal of Power Sources, vol. 178, pp. 10, 2008.
10. N.N, "Crofer 22 H material data sheet 4050", Thyssenkrupp VDM, Werdohl, Germany, June 2008.
11. L. Carrette, K. A. Friedrich, U. Stimming, "Fuel cells - fundamentals and applications". Fuel cells, vol. 1, pp. 34, 2001.
12. U. Bossel, "The Birth of the Fuel Cell", European Fuel Cell Forum, Oberrohrdorf, Switzerland, 2000.
13. N. Q. Minh, "Solid oxide fuel cell technology-features and applications". Solid State Ionics, vol. 174, pp. 6, 2004.
14. W. Z. Zhu, S. C. Deevi, "Development of interconnect materials for solid oxide fuel cells". Materials Science and Engineering vol. A348, pp. 16, 2003.
15. S. M. Haile, "Fuel cell materials and components". Acta Materialia, vol. 51, pp. 19, 2003.
16. J. C. Ruiz Morales, J. Canales Vazquez, D. Marrero Lopez, J. Pena Martinez, D. Perez Coll, P. Nunez, C. Savaniu, C. Rodriguez Placeres, V. I. Dorta Martin, B. Ballesteros, "Pilas de combustibles de oxidos solidos (SOFC)", Centro de la cultura popular canaria, ISBN 978-84-7926-567-0, 2008.
17. J. Larminie, A. Dicks, "Fuel Cell Sytems Explained". John Wiley & Sons, Chichester, UK, 2003.

18. L. Singheiser, P. Huczkowski, T. Markus, W. J. Quadakkers, "High temperature corrosion issues for metallic materials in solid state oxide fuel cells", Shreir's Corrosion, vol. 1, pp. 35, Elsevier, Amsterdam, 2010.
19. S. C. Singhal, "Solid oxide fuel cells for stationary, mobile and military applications". Solid State Ionics, vol. 152-153, pp. 5, 2002.
20. S. C. Singhal, "Science and technology of solid oxide fuel cells". MRS Bulletin, vol. 25, pp. 5, 2000.
21. F. Tietz, H. P. Buchkremer, D. Stöver, "10 Years of materials research for solid oxide fuel cells at Forschungszentrum Jülich". Journal of Electroceramics, vol. 17, pp. 6, 2006.
22. S. C. Singhal, "Advances in solid oxide fuel cell technology". Solid State Ionics, vol. 135, pp. 8, 2000.
23. L. Antoni, "Materials for solid oxide fuel cells : the challenge of their stability". Materials Science Forum, vol. 461-464, pp. 16, 2004.
24. A. Mai, V. Haanappel, S. Uhlenbruck, F. Tietz, D. Stöver, "Ferrite-based perovskites as cathode materials for anode-supported solid oxide fuel cells: Part I. Variation of composition ". Solid State Ionics, vol. 176, pp. 9, 2005.
25. N. Q. Minh, "Ceramic fuel cells". Journal of American Ceramic Society, vol. 76, pp. 25, 1993.
26. S. P. Jiang, "Development of lanthanum strontium manganite perovskite cathode materials of solid oxide fuel cells: a review". Journal of Materials Science, vol. 43, pp. 34, 2008.
27. N. H. Menzler, F. Tietz, S. Uhlenbruck, H. P. Buchkremer, D. Stöver, "Materials and manufacturing tecnologies for solid oxide fuel cells". Journal of Materials Science vol. 45, pp. 26, 2010.
28. W. Z. Zhu, S. C. Deevi, "A review on the status of anode materials for solid oxide fuel cells". Materials Science and Engineering A, vol. 362, pp. 11, 2003.
29. R. J. Gorte, J. M. Vohs, "Nanostructured anodes for solid oxide fuel cells". Current Opinion in Colloid & Interface Science, vol. 14, pp. 8, 2009.
30. W. J. Quadakkers, J. Pirón Abellán, V. Shemet, L. Singheiser, "Metallic interconnectors for solid oxide fuel cells - a review". Materials at High Temperatures, vol. 20, pp. 12, 2003.
31. S. C. Singhal, K. Kendall, "High Temperature Solid Oxide Fuel Cells: Fundamentals, Design and Applications", Elsevier, Oxford, UK, 2006.
32. A. C. Muller, D. Herbstritt, E. Ivers-Tiffee, "Development of a multilayer anode for solid oxide fuel cells". Solid State Ionics, vol. 152-153, pp. 5, 2002.
33. P. Kofstad, R. Bredesen, "High Temperature corrosion in SOFC environments". Solid State Ionics vol. 52, pp. 6, 1992.
34. P. Kofstad, "High Temperature Corrosion". Elsevier, Barking, UK, 1988.
35. D. J. Young, "High temperature oxidation and corrosion of metals", Elsevier, Oxford, 2008.
36. N. Birks, G. H. Meier, F. S. Pettit, "Introduction to the High Temperature Oxidation of Metals". Cambridge University Press, Cambridge, 2006.
37. A. S. Khanna, "Introduction of high temperature oxidation and corrosion", ASM International, 2002.

38. A. Atkinson, R. I. Taylor, A. E. Hughes, "A quantitative demonstration of the grain boundary diffusion mechanism for the oxidation of metals". Philosophical Magazine A, vol. 45, pp. 10, 1982.
39. C. Wagner, "Beitrag zur Theorie des Anlaufvorgangs". Z. Phys. Chem., vol. 21, pp. 16, 1933.
40. Z. Yang, P. Singh, J. W. Stevenson, G. G. Xia, "Investigation of modified Ni–Cr–Mn base alloys for SOFC interconnect applications". Journal of the Electrochemical Society, vol. 153, pp. 6, 2006.
41. H. E. Evans, “Interfacial crack growth during temperature changes”, in Cyclic Oxidation of High Temperature Materials, M. Schütze, W.J. Quadakkers Edts, Frankfurt/Main, vol.27, pp. 3, 1999.
42. B. C. H. Steele, "Materials for IT-SOFC stacks: 35 years R&D: the inevitability of gradualness?". Solid State Ionics, vol. 134, pp. 17, 2000.
43. D. England, A. Virkar, "Oxidation kinetics of some nickel-based superalloy foils and electronic resistance of the oxide scale formed in air. Part I". Journal Electrochemical Society, vol. 146, pp. 6, 1999.
44. F. Tietz, H.-P. Buchkremer, D. Stöver, "Components manufacturing for solid oxide fuel cells". Solid State Ionics, vol. 152-153, pp. 8, 2002.
45. K. Huang, P. Y. Hou, J. B. Goodenough, "Reduced area specific resistance for iron-based metallic interconnects by surface oxide coatings". Materials Research Bulletin, vol. 36, pp. 14, 2000.
46. P. Kofstad, "Defects and transport properties of metal oxides". Oxidation of Metals, vol. 44, pp. 24, 1995.
47. A. Holt, P. Kofstad, "Electrical conductivity and defect structure of Cr_2O_3. I. High temperatures (>~1000°C)". Solid State Ionics, vol. 69, pp. 9, 1994.
48. J. H. Park, K. Natesan, "Electronic transport in thermally grown Cr_2O_3". Oxidation of Metals, vol. 33, pp. 23, 1990.
49. A. Holt, P. Kofstad, "Electrical conductivity and defect structure of Cr_2O_3. II. Reduced temperatures (<~1000°C)". Solid State Ionics, vol. 69, pp. 6, 1994.
50. A. Holt, P. Kofstad, "Electrical conductivity and defect structure of Mg-doped Cr_2O_3". Solid State Ionics, vol. 100, pp. 8, 1997.
51. A. Holt, P. Kofstad, "Electrical conductivity of Cr_2O_3 doped with TiO_2". Solid State Ionics, vol. 117, pp. 4, 1999.
52. W. C. Hagel, A. U. Seybolt, "Cation Difussion in Cr_2O_3". Journal of Electrochemical Society, vol. 108, pp. 6, 1961.
53. H. Nagai, T. Fujikawa, "Electrical conductivity of chromia doped with La_2O_3, Y_2O_3 and NiO". Transactions of the Japan Institute of Metals, vol. 24, pp. 7, 1983.
54. M. Y. Su, Dissertation Abstract International, vol. 48, 1988.
55. J. A. Crawford, R. W. Vest, "Electrical conductivity of single crystal Cr_2O_3". Journal of Applied Phisics, vol. 35, pp. 5, 1964.
56. H. Nagai, S. Ishikawa, N. Amano, "Electrical conductivity of sintered Cr_2O_3 simultaneously doped with NiO and rare earth oxide at low oxygen potential". Transactions of the Japan Institute of Metals, vol. 26, pp. 9, 1985.
57. H. Nagai, K. Ohbayashi, "Effect of TiO_2 on the sintering and the electrical conductivity of Cr_2O_3,". Journal of the American Cerarmic Society, vol. 72, pp. 3, 1989.

58. P. Huczkowski, W. J. Quadakkers, “Effect of geometry and composition of Cr steels on oxide scale properties relevant for interconnector applications in solid oxide fuel cells (SOFCs)”, RWTH Aachen, Report Forschungszentrum Jülich, Energy Technology, Vol. 65, ISBN 978-3-89336-484-8, 2007.
59. F. J. Pirón Abellán, W. J. Quadakkers, “Development of ferritic steels for application as interconnect materials for intermediate temperature solid oxide fuel cells (SOFCs)”, Report Forschungszentrum Jülich, Jül-4170, ISSN 0944-2952, 2005.
60. J. Piron Abellan, F. Tietz, V. Shemet, A. Gil, T. Ladwein, L. Singheiser, W. J. Quadakkers, “Long term oxidation behaviour and compatibility with contact materials of newly developed ferritic interconnector steels”, Proceedings 5th European Solid Oxide Fuel Cell Forum, J. Huijsmans Edt, Lucerne, Switzerland, vol. 1, pp.8, 2002.
61. I. G. Wright, "Metals Handbook". 9th Edition. Metals Park, OH, 1987.
62. R. W. K. Honeycombe, "Steels microstructure and properties". Edward Arnold, London, UK, 1987.
63. S. M. Dubiel, "Sigma phase- one of the main reasons for deterioration of stainless steels properties". Hyperfine Interact, vol. 189, pp. 8, 2009.
64. G. F. Vander Voort, "Embrittlement of steels". Materials Park, OH, 1990.
65. H. Okamoto, "Phase diagrams of binary iron alloys", ASM Materials Park, US, 1993.
66. L. Niewolak, E. Wessel, L. Singheiser, W. J. Quadakkers, "Potential suitability of ferritic and austenitic steels as interconnect materials for solid oxide fuel cells operating at 600 °C". Journal of Power Sources, vol. 195, pp. 8, 2010.
67. G. Sauthoff, W. Speller, "Kinetic of sigma phase precipitation in Fe-Cr-Si alloys". Zeitschrift fur Metallkunde, vol. 72, pp. 6, 1981.
68. J. E. Hammer, S. J. Laney, R. W. Jackson, K. Coyne, F. S. Pettit, G. H. Meier, "The oxidation of ferritic stainless steels in simulated solid-oxide fuel-cell atmospheres". Oxidation of Metals, vol. 67, pp. 38, 2007.
69. ThermoCalc Software AB. Stockholm, SE, 1991.
70. T. B. Massalski, "Binary alloy phase diagrams". T.B. Massalski, H. Okamoto Edts. ASM International, Metals Park, OH, 1986.
71. M. Hättestrand, P. Larsson, G. Chai, J. Nilsson, J. Odqvist, "Study of decomposition of ferrite in a duplex stainless steel cold worked and aged at 450–500 °C". Materials Science and Engineering A, vol. 499, pp. 3, 2009.
72. M. Ueda, H. Taimatsu, “Thermal expansivity and high-temperature oxidation resistance of Fe-Cr-W alloys developed for a metallic separator of SOFC”, 4th European Solid Oxide Fuel Cell Forum, J. McEvoy Edt, Oberrohrdorf, Switzerland, vol.2, pp. 8, 2000.
73. K. Hilpert, D. Das, M. Miller, D. H. Peck, R. Weiss, "Chromium vapor species over solid oxide fuel cell interconnect materials and their potential for degradation processes". The Electrochemical Society, vol. 143, pp. 5, 1996.
74. C. Sun, R. Hui, J. Roller, "Cathode materials for solid oxide fuel cells: a review". Journal of Solid State Electrochemical, vol. 14, pp. 19, 2010.

75. J. W. Fergus, "Effect of cathode and electrolyte transport properties on chromium poisoning in solid oxide fuel cells". International Journal of Hydrogen Energy, vol. 32, pp. 7, 2007.
76. M. Stanislowski, J. Froitzheim, L. Niewolak, W. J. Quadakkers, K. Hilpert, T. Markus, L. Singheiser, "Reduction of chromium vaporization from SOFC interconnectors by highly effective coatings". Journal of Power Sources, vol. 164, pp. 11, 2007.
77. W. J. Quadakkers, J. Pirón Abellán, V. Shemet, "Metallic materials in solid oxide fuel cells". Materials Research, vol. 7, pp. 5, 2004.
78. W. J. Quadakkers, L. Niewolak, P. J. Ennis, "Ferritic steel used for a fuel cell stack or a bipolar plate for a fuel cell stack containing precipitations of an intermetallic phase". Patent number(s):PCT/DE2007/000166, WO2007093148-A1; DE102006007598-A1 (18.02.2006).
79. J. Froitzheim, “Ferritic steel interconnects and their interactions with Ni base anodes in solid oxide fuel cells (SOFC)”, RWTH Aachen, Report Forschungszentrum Jülich, Energy and Environment, Vol. 16, ISBN 978-3-89336-540-1, 2008.
80. K. Honegger, A. Plas, R. Diethelm, W. Glatz, H. Yokokawa, S. C. Singhal, "Evaluation of ferritic steel interconnects for SOFC stacks". Solid Oxide Fuel Cell VII, The Electrochemical Society Proceeding Series, vol. PV 2001-16, pp. 8, 2001.
81. N. Sakai, T. Horita, Y. P. Xiong, K. Yamaji, H. Kishimoto, M. E. Brito, H. Yokokawa, T. Maruyama, "Structure and transport property of manganese-chromium-iron oxide as a main compound in oxide scales of alloy interconnects for SOFCs". Solid State Ionics, vol. 176, pp. 5, 2005.
82. P. Huczkowski, N. Christiansen, V. Shemet, L. Niewolak, J. Pirón Abellán, L. Singheiser, W. J. Quadakkers, "Growth mechanisms and electrical conductivity of oxide scales on ferritic steels proposed as interconnect materials for SOFC's". Fuel Cells, vol. 6, pp. 6, 2006.
83. H. P. Buchkremer, U. Dieckmann, L. De Haart, H. Kabs, U. Stimming, D. Stöver, "Advances in the anode supported planar SOFC technology". The Electrochemical Society Proceeding Series, Solid Oxide Fuel Cell V, vol. PV 97-40, pp. 10, 1997.
84. P. Lamp, J. Tachtler, O. Finkenwirth, S. Mukerjee, S. Shaffer, "Development of an Auxiliary Power Unit with Solid Oxide Fuel Cells for Automotive Applications". Fuel Cells, vol. 3, pp. 6, 2003.
85. P. Huczkowski, S. Ertl, J. Piron Abellan, N. Christiansen, T. Höfler, V. Shemet, L. Singheiser, W. J. Quadakkers, "Effect of component thickness on lifetime and oxidation rate of chromia forming ferritic steels in low and high pO_2 environments". Materials at High Temperatures, vol. 22, pp. 9, 2005.
86. P. Huczkowski, N. Christiansen, V. Shemet, J. Pirón Abellán, L. Singheiser, W. J. Quadakkers, "Oxidation limited life times of chromia forming ferritic steels". Materials and Corrosion, vol. 55, pp. 5, 2004.
87. P. Huczkowski, N. Christiansen, V. Shemet, J. Pirón Abellán, L. Singheiser, W. J. Quadakkers, "Oxidation induced lifetime limits of chromia forming ferritic

interconnector steels". Journal of Fuel Cell Science and Technology, vol. 1, pp. 4, 2004.
88. J. Zurek, G. H. Meier, E. Essuman, M. Hansel, L. Singheiser, W. J. Quadakkers, "Effect of specimen thickness on the growth rate of chromia scales on Ni-base alloys in high- and low-pO_2 gases". Journal of Alloys and Compounds, vol. 467, pp. 8, 2009.
89. F. Abe, "Creep-resistant steels", F, Abe, T-U Kern and R. Viswanathan Edt. Woodhead Publishing Limited and CRC Press LLC, 2008.
90. R. W. Evans, B. Wilshire, "Introduction to Creep", The Institute of Materials, London, 1993.
91. B. Kuhn, C. Asensio Jimenez, L. Niewolak, T. Hüttel, T. Beck, H. Hattendorf, L. Singheiser, W. J. Quadakkers, "Effect of Laves phase strengthening on the mechanical properties of high Cr ferritic steels for solid oxide fuel cell interconnect application". Materials Science and Engineering A vol. 528, pp. 11, 2011.
92. http://www.fz-juelich.de/iek/iek-3/EN/UeberUns/Kooperationen/ZeuS-III.html;jsessionid=E3F73CFB082C16AA28B0A25918B37B0D. Latest visit 1.8.2012.
93. F. Stein, M. Palm, G. Sauthoff, "Structure and stability of Laves phases. Part I. Critical assessment of factors controlling Laves phase stability". Intermetallics, vol. 12, pp. 7, 2004.
94. F. Stein, M. Palm, G. Sauthoff, "Structure and stability of Laves phases. Part II – structure type variatians in binary and ternary systems". Intermetallics, vol. 13, pp. 18, 2005.
95. J. Zurek, M. Michalik, L. Singheiser, W. J. Quadakkers, "The effect of gas flow rate on the oxide scale morphology of a 10%Cr-ferritic steels in Ar-H_2O and Ar-H_2-H_2O mixtures". Materials Science Forum, vol. 522-523, pp. 7, 2006.
96. D. J. O'Connor, B. A. Sexton, R. S. C. Smart, “Surface analysis methods in materials science”, Springer, ISSN 0931-5195, 2003.
97. W. J. Quadakkers, H. Viefhaus, “The application of surface analysis techniques in high temperature corrosion research”, EFC Publication No. 14, Guidelines for Methods of Testing and Research in High Temperature Corrosion, The Institute of Materials, London, pp. 28, 1995.
98. W. J. Quadakkers, A. Elschner, H. Holzbrecher, K. Schmidt, W. Speier, H. Nickel, "Analysis of composition and growth mechanisms of oxide scales on high temperature alloys by SNMS, SIMS, and RBS". Mikrochimica Acta, vol. 107, pp. 9, 1992.
99. W. Ostwald, "Stoechiometrie und Verwandtschaftslehre". Zeitschrift fuer Physikalische Chemie, vol. 22, pp. 41, 1897.
100. W. Ostwald, "Stochiometrie und Verwandtschaftslehre". Zeitschrift fuer Physikalische Chemie, vol. 34, pp. 8, 1900.
101. A. Naoumidis, H. A. Schulze, W. Jungen, P. Lersch, "Phase studies in the chromium-manganese-titanium oxide system at different oxygen partial pressures". Journal of the European Ceramic Society, vol. 7, pp. 8, 1991.

102. P. J. Ennis, W. J. Quadakkers, “Corrosion and creep of nickel-base alloys in steam reforming gas”, High Temperature Alloys - Their Exploitable Potential. Elsevier, London. Petten, NL, pp. 9, 1985.
103. S. R. J. Saunders, M. Monteiro, F. Rizzo, "The oxidation behaviour of metals and alloys at high temperatures in atmospheres containing water vapour: A review". Progress in Material Science, vol. 53, pp. 62, 2008.
104. A. N. Hansson, M. A. J. Somers, "Influence of the oxidation environment on scale morphology and oxidation rate of Fe–22Cr". Materials at High Temperatures, vol. 22, pp. 6, 2005.
105. L. Mikkelsen, S. Linderoth, "High temperature oxidation of Fe-Cr alloy in O_2-H_2-H_2O atmospheres; microstructure and kinetics". Materials Science and Engineering A, vol. 361, pp. 14, 2003.
106. J. Zurek, D. J. Young, E. Essuman, M. Hänsel, H. J. Penkalla, L. Niewolak, W. J. Quadakkers, "Growth and adherence of chromia based surface scales on Ni-base alloys in high- and low-pO2 gases". Materials Science and Engineering A, vol. 477, pp. 11, 2008.
107. T. Malkow, W. J. Quadakkers, L. Singheiser, H. Nickel, “Untersuchungen zum Langzeitverhalten von metallischen Interkonnektorwerkstoffen der Hochtemperatur-Brennstoffzelle (SOFC) im Hinblick auf die Kompatibilität mit kathodenseitigen Kontaktschichten”, RWTH Aachen, Report Forschungszentrum Jülich, Jül-3589, ISSN 0944-2952, 1998.
108. R. C. Reed, "The Superalloys: Fundamentals and Applications", Cambridge University Press, 2006.
109. S. Kihara, J. B. Newkirk, A. Ohtomo, Y. Saiga, "Morphological changes of carbides during creep and their effects on the creep properties of Inconel 617 at 1000°C". Metallurgical Transactions A, vol. 11, pp. 12, 1980.
110. T. Sourmail, "Precipitation in creep resistant austenitic stainless steels". Materials Science and Technology, vol. 17, pp. 14, 2001.
111. P. J. Ennis, W. J. Quadakkers, H. Schuster, "The effect of oxidation induced chromium carbide depletion on the creep strength of alloy 617". Journal de Physique IV, vol. 3 pp. 7, 1993.
112. D. J. Young, B. Gleeson, "Alloy phase transformations driven by high temperature corrosion processes". Corrosion Science, vol. 44, pp. 12, 2002.
113. R. Bauer, M. Baccalaro, L. P. H. Jeurgens, M. Pohl, E. J. Mittemeijer, "Oxidation behavior of Fe-25Cr-20Ni-2.8Si during isothermal oxidation at 1,286 K; life time prediction". Oxidation of Metals, vol. 69, pp. 20, 2008.
114. H. E. Evans, A. T. Donaldson, "Silicon and chromium depletion during long-term oxidation of austenitic steel". Oxidation of Metals, vol. 50, pp. 18, 1998.
115. T. J. Nijdam, L. P. H. Jeurgens, W. G. Sloof, "Modelling the thermal oxidation of ternary alloys - Compositional changes in the alloy and the development of oxide phases". vol. 51, pp. 12, 2003.
116. D. P. Whittle, "The oxidation of finite samples of heat-resistant alloys". Corrosion Science, vol. 12, pp. 3, 1972.
117. R. N. Durham, B. Gleeson, D. J. Young, "Factors affecting chromium carbide precipitate dissolution during alloy oxidation". Oxidation of Metals, vol. 50, pp. 26, 1998.

118. A. Borgenstam, A. Engström, L. Höglund, J. Ågren, "DICTRA, a tool for simulation of diffusional transformations in alloys". Journal of Phase Equilibria, vol. 21, pp. 11, 2000.
119. D. J. Young, B. A. Pint, "Chromium volatilization rates from Cr2O3 scales into flowing gases containing water vapor". Oxidation of Metals, vol. 66, pp. 16, 2006.
120. T. A. Ramanarayanan, R. Ayer, R. Petkovic-Luton, D. P. Leta, "The influence of yttrium on oxide scale growth and adherence". Oxidation of Metals, vol. 29, pp. 28, 1988.
121. W. J. Quadakkers, "Growth mechanisms of oxide scales on ODS alloys in the temperature range 1000-1100 "C". Werkstoffe und Korrosion, vol. 41, pp. 9, 1990.
122. A. Chyrkin, P. Huczkowski, V. Shemet, L. Singheiser, W. J. Quadakkers, "Sub-scale depletion and enrichment processes during high temperature oxidation of the nickel base alloy 625 in the temperature range 900-1000 °C". Oxidation of Metals, vol. 75, pp. 23, 2011.
123. H. Strandlund, H. Larsson, "Diffusion process simulations - an overview of different approaches". Defects and Diffusion Forum vol. 233-234, pp. 17, 2004.
124. C. Gindorf, L. Singheiser, K. Hilpert, "Determination of chromium vaporisation from Fe,Cr base alloys used as interconnect in fuel cells (SOFC)". Steel Research, vol. 72, pp. 5, 2001.
125. S. P. Jiang, J. P. Zhang, X. G. Zheng, "A comparative investigation of chromium deposition at air electrodes of solid oxide fuel cells". Journal of the European Ceramic Society, vol. 22, pp. 12, 2002.
126. H. Asteman, J. E. Svensson, L. G. Johansson, M. Norell, "Indication of chromium oxide hydroxide evaporation during oxidation of 304L at 873 K in the presence of 10% water vapor". Oxidation of Metals, vol. 52, pp. 6, 1999.
127. J. Piron-Abellan, V. Shemet, F. Tietz, L. Singheiser, W. J. Quadakkers, "Ferritic Steel Interconnect for Reduced Temperature SOFC". The Electrochemical Society Proceeding Series, vol. PV 2001-16, pp. 811, 2001.
128. H. Greiner, T. Grögler, W. Köck, R. F. Singer, “Chromium based alloys for high temperature SOFC application”, Proceedings of the 4th International Symposium on Solid Oxide Fuel Cells, Solid oxide fuel cells IV, pp.10, 1995.
129. W. J. Quadakkers, J. Zurek, "Oxidation in steam and steam/hydrogen environments", Shreir's Corrosion, vol. 1, pp. 49, Elsevier, Amsterdam, 2010.
130. J. Zurek, W. J. Quadakkers. Forschungszentrum Jülich, unpublished results, 2007.
131. S. T. Ertl, “Investigations of the oxidation induced lifetime limits of Cr steels relevant for applications in Solid Oxide Fuel Cells (SOFCs)”, PhD Thesis, RWTH Aachen, 2006.
132. T. Horita, Y. Xiong, K. Yamaji, N. Sakai, H. Yokokawa, “Stability of Fe-Cr based alloys in H2-H2O atmosphere for SOFC interconnector”, Proceeding 5th European Solid Oxide Fuel Cell Forum, Lucerne, Switzerland, Vol. 1, pp. 7, 2002.
133. FactSage Software, GTT Technologies. Aachen, Germany.
134. W. J. Quadakkers, P. Huczkowski, D. Naumenko, J. Zurek, G. H. Meier, L. Niewolak, L. Singheiser, "Why the growth rates of alumina and chromia scales on

thin specimens differ from those on thick specimens". Materials Science Forum, vol. 595-598, pp. 7, 2008.
135. M. Schütze, "Plasticity of protective oxide scales". Materials Science and Technology, vol. 6, pp. 6, 1990.
136. M. Schütze, “Mechanical interactions in oxide scales”, Pennington, 1998.
137. I. Küppenbender, M. Schütze, "The deformation behavior of NiO scales on Ni in argon and air at temperatures from 20 to 800°C with respect to the relief of growth stresses". Oxidation of Metals, vol. 42, pp. 35, 1994.
138. H. Echsler, E. Alija Martinez, L. Singheiser, W. J. Quadakkers, "Residual stresses in alumina scales grown on different types of Fe-Cr-Alo alloys: effect of specimen geometry and cooling rate". Material Science and Engineering A, vol. 384, pp. 11, 2004.
139. H. Mehrer, "The effect of pressure on diffusion". Defect and Diffusion Forum, vol. 129-130, pp. 19, 1996.
140. R. W. Evans, B. Wilshire, "Introduction to Creep", The Institute of Materials, London, 1985.
141. M. Schütze, "Protective oxide scales and their breakdown", The Institute of Corrosion and Wiley Series on Corrosion and Protection, John Wiley & Sons, Chichester, 1997.
142. S. J. Bull, “Modeling of residual stress in oxide scales”, Oxidation of Metals, vol.49, nos.1/2, pp. 17, 1998.
143. W. Przybilla, M. Schütze, "Growth stresses in the oxide scales on TiAl alloys at 800 and 900°C". Oxidation of Metals, vol. 58, pp. 22, 2002.
144. Y.-T. Chiu, C.-K. Lin, "Effects of Nb and W additions on high-temperature creep properties of ferritic stainless steels for solid oxide fuel cell interconnect". Journal of Power Sources, vol. 198, pp. 8, 2012.
145. J. P. Wilber, M. J. Bennett, J. R. Nicholls, “Cyclic oxidation of high temperature materials”, vol. 27, pp. 14, Maney Publishing, London, 1999.
146. A. M. Huntz, M. Schütze, "Stresses generated during oxidation sequences and high temperature fracture". Materials at High Temperatures, vol. 12, pp. 10, 1994.
147. H. E. Evans, "Stress effects in high temperature oxidation of metals". International Material Reviews, vol. 40, pp. 40, 1995.
148. A. G. Evans, G. B. Crumley, R. E. Demaray, "On the mechanical behavior of brittle coatings and layers". Oxidation of Metals, vol. 20, pp. 23, 1983.
149. W. N. Liu, X. Sun, E. Stephens, M. Khaleel, "Effect of substrate thickness on oxide scale spallation for solid oxide fuel cells". Corrosion Science, vol. 53, pp. 6, 2011.
150. G. Meier. University of Pittsburgh, private comunication, 2011.
151. P. Villars , A. Prince , H. Okamoto "Handbook of ternary alloy phase diagrams". ASM International, Materials Park, OH, 1995.
152. P. Huczkowski, W. J. Quadakkers, in Schriften des Forschungszentrums Jülich, Reihe Energietechnik/Energy Technology 65, Jülich Germany. ISSN 1433-5522, 2007.
153. D. W. Yun, H. S. Seo, J. H. Jun, J. M. Lee, D. H. Kim, K. Y. Kim, "The effect of tungsten addition on the oxidation behavior of Fe-22Cr-0.5Mn ferritic stainless steel". ECS Transactions, vol. 25, pp. 9, 2009.

154. Z. Yang, K. S. Weil, D. M. Paxton, J. W. Stevenson, "Selection and evaluation of heat-resistant alloys for SOFC interconnect applications". Journal of The Electrochemical Society, vol. 150, pp. 13, 2003.
155. J. W. Fergus, "Metallic interconnects for solid oxide fuel cells". Materials Science and Engineering A, vol. 397, pp. 12, 2005.

Acknowledgements

I would like to thank Prof. L. Singheiser not only for giving me the opportunity of working at the IEK-2 Institute at Forschungszentrum Jülich but also for his fruitful supervision and helpful discussions and advice, and, for his pleasing and encouraging leadership.

I would also like to thank Prof. Quadakkers for welcoming me in his group, for his positive impact on my scientific work, sound suggestions and contributions, which made the work stimulating and productive.

Special thanks go to Dr. Niewolak for his logical approach of the scientific work, accurate and constructive criticisms to reach high effectiveness during the interpretation of experimental results and for the excellent teamwork.

I am grateful to Dr. H. Hattendorf for the good coordination and collaboration in the frame of Zeus III project as well as to N. Merki, H. Lippert for the chemical analysis of the materials.

Many thanks to A. Kick and H. Cosler for conducting the high temperature exposures, Dr. Wessel and Dr. Grüner for their help, time and knowledge with the SEM, V. Gutzeit and J. Bartsch for the optical microscopy and assistance with metallographic preparation of the sample, Mr. Ziegner for XRD analysis, Mr. Borzikov for SNMS analysis as well as Dr. Shemet and Mr. Nowak for GDOES measurements.

In addition, I want to address thanks to my colleagues at IEK-2 for the nice environment to work in.

Finally, special thanks to my family and friends for their constant support and encouragements in countless issues.

Band / Volume 192
Analyse des Betriebsverhaltens von Hochtemperatur-Polymerelektrolyt-Brennstoffzellen
L. Lüke (2013), 150 pp
ISBN: 978-3-89336-909-6

Band / Volume 193
Full-waveform inversion of crosshole GPR data for hydrogeological applications
A. Klotzsche (2013), X, 164 pp
ISBN: 978-3-89336-915-7

Band / Volume 194
Long Term Stability and Permeability of Mixed Ion Conducting Membranes under Oxyfuel Conditions
X. Li (2013), III, 143 pp
ISBN: 978-3-89336-916-4

Band / Volume 195
Innovative Beschichtungs- und Charakterisierungsmethoden für die nasschemische Herstellung von asymmetrischen Gastrennmembranen auf Basis von SiO_2
J. Hoffmann (2013), V, 152 pp
ISBN: 978-3-89336-917-1

Band / Volume 196
Aerosol processes in the Planetary Boundary Layer: High resolution Aerosol Mass Spectrometry on a Zeppelin NT Airship
F. Rubach (2013), iii, 141 pp
ISBN: 978-3-89336-918-8

Band / Volume 197
Institute of Energy and Climate Research IEK-6: Nuclear Waste Management - Report 2011 / 2012 Material Science for Nuclear Waste Management
M. Klinkenberg, S. Neumeier, D. Bosbach (Eds.) (2013), 195 pp
ISBN: 978-3-89336-980-1

Band / Volume 198
Material migration in tokamak plasmas with a three-dimensional boundary
R. Laengner (2013), vi, 140, XVII pp
ISBN: 978-3-89336-924-9

Band / Volume 199
Improved characterization of river-aquifer interactions through data assimilation with the Ensemble Kalman Filter
W. Kurtz (2013), xxv, 125 pp
ISBN: 978-3-89336-925-6

Band / Volume 200
Innovative SANEX process for trivalent actinides separation from PUREX raffinate
A. Sypula (2013), 220 pp
ISBN: 978-3-89336-927-0

Band / Volume 201
Transport and deposition of functionalized multi-walled carbon nanotubes in porous media
D. Kasel (2013), 103 pp
ISBN: 978-3-89336-929-4

Band / Volume 202
Full-waveform inversion of surface ground penetrating radar data and coupled hydrogeophysical inversion for soil hydraulic property estimation
S. Busch (2013), 112 pp
ISBN: 978-3-89336-930-0

Band / Volume 203
Politikszenarien für den Klimaschutz VI – Treibhausgas-Emissionsszenarien bis zum Jahr 2030
Advances in Systems Analysis 5
P. Hansen, S. Gores und F. Chr. Matthes (Hrsg.)
(2013), XX, 257 pp
ISBN: 978-3-89336-932-4

Band / Volume 204
Effect of Composition, Microstructure and Component Thickness on the Oxidation Behaviour of Laves Phase Strengthened Interconnect Steel for Solid Oxide Fuel Cells (SOFC)
C. Asensio Jimenez (2014), 210 pp
ISBN: 978-3-89336-935-5

Weitere ***Schriften des Verlags im Forschungszentrum Jülich*** unter
http://wwwzb1.fz-juelich.de/verlagextern1/index.asp

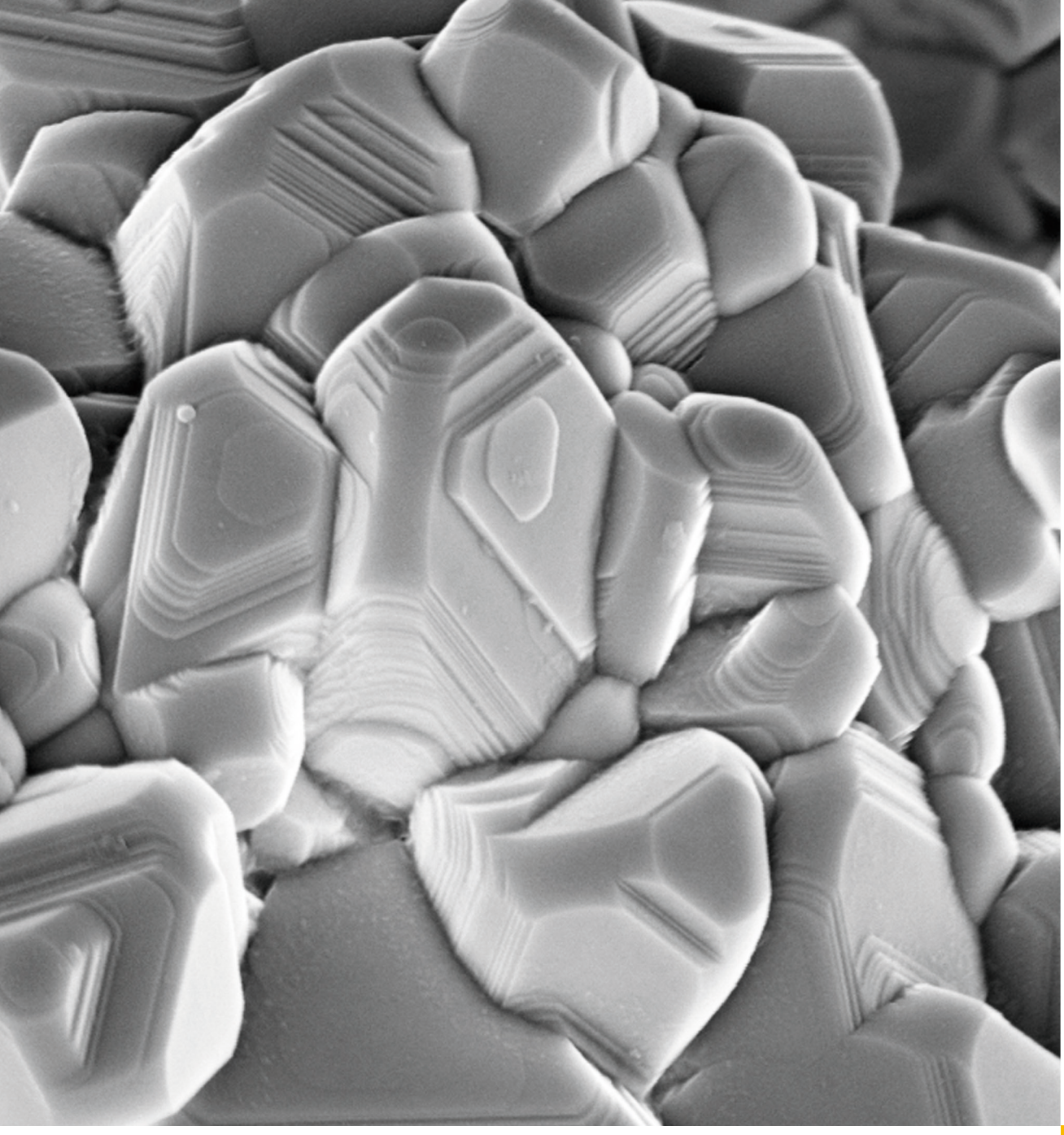

Energie & Umwelt / Energy & Environment
Band / Volume 204
ISBN 978-3-89336-935-5

JÜLICH
FORSCHUNGSZENTRUM